Discovery of small molecule inhibitors of immune checkpoint proteins

By

Evan Thomas Perry

Dissertation

Submitted to the Faculty of the

Graduate School of Vanderbilt University

in partial fulfillment of the requirements

for the degree of

DOCTOR OF PHILOSOPHY

in

Biochemistry

May 10th, 2019

Nashville, Tennessee

Approved:

Stephen W. Fesik, Ph.D.

Walter J. Chazin, Ph.D. (Chair)

Charles R. Sanders, Ph.D.

Jens Meiler, Ph.D.

Borden Lacy, Ph.D.

This work is dedicated to my loving wife, Anna, and our wonderful son, Hudson.

ACKNOWLEDGEMENTS

I would like to gratefully acknowledge and thank Dr. Stephen W. Fesik for his mentorship and guidance throughout my graduate studies. Steve has continuously set an exceptional example of a successful and passionate scientist that I strive to emulate. The training environment in the Fesik lab is unparalleled, and I would like to thank Drs. Taekyu Lee, Edward Olejniczak, Jason Phan and Alex Waterson for their mentorship in the Fesik lab. I would also like to think my committee members Drs. Walter Chazin, Chuck Sanders, Jens Meiler and Borden Lacy for their collective support, critical feedback, and career advice. I also wish to thank research scientists Bin Zhao and Feng Wang for their numerous contributions to my project and mentorship during my training. I also want to thank all staff, post-docs, and graduate students that I had the opportunity to work with at Vanderbilt. Best of luck in all your endeavors moving forward.

Drug discovery projects are team efforts and I have been fortunate to work with highly talented scientists. I thank Taekyu Lee for his exceptional leadership on my projects. I thank Feng Wang for his early contributions to the project prior to my entry to the lab. I also gratefully acknowledge his screening support, PD-L1 construct design, and assay development. I thank Bin Zhao for his important contributions in PD-L1 construct design and X-ray crystallography support. I thank John Sensintaffar, Tammy Sobolik and Stuart Fogarty for cell and biochemical assay support. I thank Tyson Rietz and Amyn Muriji for help with protein purification. I thank Chris Tarr, Jonathan Mills and Jianwen Cui for the medicinal chemistry support. Vanderbilt has outstanding research cores to support drug discovery. I would like to thank Corbin Whitwell and Josh Bower from the high throughput screening core for their assistance. I also thank Markus Voehler from the

biomolecular NMR center for his assistance for designing NMR experiments and troubleshooting. I thank Joel Harp from the X-ray crystallography core for his training in data processing and assistance in small molecule crystallography. Finally, I would like to thank Plamen Christov of the chemical synthesis core for synthesizing the macrocyclic peptide for the PD-L1 project.

Finally, I also gratefully acknowledge financial support from the NIH sponsored chemistry-biology interface training grant # 5T32GM065086. The biomolecular NMR facility at Vanderbilt University is supported in part by grants for NMR instrumentation from the NSF (0922862), NIH (S10 RR025677) and Vanderbilt University matching funds. Vanderbilt robotic crystallization facility is supported by NIH grant S10 RR026915. Use of the Advanced Photon Source was supported by the U.S. Department of Energy, Office of Science, Office of Basic Energy Sciences, under Contract No. DE-AC02-06CH113.

TABLE OF CONTENTS

Page
DEDICATION ii
ACKNOWLEDGMENTS iii
LIST OF TABLES viii
LIST OF FIGURES ix
Chapter
1 Introduction 1
1.1 Cancer and the immune system 1
1.2 CTLA-4 is a validated target for cancer immunotherapy 6
1.3 PD-1 is validated target for cancer immunotherapy 9
1.4 Current immunotherapy clinical trial landscape 11
1.5 Immune-related adverse events 14
1.6 Rationale for small molecule inhibitors of immune checkpoints 15
1.7 Fragment-based drug discovery 18
1.8 Scope of this thesis 23
2 Fragment Screen of CTLA 24
2.1 Introduction 24
2.1.1 CTLA-4 is a negative regulator of T cell activation 24
2.1.2 CTLA-4 Structure and function 24
2.1.3 CLTA-4 hotspot for small molecules 28
2.2 Results 30
2.2.1 Expression and purification of monomeric CTLA-4 30
2.2.2 Fragment screen of CTLA-4 33
2.3 Conclusions and Discussion 34
2.4 Methods 35
3 Fragment Screen of PD-1 38
3.1 Introduction 38

3.1.1 PD-1 is a negative regulator of T cell function 38
3.1.2 PD-1 Structure and function 40
3.1.3 PD-1 hotspot for small molecules 41
3.2 Results 45
3.2.1 Expression and purification of PD-1 45
3.2.2 Fragment screen of PD-1 46
3.2.3 Molecular modeling of PD-1 hits and analog screen 49
3.2.4 NMR-based PD-1 / PD-L1 displacement assay 51
3.3 Conclusions and Discussion 51
3.4 Methods 53
4 Fragment screen of Programmed Death Ligand PD-L1 (PD-L1) 57
4.1 Introduction 57
4.1.1 PD-L1 is a validated target for cancer immunotherapy 57
4.1.2 PD-L1 structure and function 58
4.1.3 PD-L1 hotspot for small molecules 59
4.2 Results 61
4.2.1 PD-L1 construct optimization 61
4.2.2 Expression and purification of PD-L1 70
4.2.3 Fragment screen of PD-L1 72
4.2.4 Hit classes from fragment screen 72
4.2.5 Fragment hit titrations 75
4.2.6 NMR displacement assay 78
4.2.7 PD-L1 hit clusters and analog screening 78
4.2.8 Co-crystal structures of fragments bound to PD-L1 81
4.2.9 Hit to lead optimization by structure-based design 87
4.2.10 High throughput screen of PD-L1 96

4.3 Conclusions and Discussion 97
4.4 Methods 99
5 Validation of literature reported PD-L1 inhibitors 105
5.1 Introduction 105
5.2 Results 108
5.2.1 Validation of Aurigene inhibitors 108
5.2.2 Validation of BMS macrocyclic peptide inhibitors 109
5.2.3 Validation of BMS small molecule inhibitors 113
5.2.4 Fragment incorporation into BMS macrocyclic peptides 119
5.2.5 Modification of the BMS macrocyclic peptide linker 122
5.2.6 Modeling of fragment analogs to mimic MCP interactions 123
5.3 Conclusions and discussion 125
5.4 Methods 126
6 General Conclusions and Future Outlook 130
Appendix A 135
Appendix B 148
BIBLIOGRAPHY 153

LIST OF TABLES

Table Page

Table 4-1: List of all PD-L1 constructs designed and tested……69

Table 4-2: Fragments that co-crystalized with PD-L1……84

Table 5-1: Synthesized PD-1/L1 inhibitors reported in the patent literature……108

LIST OF FIGURES

Figure Page

Figure 1-1: Cancer-Immunity Interface 4

Figure 1-2: Immune checkpoints that regulate T cell function 5

Figure 1-3: CTLA-4 inhibits T cell activation 7

Figure 1-4: Mechanism of PD-1 inhibition of effector T cell function 10

Figure 1-5: Timeline of immune checkpoint targeting monoclonal antibodies 12

Figure 1-6 Immune checkpoint inhibitor combinations in clinical trials 13

Figure 1-7: Overview of fragment-based drug discovery 19

Figure 1-8: 2D NMR methods for fragment screening 22

Figure 2-1: Inhibition of CTLA-4 restores T cell activation 25

Figure 2-2: CTLA-4 primary and tertiary structure 26

Figure 2-3 CTLA-4 bivalent binding modes to B7 proteins 27

Figure 2-4: CTLA-4 hotspot 29

Figure 2-5 Purification of CTLA-4 31

Figure 2-6: CTLA-4 mutants to produce monomeric CTLA-4 32

Figure 2-7 CTLA-4 chemical shifts seen in a “hit” of a mixture of 12 fragments 34

Figure 3-1: Targeting PD-1 pathway to reactive T cell activity against cancer cells 38

Figure 3-2: Previously identified PD-1 inhibitors 39

Figure 3-3: Structure of the extracellular portion of PD-1 41

Figure 3-4: PD-1/PD-L1 binding interaction 42

Figure 3-5: Conformational changes of PD-1 when bound to PD-L1 43

Figure 3-6: PD-1 binding hotspot 44

Figure 3-7: PD-1 protein purification 46

Figure 3-8: Mapping fragment binding site to PD-1 47

Figure 3-9: Molecular modeling of PD-1 fragment hits 48

Figure 3-10: Analogs of PD-1 fragment hits screened 49

Figure 3-11: PD-1 fragment hits fail to displace PD-L1 in solution 52

Figure 4-1: Structure of the extracellular portion of PD-L1 59

Figure 4-2: PD-L1 hotspot for small molecule binding 60

Figure 4-3: Preliminary PD-L1 constructs HMQC Spectra 62

Figure 4-4: Construct optimization overview 63

Figure 4-5: Construct design to improve protein stability 64

Figure 4-6: Design of H140E mutation on IgV-6His construct 67

Figure 4-7: PD-L1 IgV-6His is properly folded and binds to PD-1 68

Figure 4-8: PD-L1 protein production summary 71

Figure 4-9: Hit classes identified in the fragment screen 73

Figure 4-10: Class B hit validation 74

Figure 4-11: NMR Titrations of fragment hits 76

Figure 4-12: Fragment hits bind to the PD-1 binding site of PD-L1 77

Figure 4-13: PD-1 displacement assay by NMR spectroscopy 79

Figure 4-14: Percent rescue of PD-1 G90 with 2 mM VU0432747 80

Figure 4-15: Crystal packing of unliganded PD-L1 82

Figure 4-16: Co-crystal structures of fragments bound to PD-L1 83

Figure 4-17: PD-L1 homodimer hydrophobic pocket 85

Figure 4-18: Fragments bind to PD-L1 at the PD-1 binding site 86

Figure 4-19: Fragment binding to a PD-L1 dimer results in two binding poses 87

Figure 4-20: Triage of fragment hits to 3 lead series for medicinal chemistry 88

Figure 4-21: Series 1 hit to lead optimization 90

Figure 4-22: Series 2 hit to lead optimization 92

Figure 4-23: Series 3 analogs to determine fragment binding pose to PD-L1 monomer..... 93

Figure 4-24: Series 3 hit to lead optimization 94

Figure 4-25: Molecular modeling of fragment analogs..... 96

Figure 5-1: Aurigene reported peptidomimetic inhibitors of the PD-1 signaling pathway..... 105

Figure 5-2: BMS reported small molecule inhibitors of PD-L1 106

Figure 5-3: BMS reported macrocyclic peptides inhibitors of PD-L1 107

Figure 5-4: BMS macrocyclic peptide inhibitors bind to PD-L1 110

Figure 5-5: Biochemical assay development using a FITC-labeled macrocyclic peptide..... 111

Figure 5-6: BMS macrocyclic peptide has comparable activity to anti-PD-1 in vivo 112

Figure 5-7: BMS small molecule inhibitors bind to PD-L1 and form PD-L1 homodimers 114

Figure 5-8: BMS compounds co-crystalize as a PD-L1 homodimer 115

Figure 5-9: BMS small molecule and fragment structures have similar binding poses 116

Figure 5-10: BMS compounds are not active in a PD-L1 FPA assay 117

Figure 5-11: BMS small molecules are not active in PD-1 / PD-L1 cell-based assays..... 118

Figure 5-12: BMS MCP co-crystal structure reveals key interactions 119

Figure 5-13: Fragment incorporation strategy to macrocyclic peptide 121

Figure 5-14: Modification of the linker portion of the macrocyclic peptide..... 122

Figure 5-15: Macrocyclic peptide linker has inter and intra molecular interactions 123

Figure 5-16: Modeling of VU0432747 analogs that mimic MCP interactions 124

Chapter 1

Introduction

1.1 Cancer and the immune system

Cancer is now the second leading cause of death in the United States.[1] In 2018 alone, 1,735,350 new patients are expected be diagnosed with cancer resulting in 609,640 deaths in the United States.[1] Furthermore, cancer diagnoses are expected to double by 2030.[2] The toll of cancer is not only felt through the number of lives lost but also by the significant economic impact. The estimated financial burden of cancer in the United States in 2014 was $87.6 billion alone.[2] While these numbers are troubling, a significant amount of process has been made in combating this deadly disease since President Nixon's infamous declaration of a national "War on cancer" in 1971 by signing the National cancer act. Indeed, the annual death rate attributed to cancer has been steadily declining the past 2 decades and has dropped a total of 26% since 1990, corresponding to approximately 2.1 million fewer deaths than what would have been expected.[2] The decline in cancer-related deaths are attributed to the tremendous scientific advances made in understanding cancer at the molecular level. We now understand that cancer is a result of mutations, aberrant protein expression, or the ineffective turnover of proteins that drive tumorigenesis.[3] These advances have allowed a transition from a "one size fits all" therapeutic approach, for example chemotherapy, to the era of rationally designed therapeutics that target specific signaling pathways that are defective in a specific cancer.[4]

Targeted therapies allow healthcare providers to personalize therapeutic strategies based on the molecular cause of cancer revealed by gene sequencing and pathology of the tumor from the individual patient.[5] Indeed, targeted therapies and personalized medicine have played a large role in the recent successes of fighting cancer.[6] However, cancer is a heterogeneous disease and developing targeted therapies that are effective for all patients remains a difficult challenge.[7] Furthermore, cancer cells are constantly evolving which often results in resistance to targeted therapies in many patients.[7] Mechanisms of resistance previously identified in clinical studies include mutation of the drug target that negates drug binding, reactivation by the signaling pathway via another mechanism, or activation of an alternative pathway.[8, 9] Thus, new therapeutic approaches that account for the heterogeneous and elusive nature of cancer are urgently needed to make cancer therapies more effective.

The immune system is adequately equipped to combat cancer due to the high degree of specificity and adaptability that can match the heterogeneity of cancer.[10] Furthermore, the immune system can protect against similar cancers from reappearing by developing immunological memory against cancer cells. The genetic and epigenetic alterations that take place in all cancer cells provide numerous mutated or aberrantly expressed proteins (termed neoantigens) that immune cells can use to differentiate a cancerous cell from normal cells, by a process referred to as immune surveillance.[11] Indeed, seminal studies by Schreiber and colleagues in 2001 were the first to demonstrate that $CD8^+$ cytotoxic T cells protect against carcinogen-induced cancers in mice.[12] Unless

otherwise noted, the term "T cell" will refer to $CD8^+$ cytotoxic T cells for purposes of this thesis.

Since these studies, efforts to invigorate the immune system by the development of vaccines and T cell activating cytokines were largely unsuccessful and little was known why these approaches were ineffective.[13] However, recent developments have further elucidated the cellular and molecular mechanisms that orchestrate the complexities of T cell function.[10] These discoveries have resulted in a greater understanding of how T cells modulate anti-tumor responses allowing for the design of novel therapeutic strategies to activate the immune response towards cancer.[11]

T cell immunity includes multiple sequential steps involving clonal selection, activation, and proliferation by dendritic cells, trafficking, recognition, and elimination of foreign antigen displaying cells (Figure 1-1).[14] A major breakthrough in cancer immunotherapy was the discovery that T cell activation and function is highly regulated by an intricate balance between activating and inhibitory signaling pathways, termed immune checkpoints (Figure 1-2).[11] These checkpoints either inhibit or activate T cell activity at differences stages of the T cell life cycle. Under normal physiological conditions, the inhibitory checkpoints avoid uncontrolled immune responses, protect healthy cells from collateral damage during an immune response, and prevent autoimmunity.[15]

James Allison and colleagues were the first to hypothesize that inhibiting negative immune checkpoints with therapeutics could enhance the anti-tumor activity of T cells.[16] Indeed, monoclonal antibodies (mABs) that target the first two inhibitory immune

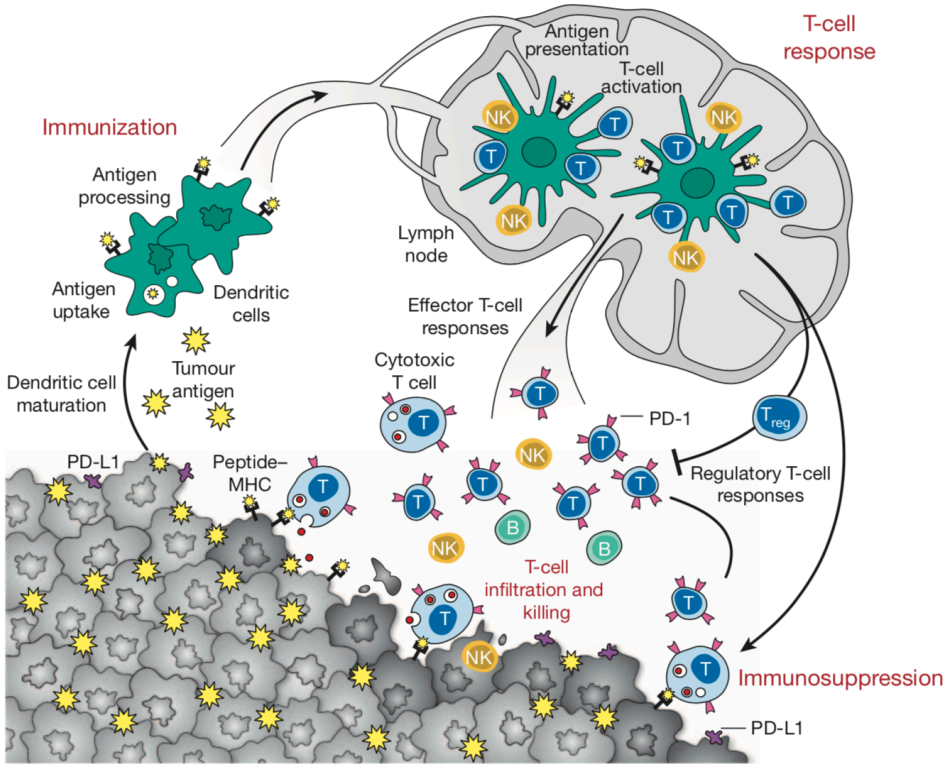

Figure 1-1: Cancer-Immunity Interface

The complex interactions of the immune system with cancer cells (gray). Tumor antigen (yellow stars) are taken up by dendritic cells and used to activated T cells in the lymph node. Activated T cells with TCR that recognize tumor antigen then migrate to the tumor microenvironment where they bind to antigen-MHC complexes and kill the cancer cells. Image adapted from Mellman *et al*, 2011.[14]

checkpoints identified, cytotoxic T-lymphocyte-associated protein 4 (CTLA-4) and programmed cell death protein 1 (PD-1) demonstrated remarkable success in patients with advanced staged melanoma.[17] Because these therapies target the immune system and not the cancer cell, these therapeutics could be effective in many different histologic cancers and cancers caused by different genetic lesions.[10] To date, both CTLA-4 and PD-1

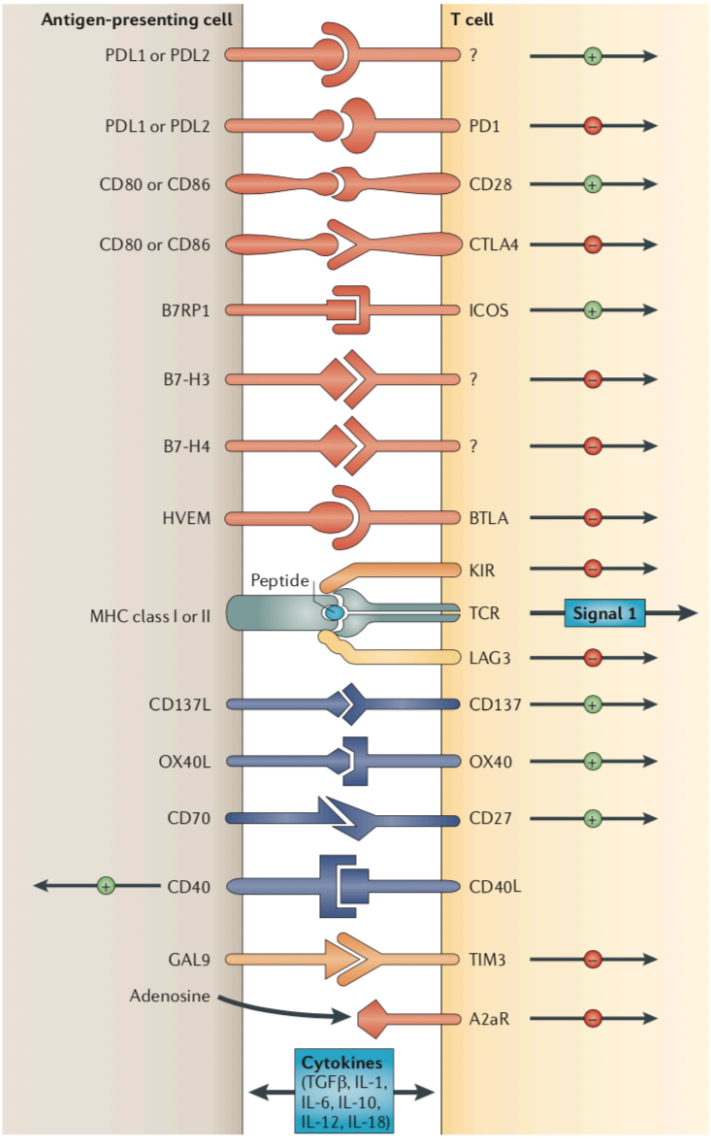

Figure 1-2: Immune checkpoints that regulate T cell function

Recently identified activating and inhibitory immune checkpoint interactions that regulate T cell activation and function. Image adapted from Pardoll 2012.[11]

blocking agents have demonstrated durable responses in 11 different cancer types and their indications are continuously expanding.[18] Theses success combined with the success of other immune activating therapies including anti-tumor vaccines, CAR T cells, oncolytic viruses, and bi-specific T cell engagers fusion proteins (BiTEs) were designated as

"breakthrough of the year" by science in 2013 and are revolutionizing the way physicians treat many cancer patients.[19-22] Indeed, immunotherapy is now considered the 5th pillar in cancer care alongside surgery, radiation, targeted therapy, and chemotherapy.[23]

1.2 CTLA-4 is a validated target for cancer immunotherapy

T cell activation is a highly regulated process to avoid over-stimulation of the immune response.[24] Antigen presenting cells (APCs) process tumor-specific proteins that originate from aberrant expression and/or highly mutated proteins originating from tumor cells. APCs present small peptide segments of the tumor-specific protein bound to the major histocompatibility complex (MHC) on the surface of the cell to interact with the TCR on naïve T cells.[25] If the TCR of a naïve T cells binds to the antigen-MHC complex, the first activation signal is sent via TCR signaling. A secondary co-stimulatory signal by CD28 binding to either B7-1 or B7-2 (also known as CD80 and CD86, respectively) is also required for T cell activation.[26] Sufficient levels of CD28: B7 stimulatory signaling causes the production of interleukin 2 (IL-2) resulting in T cell proliferation and cell survival (Figure 1-3A). Activated T cells migrate to the tumor microenvironment and eliminate cells that display the tumorigenic antigen bound to MHC molecules.[24]

T cell activation is counterbalanced by the inhibitory co-receptor CTLA-4.[27] The importance of CTLA-4 is demonstrated by the lethal T cell proliferative disorder found in CTLA-4 knockout mice.[28] In naïve T cells, CTLA-4 is sequestered in intracellular vesicles. TCR: MHC signaling causes CTLA-4 to be translocated to the surface of the T cell.[29] The

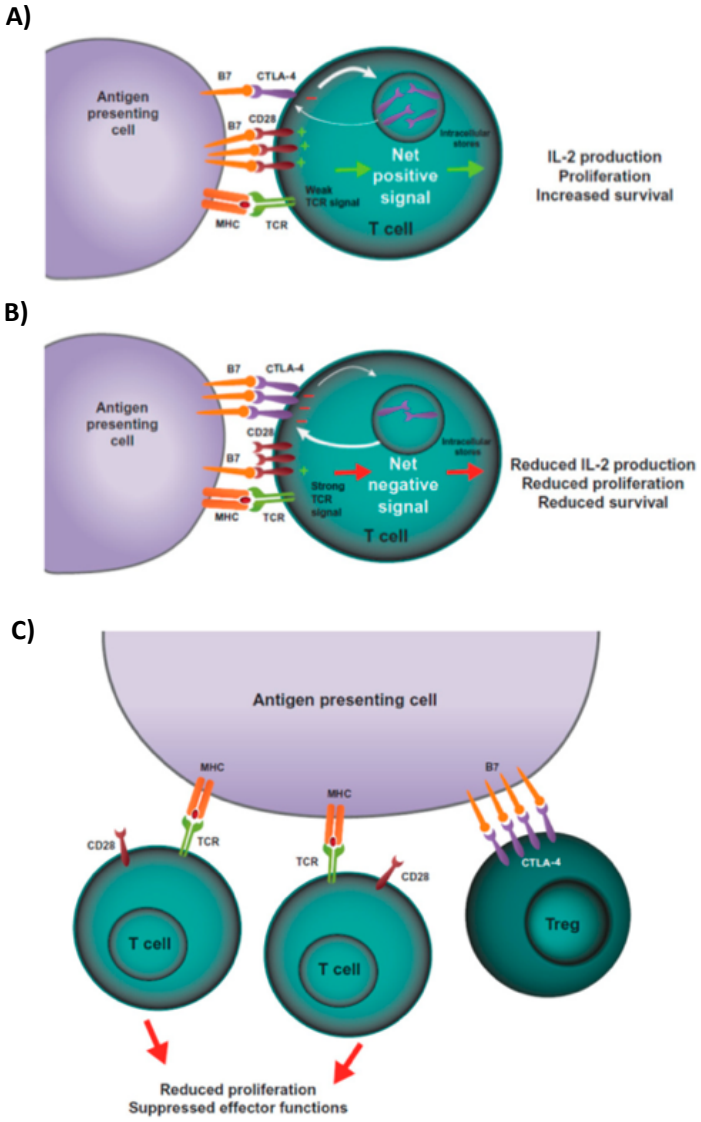

Figure 1-3: CTLA-4 inhibits T cell activation

CTLA-4 mechanism of T cell activation. A) When TCR recognizes MHC-antigen complex T cells are primed for activation by the co-stimulatory signal CD28 binding to B7. B) After TCR signaling CTLA-4 is translocated to the cell membrane and outcompetes CD28 for binding to B7 preventing activation. C) Cell extrinsic mechanisms of inhibition by CTLA-4 expression on Treg cells that can compete with CD28 for binding to B7. Image adapted from Buchbinder et al. 2016.[31]

amount of CTLA-4 that is translocated is proportional to the strength of the TCR signal creating a graded inhibitory feedback loop of T cell activation (Figure 1-3).[30, 31] CTLA-4 is a homolog of CD28 but binds to B7-1 and B7-2 with higher affinity (> 7 fold).[32] Thus, the

proposed mechanism of CTLA-4 mediated T cell inhibition is by outcompeting CD28 for binding to B7-1 and B7-2 preventing the secondary co-stimulatory signal (Figure 3B).[33] However, more recent data suggest CTLA-4 may inhibit T cell activation by cell-extrinsic mechanisms.[34] CLTA-4 is highly expressed on Treg cells and can bind to B7 ligands on the APC preventing CD28 co-stimulation (Figure 3C).[35] Interestingly, Treg cells can also physically remove B7 ligands from APC cells by trans-endocytosis.[36] While the precise mechanism(s) of CTLA-4 is currently debated in the literature, inhibition of CTLA-4 has been demonstrated to be a highly validated strategy to reverse the inhibition of T cell activation.

Preclinical studies of CTLA-4 blocking antibodies achieved complete tumor rejection and long-lived immunity in mouse models with immunogenic tumors.[16] These results translated into human clinical trials using an anti-CTLA-4 fully humanized antibody (ipilimumab, developed by Medarex and Bristol-Myers Squibb).[37] Ipilimumab demonstrated a 3.5-month survival benefit for patients with advanced melanoma compared to a melanoma-specific protein vaccine (gp100).[37] Strikingly, 20% of patients treated with ipilimumab demonstrated long-term durable responses.[38] Notably, ipilimumab was the first therapy to significantly improve the survival of metastatic melanoma patients.[39] Recent updates from this clinical trial indicate that a subset of these patients are cancer free 10 years post-treatment.[40] Given these successes, ipilimumab was FDA approved in 2010 for patients with advanced melanoma.[41] Ipilimumab has also resulted in tumor regression in phase I/II clinical trials in patients with renal cell

carcinoma, prostate cancer, urothelial carcinoma, and ovarian cancer.[42-44] Many other clinical trials for ipilimumab and other anti-CTLA-4 antibodies are currently ongoing.

1.3 The PD-1 signaling pathway is a validated target for cancer immunotherapy

Shortly after the success of CTLA-4, another inhibitory checkpoint protein was identified termed programmed cell death 1 (PD-1).[45, 46] PD-1 is expressed on activated T cells and inhibits T cell activity when bound to its ligands PD-L1 and PD-L2.[47] PD-L2 is primarily expressed on antigen presenting cells whereas PD-L1 is expressed on many cell types including immune cells, epithelial cells, and endothelial cells.[10] Thus, PD-L1 mediated PD-1 signaling is thought to be a key regulator of immune homeostasis by controlling inflammation in the periphery.[48, 49]

Upon antigen recognition, T cells produce inflammatory cytokines that initiate an immune response. Pro-inflammatory cytokines released from immune cells, namely interferon gamma (IFN-γ), result in PD-L1 expression in cells (Figure 1-4).[50] When engaged to PD-L1, PD-1 recruits SHP phosphatases to its ITIM signaling motifs causing dephosphorylation of ZAP70 and PI3K which ultimately results in decreased cytokine production, cell cycle arrest and a decrease in the pro-survival factor Bcl-X_L.[51] The final result is the inactivation of the T cell and the survival of the target cell.[52] Failure to counterbalance T cell activity can cause serious immune-related tissue damage that can be fatal to the host.[53] Indeed, PD-1 or PD-L1 deficient mice develop lethal immunopathology following chronic infection with a lymphocytic choriomeningitis virus.[54] In addition to downregulating inflammation, PD-1 also plays a role in regulating

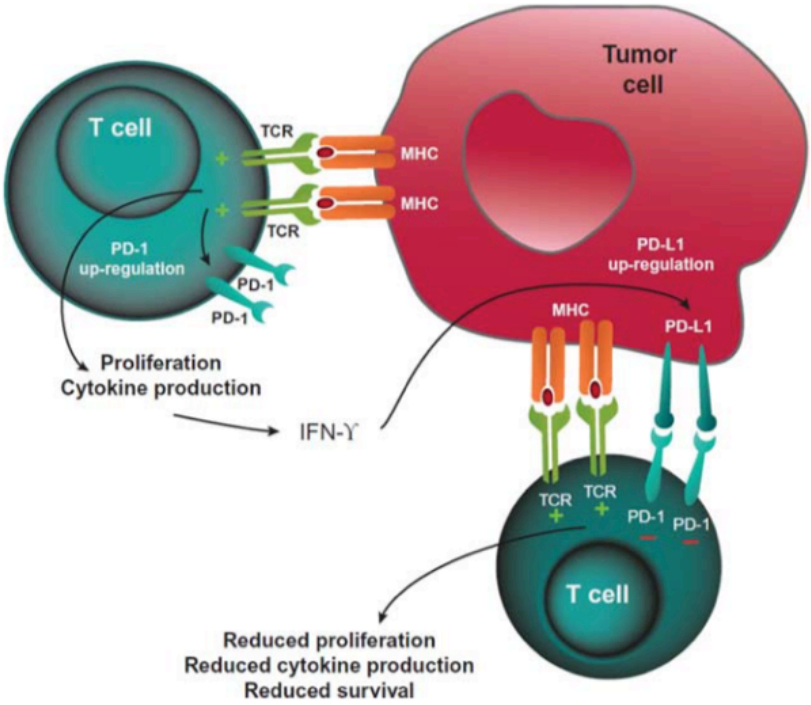

Figure 1-4: Mechanism of PD-1 inhibition of effector T cell function.

PD-1 is expressed after T cell activation and is inhibited by binding to its ligand PD-L1. PD-L1 expression is induced by IFN-gamma release from T cells and by oncogenic activation. Image adapted from Buchbinder et al. 2016.[31]

autoimmunity.[55] The activation, proliferation, and differentiation of T cells that recognize healthy cell antigens (autoreactive T cells) are downregulated by PD-1 signaling. The diverse functions of how PD-1 regulates immune homeostasis remains a highly active area of research.

Given these mechanistic insights, PD-1 has obvious implications in cancer therapy.[56] Indeed, many different types of cancer cells have been shown to upregulate expression of PD-L1 by the activation of myc and other oncoproteins. [57, 58] The overexpression of PD-L1 on tumor cells is thought to be one of the major mechanisms by which cancer cells evolve to evade the immune response. Indeed, PD-L1 expression on

cancer cells induced by INFγ and by oncogenic activation generally correlates with a poor prognosis compared to PD-L1$^-$ tumors in a variety of different cancer types.[59-61] PD-1 and PD-L1 blocking mABs have been developed to remove the immune evasion mechanism of cancer cells and "release the brakes" from cancer-specific T cells.

PD-1 and PD-L1 blocking mABs have been developed to remove the immune evasion mechanism of cancer cells and "release the brakes" from cancer-specific T cells. The first clinical trials of these agents in 2010 resulted in antitumor activity in patients with colorectal cancer, melanoma, and renal cell carcinoma with acceptable toxicity profiles.[11] Since then the FDA has approved anti-PD-1/PD-L1 agents in a large variety of cancers including melanoma, non-small cell lung cancer, MSI-H/dMMR cancers, renal cell carcinoma, Hodgkin's lymphoma, urothelial carcinoma, head and neck squamous cell carcinoma, Merkel-cell carcinoma, hepatocellular carcinoma, and gastric cancer within a 4-year period (Figure 1-5). While the response rate is relatively low (20 – 30%), patients that respond to anti-PD-1 therapy have remarkable long-term durable responses.[62] To date, there are 5 anti-PD-1/PD-L1 antibodies that are FDA approved in 11 different cancer indications that are continuously expanding (Figure 1-5). Taken together, the development of therapeutics that target the PD-1 pathway has been one of the most important advances in the history of cancer treatment.[17]

1.4 Current immunotherapy clinical trial landscape

One of the major questions that have resulted from both CTLA-4 and PD-1 blocking therapy is why a 70 to 80% of patients fail to respond.[63] The heterogeneous

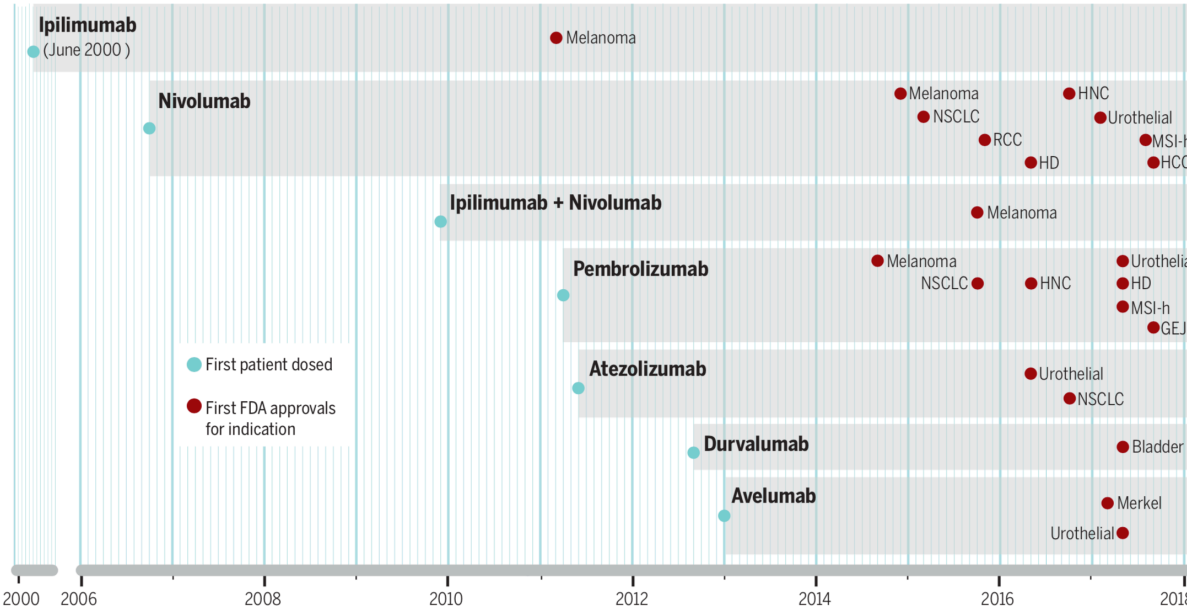

Figure 1-5: Timeline of immune checkpoint targeting monoclonal antibodies

Blue dot indicates first patient dosed. Red dot indicates first FDA approval for indication. Ipilimumab is a anti-CTLA-4 antibody. Nivolumab (BMS) and Pembrolizumab (Merck) are anit-PD-1 antibodies. Atelizumab (Genentech/Roche), Durvalumab (Medimmune/AstraZeneca) and Avelumab (Merck/Pfizer/Eli Lilly) are anti-PD-L1 antibodies. Figure adapted from Ribas et al. 2018 [17]

response to these agents has resulted in large efforts to develop biomarkers to predict clinical responses. Current biomarkers that are being used include PD-L1 expression on tumor and immune cells [64], mutational/neoantigen load [65, 66], and inflammatory gene signatures [67, 68]. However, the complexity of the cancer-immunity response has made finding reliable markers that correlate with clinical responses challenging.[69] In parallel, massive efforts have been placed on designing combination studies to try and improve the overall response rate and improve the quality of the response.[68] Because the CTLA-4 and PD-1 checkpoint pathways have different mechanisms of T cell regulation, combinations of the two checkpoint inhibitors are predicted to be synergistic and increase the response rate. This combination was tested in melanoma patients and resulted in

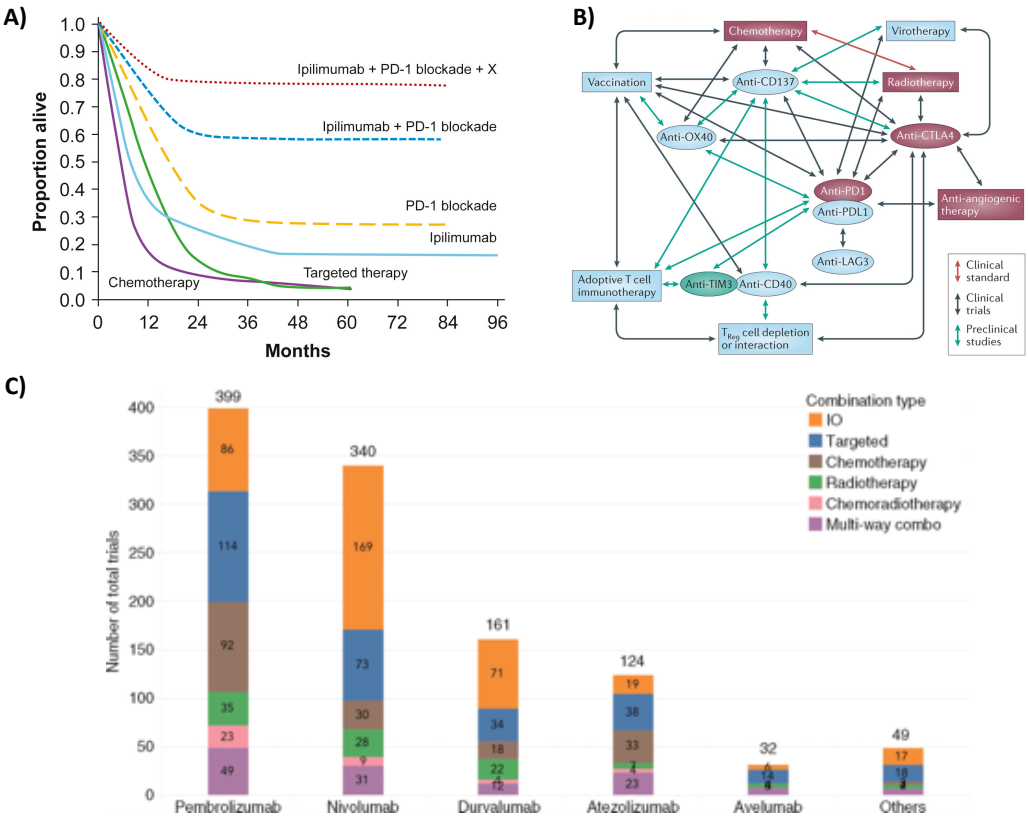

Figure 1-6 Immune checkpoint inhibitor combinations in clinical trials.

A) Representative survival curve of chemotherapy, targeted therapy, CTLA-4 and PD-1 monotherapy and combination of CTLA-4 and PD-1 compared to a hypothetical survival curve of CTLA-4, PD-1 and some other therapy designated X. B) Diagram of combinations clinical trials combining different aspects of cancer therapies. C) Number of clinical trials ongoing for PD-1/PD-L1 inhibitors. A) adapted from Emens et al 2017,[62] B) adapted from Melero et al. 2015,[71] C) adapted from Tang et al. 2018.[72]

greater than 50% response rate which is approximately 2 times higher than either alone (Figure 1-6A).[70] However, this combination also resulted in significantly higher incidents of high-grade toxicities (60%) than seen in either therapy alone.[70]

With precedent for synergistic combinations, there are now considerable efforts to find additional combinations with checkpoint mABs that increase the response rate while limiting immune-related adverse events (irAEs).[68] The primary rationale is to utilize

chemotherapy, radiotherapy or targeted therapy that cause cancer cell death and the release of a diverse set of cancer antigens that can activate naïve T cells. Activated tumor-specific T cells that recognize a diverse series of tumor antigens in the presence of immune activators may generate a higher response rate than seen in previously (Figure 1-6A, red dashed line).[62] Indeed, there are currently over 1,000 clinical trials involving anti-PD-1/PD-L1 antibodies as monotherapy or in combination with numerous diverse therapies including chemotherapy, radiotherapy, virotherapy, targeted therapies, vaccines, and other immune modulators (Figure1-6 B-C).[71, 72] Preliminary data from many of these trials are promising and the results will lead to a greater understanding of how to further optimize checkpoint immunotherapy.[73]

1.5 Immune-related adverse events

Therapies that activate the immune system can result in irAEs. The prevalence, severity, and management of various irAE's with checkpoint inhibitors in many cancer types have been reviewed extensively.[70, 74-82] In large clinical trials, approximately 70% of patients treated with anti-PD-1 antibodies as a single agent have documented treatment-related AEs (of any grade), with 35% of patients needing immunosuppressants to control irAEs.[70, 78] While most of these adverse events are low grade, high grade irAE's occur in 14% of patients with 7% of patients ultimately discontinue treatment.[83-86] While every organ system can be affected by these therapies, the most common irAEs include dermatitis, hepatitis, endocrinopathies, and pneumonitis.[87-93] Less frequent irAEs have been reported that affect the renal, cardiac, neurological, ocular and pancreatic systems.[84, 86, 88, 89, 94-100] Permanent thyroid dysfunction, type 1 diabetes, and deaths

resulting from cardiotoxicity and pneumonitis have also been reported.[83, 92, 101-103] While there are now trials to lower the doses of these antibodies to limit the toxicities, higher toxicity rates are expected in combination with other therapies in attempt to increase the clinical efficacy rate.

1.6 Rationale for small molecule inhibitors

Therapeutic antibodies that selectively target immune checkpoints have been successful as single agents in numerous clinical trials. Although the current antibody-based therapies can offer substantial benefits, there are inherent drawbacks to therapeutic antibodies that have implications when targeting immune modulating signaling pathways.[104] First, PD-1 expressing effector T cells are found to be infiltrated within the solid tissue of PD-L1 expressing tumors. Deep tissue penetration of antibodies is problematic due to their large size (150 kDa) and may suggest why current therapeutics have sub-optimal efficacy.[104, 105] Another inherent problem with antibodies is the presence of the Fc chain that may have off-target immune responses by macrophages and natural killer cells.[106] Given that both PD-1 and PD-L1 are expressed on effector T cells, antibodies that bind to either protein may counterproductively deplete effector T cells via Fc mediated cytotoxicity.[104] Indeed, clinical data suggests there is a correlation between anti-PD-1 antibodies and lower amounts of circulating effector T cells in patients.[107]

Furthermore, currently used antibodies have half-lives on the order of 3 to 4 weeks.[107] In fact, the current antibodies bind PD-1 with such high affinity, they stay engaged to the receptor for more than 2 months after circulating antibodies have been

cleared from the system.[87, 107] Long-term inhibition of the CTLA-4 and PD-1 signaling pathways can potentially result in off-target T-cell activation to induce unexpected autoimmunity.[74] Indeed, clinical data suggests that long term immune checkpoint blockade is a significant contributor to irAEs.[87, 107] Hence, other blocking agents with improved toxicity profiles may offer a more tolerable combinatorial therapy for cancer patients.

These disadvantages of mABs have been partially corroborated by a group that engineered PD-1 (15 kDa) with a series of mutations that resulted in a 30,000 fold increase in binding to PD-L1.[104] When compared to an anti-PD-1 antibody using *in vivo* tumor models, the PD-1 mutant demonstrated superior tissue penetration, maintained normal peripheral effector T cell counts and had superior tumor suppression efficacy. These findings suggest therapeutic strategies to inhibit PD-L1 / PD-1 signaling in the tumor microenvironment can be further optimized by using low molecular weight inhibitors of PD-L1 compared to the large antibodies used currently.

An alternative therapeutic approach is to use small molecules to block the PD-1 / PD-L1 or CTLA-4 / B7 interactions. Small molecule inhibitors of these pathways have the potential to address the problems associated antibody-based therapeutics. A small molecule inhibitor could be more cost-effective, have enhanced tumor penetration, and will not deplete T cells via Fc mediated toxicity mechanisms. Because the pharmaceutical and pharmacokinetic profile of a small molecule can be more easily modulated during the drug discovery process, they offer the potential for designing inhibitors with shorter half-lives and enhanced tissue penetration and distribution. Small molecule inhibitors with

dynamic pharmacokinetic profiles will allow for patient-dependent dosing strategies to achieve the maximum efficacy while minimizing irAEs, thereby broadening the therapeutic window. If significant irAEs are detected, a small molecule inhibitor would be rapidly cleared from the body such that treatment could be simply discontinued rather than supplementing with high doses of steroids with their own set of toxicities into the patients. As clinicians expect greater adverse effects from immunotherapy combinations moving forward, small molecule inhibitors can potentially lower significant immune-related toxicities to allow for more successful combinatorial immunotherapies.

In addition to toxicity, the expense of using antibodies as single agents and in combination is a significant concern. Given that the production of antibodies is a complex process, they generally have a higher cost of production and are more expensive compared to small molecule therapeutics.[108] Indeed, pembrolizumab (Merk's anti-PD-1 antibody) costs $150,000 per patient per year and a combination of pembrolizumab with Ipilimumab (BMS's anti-CTLA-4 antibody) costs $254,000 per patient per year.[109] Expensive therapeutics place a large burden on both patients and health care systems throughout the world. In fact, the National Institute for Health and Care Excellence (NICE) that advises English and Welsh sectors of the U.K.'s National Health service has recently rejected Nivolumab (BMS's anti-PD-1 antibody) for patients with head and neck cancer because Nivolumab's price is too high.[110] Hence, the development of a PD-L1 small molecule inhibitor with a lower cost of production could greatly reduce the expense of this therapy making the promising advances of immunotherapy available to patients in

health care markets throughout the world and to patients who cannot afford the current therapeutics.

Despite these potential advantages, the discovery of small molecule inhibitors has lagged behind mABs. This is likely because CTLA-4, PD-1 and PD-L1 proteins are predicted to be highly challenging drug targets for small molecules.[111] The protein-ligand interaction interfaces are large (> 1,200 A^2) and lack deep hydrophobic pockets traditionally found in more druggable proteins.[112] Consistent with this notion, no small molecule inhibitors have entered clinical trials for CTLA-4 or PD-1. A peptidomimetic inhibitor of PD-L1 from Curis Inc. has entered clinical trials, but the series of these molecules lack direct binding data to PD-L1.[113, 114] We (and others)[115] have profiled these compounds and found no direct binding to either PD-1 or PD-L1, suggesting an alternative mechanism for these compounds. Thus, there is a need for the development of novel small molecule inhibitors of CTLA-4, PD-1, and PD-L1.

1.7 Fragment-based drug discovery

Protein-protein interactions that consist of flat and large surface areas can be extremely difficult to target by small molecules. Given that many validated cancer targets are also some of the most challenging for small molecules, many have explored novel drug discovery methods to discover small molecules that bind to challenging targets. Fragment-based drug discovery (FBDD) methods in combination with structure-based

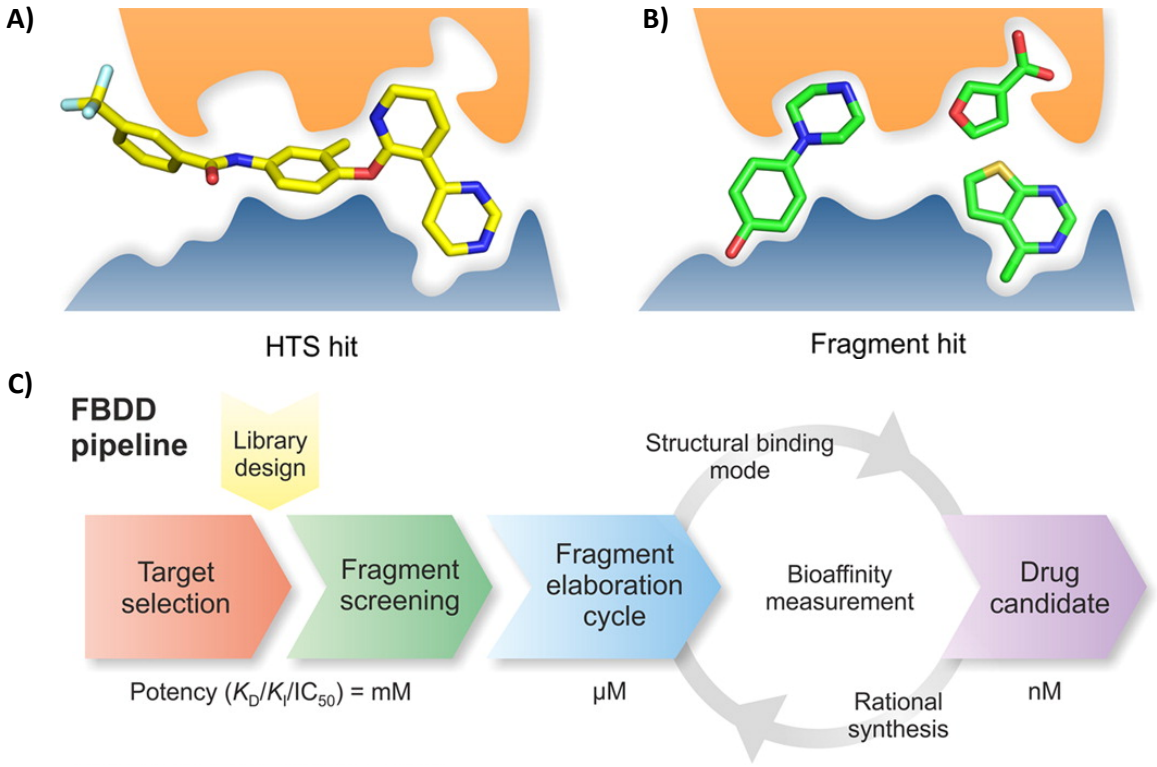

Figure 1-7: Overview of fragment-based drug discovery

Overview of FBDD. A) Hypothetical hit compound identified from an HTS screen. Ligand binds with moderate affinity but fails to occupy all sub-pockets at the binding site. B) Hypothetical fragment hit identified from a fragment screen. Fragments binds with lower affinity but more efficiently occupy sub-pockets at the binding site. C) Optimization of fragments is an iterative process involving many rounds of structure determination, modeling and rational synthesis and determination of binding affinities. Images adopted from Scott et al 2012. [122]

design was first shown by Fesik and co-workers at Abbott labs to be a highly effective way to target difficult targets.[116] Over the past 20 years, FBDD has been used to successfully generate high-affinity ligands to targets that were previously thought to be "undruggable". Examples include Venetoclax and Vemurafenib that are FDA approved to target Bcl-2 and B-Raf(V600E), respectively.[117, 118] There are many more molecules that originated from fragments that are currently in optimization development and clinical trials.[119]

Fragment-based approaches consist of screening low molecular weight "fragments" (less than 300 Dalton) for direct binding to the protein. Fragments can cover more chemical space with much smaller libraries compared to traditional high throughput screening (HTS) methods that use compounds with higher molecular weights.[120] The number of hits per number of compounds screened (hit rate) from an HTS screen can be low depending on the druggability of the target and hits are predicted to bind with lower micromolar affinity. Given the complexity of the molecules, they often make numerous suboptimal interactions in the binding pocket requiring extensive SAR to optimize compound binding (Figure 1-7A).[121] Conversely, fragments make fewer interactions that are often higher quality and result in high ligand efficiency (Figure 1-7B).[122] Thus, fragment screens often identify chemotypes that bind to proteins containing shallow binding pockets that would otherwise be missed in a HTS screen.[120] However the binding affinity of fragments are typically in the high micromolar to low millimolar affinity due to their small size and need extensive optimization to discover drug-like molecules.

With structural information of fragments bound protein, fragments can be further optimized to bind to the target with high-affinity using multiple structure-based design strategies. If two fragments were identified in the screen to bind in close proximity, fragments can be covalently linked to rapidly increase the binding affinity. Indeed, the predicted binding affinity of a linked compound is equal to the product of the K_d of the first ligand and the K_d of the second ligand multiplied by a linking constant ($K_d$linked = K_d1st * K_d2nd * L).[116] If all fragments identified in the screen bind to the same location on the protein, typically a second fragment screen is necessary to find fragments that bind to

an adjacent pocket that may be induced by the first fragment binding. To conduct a second site screen, the first fragment is often optimized by fragment growing or fragment merging approaches to improve the binding affinity of the first ligand. The library is then screened again at saturating concentration of the first-site ligand. Lead compounds are iteratively optimized to improve binding affinity using structural information obtained by X-ray crystallography or NMR and molecular modeling experiments to generate high-affinity molecules (Figure 1-7C).[121]

Fragment-based methods require a reliable assay to monitor the binding of compounds with weak binding affinities (< 5 mM). Compared to other biophysical methods, protein observed NMR is arguably the most robust method for conducting fragment-based screens.[123] This method utilizes uniformly ^{15}N (or ^{13}C) labeled protein and obtaining $^{1}H/^{15}N$ (or ^{13}C) HSQC spectra of the protein of interest in the presence and absence of fragment mixtures (Figure 1-8). Peaks observed in HSQC spectra correspond to the amide backbone NH groups on the protein. Each peak in the HSQC spectrum corresponds to a specific amino acid in the protein. Ligand binding to the protein causes chemical shift changes in peaks at the protein binding site. The chemical shift changes can be easily observed by overlays of an HSQC with and without ligands (Figure 1-8C). Advantages of screening by protein-observed NMR methods include (1) monitoring of the

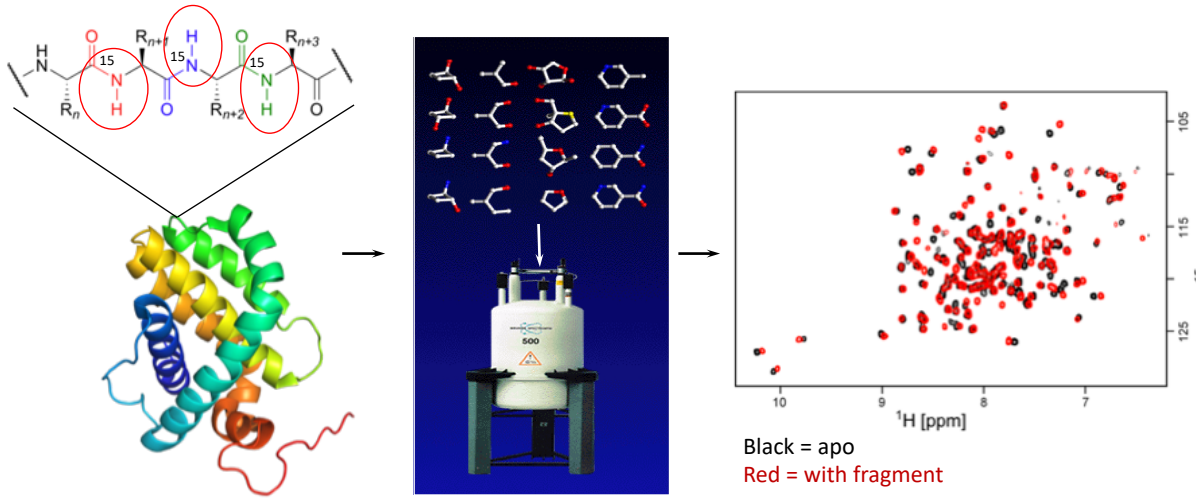

Figure 1-8: 2D NMR methods for fragment screening.

Overview of fragment screening by 2D NMR. Protein of interest is 15N labeled by expression in 15N rich media. Purified 15N labeled protein is mixed with fragment mixtures. A HSQC or similar experiment is run on an NMR spectrometer to generate a HSQC Spectrum. Overlays of spectra with and without fragment reveals fragment interacting with the protein by observation of chemical shift changes in peaks. Each peak corresponds to an amino acid on the protein and can be used to map the binding site of the fragment to the protein structure if the resonance assignments are known.

direct interaction with the protein that results in very few false positives; (2) ability to measure the binding affinity without the need for a secondary assay; (3) ability to distinguish between fragments that bind to different sites on the protein by monitoring chemical shift patterns; and (4) ability to identify binding sites on the protein if the backbone resonance assignments are known.[123, 124] Additionally, recent advances in NMR technologies have allowed for rapid acquisition of ^{1}H/^{15}N HMQC spectra and automated sample changers allowing for fragment screening by NMR to be a medium throughput assay.[125]

If the protein structure of a target is known prior to the screen, druggability analysis by various algorithms can be used to identify “hotspots” for small molecules and

predict the ability to find hits from a screen.[126, 127] However, these computational methods often assume a rigid protein and fail to account for protein dynamics or ligand-induced binding. Thus, experimental assessments of a target's druggability are often warranted. Previous studies have demonstrated that fragment screening by NMR has a high correlation with the ability to identify high-affinity protein ligands.[128] Indeed, experimental evidence suggests targets with hit rates > 0.1% from a fragment screen are likely druggable targets. Thus, fragment screens can be used to experimentally assess protein druggability and aid in important decisions about the prioritization of targets in a drug discovery program.

1.8 Scope of this thesis

In the following chapters, I describe my efforts to develop novel small molecule inhibitors of the immune checkpoints CTLA-4, PD-1 and PD-L1 using fragment-based methods and structure-based design. In chapter 2, I describe the design of a monomeric CTLA-4 construct and the results of a fragment-based screen of monomeric CTLA-4. In chapter 3, I describe results of a fragment-based screen of PD-1, results from an analog screen and preliminary hit validation. In chapter 4, I describe efforts to optimize a PD-L1 construct to conduct a fragment screen, the results from the fragment screen, hit validation and optimization of fragment hits by structure-based design. In chapter 5, I describe efforts to validate literature reported PD-1 and PD-L1 inhibitors and efforts to merge fragment hits with other inhibitors. In chapter 6, I summarize all results and discuss the future direction for the development of small molecule inhibitors of these highly validated but challenging targets.

Chapter 2

Fragment Screen of Cytotoxic T-lymphocyte Associated Protein 4 (CTLA-4)

2.1 Introduction

2.1.1 CTLA-4 is a negative regulator of T cell activation

After T cells are primed for activation by TCR signaling, CTLA-4 is translocated to the cell surface and outcompetes CD28 for binding to its ligands B7-1/B7-2 (also called CD80/86).[33] B7 ligands occupied by CTLA-4 results in the removal of the secondary activation signal from CD28. Without the secondary activation signal, the naïve T cell becomes anergic and undergoes apoptosis (Figure 2-1). CTLA-4 inhibitors restore the ability of CD28 to bind to B7-1/2 resulting in increased levels of T cell proliferation, differentiation, and T cell survival (Figure 2-1).[129] Inhibition of CTLA-4 by mABs have been highly effective in the clinical setting making CTLA-4 a validated anti-cancer target.[130] While small molecule inhibitors are predicted to have many pharmaceutical advantages over mABs, there are no reported small molecules that bind to CTLA-4 reported in the literature.

2.1.2 CTLA-4 Structure and function

CTLA-4 is a highly conserved protein that shares 30% sequence identity to CD28 (Figure 2-2D).[131] The 3D structure of monomeric CTLA-4 and dimeric CTLA-4 have been determined by NMR spectroscopy and X-ray crystallography, respectively (Figure 2A-

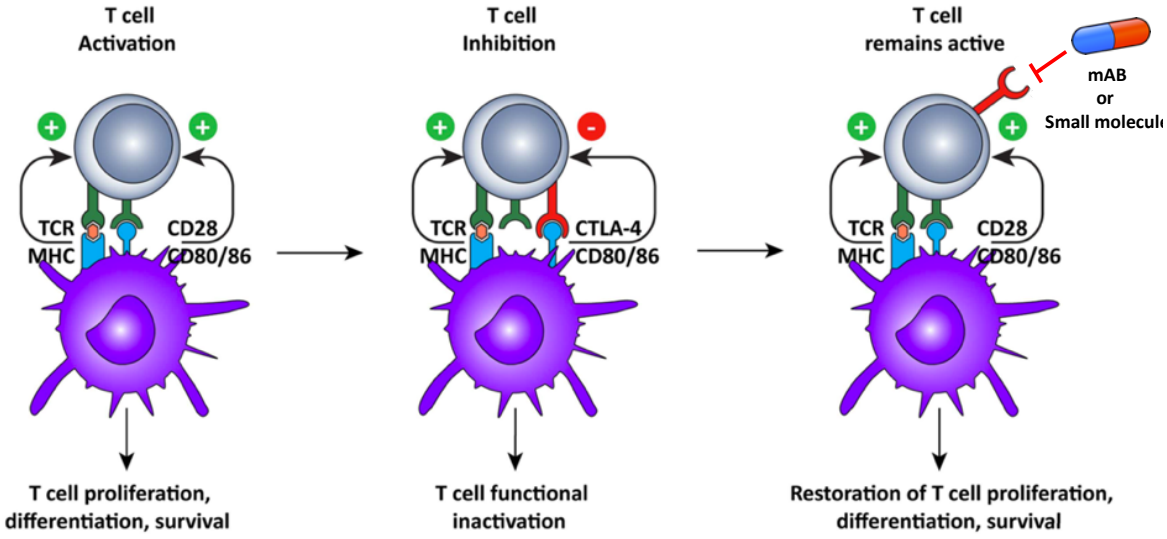

Figure 2-1: Inhibition of CTLA-4 restores T cell activation

T cell activation requires signaling from both TCR and CD28. CTLA-4 is expressed after TCR signaling and outcompetes CD28 binding to CD80/86 (also referred to as B7-1/B7-2). Therapies that target CTLA-4 restore the CD28 / B7 interaction resulting in T cell activation. Image adapted from Vasaturo et al. 2013. [129]

B).[132-134] Based on its tertiary structure, CTLA-4 belongs to the immunoglobulin superfamily (IgSF) protein class, sharing key structural characteristics with immunoglobulin variable domain folds (IgV). Two β-sheets of the V-fold make the ABED and A'GFCC' strands in the extracellular portion of CTLA-4. The two sheets are connected by a canonical Ig-disulfide (Cys 23 – Cys 94) between B and F strands in IgV folds and an additional internal disulfide bond (Cys 49 – Cys 68) between C and D strands.

CTLA-4 is thought to function as a homodimer at the cell surface. In addition to an intramolecular disulfide bond at C122, a series of highly conserved hydrophobic residues (YVIDPE) stabilize the dimer conformation (Figure 2-2C).[132] Given the high homology with CD28, a different conserved sequence is observed at this position for CD28 (HVKQKH) is thought to prevent CTLA-4 and CD28 forming heterodimers (Figure 2-2D).[133] CTLA-4 is

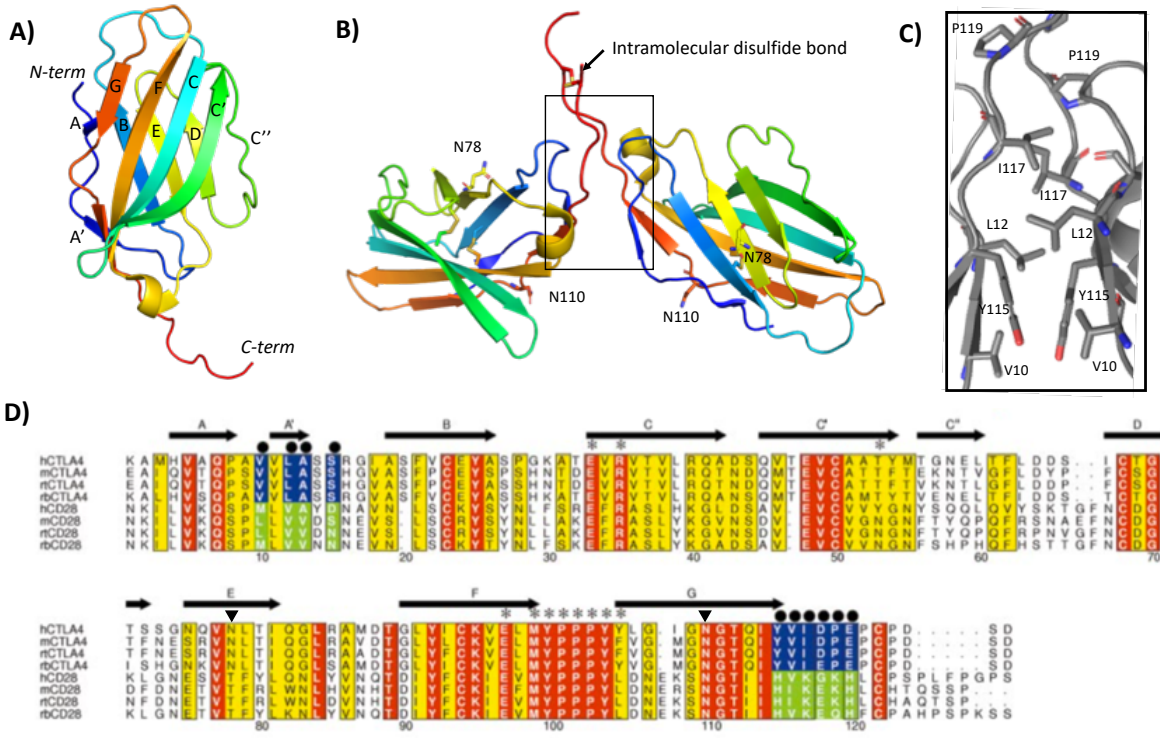

Figure 2-2: CTLA-4 primary and tertiary structure

A) 3D Structure by NMR with labeled ß-strands. B) X-ray structure of dimeric CLTA-4. Disulfide bonds are highlighted by sticks. Glycosylation residues are highlighted by sticks and labels. C) Highlight of the highly conserved and hydrophobic CTLA-4 homodimer interface D) Multiple sequence alignment of CLTA-4 and CD28 from human, mouse, and rat species. Highly conversed resides for both proteins are highlighted red, conserved residues for only CTLA-4 are highlighted in blue and green for CD28. Residues that are conserved by similar chemical properties are highlighted in yellow. Figure adapted from Schwartz et al. 2001. [133]

glycosylated at two highly conserved N-linked glycosylation sites (Asn 78 and Asn 110) that are distant from the B7 binding site (Figure 2B, sticks). Glycosylation is thought to play a role in CTLA-4 dimer formation, as CTLA-4 mutants of both N78 and N110 to alanine fail to dimerize on cells.[135] However, a monomeric triple mutant of CTLA-4 (N78A, N110A, C122A) does not prevent CTLA-4 from localizing to the immunological synapse and inhibiting T cell function.[135] Thus, the exact role that glycosylation and dimerization play in CTLA-4 function remains unclear.

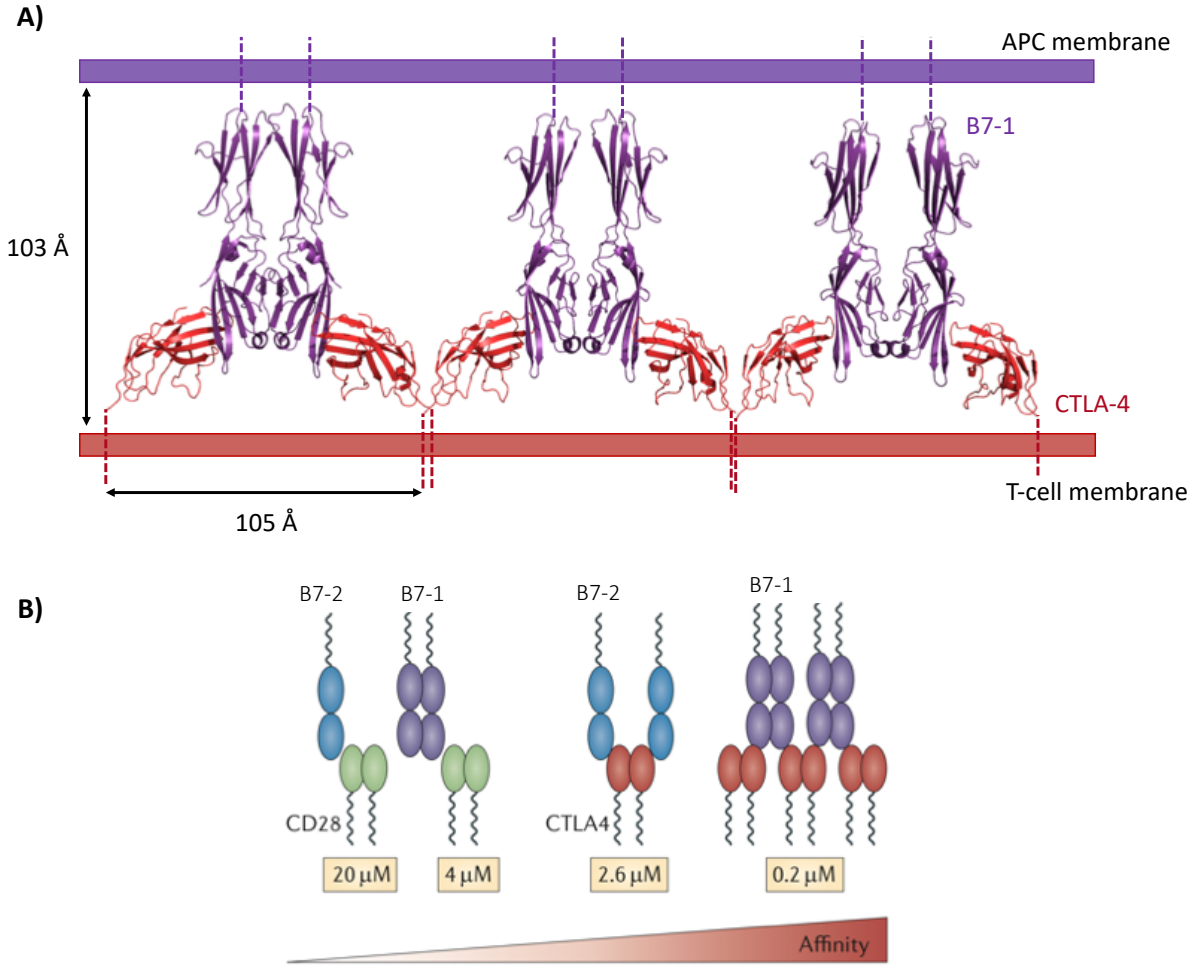

Figure 2-3 CTLA-4 bivalent binding modes to B7 proteins

A) X-ray structure of CLTA-4 bound to B7-1 results in a repeated array of CTLA-4 and B7-1 homodimers thought to be biologically relevant. B) Model to explain why CTLA-4 has higher binding affinity to B7 proteins compared to CD28 by bivalent binding modes. Image adapted from Walker et al. 2011.[34]

CTLA-4 and B7 proteins have been co-crystallized as alternating networks of bivalent CTLA-4 homodimers binding to B7 ligands (Figure 2-3A).[133, 134] The periodic assembly of dimeric molecules is characterized by a 105 Å repeat that extends throughout the crystal packing network. The 103 Å distance from B7 to CTLA-4 is consistent with the maximum dimensions of receptor/ligand pairs that co-localize to the central region of the

immunological synapse, including the MHC / TCR complex.[133] This zipper-like oligomerization could rationalize the formation of highly stable inhibitory complexes at the T cell / APC interface. Indeed, bivalent binding modes can offer an explanation of differences in the measured binding affinities of the B7 proteins and CTLA-4 or CD28 (Figure 2-3B).[32] The B7-1 / CTLA-4 is the highest affinity interaction due to bivalent binding mode of both CTLA-4 and B7-1. While CTLA-4 the binds B7-2 bivalently, B7-2 cannot homodimerize and inability to form the zipper-like oligomerization rationalizes a ~ 10-fold decrease in binding affinity. CD28 forms a homodimer but does not bind to either B7 protein bivalently resulting in weaker binding. These structures and kinetic studies support the hypothesis that CTLA-4 outcompetes CD28 for binding to the B7 proteins and preventing co-stimulatory signals and T cell activation.

2.1.3 CTLA-4 binding hotspot

The CTLA-4 binding interactions to B7-1 and B7-2 are highly similar.[133, 134] The binding interface is formed by a shallow surface of the G, F, C, C' and C'' strands of B7. The total buried surface area is ~ 1,200 Å consists of 13 CTLA-4 residues and 13 residues of B7-1. In total, there are 85 interatomic interactions consisting of 5 hydrogen bonds and many hydrophobic interactions. CTLA-4 makes significant contacts to this surface via the FG loop (also referred to as the CDR3 loop) containing the highly conserved MYPPPK sequence found in both CTLA-4 and CD28 proteins. These interactions exhibit a high degree of shape complementarity as neither protein undergoes significant conformational changes when bound compared to unliganded structures.[136]

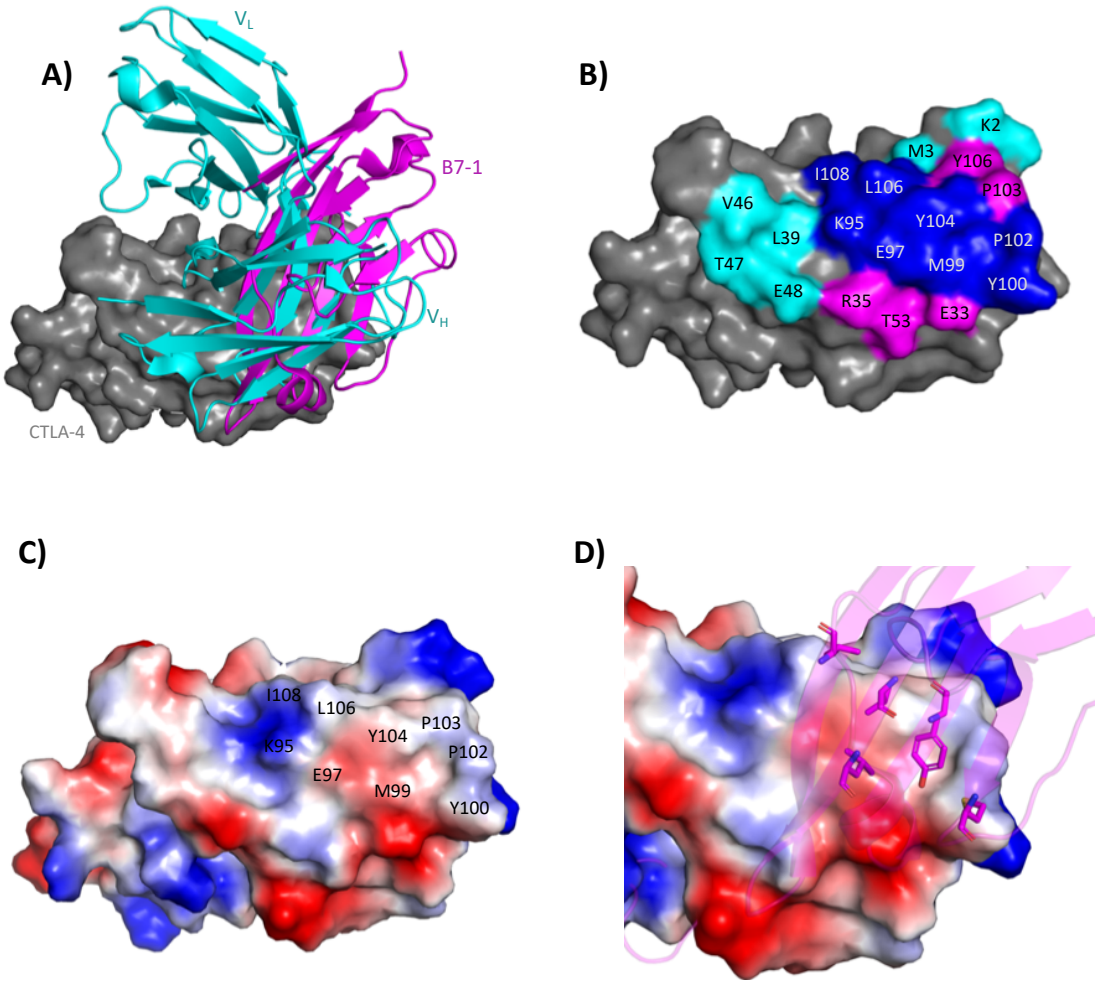

Figure 2-4: CTLA-4 hotspot

A) Overlay of co-crystal structures of B7-1 (purple) bound to PD-1 (gray) and ipilimumab (teal) bound to PD-1. B) surface of CTLA-4 that interacts with B7-1 (purple) and ipilimumab (teal) and the shared residues (blue). C) electrostatic potential of CTLA-4 with residues involved in the interaction with B7-1. D) CTLA-4 residues in green sticks that interact B7-1 suggesting potential binding sites for small molecules.

In addition to CTLA-4 and B7 crystal structures, a structure of ipilimumab has also been determined.[137] Ipilimumab and B7 proteins all bind to the highly conserved MYPPPK segment of CTLA-4 (Figure 2-4A-B). This overlap in suggests this region of the protein could be a hot spot for small molecule binding to displace B7 proteins (Figure 2-4C-D). Careful analysis of the MYPPPK surface reveals a shallow hydrophobic region of the

protein where fragments could potentially bind (Figure 4C-D). It is also possible that fragments could bind to an inducible binding pocket on CTLA-4 not seen in previous structures and thus warrants a fragment screening effort to assess the druggability of CTLA-4 by small molecules.

2.2 Results

2.2.1 Expression and purification of monomeric CTLA-4

Large amounts of recombinant ^{15}N-labeled protein are necessary to conduct a fragment-based screen. CTLA-4 (residues 2 – 126) was cloned into a pET28b *E. coli* expression vector to express CLTA-4 with a thrombin cleavable 6His tag at the N-terminus. 6his-CTLA-4 was expressed as inclusion bodies. Insoluble inclusion bodies were first purified by a series of Triton X-100 and salt washing steps using centrifugation to pellet the inclusion bodies between wash steps. 6His-CTLA-4 inclusion bodies were solubilized in 6M guanidine HCl and refolded dropwise into CTLA-4 refolding buffer. 6His-CTLA-4 was further purified and concentrated by loading to a nickel column. Eluted protein was dialyzed to remove imidazole and treated with thrombin to remove the 6His tag. CTLA-4 was separated from the 6His tag and thrombin by size exclusion chromatography (Figure 2-5A).

Previous X-ray studies have indicated CTLA-4 forms a disulfide-linked homodimer.[133] Indeed, the initial CTLA-4 construct (2 – 126) containing cystine 122 eluted mostly as a dimer from size exclusion chromatography (Figure 2-6A, gray line). ^{1}H-^{15}N HMQC spectra of both dimer and monomer peaks from size exclusion have similar peak

A)

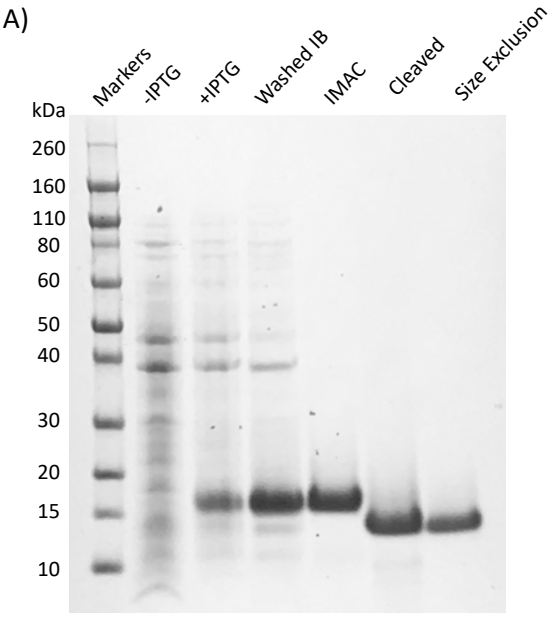

B)

Purification step	Protein Recovered per Liter	Yield (%)
Washed IBS	1.2 g	N/D
Denatured IBS	88 mg	100
Ni Affinity	12.5 mg	14
Thrombin Cleavage	11 mg	13
SE	7 mg	8

C)

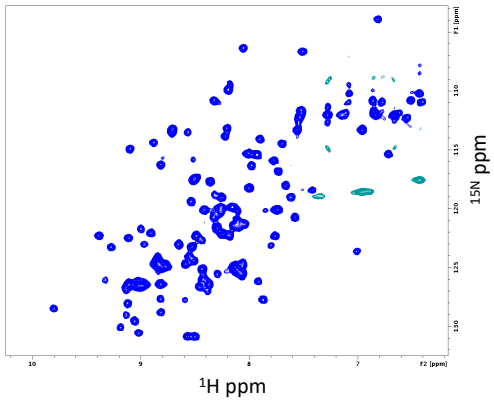

Figure 2-5 Purification of CTLA-4

A) SDS PAGE gel of the CTLA-4 purification process. Lane 1: marker Lane 2: cell lysate prior to CTLA-4 induction by IPTG. Lane 3: CTLA-4 expression induced by IPTG indicated by band at 16.5 kDa. Lane 4: Washed inclusion bodies (IB). Lane 5: Nickel affinity purification (IMAC) of refolded 6His-CTLA-4. Lane 6: CTLA-4 with 6his tag removed by thrombin protease. Lane 7: Final purification step of size exclusion chromatography. B) Protein yields per liter of cell culture for each step of the purification process. C) HSQC of ^{15}N labeled CTLA-4 indicates a well folded protein suitable for fragment screening.

dispersion in HMQC spectra with dimer peaks having slightly lower peak intensity compared to the monomer peaks (Figure 2-6B). Peak dispersion is expected to be similar due to the dimer formation being at the flexible C-terminal tail of the protein. A weaker signal for the dimer peak is also expected due to the higher molecular weight and slower tumbling rate of a CTLA-4 dimer.

X-ray structures of CTLA-4 bound to its ligands demonstrate that the binding site is distant to the dimerization site. Thus, screening a CTLA-4 monomer is preferred due to the enhanced signal and uniformity of the NMR sample. To prevent CTLA-4 dimer

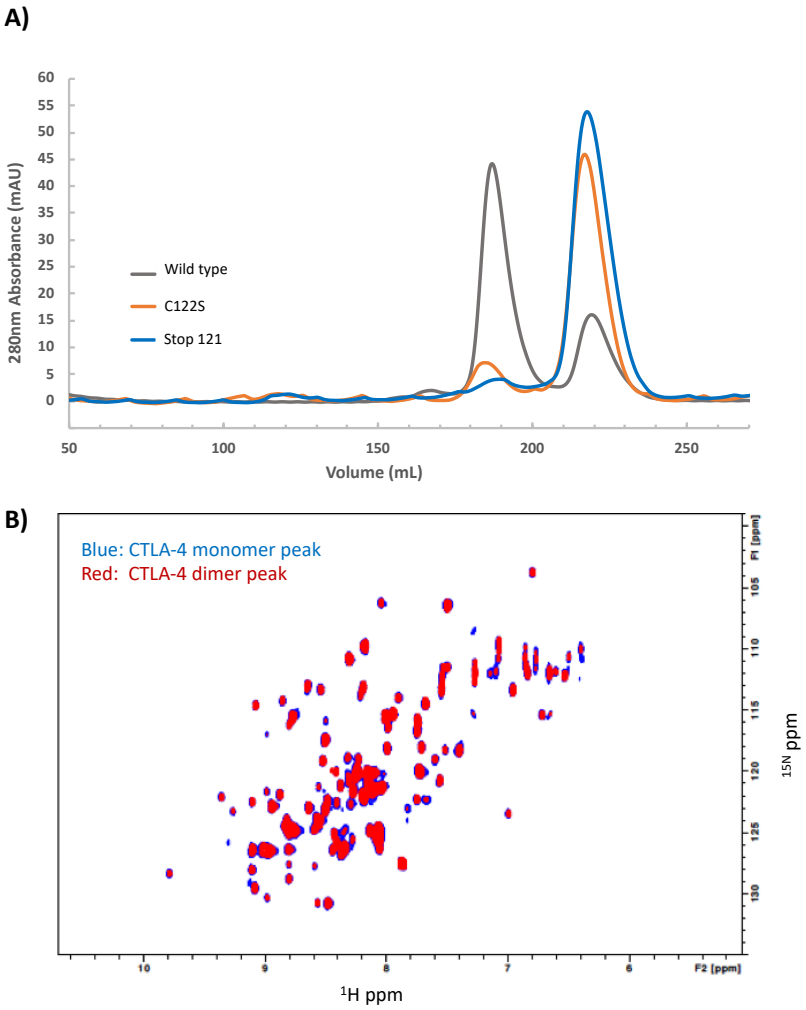

Figure 2-6: CTLA-4 mutants to produce monomeric CTLA-4

A) Size exclusion elution profiles of wildtype CTLA-4 (gray), CTLA-4 C122S (orange), CTLA-4 stop121 (blue). Wildtype with C122 forms a mixture of a dimer a monomer in solution. Mutants designed to prevent protein dimerization elute as monomers. B) HSQC of dimer and monomer peaks show similar peak dispersions with the dimer having slightly weaker signal intensity consistent with a larger protein.

formation, two constructs were designed to remove the C122 disulfide using site-directed mutagenesis. The first construct mutated C122 to serine and the second truncated the amino acid sequence to 2 – 121 by introducing a stop codon at 122. Neither mutant affected expression, refolding, and purification. However, both mutants eluted as a monomer on size exclusion as designed (Figure 2-6A). CTLA-4 C122S was selected for

fragment screening over truncated CTLA-4 (2 – 122) due to a slightly higher yield in the purification process. Purification of CTLA-4 C122S resulted in highly pure protein with yields of 4.6 mg/L of ^{15}N M9 cell culture and high-quality HMQC spectra (Figure 5).

2.2.2 Fragment Screen of CTLA-4

NMR screening conditions were optimized by monitoring peak intensity in ^{1}H-^{15}N SOFAST HMQC spectra and adjusting the pH, salt concentrations, and protein concentrations. Optimal conditions were found to be 0.27 mg/mL protein (20 µM) in buffer containing 25 mM Sodium Phosphate, 100 mM NaCl, 1 mM DTT. Our 13,824 membered fragment library was screened by recording ^{1}H-^{15}N SOFAST HMQC spectra of ^{15}N labeled CTLA-4 C122S in the presence of mixtures of 12 fragments at 800 µM concentration each. A mixture sample was labeled as a "hit" if chemical shift changes were observed in fragment mixture samples relative to a sample containing only DMSO (Figure 2-7). From the mixture screen, 25 mixtures were identified as hits. These mixtures were deconvoluted by testing all 300 fragments as singletons at 800 µM concentration. Surprisingly, none of the 300 fragments selected for deconvolution had detectable binding to CTLA-4. This phenomenon is common when selecting mixtures with weak chemical shifts for deconvolution. High concentrations of fragments mixtures (12 x 800 µM, 9.6 mM concentration of organic compounds) can cause slight changes in the sample pH or cause minor destabilization of the protein that is not present when testing compounds as singletons.

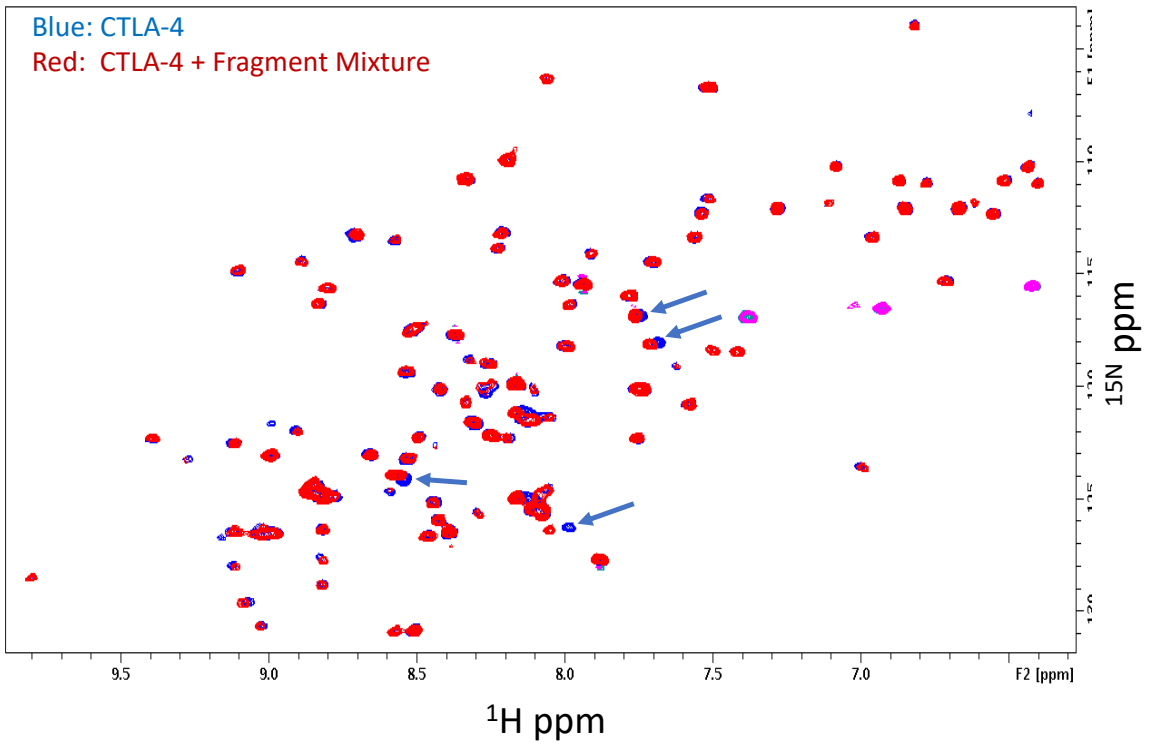

Figure 2-7 CTLA-4 chemical shifts seen in a "hit" of a mixture of 12 fragments. Chemical shift changes are highlighted by blue arrows.

2.3 Conclusions and Discussion

Fragment screening is known to be a reliable predictor of the ability to develop small molecules that bind to a protein with high affinity. Despite screening our entire library, we were unable to discover any fragments that bind to CTLA-4. These results strongly suggest that CTLA-4 is undruggable by small molecules. We considered re-screening the library against the dimeric form of CTLA-4 with aspirations to find hits that bind to the CTLA-4 dimer, presumably at the hydrophobic interface between the two monomers. However, CTLA-4 binds to its ligands at the FG loop which is distant from the dimer interface. Identification of fragments that bind to dimeric CTLA-4 would need to inhibit binding to B7-1 and B7-2 via an allosteric effect. Given the rigidity of the IgV fold

containing two internal disulfide bonds, it is unlikely that fragment binding to a CTLA-4 dimer would induce large conformational changes to disrupt binding to its ligands. For these reasons, we decided to deem CTLA-4 undruggable by small molecules and shift fragment screening efforts to other immune checkpoint proteins.

2.4 Methods

Cloning

The extracellular domain of human CTLA-4 (residues 2 - 126) was cloned into the pET28b vector using *NdeI* and *XhoI* to contain a thrombin cleavable N-terminal 6-His tag and transformed into E. coli BL21 (DE3) cells. C122S and C122stop mutations were made by site-directed mutagenesis. Primers were designed using PrimerX (bioinformatics.org/primerx). PCR reactions contained 10 ng of template DNA, 10 µM forward primer, 10 µM reverse primer, and 1X Phusion High-fidelity Master Mix (NEB). Methylated DNA was removed by treatment with 1 µL of DPN1 for 1 hour at 37 ºC. The digested PCR product was transformed to competent E. coli DH5α by heat shock (45 seconds at 42 ºC) and plated on Kanamycin treated LB-agar plates overnight at 37 °C. Isolated colonies were picked and grown overnight in 10 mL LB cultures. Plasmid DNA was extracted using a miniprep kit (Qiagen) and sequenced using a primer for the T7 promoter (Genhunter).

Protein Expression and Purification

Uniformly ^{15}N labeled CTLA-4 was expressed as inclusion bodies in M9 minimal media containing ^{15}N ammonium chloride. Protein production was induced with 1 mM

IPTG at OD600 at 0.8 and harvested 5 hours later. The cell pellet was frozen and resuspended in lysis buffer (50 mM Tris-HCl pH = 8.5, 150 mM NaCl, 20 mM DTT, 2 mM EDTA and 1 mM PMSF) prior to lysis by homogenization (APV-2000, APV). Inclusion bodies were collected by centrifugation and washed twice with the lysis buffer containing 2% Triton. Inclusion bodies were additionally washed with lysis buffer containing 1% Triton, 0.5% Triton, and 1.5 M NaCl wash steps. Purified inclusion bodies were solubilized in 50 mM Tris-HCl pH = 8.5, 250 mM, 6M Guanidine HCl for 4 hours at room temperature. The solubilized inclusion bodies were filtered through a 0.45 μm filter and refolded dropwise into the CTLA-4 refolding buffer (50 mM Tris-HCl pH = 8.5, 240 mM NaCl, 10 mM KCl, 2 mM CaCl2, 2 mM MgCl2, 0.5% Triton X-100, 0.5 mM PMSF, 0.2 M arginine, 1M urea, 1 mM reduced glutathione and 0.1 mM oxidized glutathione). After 48 hours the refolding buffer containing CTLA-4 was filtered and loaded to a ProBond nickel column (Thermo) using the refolding buffer as Buffer A and the refolding buffer + 500 mM imidazole as buffer B. Eluted CTLA-4 was dialyzed against 50 mM Tris-HCl pH = 8.5, 150 mM NaCl, 2 mM DTT to remove imidazole. After dialysis, the N-terminal 6-His tag was removed with thrombin (10 units of thrombin per mg of CTLA-4). Monomeric CTLA-4 was collected from size exclusion chromatography (Superdex75 26/60) pre-equilibrated with NMR buffer (50 mM Sodium Phosphate pH = 7, 25 mM NaCl).

Fragment Screening

NMR screening was performed at 30 °C using a Bruker Avance III 600 MHz spectrometer equipped with a 5 mm single-axis z-gradient cryoprobe and Bruker SampleJet sample changer. Screening samples (500 μL) screened contained 20 μM of ^{15}N

CTLA-4 C122S, 12 fragments at 800 μM each, and 5% DMSO-d6. $^{1}H,^{15}N$ SOFAST-HMQC spectra were obtained using 26 scans and analyzed using Topspin (Bruker BioSpin). Deconvolution of hit mixtures was performed as a single fragment at 800 μM concentration. CTLA-4 proteins were able to be recycled by filtering and loading to a buffer exchange column.

Chapter 3

Fragment Screen of Programmed Cell Death-1 (PD-1)

3.1 Introduction

3.1.1 PD-1 inhibits activated T cell function

PD-1 is expressed on all activated T cells and acts as an inhibitory brake to tamper T cell immune responses as an immune tolerance mechanism.[11] PD-1 inhibits T cell function when bound to either of its binding partners, PD-L1 or PD-L2. Cancer cells have exploited PD-1 tolerance signaling by overexpressing PD-L1. Expression of PD-L1 on cancer cells is thought to be one of the major mechanisms of immune evasion to promote cancer cell survival and growth.[138] Inhibitors of PD-1 reactivate T cells and prevent the

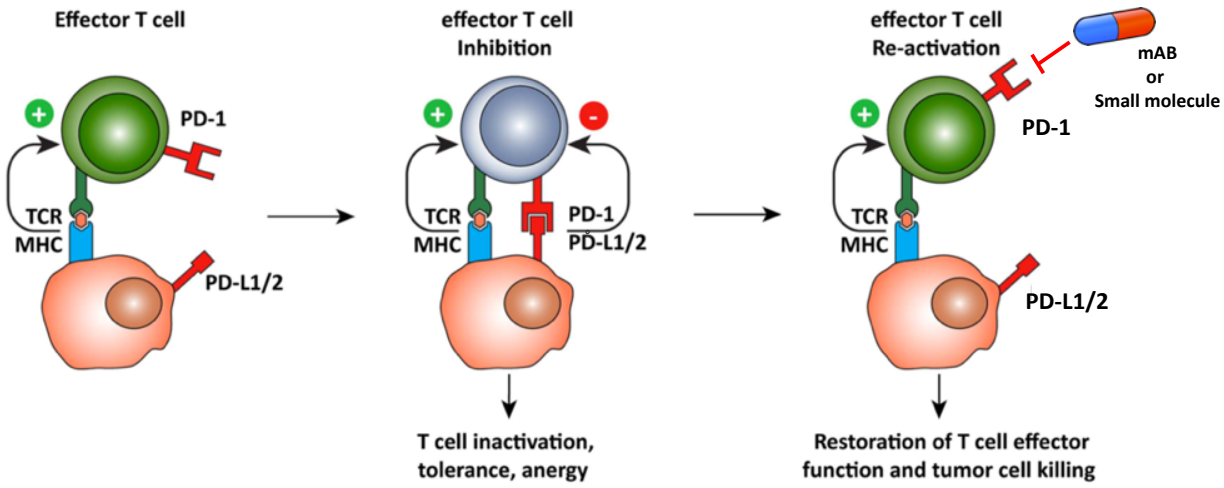

Figure 3-1: Targeting PD-1 pathway to reactive T cell activity against cancer cells.

PD-1 binding to its ligand PD-L1/2 inactivates T cells that recognize cancer cells. PD-L1 is overexpressed on cancer cells as an immune evasion mechanism. Inhibitors of PD-1 prevent T cells from being inactivated by cancer cell expression of PD-L1. Image adapted by Vasaturo et al. 2013. [129]

Compounds	Structure	Inhibitory percentage
Sulfamethizole	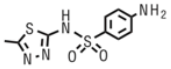	10.2%
Sulfamethoxypyridazine	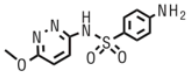	29.3%
1	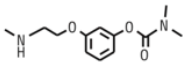	18.5%
5	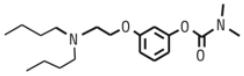	41.9%
9	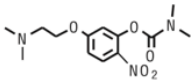	43.0%

Figure 3-2: Previously identified PD-1 inhibitors.

Inhibitory percentage reported from TR-FRET assay developed by Cisbio China. Image adapted from An Liu et al. 2016. [141]

immune evasion mechanism of cancer cells. (Figure 3-1). Indeed, mAbs antibodies that target PD-1 have been remarkably successful in patients in a variety of cancer types.

Given the potential pharmaceutical advantages of small molecules inhibitors, two examples of small molecules that target PD-1 have been reported in the literature.[139] Molecules containing a sulfonamide moiety were reported first by a group at Harvard in 2011, however, no follow-up to these molecules have been reported (Figure 3.2).[140] Amino and dimethyl carbamate-substituted resorcinol compounds have also been reported by a group in China in 2016 (Figure 3-2).[141] All of these molecules are active in PD-1 / PD-L1 FRET assays with percent inhibition values that range from 10% to 42%. 1D NMR experiments suggest these molecules bind to PD-1, however, no binding affinities or structural information of the molecules bound to PD-1 have been reported. These results

could serve as potential starting points for further optimization and suggest that PD-1 could be druggable by small molecules.

3.1.2 PD-1 Structure and function

PD-1 is a type I membrane protein that consists of 288 amino acids. The C-terminus in the cytosol is highly conserved and consists of an ITIM signaling domain that is responsible for inhibition of TCR signaling. When engaged by ligand, PD-1 is phosphorylated at two tyrosine residues within the ITIM domain that recruits the tyrosine phosphatases (PTPs) SHP1 and SHP2.[142] SHPs dephosphorylate multiple different kinases and antagonize TCR and CD28 signaling through the ERK and AKT signaling pathways. These inhibitory signals result in decreased T cell proliferation, cytokine production and survival of T cells.[142]

PD-1 has one extracellular domain (21 - 170) that belongs to the IgV family of proteins and is moderately conserved with mouse PD-1 (Figure 3-3). The 3D structure of human PD-1 has been determined by NMR spectroscopy and X-ray crystallography.[112, 143] Two B-sheets of PD-1 adopt a ß-sandwich fold stabilized by the conical IgV disulfide bond (Cys54 – Cys123). PD-1 has four predicted N-linked glycosylation sites (N49, N58, N75, and N116). However, glycosylation at these sites are not close the PD-L1 binding site of PD-1 and do not play a role in binding of anti-PD-1 mABs or PD-L1.[144]

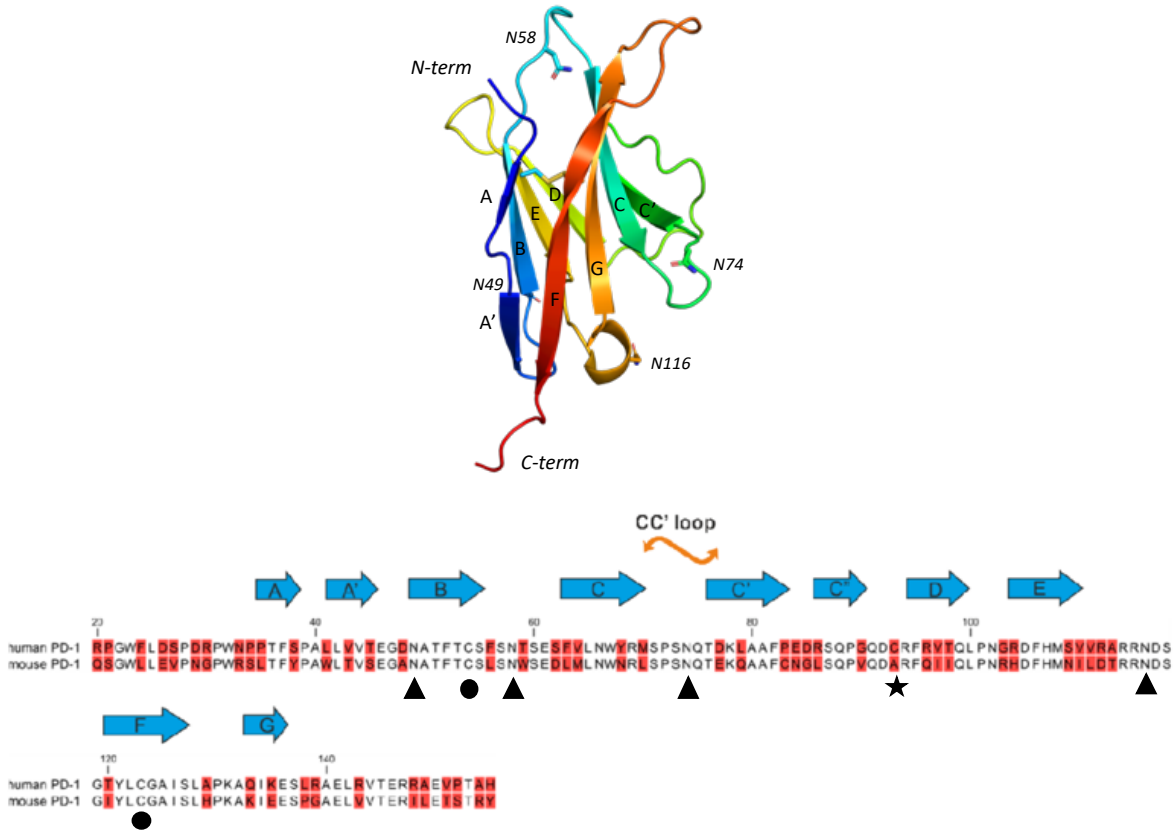

Figure 3-3: Structure of the extracellular portion of PD-1.

Ribbon structure of PD-1 with labeled strands. Disulfide bond is shown by sticks. Glycosylation sites are shown by sticks and labeled. Multiple sequence alignment of human and mouse PD-1. Identical residues are highlighted in red. Glycosylation sites are labeled by triangles, cysteines in disulfide bonds are labeled by circles and the free cysteine residue mutated to serine is labeled by a star. Image adapted by Zak et al. 2015. [112]

3.1.3 PD-1 hotspot for small molecules

PD-1 binds to both ligands with moderate affinity (8 µM for PD-L1 and 2 µM for PD-L2).[143] The complex structure of PD-1 bound to PD-L1 was recently determined.[112] PD-1 binds to PD-L1 with 1:1 stichometry and neither protein is known to dimerize causing repeated oligomers as seen in CTLA-4. The total surface area of the interaction is 1970 Å^2 comprising of C'CFG strands of PD-1. The interface is mostly flat and consists of both

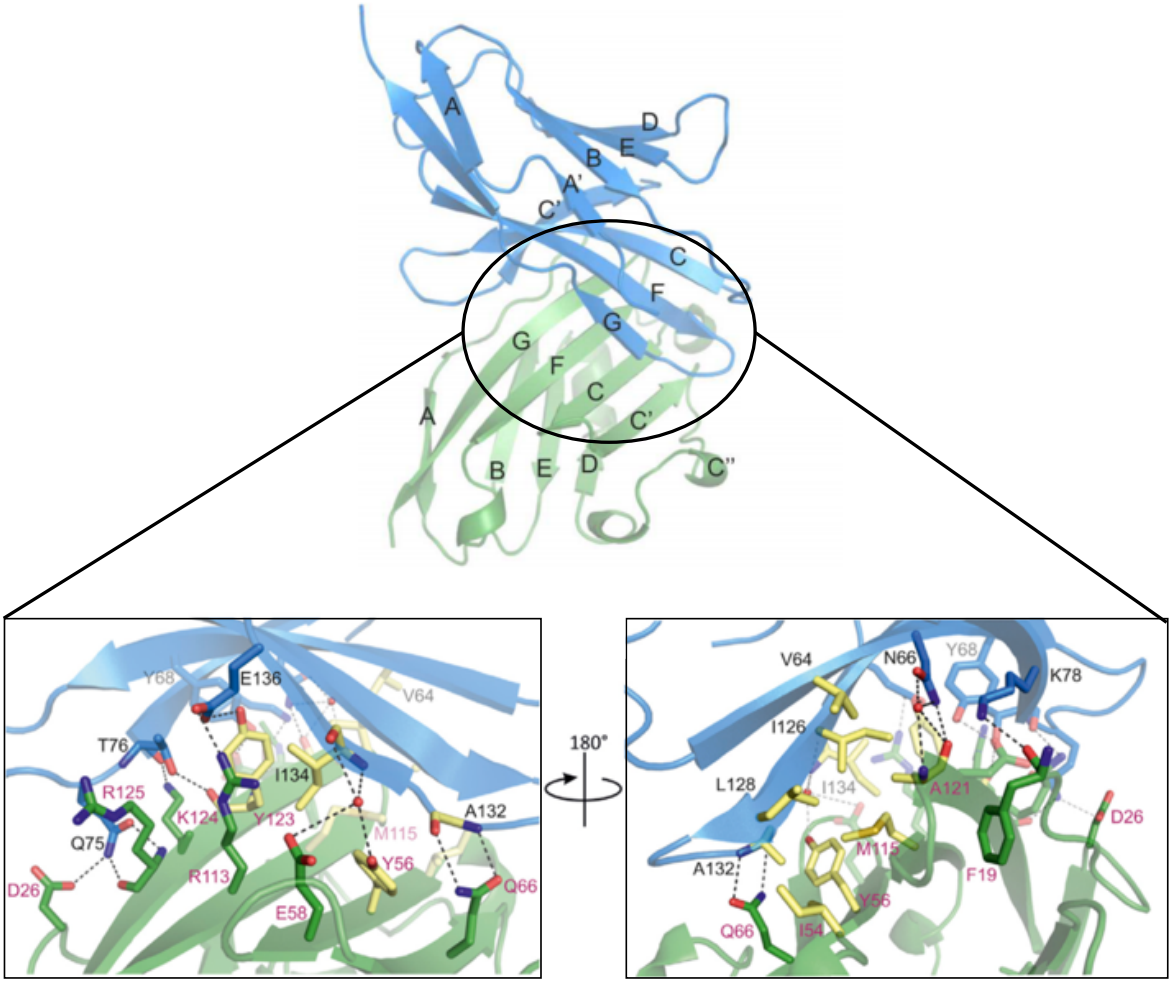

Figure 3-4: PD-1 / PD-L1 binding interaction

Highlighted contacts of the PD-1 (blue) interaction with PD-L1 (green). Hydrophobic residues shown as yellow sticks. Hydrogen bonds shows as dotted lines. Image adapted from Zak et al 2015.[112]

hydrophobic and polar interactions. The hydrophobic residues of PD-1 (V64, I126, L128, A132, and L134) make key contacts to PD-L1 (Figure3-4, yellow sticks). The hydrophobic core is surrounded by a network of polar interactions including 18 hydrogen bonds (Figure 3-4). Notably, PD-L1 binding induces a conformational change of the C C' loop in PD-1 (Figure 3-5, orange strand). This rearrangement results in the formation of 4 additional hydrogen bonds between residues of $_{PD\text{-}1}$Q75 to $_{PD\text{-}L1}$D26 and $_{PD\text{-}1}$T76 to the backbone

carbonyl to $_{PD\text{-}L1}$Y123(Figure 3-5). E136 and Y68 of PD1 also undergo conformational changes that result in Pi-Pi stacking of $_{PD\text{-}L1}$Y56 to $_{Y68}$PD-1. This results in the formation of a pocket at the center of the PD-1 interaction (Figure 3-5). The authors speculated that this pocket could be suitable for the binding of small molecule tyrosine mimetics. However, no such molecules were found that bound to the protein by screening a small library of compounds.[112]

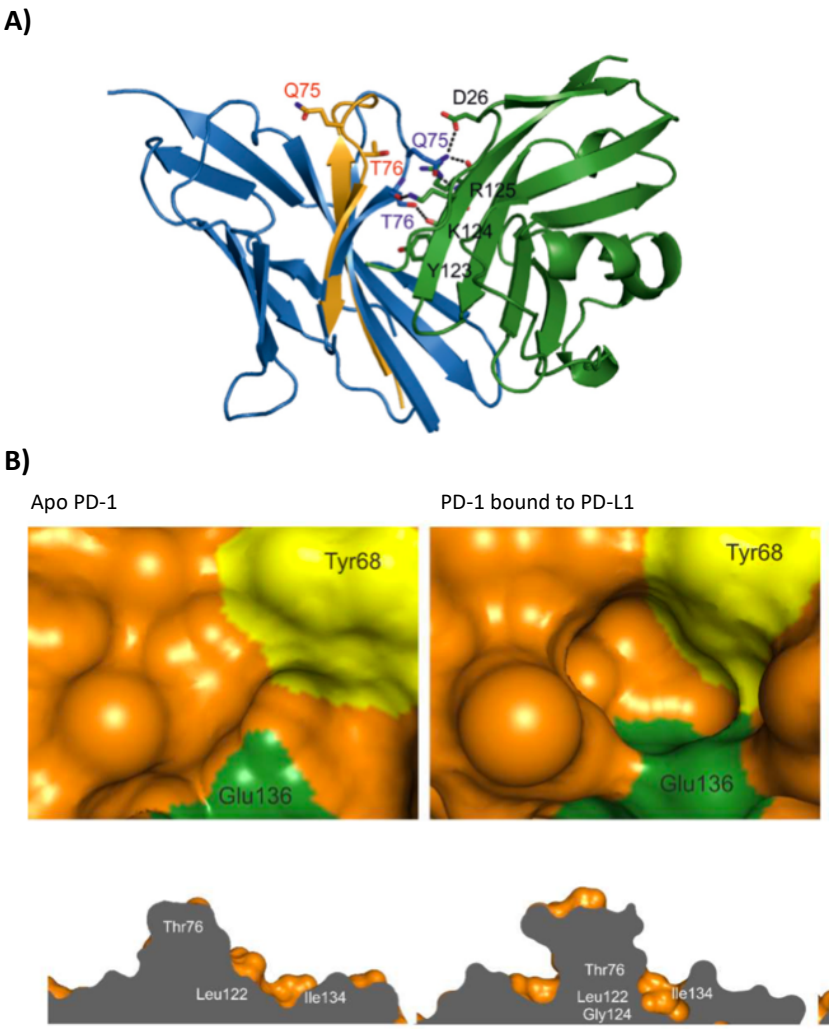

Figure 3-5: Conformational changes of PD-1 when bound to PD-L1.

A) PD-1 (blue) interaction with PD-L1 (green). Conformational changes shown by orange strands of apo PD-1. B) pocket formed by the conformational change of Tyr 68 and Glu 136. Image adapted from Zak et al. 2015.[112]

Both nivolumab (BMS) and pembrolizumab (Merck) have been co-crystallized with PD-1.[144, 145] Both antibodies bind to the PD-L1 binding site but occupy different neighboring regions of the protein. Nivolumab binds primarily to the FC and BC loops of PD-1. Pembrolizumab binds on the surface of the GFC strands in a similar fashion to PD-L1. Pembrolizumab and PD-L1 interaction with many of the same residues (Figure 3-6, yellow). The shared residues are mostly hydrophobic and suggest a "hotspot" for binding of a small molecule. Highlighted interactions of PD-L1 with this hotspot is depicted in Figure 3-6D which includes the inducible pocket formed by Y68 and E136. While this site is

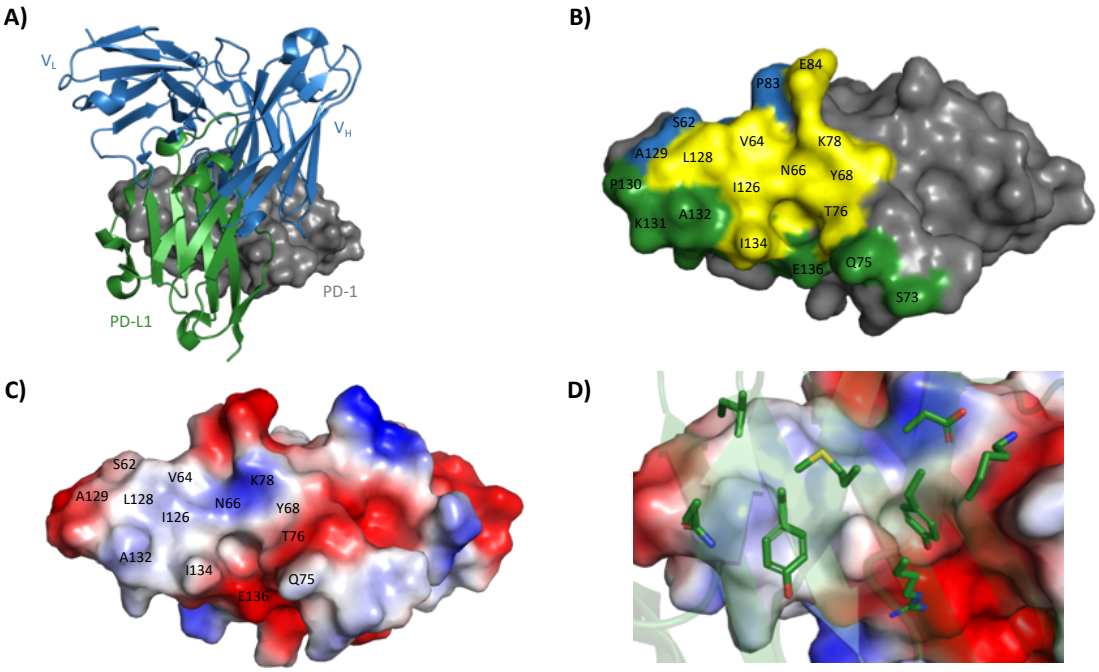

Figure 3-6: PD-1 binding hotspot

A) Overlay of co-crystal structures of PD-L1 (green) bound to PD-1 and pembrolizumab (blue) bound to PD-1. B) surface of PD-1 that interacts with PD-L1 (green) and pembrolizumab (blue) and the shared residues (yellow). C) electrostatic potential of PD-1 with residues involved in the interaction with PD-L1. D) PD-L1 residues in green sticks that interact PD-1 suggesting potential binding sites for small molecules.

of interest for binding of small molecules, binding to other sites may also disrupt the PD-L1 interaction by an allosteric effect from dynamics of PD-1 protein in solution.

3.2 Results

3.2.1 Expression and purification of PD-1

The extracellular domain of human PD-1 (residues 34 – 150) was cloned into the pET28b expression vector to contain a thrombin cleavable N-terminal 6-His tag and transformed into *E. coli* BL21 (DE3) cells. Uniformly ^{15}N labeled PD-1 was expressed as inclusion bodies in M9 media containing ^{15}N ammonium chloride after a 5 induction with IPTG at 0.8 OD_{600}. Insoluble inclusion bodies were first purified by a series of Triton X-100 and salt washing steps using centrifugation to pellet the inclusion bodies between steps. 6His-PD-1 inclusion bodies were solubilized in 6M guanidine HCl and refolded dropwise into PD-1 refolding buffer. 6His-PD-1 was further purified and concentrated by loading to a nickel column. Eluted protein was dialyzed to remove imidazole and treated with thrombin to remove the 6xHis tag. PD-1 was separated from aggregated misfolded protein, the cleaved 6His tag, and thrombin by size exclusion chromatography (Figure 3-7A). Purification of PD-1 resulted in highly pure protein with yields of 6 mg/L of ^{15}N M9 cell culture (Figure 3-7A-B).

A)

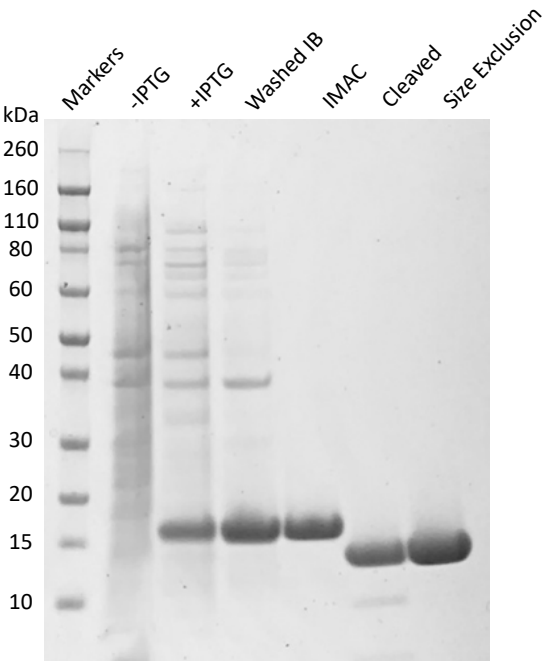

B)

Purification step	Protein Recovered per Liter	Yield (%)
Washed IBS	0.6 g	N/D
Denatured IBS	40 mg	100
Ni Affinity	10 mg	25
Thrombin Cleavage	8 mg	20
Size Exclusion	6.75 mg	17

C)

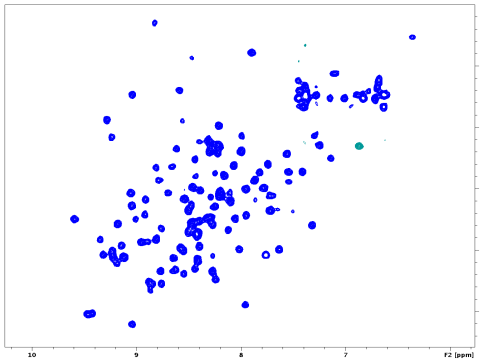

Figure 3-7: PD-1 protein purification

A) SDS PAGE gel of the PD-1 purification process. Lane 1: marker Lane 2: cell lysate prior to PD-1 induction by IPTG. Lane 3: PD-1 expression induced by IPTG indicated by band at 16 kDa. Lane 4: Washed inclusion bodies (IB). Lane 5: Nickel affinity purification (IMAC) of refolded 6His-PD-1. Lane 6: PD-1 with 6his tag removed by thrombin protease. Lane 7: Final purification step of size exclusion chromatography. B) Protein yields per liter of cell culture for each step of the purification process. C) HSQC of ^{15}N labeled PD-1 indicates a well folded protein suitable for fragment screening.

3.2.2 Fragment screen of PD-1

Screening conditions were optimized monitoring peak intensity in ^{1}H-^{15}N SOFAST HMQC spectra and adjusting the sample pH, salt concentrations, and protein concentration. Optimal conditions were found to be 0.27 mg/mL protein (20 µM) in buffer containing 50 mM Sodium Phosphate pH = 7 and 25 mM NaCl. All 13,824 fragments in the library were screened by recording ^{1}H-^{15}N SOFAST HMQC spectra of ^{15}N labeled PD-1 in the presence of mixtures of 12 fragments at 800 µM concentration each.

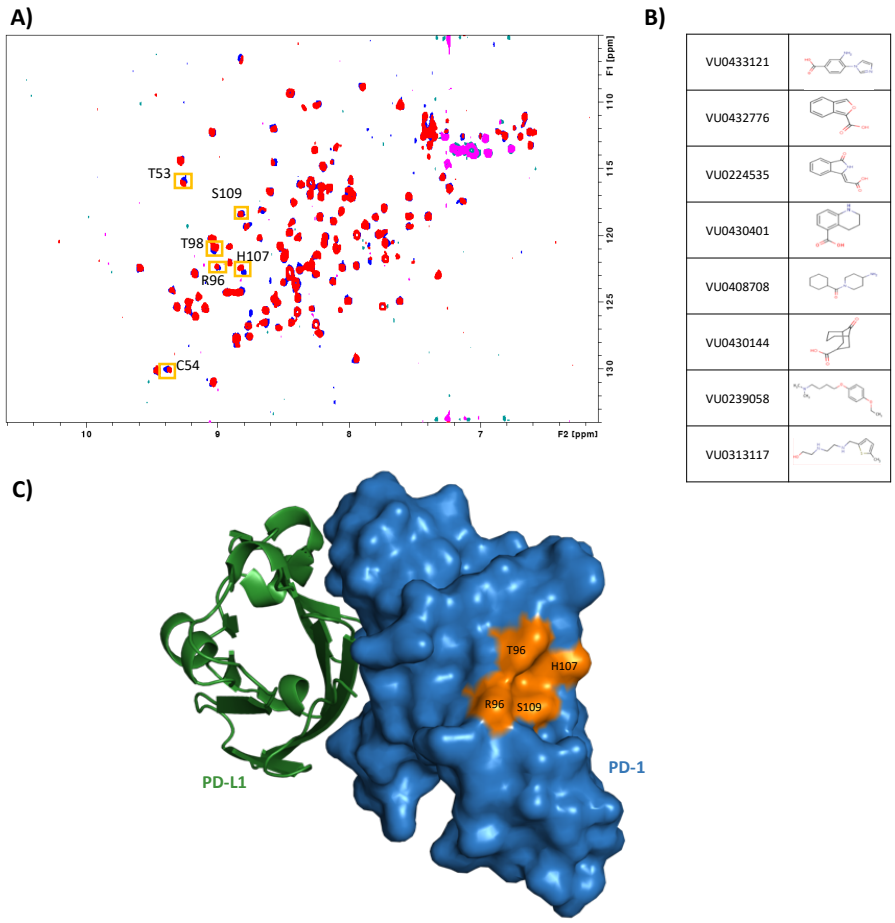

Figure 3-8: Mapping fragment binding site to PD-1

A) 1H-15N HMQC of a PD-1 fragment hit. Shifted residues are boxed in orange and labeled. B) Structures of the fragment hits identified to bind to PD-1. C) highlighted residues on the PD-1/PD-L1 cocrystal structure shows the fragment binding site is distant to the PD-L1 binding site on PD-1.

A mixture sample was labeled as a "hit" if chemical shift changes were observed in fragment mixture samples relative to a sample containing only DMSO (Figure 3-8A). Deconvolution of the mixture screen resulted in 8 hits to PD-1 (hit rate = 0.05%, Figure 3-8B). These hits have small resonance perturbations and weak binding affinity by HMQC titration experiments (> 2 mM) (Figure 3-8A). The fragment hits could be clustered into three main chemotypes. The first being a carboxylic acid bicyclic series, the second being

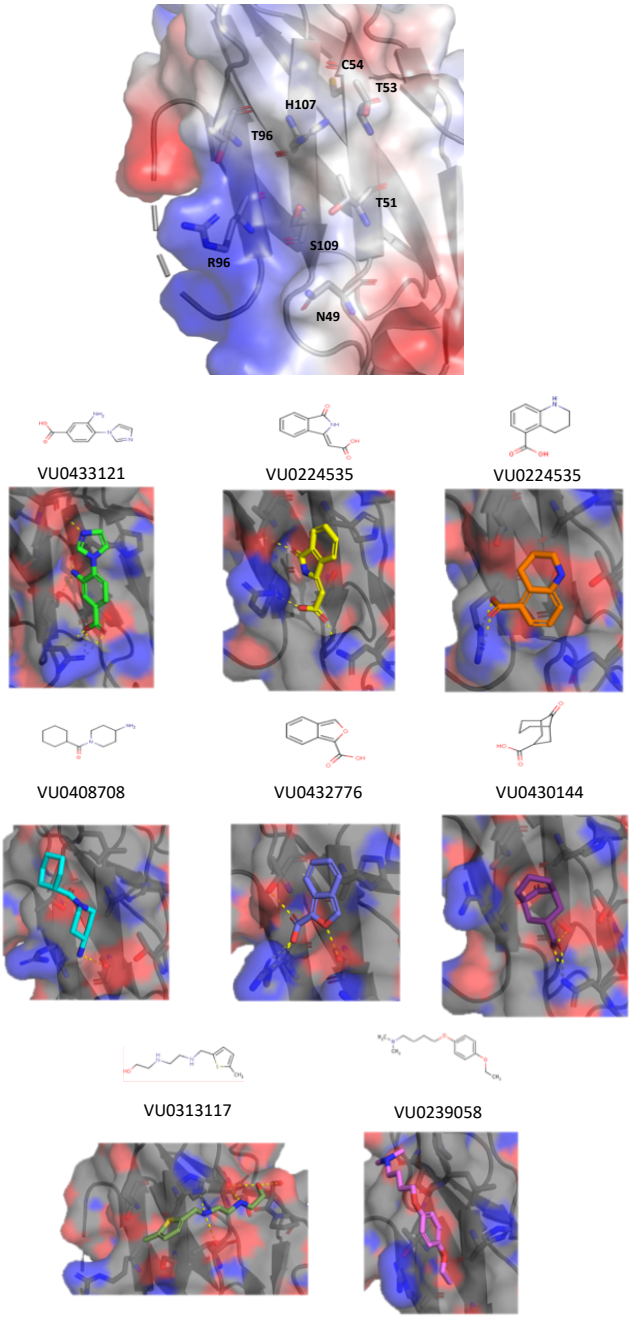

Figure 3-9: Molecular modeling of PD-1 fragment hits

Docking using Maestro Glide at the binding site defined by HMQC spectra of fragment hits. Ligand binding poses for all 8 hits are shown with hydrogen bonds shown as dotted lines

an aromatic ring with a 6-8 atom flexible tail, and a third with saturated ring systems. All the fragments are highly polar and potentially make electrostatic interactions with PD-L1.

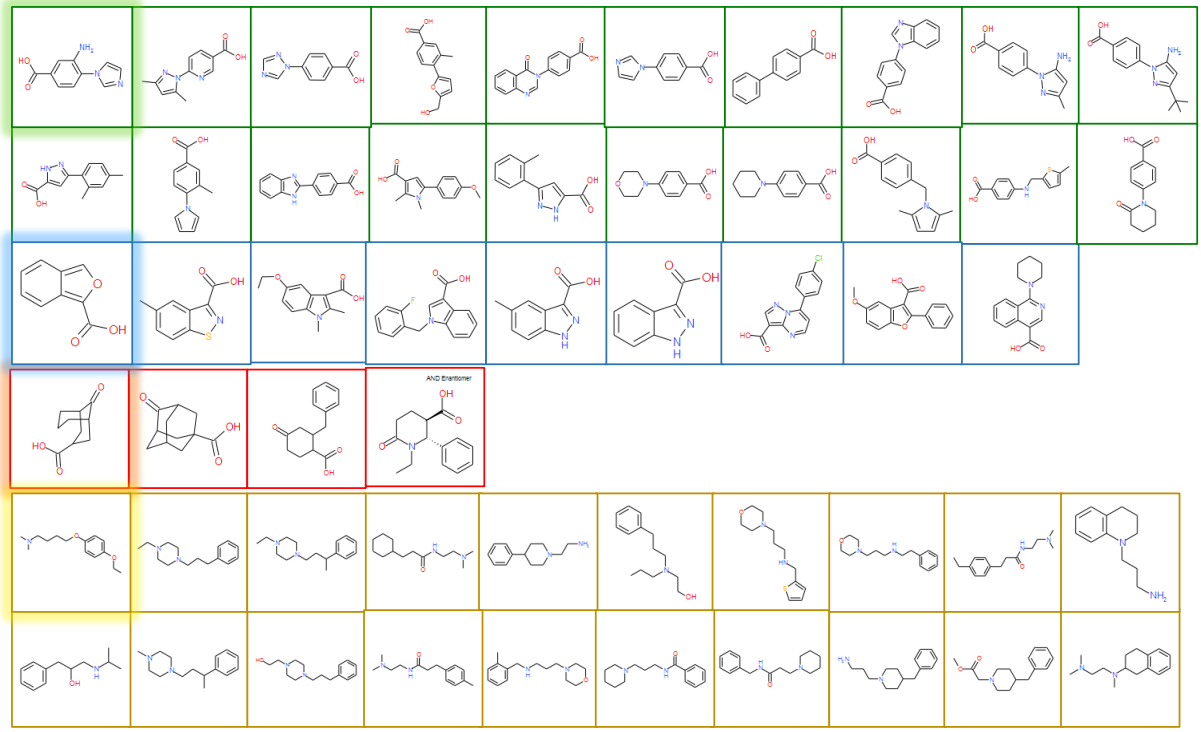

Figure 3-10: Analogs of PD-1 fragment hits screened.

Analogs selected and screened from a substructure similarity search of Vanderbilt's high throughput screening cores compound library. Each series of fragment is indicated by box color.

3.2.3 Molecular modeling of PD-1 hits and analog screening

Mapping the chemical shifts to the structure PD-1 using previously reported HSQC peak assignments suggest fragment hits bind to the AED strands of PD-1 (Figure 3-8). These residues form a shallow hydrophobic surface on the edge of T53 and T51 neighbored by an electropositive area from R96 (Figure 3-9). The presence of an electropositive area is consistent with many of the hits containing carboxylic acids. However, attempts to generate X-ray co-crystal structures of the fragments bound to PD-1 were unsuccessful.

To generate a model of how the fragments may bind to PD-1 to guide fragment SAR molecular docking experiments were utilized. Maestro InducedFit docking experiments were run to account for a high degree of flexibility seen electrophilic side chains, namely R96 which has high B-factors in PD-1 crystal structures. Docking results suggest fragments occupy a very shallow pocket between S109 and H107 and all but one fragment made electrostatic interactions with surrounding electrophilic residues. Notably, R96 was the most flexible residue in the docking experiments and forms hydrogen bonding interactions with fragments containing carboxylic acids and is predicted to form a cation-pi interaction with VU0239058.

To further elaborate the SAR of the identified hits, a small set of analogs of VU0433121, VU0432776, VU0430144, and VU0239058 were ordered for screening. By substructure similarity searches of the compound library in the Vanderbilt High Throughput Screening Facility 49 compounds were screened (Figure 3-10). Most of the analogs did not bind to PD-1. Of the analogs that did bind, they had even smaller chemical shifts changes than the original fragment hits. SAR generated from the screen is consistent with the docking models, as many analogs remove hydrogen bonding interactions or place functional groups that are predicted to clash with the protein. However, no analogs were identified that were markedly better than the fragment hits identified in the large fragment screen. Furthermore, X-ray co-crystal structures of fragments bound would be useful to models to guide analog development as docking weakly binding fragments is highly speculative.

3.2.4 NMR-based PD-1 / PD-L1 displacement assay by NMR

Because the hits are predicted to bind on the opposite side of the PD-L1 binding site, large conformational changes would be required to disrupt binding to PD-1 via an allosteric effect. Large conformational changes in proteins are typically observed in HMQC spectra by the shifting of many peaks. However, fragment hits only shift select few of peaks. To validate this experimentally, all 8 PD-1 fragment hits were tested for the ability to disrupt the PD-1 / PD-L1 interaction using an NMR based assay antagonist induced dissociation assay (AIDA) (Figure 3-11). In the presence of unlabeled (^{14}N) PD-1, PD-1 and PD-L1 form a complex causing a higher molecular weight complex that broadens the signal intensity of ^{15}N PD-L1. If the fragment can interrupt the complex, the signal intensity of ^{15}N PD-L1 is rescued. Addition of high molar excess (4 mM) of all 8 fragment hits of PD-1 failed to displace PD-L1. Either the fragments binding affinities are too weak to successfully displace the PD-1 PD-L1 interaction (~1 uM) or binding adjacent pocket fails to produce conformational changes that disrupt binding to PD-L1.

3.3 Conclusions and Discussion

PD-1 is a highly validated target for cancer immunotherapy. Currently, antibodies that target PD-1 outnumber those that target CTLA-4 or PD-L1. Compared to the CTLA-4 signaling pathway, PD-1 blocking antibodies have demonstrated higher response rates with fewer side effects.[11] CTLA-4 and PD-1 are structurally similar and thus we expected PD-1 to be a challenging target for small molecules. Indeed, the fragment screen resulted in only 8 weak hits. The hit rate of 0.06% puts PD-1 in the “undruggable” category of

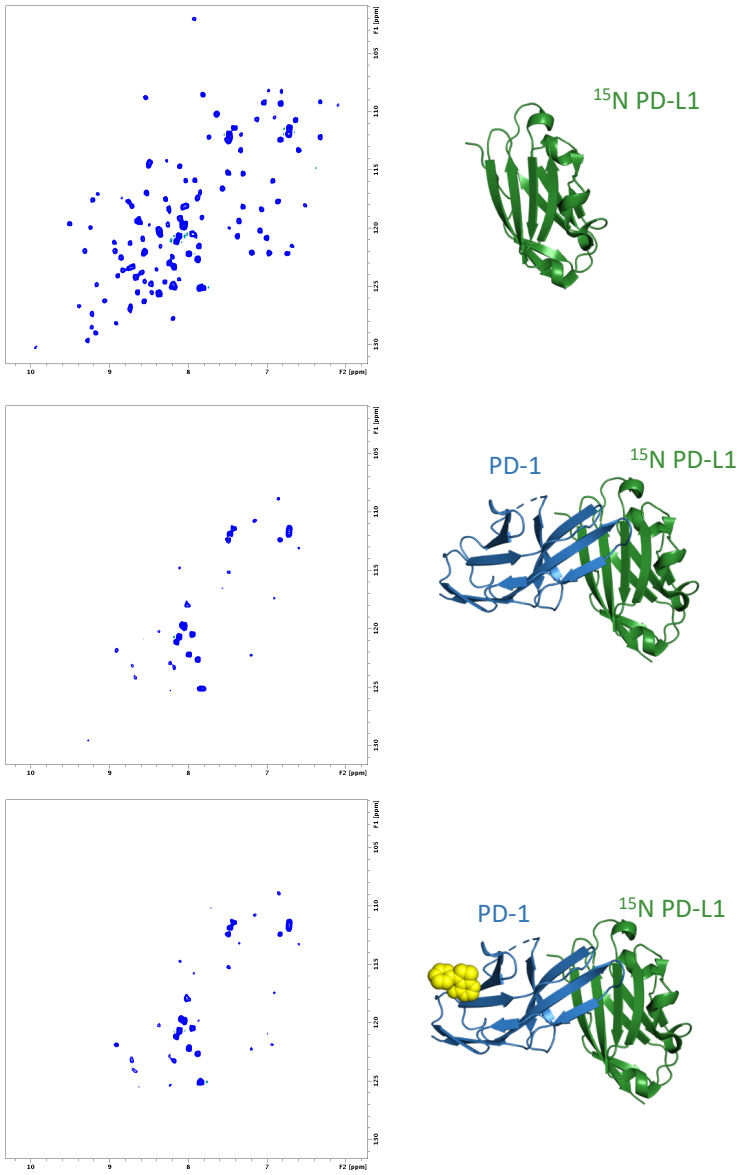

Figure 3-11: PD-1 fragment hits fail to displace PD-L1 in solution.

Displacement assay by 2D NMR experiments. Panel 1) HMQC of ^{15}N labeled PD-1 alone. Panel 2) HMQC of equal molar concentrations of ^{15}N PD-1 and unlabeled PD-L1 causes the formation of a higher molecular weight complex causing peak broadening. Panel 3) HMQC ^{15}N PD-1, equal molar concentrations of unlabeled PD-L1, and 1 mM of PD-1 fragment hit. Failure to rescue signal intensity suggests the fragment hits do not displace the PD-1/PD-L1 interaction.

protein targets. These 8 hits bind with > 2 mM binding affinity and appear to bind on the opposite side of the PD-L1 binding site on PD-1. Furthermore, we were unable to generate co-crystal structures of these hits to confirm binding to this site. We found no

evidence that these fragments induce a large conformational change in the protein by HMQC spectra and saw no evidence that these fragments displace PD-L1 using an AIDA NMR assay. We also failed to generate fragment SAR by screening structurally similar analogs.

Taken together, these results indicate that, like CTLA-4, PD-1 is an extremely challenging target for small molecules. Despite the effort to find fragments that could serve as starting points for further optimization, the quality of hits were too weak and the lack of structural information of the fragments bound make it difficult to move forward. Additionally, if the optimization of the hits bound to this site was possible, these fragments are not likely to displace PD-L1 by an allosteric effect as evidence from the PD-1 / PD-L1 AIDA assay. For these reasons, we concluded that PD-1 is undruggable by small molecules and shifted efforts to finding small molecules that bind to PD-L1 and disrupt this protein-protein interaction.

3.4 Methods

Cloning and expression tests

The extracellular domain of human PD-1 (residues 14 - 130) was cloned into the pET28b vector using *NdeI* and *XhoI* restriction sites to contain a thrombin cleavable N-terminal 6His tag and transformed into *E. coli* DH5α cells (Thermo Fisher). Transformed cells were grown on kanamycin plates overnight at 37 ˚C. DNA of single colonies was isolated by miniprep DNA extraction and sequenced to ensure the correct ligation of the PD-1 into the expression vector. Small scale (10 mL) expression tests were performed

using colonies with correct plasmids. Overnight cultures consisting of LB with 50 ug/mL kanamycin and picking colonies on the kanamycin treated plate. Small aliquots of media (10 mL of LB + 50 ug/mL Kan) were inoculated with 100 µL of overnight culture to 10 mL cultures for expression tests (1% inoculation rate). Colonies with the highest level of expression in the expression tests (qualitatively determined by SDS PAGE gels) were used to make glycerol stocks stored at -80 ˚C.

Protein production

Uniformly ^{15}N labeled PD-1 was expressed as inclusion bodies in M9 minimal media containing ^{15}N ammonium chloride. Protein production was induced with 1 mM IPTG at OD_{600} at 0.8 and harvested 5 hours later. The cell pellet was frozen at -80 C until needed for purification. Inclusion body purification was identical to methods described in Chapter 2 for CTLA-4 inclusion bodies. Purified PD-1 inclusion bodies were solubilized in 50 mM Tris-HCl pH = 8.5, 250 mM, 6M Guanidine HCl for 4 hours at room temperature. PD-1 was refolded dropwise into PD-1 refolding buffer (50 mM HEPES pH 7.5, 24 mM NaCl, 1 mM KCl, 1 mM PMSF, 0.2 M arginine, 9 mM reduced glutathione, 1 mM oxidized glutathione) at 4 C overnight (12 – 16 hours). Refolded PD-1 was filtered through a 0.45-micron filter and loaded to a NiNTA column using PD-1 refolding buffer as Buffer A and PD-1 refolding buffer + 500 mM imidazole as buffer B. Eluted PD-1 was pooled and dialyzed in PD-1 dialysis buffer (50 mM Tris pH = 7.5, 150 mM NaCl and 2 mM DTT). After 8 hours of dialysis, thrombin was added to the dialysis buffer at 10 units/mg of protein to cleave the 6xHis-tag. Cleavage of the tag was monitored by SDS PAGE gel. After 100% of the tag had been cleaved, PD-1 was concentrated to 1 mg/mL using a stirred amicon

under nitrogen pressure using a 5 kDa molecular weight cutoff. Concentrated PD-1 was loaded to a size exclusion column (Superdex76 26/60) pre-equilibrated with NMR buffer (50 mM Sodium Phosphate pH = 7 and 25 mM NaCl). Purification of unlabeled protein for PD-L1 displacement assay was identical to the described method but with LB media instead of M9 media.

Fragment Screening

NMR screening was performed at 30 °C using a Bruker Avance III 600 MHz spectrometer equipped with a 5 mm single-axis z-gradient cryoprobe and Bruker SampleJet sample changer. Screening samples (500 μL) screened contained 30 μM of ^{15}N PD-1, 12 fragments at 800 μM each, and 5% DMSO-d6. ^{1}H,^{15}N SOFAST-HMQC spectra were obtained using 20 scans and analyzed using Topspin (Bruker BioSpin). Deconvolution of hit mixtures was performed as a single fragment at 800 μM concentration. PD-1 proteins were able to be recycled by filtering through a 0.45 μm filter and loading to a buffer exchange column.

Docking and substructure similarity searching.

Maestro (Schrodinger) was used for all molecular modeling. The human PD-1 crystal structure (PDB ID: 3RRQ) protein was prepared for modeling by adding missing side chains/residues, charged in pH 7 buffer, and energy minimized by the Protein Prep Wizard. A docking grid was generated around amino acids identified in the fragment screen for binding. All 8 of the fragment hits were imported as SD files and prepared for ligand docking using Ligprep. Fragments were docked using Glide with normal settings

and extra precision. Substructure searching was performed by searching the Vanderbilt high throughput screening core's compound library using ChemCart. Substructure searches included placement of heteroatoms in the core rings and allowing multiple substitutions off the core ring structure.

Chapter 4

Fragment Screen of Programmed Death Ligand-1 (PD-L1)

4.1 Introduction

4.1.1 PD-L1 is a validated target for cancer immunotherapy

In the context of cancer, the primary binding partner of PD-1 is PD-L1. PD-L1 is normally expressed on somatic cells in response to pro-inflammatory cytokines as a defense mechanism against autoreactive T cells. However, PD-L1 is also found to be upregulated in many cancer types by oncogenic activation of PD-L1 transcription factors.[17] PD-L1 expression on tumor cells results in PD-1 mediated inactivation of tumor targeting T cells in the tumor microenvironment and is thought to be the primary mechanism cancer cells use to evade the immune response.[11] Therapeutic antibodies that target either PD-1 and PD-L1 have been developed remove this evasion mechanism and both have been successful at generating antitumor responses in clinical trials.[146]

Targeting PD-L1 is thought to offer some potential advantages compared to targeting PD-1.[147] Antibodies that target PD-1 block the interaction with both PD-L1 and PD-L2. PD-L2 has been shown to be an important regulator of autoimmunity in lung tissue and downregulates T helper-2 (T_h-2) cells that promote tumor development.[148] Given that PD-L2 is only expressed in the minority of human cancers, leaving PD-L2 un-inhibited with PD-L1 inhibitors might mediate autoimmunity in certain tissues.[149] Indeed, clinical trials with PD-1 antibody compared to PD-L1 noted a slightly higher incidence of irAEs and drug-related pneumonitis.[150, 151] Antibodies targeting PD-L1 entered clinical trials in 2011,

5 years after the first PD-1 antibodies entered the clinical. Three PD-L1 antibodies are currently FDA approved as monotherapy in a total of four different cancer types including urothelial cancer, non-small cell lung cancer, bladder cancer, and Merkel cell carcinoma.[17]

4.1.2 PD-L1 structure and function

PD-L1 is a type I transmembrane protein consisting of IgV and IgC domains in the extracellular region. PD-L1 contains two disulfide bonds, one in the IgV domain (C40 – C114) and one in the IgC domain (C155 – C209). Co-crystal structures suggest the IgV domain of PD-L1 is the sole interaction domain with PD-L1 (Figure 4-1 A). PD-L1 is N-glycosylated at 3 asparagine residues in the IgC domain (N192, N200 and N219) and 1 asparagine residues in the IgV domain (N35, Figure 4-1 B).[112] Notably, N-glycosylation of the IgC domain plays an important role in the regulation of PD-L1.[152] Un-glycosylated PD-L1 interacts with GSK3B forming a complex with B-trCP that induced phosphorylation-dependent proteasome degradation of PD-L1.[152] However, N35 glycosylation in the IgV domain does not play a role in effecting PD-L1 stability.[152] N35 is on the opposite face of PD-L1 from the PD-1 binding site and is not expected to alter binding to PD-1. Unlike PD-1, PD-L1 lacks traditional signaling motifs in the cytosolic region of the protein and is not expected to be a signaling molecule. However, recent reports suggest that non-classical conserved motifs in the PD-L1 cytolytic region may protect cells from interferon-mediated toxicity which is thought to aid in immune evasion.[153] Elucidating the diverse functions of PD-L1 is currently an active area of research and will contribute a greater understanding of the tumor-promoting function of PD-L1.

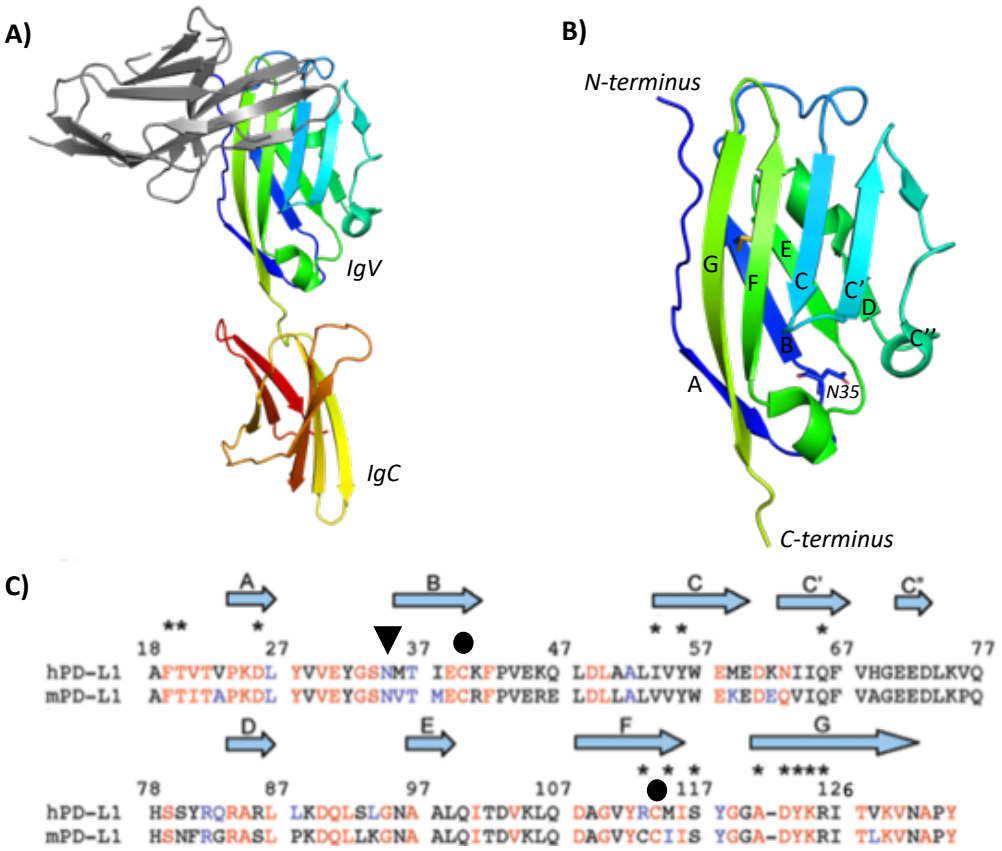

Figure 4-1: Structure of the extracellular portion of PD-L1.

A) PD-L1 (rainbow) bound to PD-1 (gray). The extracellular portion of PD-L1 consists of an IgV and IgC domain. PD-1 interacts with only the IgV domain of PD-L1. B) PD-L1 IgV domain strands labeled with disulfide bonds and glycosylation site (N35) highlighted. C) Multiple sequence alignment of human and mouse PD-L1. Identical residues (red), conserved residues (blue), differing residues (black), and residues that interact to form the PD-1/PD-L1 complex (asterisks) are shown. Glycosylation sites are labeled by triangles, cysteines in disulfide bonds are labeled by circles and the free cysteine residue mutated to serine is labeled by a star. Image adapted by Lin et al. 2008. [155]

4.1.3 PD-L1 binding hotspot for small molecules

Numerous co-crystal structures of PD-L1 bound to ligands have been reported in the literature. In addition to the human PD-1 / human Pd-L1 co-crystal structure, four clinically used monoclonal antibodies have also been determined.[154] These structures have yielded valuable information of potential hot spots of binding to PD-L1. Indeed, PD-1

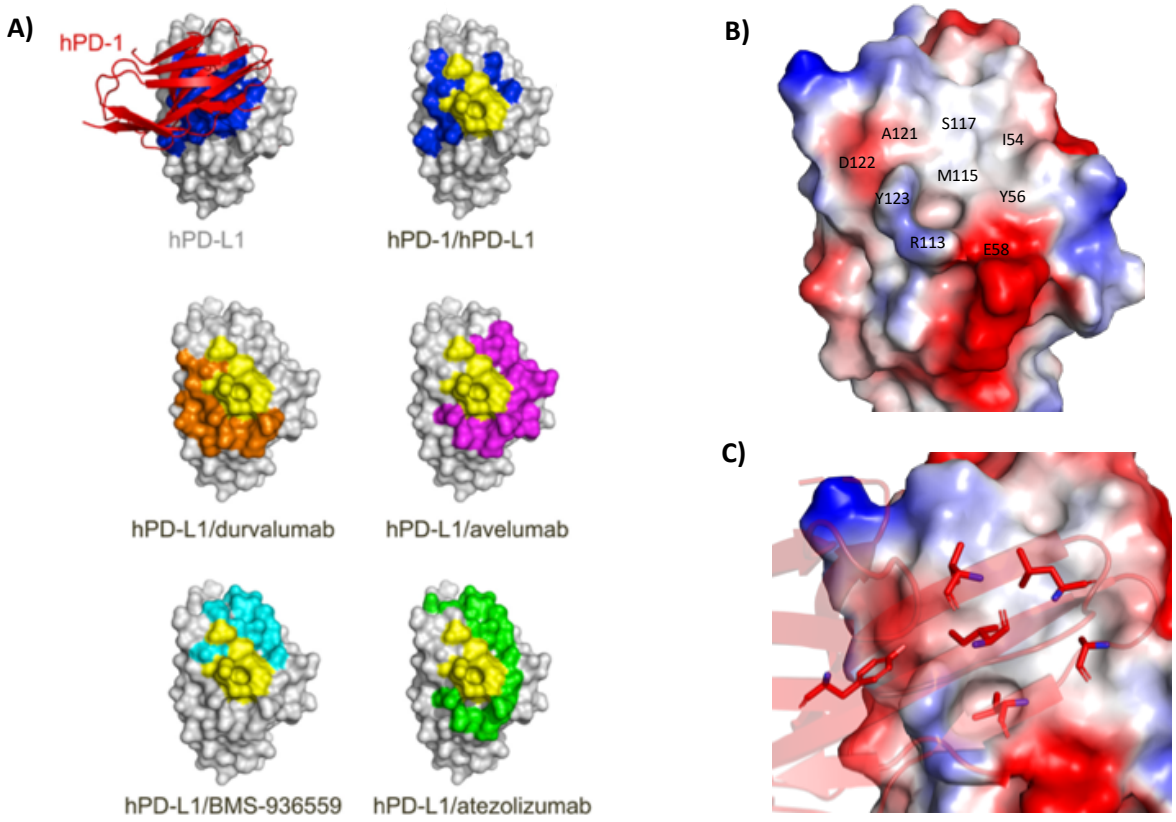

Figure 4-2: PD-L1 hotspot for small molecule binding.

A) Mapping the binding of PD-1 and anti-PD-L1 antibodies to PD-L1. Colored surface indicates binding surface of the PD-L1. Yellow surface is the shared region between PD-L1 and anti-PD-L1 antibodies. B) Electrostatic map of the shared binding site on PD-L1 highlights the hydrophobic pocket C) Specific interactions PD-1 makes at the hotspot suggesting potential binding sites for small molecules. Image adapted by Zak et al. 2017. [154]

and all four antibodies occupy a similar hydrophobic core on PD-L1 (Figure 4-2A, yellow surface). This core consists of five hydrophobic resides I54, Y56, M115, A121, and Y123 (Figure 4-2B). Interestingly, all antibodies occupy different surrounding electrostatic regions outside of the hydrophobic core (Figure 4-2A, colored surfaces). These structural insights suggest this hydrophobic core to be a potential hotspot for small molecule to bind and disrupt the interaction with PD-1. However, the surface at this site is mostly flat

with one shallow pocket formed by Y123 and R113 where PD-1 inserts an isoleucine residue (Figure 4-2C).

4.2 Results

4.2.1 PD-L1 construct optimization

The first PD-L1 construct tested consisted of both IgV and IgC domains (1 – 239, 25 kDa). This construct was cloned into the pET28b expression vector to contain a thrombin cleavable N-terminal 6His tag to aid in purification. This construct was expressed as ^{15}N labeled protein and purified according to previously reported protocols.[155] The ^{1}H-^{15}N HMQC spectra of this construct was missing approximately 100 peaks, contained many poorly resolved peaks and had varying peak intensities which would complicate data analysis for screening (Figure 4-3A). Buffer optimization, the addition of an anion exchange purification step, and modifications of the N-terminus failed to improve the quality of the HMQC spectra. Given that the IgV domain is the sole interaction domain for PD-L1, constructs of the IgV domain alone (18 – 132) were designed to improve the HMQC spectrum. However, attempts to express and purify these constructs resulted in protein that was not stable at concentrations required for NMR experiments (> 15 μM). Like the construct with both domains, the spectrum of the IgV domain at 10 μM with longer scan times is also missing numerous peaks (Figure 4-3B).

Because both PD-L1 constructs needed to be refolded, we speculated that the fold of the protein was incorrect. To express soluble protein from *E. coli*, we did expression tests with special Shuffle E. coli (NEB) strains that have been engineered to have a

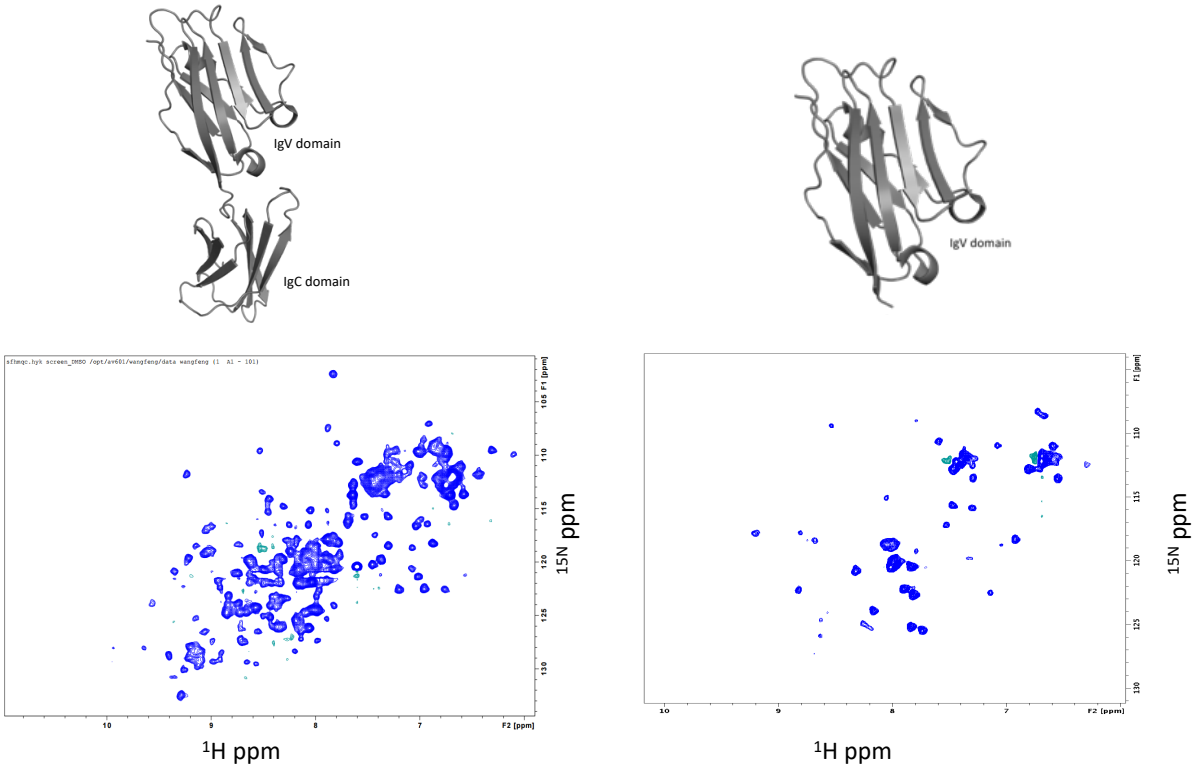

Figure 4-3: Preliminary PD-L1 constructs HMQC Spectra

PD-L1 constructs containing both IgV and IgC domains (left) and only the IgV domains (right) with HMQC spectra of each construct.

reducing cytosol and correctly fold proteins with disulfide bonds. To further promote the proper folding of PD-L1 in the cytosol, we engineered a fusion construct with the chaperone protein thioredoxin.[156] We also engineered PD-L1 fusion constructs with solubilizing proteins such as MBP and GST. Expression tests constructs containing thioredoxin, MBP, or GST fusion proteins resulted in a small fraction (estimated < 5%) of the PD-L1 fusion to be expressed as soluble protein. However, cleaving the MBP or Thioredoxin fusion from the IgV domain resulted in significant protein aggregation seen in previous refolded constructs.

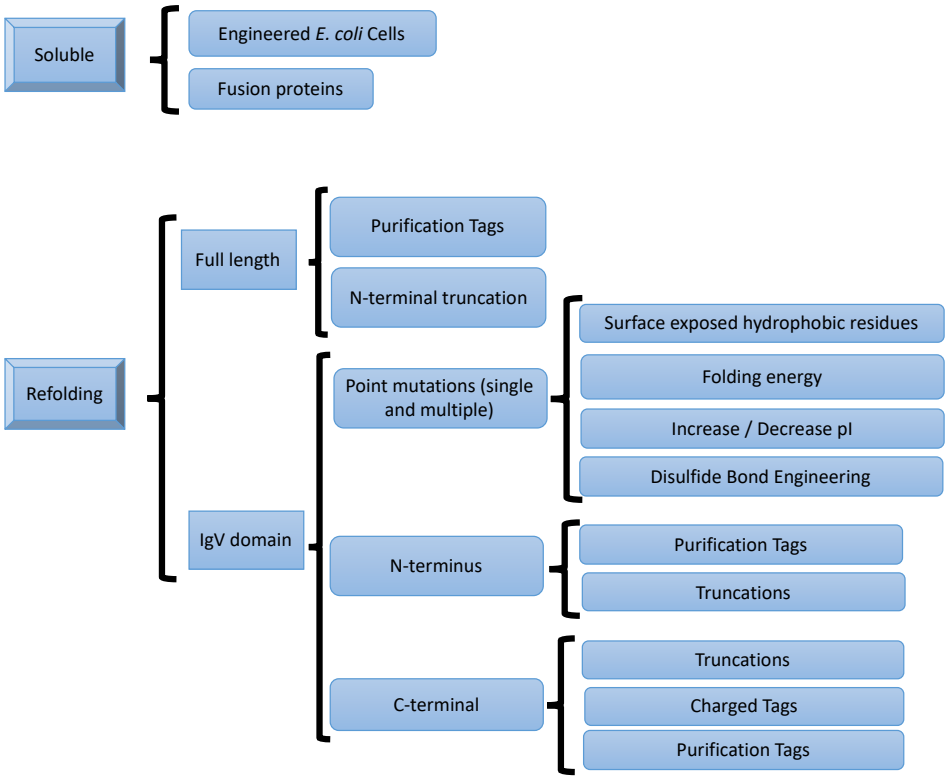

Figure 4-4: Construct optimization overview

Flow chart of the diverse strategies taken to optimize the PD-L1 IgV protein stability.

With no success in expression with fusion partners, other strategies were utilized to enhance the stability of the IgV domain. These strategies included adding purification tags at both N and C termini, extensions and truncations at both termini and rational design of mutations (Figure 4-4). The PD-L1 construct (18 – 132) was first modified by engineering mutations of solvent-exposed residues that were distant to the PD-1 binding site to increase the solubility and/or the stability of the protein (Figure 4-5A). Many of these mutations were designed by computational methods using protein engineering tools in Maestro modeling software developed by Schrödinger. Solvent-exposed hydrophobic residues were mutated to charged residues to remove potential aggregation

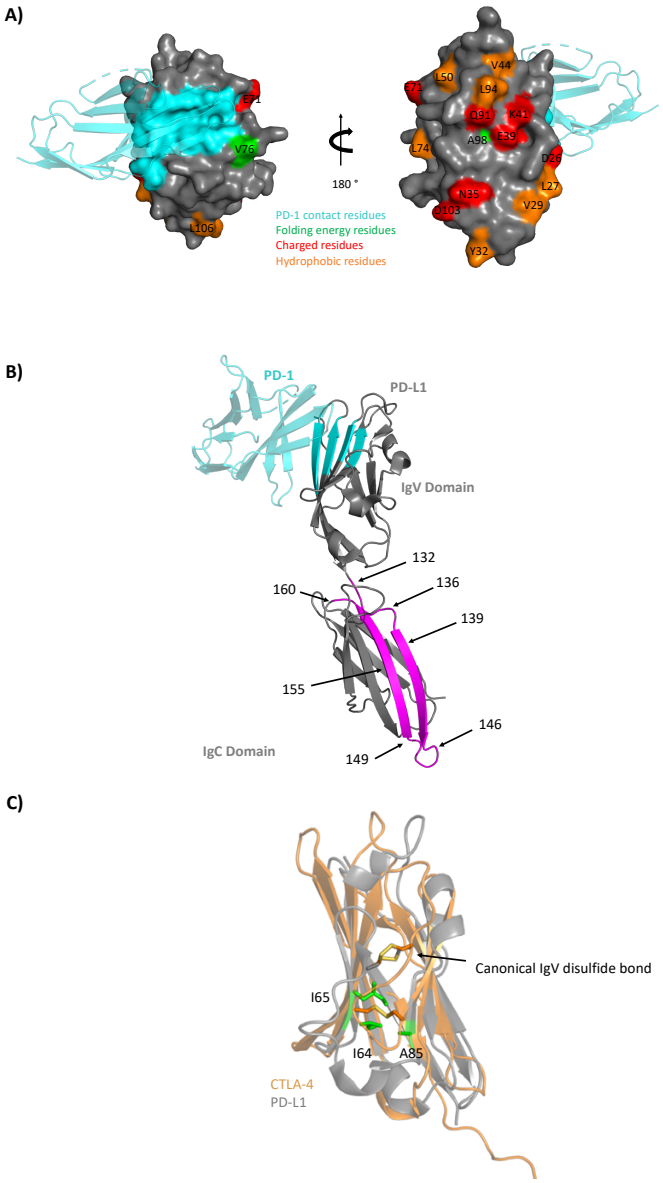

Figure 4-5: Construct design to improve protein stability.

A) Mutations made on the IgV domain distant from the PD-1 binding site (Teal). Orange residues are hydrophobic residues mutated to charged residues. Red residues are charged residues that were mutated to adjust the pI of the protein. Green residues are computationally predicted to enhance protein stability. B) C-terminal extensions into the IgC domain. Each label indicates a stop codon at the specific amino acid number. C) Disulfide engineering of PD-L1 (gray) based on homology to CTLA-4 (orange). Residues that were mutated to cysteines in pairs are indicated by green sticks and labeled.

sites (Figure 4-5A, orange surface). Charged residues were mutated to opposite charges to alter the pI of the construct (wildtype pI = 6.3) (Figure 4-5A, red surface). Additionally, Amanda Duran in Dr. Jens Meiler's lab at Vanderbilt University used Rosetta Protein Design to predict residues that lower the folding energy and increase protein stability. Rosetta suggested that residue valine 76 be mutated to lysine and alanine 98 be mutated to arginine for increases in protein stability (Figure 4-5A, green surface).

Mutations were tested in small scale productions and effects on stability were quantified by noting the max concentration that the construct was able to achieve before precipitating out of solution. Despite the variety of different mutations made, only minor effects on the stability were observed. Combinations of beneficial mutations resulted in constructs that were much worse than the wildtype or single mutation constructs. Because mutants had little benefit on protein stability, we hypothesized that other aspects of the construct were causing instability of the IgV domain.

The N and C termini were modified next to explore other modifications that may affect stability. Like the PD-L1 construct containing an IgV and IgC domain, extending or shorting the sequence at the N-terminus resulted in no effect on the protein stability. Short extensions or deletions at the C-terminus also had no effect. However, longer C-terminal extensions into the IgC domain resulted in significant improvements in stability. A series of constructs were designed that extended 28 residues into the IgC domain (Figure 4-5B, purple cartoon). The best construct contained a stop codon at residue 149. The HMQC spectra of the IgV-149 construct had disperse peaks, good signal intensity and the protein was stable to 1.5 mg/mL in the presence of 4% DMSO. However, the addition

of fragment mixtures (12 fragments at 800 μM each) to this construct rapidly aggregated as monitored by disappearance of HSQC signal intensity and visually by protein precipitation. Extensive buffer optimization and reduction of the concentration of fragments in the mixture failed to improve the protein stability.

Reflecting on previous work, CTLA-4 was highly stable when conducting a fragment screen. Given that CTLA-4 and PD-L1 both share IgV type folds, the structures of both proteins were overlaid to identify potential structural differences that may enhance PD-L1 stability (Figure 4-5C). Overlay of CTLA-4 and PD-L1 structures reveal identical placement of the canonical IgV fold disulfide bond (Figure 4-5C, orange and gray sticks). CTLA-4 has a second disulfide bond that could explain the enhanced construct stability compared to PD-L1. The overlay of both structures identified residues on PD-L1 that could be mutated to cysteine to mimic CTLA-4's additional disulfide bond. Modeling of potential disulfide bonds was performed using a web-based server Disulfide by Design 2 to predict potential disulfide bond formation based on the proximity and geometry of two residues if mutated to cysteine residues. Using these predictions, another four potential disulfide bonds were tested. However, mutations of these residues to cysteine severely interfered with protein refolding during purification. The small percentage of soluble protein after refolding was found to consist of large disulfide-linked aggregates on SDS PAGE gels and size exclusion chromatography.

Shortly after our discovery that the C-terminus is important for the stability of the IgV domain, two PD-L1 IgV constructs purified from *E. coli* were reported in the literature.[112, 157] The first report added 8-arginine residues after residue 132 to increase

the solubility of the protein.[157] To reproduce this result we designed and tested both PD-L1 8-arginine and PD-L1 8-lysine constructs. In addition to positively charged tags, a PD-L1 S-tag construct was designed to add charged residues without altering the pI of the protein. While the 8-arginine construct was found to be toxic to *E. coli* cells, both the 8-lysine and Stag constructs were expressed and purified in high yields and resulted in high-quality HMQC spectra. While improved over the previously discovered IgV-149 construct, both IgV-8Lys and IgV-Stag were also unstable when mixing with fragment mixtures required for NMR screening.

The second literature report was an IgV construct with a non-cleavable C-terminal 6His tag after residue 132.[112] The published crystal structure of this construct reveals the 6His tag adapts alpha-helical secondary structure and folds back on the IgV protein

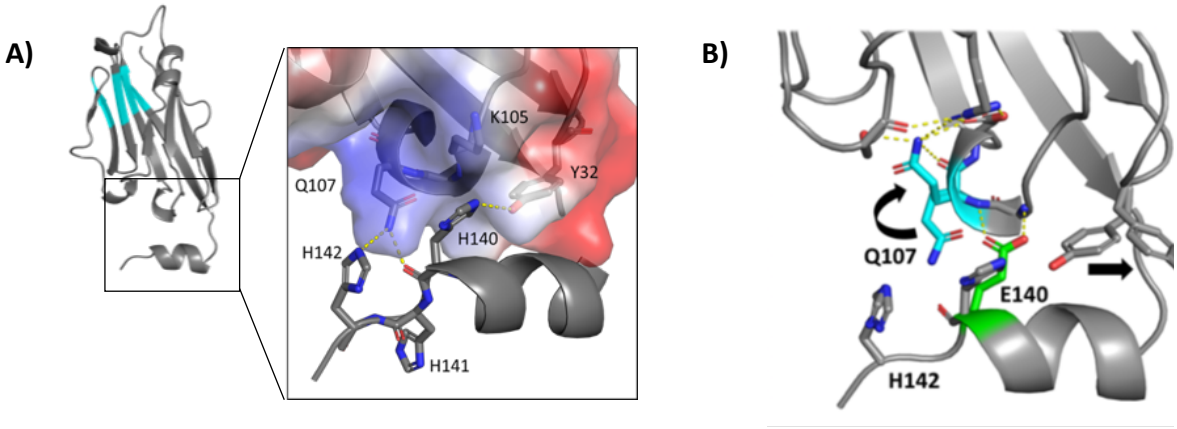

Figure 4-6: Design of H140E mutation on IgV-6His construct

A) Crystal structure of the IgV-6His construct with highlighted interactions from the 6His tag with the IgV domain. Hydrogen bonds are shown by yellow dashed lines. Surface is transparent electrostatic potential of the protein suggesting an electropositive region from K105. B) Overlay of IgV-6His and IgV-6His-H140E mutant show hydrogen bond formation of E140 with backbone amides of the IgV domain. Conformational changes of Q107 and Y32 were also identified. Q107 forms additional hydrogen bonding networks suggesting structural information of the enhanced stability of this construct. Image adapted from Perry et al 2019.[172]

forming both hydrophobic and electrostatic interactions (H140-H142) with the IgV domain (Figure 4-6A). This construct was expressed and purified in our lab but also found to be unstable with fragment mixtures. Using the structural information of the helix interacting with the IgV domain, mutations were rationally designed that could further enhance the stability. Notably, a large electropositive region of the protein formed by K105 and Q107 appeared to be in closest contact to the 6His portion of the helix. Molecular modeling experiments suggested mutation of H140 to glutamic acid could form additional hydrogen bonds with this region (Figure 4-6A). The IgV-6His-H140E construct was purified and crystallized in similar conditions to the reported wildtype construct. Indeed, the structure reveals E140 forms additional hydrogen bonding interactions with back amides of 106 and Q107 (Figure 4-6B).

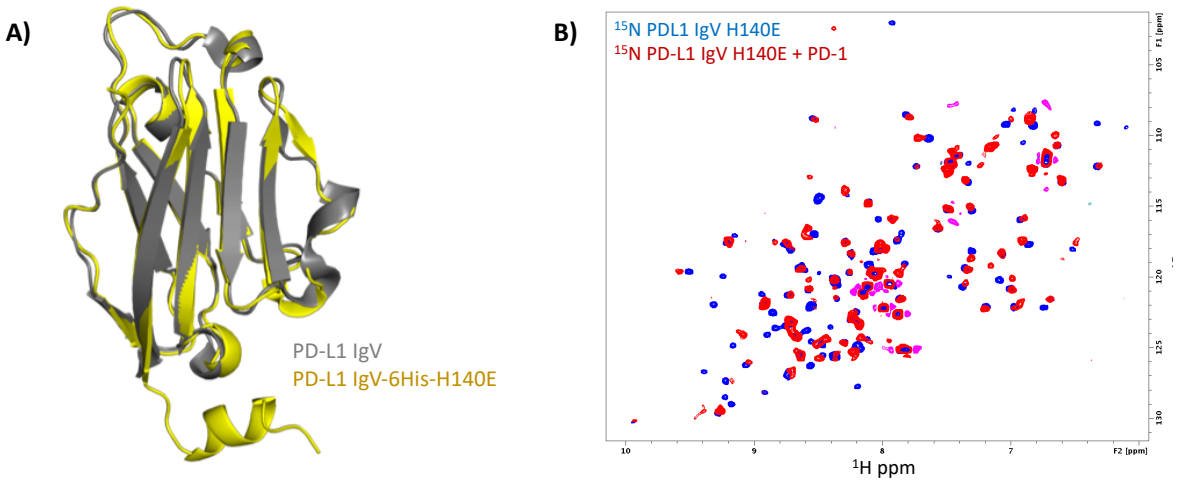

Figure 4-7: PD-L1 IgV-6His is properly folded and binds to PD-1

A) Overlay of the IgV portion of the IgV-IgC crystal structure (gray) with the mutant construct (IgV-6His-H140E, yellow) show an identical fold of the protein suggesting the mutation does not interfere with the fold of the protein. B) Overlay of HMQC spectra of ^{15}N IgV-6his-H140E (blue) and equimolar concentrations of unlabeled PD-1 added to ^{15}N IgV-6his-H140E results in peak shifts and peak broadening indicating binding of PD-1 to mutant construct suggesting the mutant is functionally active.

Table 4-1: List of all PD-L1 constructs designed and tested

Construct Name	Sequence	Removable Tag	Plasmid
	IgV-IgC		
IgV-IgC-12	12-239	none	pET29
IgV-IgC-16	16-239	none	pET29
IgV-IgC-18	18-239	none	pET29
6His-IgV-IgC	18-239	N-term 6His	pET28b
GST-IgV-IgC	18-239	N-term GST	pGEX6-1
Trx-IgV-IgC	18-239	N-term 6His-Trx-Stag	pET32a
IgV-IgC-6His	18-239	none	pET29
IgV-IgC-N-modified	18-228	N-term 6His	pET28b
MBP-IgV-IgC	18-228	N-term MBP	pAT108
IgV-IgC-MBP	18-228	C-term MBP	pAT108
SUMO-IgV-IgC	18-228	N-term SUMO	pBG102
IgV-IgC-SUMO	18-228	C-term SUMO	pBG102
	IgV Purification Tags		
IgV	18 - 132	none	pET29
6his-IgV	18 - 132	N-term 6His	pET28b
GST-IgV	18 - 132	N-term GST	pGEX6-1
Trx-IgV	18 - 132	N-term 6His-Trx-Stag	pET32a
MBP-IgV	18 - 132	N-term MBP	pAT108
IgV-MBP	18 - 132	C-term MBP	pAT108
SUMO-IgV	18 - 132	N-term SUMO	pBG102
	IgV Mutants		
IgV-D26K	18 - 132	N-term 6His	pET28b
IgV-L27K	18 - 132	N-term 6His	pET28b
IgV-V29K	18 - 132	N-term 6His	pET28b
IgV-Y32K	18 - 132	N-term 6His	pET28b
IgV-N35D	18 - 132	N-term 6His	pET28b
IgV-N35E	18 - 132	N-term 6His	pET28b
IgV-E39K	18 - 132	N-term 6His	pET28b
IgV-E39A	18 - 132	N-term 6His	pET28b
IgV-E39S	18 - 132	N-term 6His	pET28b
IgV-K41A	18 - 132	N-term 6His	pET28b
IgV-K41S	18 - 132	N-term 6His	pET28b
IgV-V44K	18 - 132	N-term 6His	pET28b
IgV-L50Y	18 - 132	N-term 6His	pET28b
IgV-L50M	18 - 132	N-term 6His	pET28b
IgV-E71K	18 - 132	N-term 6His	pET28b
IgV-L74K	18 - 132	N-term 6His	pET28b
IgV-V76K	18 - 132	N-term 6His	pET28b
IgV-Q91A	18 - 132	N-term 6His	pET28b
IgV-Q91S	18 - 132	N-term 6His	pET28b
IgV-Q91K	18 - 132	N-term 6His	pET28b
IgV-L94K	18 - 132	N-term 6His	pET28b
IgV-A98R	18 - 132	N-term 6His	pET28b
IgV-D103K	18 - 132	N-term 6His	pET28b
IgV-L106K	18 - 132	N-term 6His	pET28b
IgV-E39K,V44K	18 - 132	N-term 6His	pET28b
IgV-V76K,A98R	18 - 132	N-term 6His	pET28b
IgV-V76K,L94K	18 - 132	N-term 6His	pET28b
IgV-E71K,L106K	18 - 132	N-term 6His	pET28b
IgV-E71K,L94K	18 - 132	N-term 6His	pET28b
IgV-L94K,L106K	18 - 132	N-term 6His	pET28b
6His-IgV-D26K, V76K	18 - 132	N-term 6His	pET28b
6His-IgV-D26K, L94K	18 - 132	N-term 6His	pET28b
6His-IgV-V76K, K41S, Q91S	18 - 132	N-term 6His	pET28b
6His-IgV-D26K, V76K, L94K	18 - 132	N-term 6His	pET28b
Surface hydrophobic Residues Construt 1	18 - 132	none	pET28b
Surface hydrophobic Residues Construt 2	18 - 132	none	pET28b

Construct Name	Sequence	Removable Tag	Plasmid
	IgV Truncations		
IgV-136	18 - 136	N-term 6His	pET28b
IgV-139	18 - 139	N-term 6His	pET28b
IgV-146	18 - 146	N-term 6His	pET28b
IgV-149-N	18 - 149	N-term 6His	pET28b
IgV-149a	18 - 149	N-term 6His	pET28b
IgV-149b	18 - 149	N-term 6His	pET28b
IgV-155	18 - 155	N-term 6His	pET28b
IgV-160	18 - 160	N-term 6His	pET28b
IgV-Loop del-P43/V44; delL50; delA51; del L53; del L50A51	18 - 132	N-term 6His	pET28b
IgV-149-D26K	18 - 149	N-term 6His	pET28b
IgV-149-L94K	18 - 149	N-term 6His	pET28b
IgV-149-V76K	18 - 149	N-term 6His	pET28b
	Charged C-terminal Tags		
IgV-8Arg	18 - 132	N-term 6His	pET28b
IgV-Stag	18 - 132	N-term 6His	pET28b
IgV-8Lys	18 - 132	N-term 6His	pET28b
IgV-8Lys-6His	18 - 132	N-term 6His	pET28b
IgV-8Lys-6His-6His	18 - 132	N-term 6His	pET28b
IgV-8Lys-V76K	18 - 132	N-term 6His	pET28b
IgV-8Lys-V76T	18 - 132	N-term 6His	pET28b
IgV-8Lys-V76G	18 - 132	N-term 6His	pET28b
N-2Lys-IgV-8Lys	18 - 132	N-term 6His	pET28b
N-4Lys-IgV-8Lys	18 - 132	N-term 6His	pET28b
	Disulfide Bond Engineering		
6His-IgV-I64C, A85C	18 - 149	N-term 6His	pET28b
IgV-8Lys-I64C,A85C	18 - 132	N-term 6His	pET28b
IgV-8Lys-I65C,A85C	18 - 132	N-term 6His	pET28b
IgV-8Lys-G33C,D103C	18 - 132	N-term 6His	pET28b
IgV-8Lys-N35C, T102C	18 - 132	N-term 6His	pET28b
IgV-8Lys-S34C,V104C	18 - 132	N-term 6His	pET28b
	C-terminal 6His Tag		
IgV-6His	18 - 132	none	pET28b
IgV-6His-V76G	18 - 132	none	pET28b
IgV-6His-V76T	19 - 132	none	pET28b
IgV-6His-Y136D	18 - 132	none	pET28b
IgV-6His-H140E	18 - 132	none	pET28b
IgV-6His-8Lys	18 - 132	none	pET28b
IgV-6His-8Lys-V76K	18 - 132	none	pET28b
IgV-6His-6His	18 - 132	none	pET28b
IgV-6His-4His-6His	18 - 132	none	pET28b
IgV-8His	18 - 132	none	pET28b
SUMO-IgV-6His	18 - 132	N-term SUMO	pBG102
MBP-IgV-6His	18 - 132	N-term MBP	pAT108
	Constructs for X-ray Crystallography		
IgV-6His-V76T,H140E	18 - 132	none	pET28b
IgV-IgC-STOP228	18-228	none	pET29
IgV-6His-R113A	18 - 132	none	pET28b
IgV-6His-E58A	18 - 132	none	pET28b
IgV-6His-L27N	18 - 132	none	pET28b
IgV-6His-L50Y	18 - 132	none	pET28b
IgV-6His-L50M	18 - 132	none	pET28b
IgV-6His-L74N	18 - 132	none	pET28b
IgV-6His-A51D	18 - 132	none	pET28b
IgV-MBP	18 - 132	none	pET28b
IgV-Lysozyme	18 - 132	none	pET28b

Unexpectantly, the H140E mutation caused a conformational change of Q107 to rotate up towards PD-L1 and form additional hydrogen bonding network with S80, R84, and D108 (Figure 4-6B). This mutation significantly improved the stability of the IgV domain during purification and with the addition of fragments. The H140E mutation did not cause any other conformational changes to the protein that would cause differences in the fold of the IgV domain relative to wildtype (Figure 4-7A).

To further validate the mutation did not alter protein function, the IgV-6his-H140E construct was shown to retain binding to PD-1 by monitoring resonances shifts and resonance broadening in ^{1}H-^{15}N HMQC spectra of IgV-6his-H140E with the addition of equimolar concentrations of unlabeled PD-1 (Figure 4-7B). With increased stability and validation that this construct retained the ability to bind PD-1, this construct was used for fragment screening. Summary of all constructs designed and tested for the optimization of PD-L1 stability is outlined in Table 4-1.

4.2.2 Expression and purification of PD-L1

Large amounts of ^{15}N labeled protein was produced to conduct the fragment-based screen. This plasmid containing the IgV-6His-H140E construct was transformed into *E. coli* BL21 (DE3) cells (Thermo Fisher). Uniformly ^{15}N labeled PD-L1 was expressed as inclusion bodies in M9 media containing ^{15}N ammonium chloride after a 5-hour induction with IPTG at 0.8 OD_{600}. Insoluble inclusion bodies were first purified by a series of Triton X-100 and salt washing steps using centrifugation to pellet the inclusion bodies between steps. PD-L1 inclusion bodies were solubilized in 6M guanidine HCl and refolded dropwise

A)

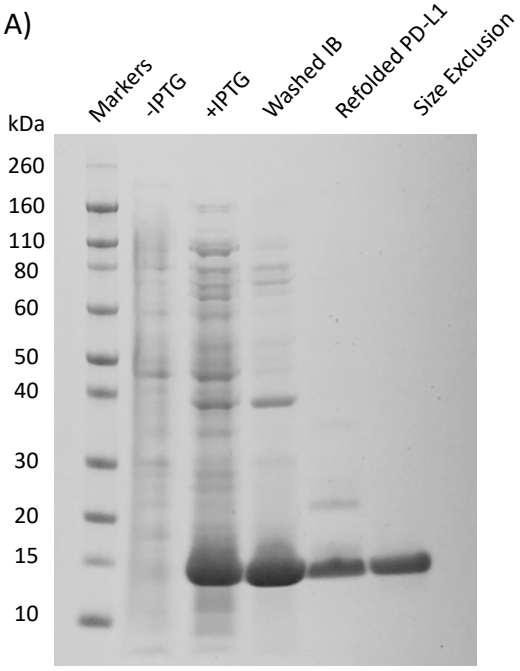

B)

Purification step	Protein Recovered	Yield (%)
Washed IBS	1.25 g	N/D
Denatured IBS	98 mg	100
Refolded PD-L1	43 mg	43
Size Exclusion	20 mg	20

C)

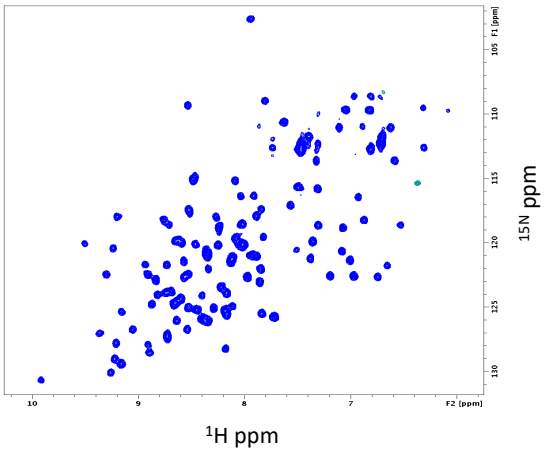

Figure 4-8: PD-L1 protein production summary

A) SDS PAGE gel of the PD-L1 purification process. Lane 1: marker Lane 2: cell lysate prior to PD-L1 induction by IPTG. Lane 3: PD-L1 expression induced by IPTG indicated by band at 14 kDa. Lane 4: Washed inclusion bodies (IB). Lane 5: concentrated refolded PD-L1. Lane 6: PD-L1 after size exclusion. B) Protein yields per liter of cell culture for each step of the purification process. C) HSQC of ^{15}N labeled PD-L1 indicates a well folded protein suitable for fragment screening.

into PD-L1 refolding buffer containing 1M Arginine. Refolded PD-L1 was dialyzed in large volumes (2L protein to 8L of buffer) of dialysis buffer 3 times for 24 hours per dialysis step to reduce the concentration of arginine. Unlike PD-1 and CTLA-4, PD-L1 was not concentrated by nickel affinity purification due to protein aggregation observed on the column. Instead, PD-L1 was concentrated using Amicon stirred cells using a 5 kDa molecular weight cut off membrane. PD-L1 at 0.5 mg/mL concentration (30 µM) was further purified by size exclusion chromatography preequilibrated with NMR buffer

(Figure 4-8A). Purification of PD-L1 resulted in highly pure protein with yields around 30 mg/L of ^{15}N M9 cell culture (Figure 4-8B).

4.2.3 Fragment Screen of PD-L1

Screening conditions were optimized by adjusting the buffer pH, salt concentration, fragment concentrations and the number of fragments per mixture. A test set of 30 diverse fragments handpicked from the fragment library were used to assess protein stability in the presence of fragment mixtures. The goal of the optimization was to achieve a minimum of 8 hours of protein stability at room temperature when mixed with fragments monitored by HMQC signal intensity at room temperature. Optimized conditions were found containing 50 mM Sodium Phosphate pH = 7, 25 mM NaCl with 4% DMSO. PD-L1 was found to be stable for 8 hours containing mixtures of 6 fragments at 400 µM each. The Fesik lab fragment library containing 13,824 fragments was screened by monitoring chemical shift changes in ^{1}H-^{15}N SOFAST HMQC spectra of ^{15}N labeled PD-L1 in optimized screening conditions as mixtures of 6 fragments. Hits in mixture samples were noted by chemical shift changes and/or peak broadening relative to a DMSO sample. Mixture samples marked as hits were deconvoluted by testing each fragment individually at 800 µM concentration. In total, the screen resulted in the identification of 226 fragments that bind to PD-L1. All hits to PD-L1 are shown in Appendix A.

4.2.4 Hit classes from fragment screen

Three types of HMQC spectra were observed in the screen (Figure 4-9). 40% of the hits had resonance shifts traditionally seen in fast exchange binding, termed class A hits.

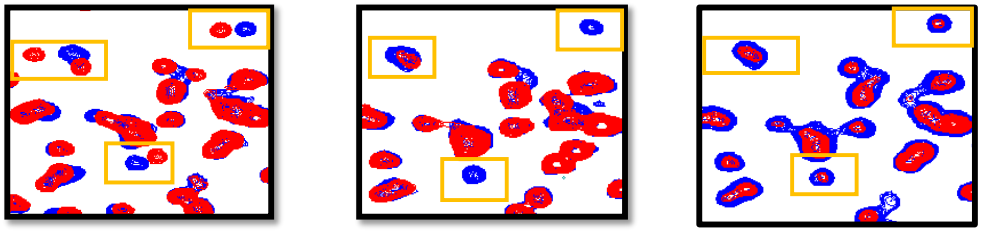

Class A
91 Hits

Class B
86 Hits

Class C
49 Hits

Figure 4-9: Hit classes identified in the fragment screen.

Class A hits classified by peak shifts. Class B hits classified by specific peak broadening. Class C hits classified by universal peak broadening. Class A and Class B hits resulted in changes in the same peaks, suggesting these fragments are interacting with the same pocket on PD-L1. Resonance broadening verses shifting is likely due to protein dynamics on the intermediate time scale.

(Figure 4-9A). 38% of hits had specifically broadened peaks, termed class B (Figure 4-9 B) and the remaining 22% of hits had uniformly broadened peaks typically associated with protein oligomerization or aggregation, termed class C (Figure 4-9C). Notably, the resonances that shift in class A are the same peaks that broaden in class B (Figure 4-9, orange boxes).

Broadening of specific peaks could be indicative of intermediate exchange binding (K_d < 10 µM). The peak intensity of a broadened peak is typically brought back at when protein is saturated with ligand at concentrations many fold higher than the K_d. To test if these fragments bind to PD-L1 with low micromolar affinity, fragments were titrated using high concentrations of fragments (up to 1.6 mM). However, fragments at high concentrations failed to bring any signal back from broadened peaks suggesting these hits may not be due to intermediate exchange binding (Figure 4-10A). Peak broadening may also be caused by minor protein precipitation. However, removal of fragments from the

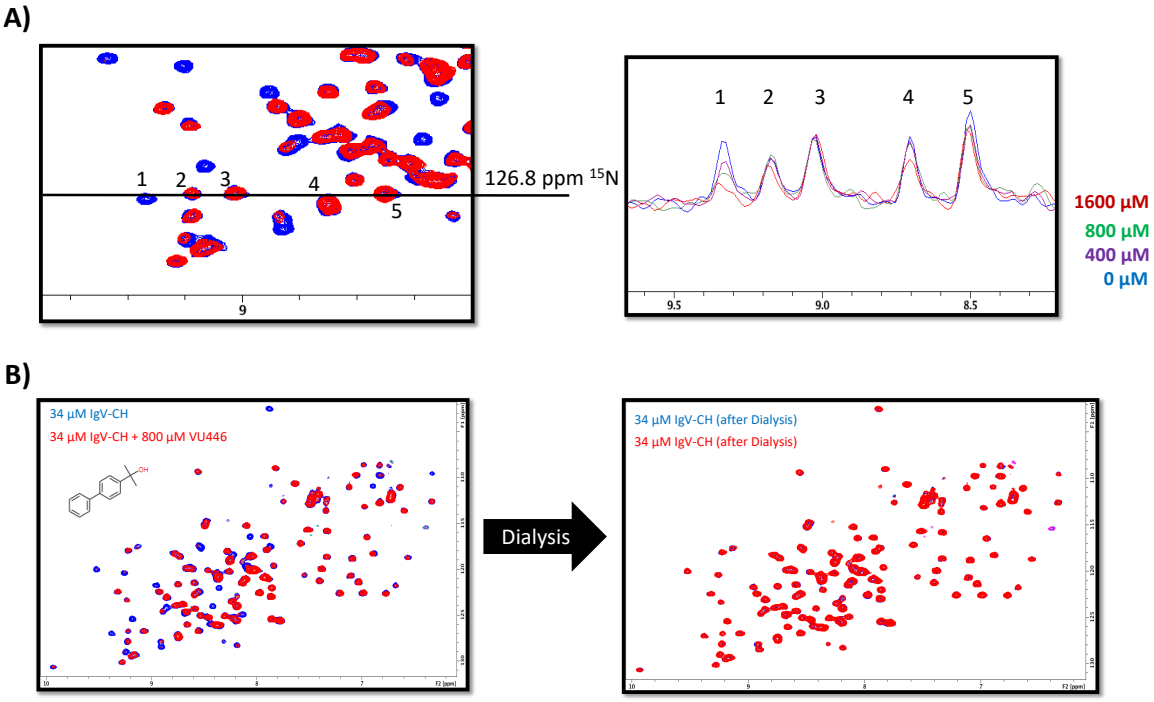

Figure 4-10: Class B hit validation

A) HMQC of a class B hit. Black line indicates the 1D extracted slide at 126.8 ppm. 1D slide extracted at 126.8 ppm ^{15}N of a titration of a class B hit shows only peak 1 results in a dose dependent broadening suggesting broadening is dependent on ligand concentration. B) Dialysis experiment of class B hit. HMQC spectra obtained of a class B hit (left). Sample is then removed from the NMR tube and dialyzed overnight to remove fragment. Sample is added back to an NMR tube and HMQC spectra is obtained (right). Rescue of signal intensity is suggesting broadening is ligand dependent and not resulting from artifacts like protein aggregation.

sample by dialysis overnight and re-running a HMQC on the dialyzed sample resulted in the rescue of the signal intensity of broadened peaks (Figure 4-10B), suggesting that broadening of class B hits are fragment specific. From these studies, we hypothesized that these hits may be due to protein dynamics or conformational changes in the protein caused by fragment binding. Indeed, a co-crystal structure obtained of class B hits later in this chapter suggest broadening seen from these hits is due to protein dimerization.

Class C hits that have universal peak broadening are typically dismissed in a fragment screen as compounds that cause protein aggregation or denaturation. Class C mixtures were also deconvoluted in case a fragment hit was contained in one of these mixtures that would otherwise be missed. Many class C hits in fragment mixture samples failed to produce a hit during deconvolution. Interestingly, deconvolution of class C hits identified 49 fragments that caused universal peak broadening. These fragments were found to be time-dependent, failed to rescue peak intensity after dialysis, and eluted as protein aggregates on size exclusion chromatography experiments. These hits were not followed up for structure determination and medicinal chemistry efforts.

4.2.5 Fragment hit titrations

Qualitative V-scores were given to each fragment mixture and deconvoluted hit. V-scores were on a scale of 0 to 4 with 0 indicating no speak shifts or broadening, 1 indicating weak shifts or broadening and 4 indicating strong shifts or broadening. However, V-scores do not always correlate with higher binding affinity due to the different shielding or de-shielding potential of the fragments. Thus, to accurately rank order hits based on the affinity to PD-L1, K_d values were generated by NMR titration experiments for class A hits (Figure 4-11A). NMR titrations were conducted using a 6-point curve with 2-fold serial dilutions starting at 1.6 mM as the top concentration. Preliminary titrations of Class A hits were weak and failed to saturate the binding curve. To accurately measure K_d values the top fragment concentration was raised to 3 mM. However, many fragments were not soluble at concentrations above 1 mM and processing data without accounting for the fragment solubility yielded inaccurate K_d

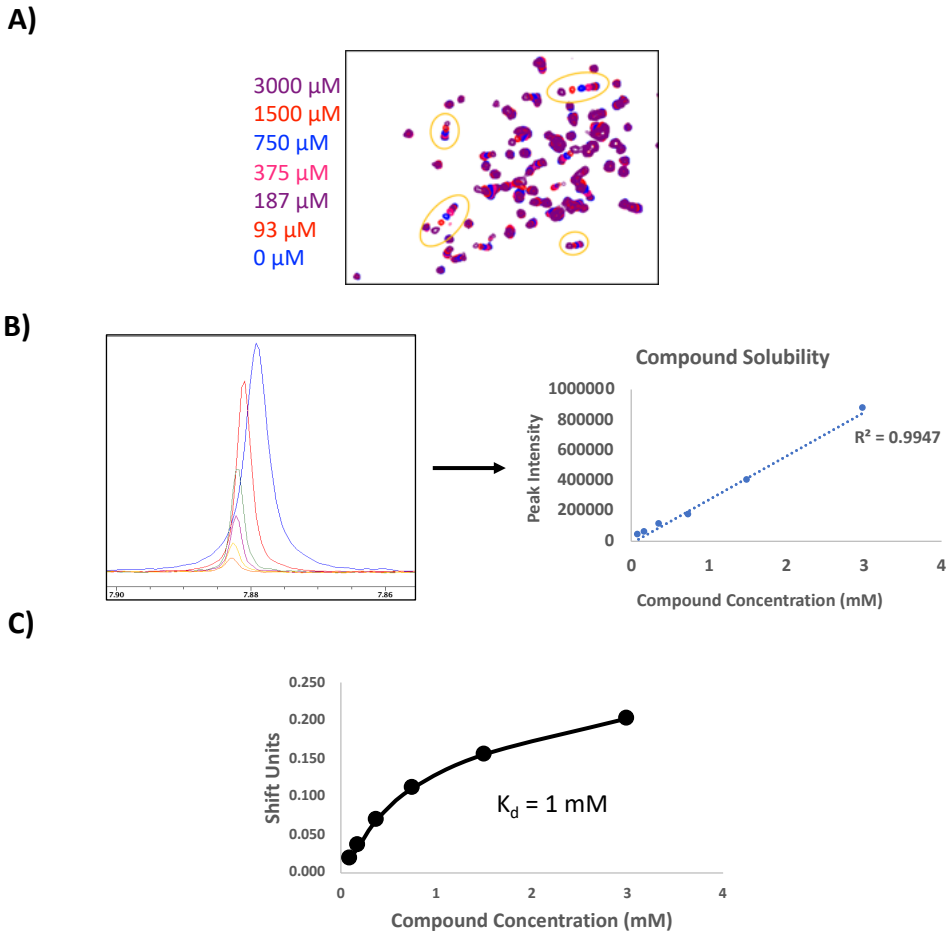

Figure 4-11: NMR Titrations of fragment hits

A) Overlay of HMQC of a fragment titration at 30 µM PD-L1. Fragment concentration is color coded based on peak color. B) Overlay of a singlet peak obtained from 1H NMR spectra from a fragment titration (left). Plot of the signal intensity verses compound concentration (right) shows a linear relationship suggesting the compound is soluble to 3 mM. C) Peak shifts in ppm verses compound concentration used to calculate K_d values of fragment hits.

estimates. To account for fragment solubility a 1D proton spectrum was taken immediately prior to a 2D HMQC spectra. The signal intensity of a singlet peak in a ^{1}H spectra was plotted against the fragment concentration (Figure 4-11B). The signal intensity of a singlet peak is proportional to the fragment concentration and thus a plateau in signal intensity indicates the fragment solubility limit has been reached. Any

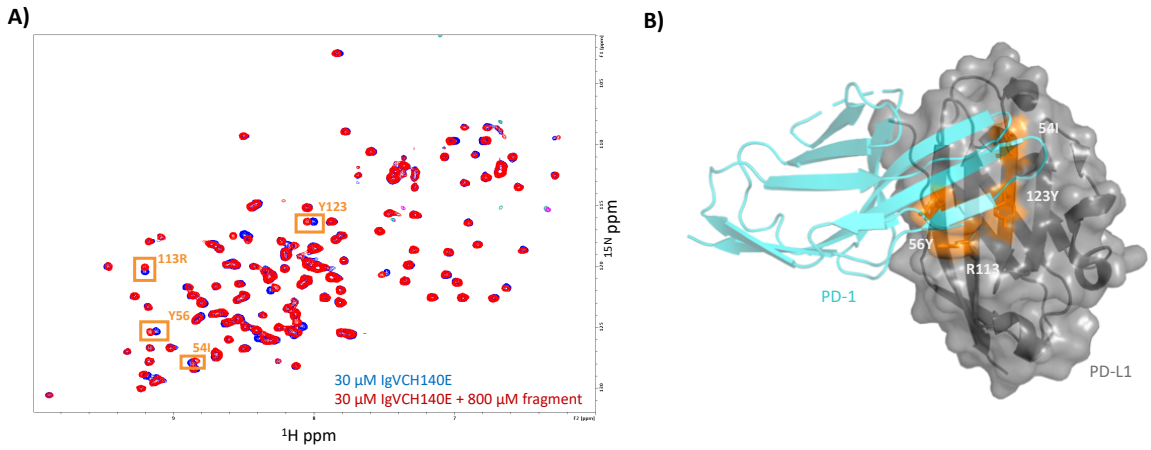

Figure 4-12: Fragment hits bind to the PD-1 binding site of PD-L1

A) Overlay of HMQC spectra of PD-L1 IgV-6His-H140E (blue) with PD-L1 with a fragment hit (red). Peaks in orange boxes and labels are assigned residues based on partial assignments of PD-L1. B) Co-crystal structure of the PD-1 / PD-L1 interaction. Boxed peaks are highlighted by orange surface on the PD-L1 surface suggesting the fragments bind to the PD-1 binding site on Pd-L1.

data points with poor solubility were excluded from titration data processing. Furthermore, if the K_d from a titration curve was predicted to be higher than the top concentration of the titration (3 mM) then the K_d was simply noted as > 3 mM. The K_d values obtained for class A hits with a V-score greater than 1 ranged from 1 mM to greater than 3 mM. Class B hits were not titrated due to the inaccuracies of K_d determination by plotting peak intensities of broadened peaks vs compound concentrations.[158]

Only one shifting and broadening pattern was identified from the screen suggesting that all hits bind to the same location on PD-L1. The assignments of the PD-L1 HSQC spectra have not been reported to date. Shifted residues that are highlighted by orange boxes were assigned by mutagenesis (Figure 4-12A). These residues map to the PD-1 binding site of PD-L1 and suggest that fragment hits bind to this site (Figure 4-12B).

4.2.6 NMR displacement Assay

To test if the fragment hits were capable of displacing PD-1 from PD-L1 an NMR based antagonist induced dissociation assay (AIDA) was utilized.[159] The AIDA assay was performed by the addition of a slight molar excess of unlabeled PD-L1 to ^{15}N PD-1 causing HMQC signals to broaden corresponding to complex formation (Figure 4-13B). Addition of fragments that displace ^{15}N PD-1 from PD-L1 result in a rescue of the ^{15}N PD-1 signal (Figure 4-13C).

In total, 104 of the top fragment hits were tested in this assay and given a score based on the percentage of peak intensity rescued by the addition of the fragment. Fragments were ranked based on their ability to rescue the signal intensity of glycine 90 of PD-1 at 800 μM fragment concentration (Figure 4-14). The best hits were assigned a score of 2 that displayed > 15% rescued signal. Hits that were between 1% and 15% were given a score 1 and hits that failed to displace PD-1 were scored 0. In total, 36 of the fragment hits were able to displace PD-1 with 14 hits as score 2 and 22 hits as score 1 (Appendix B). Increasing the fragment concentration resulted in higher percent rescue. For example, VU0432747 was found to result in approximately 75% signal rescue at 2 mM concentration (Figure 4-14).

4.2.7 PD-L1 Hit clusters and analog screening

Fragment hits obtained in the screen were highly diverse and were clustered into 18 distinct chemotypes (Appendix B). Observed ring systems included both 5-6 fused and 5-6 linked ring systems (Clusters 1 – 4, 8, 9, 10, 11, 12). In addition, 6-6 linked ring systems

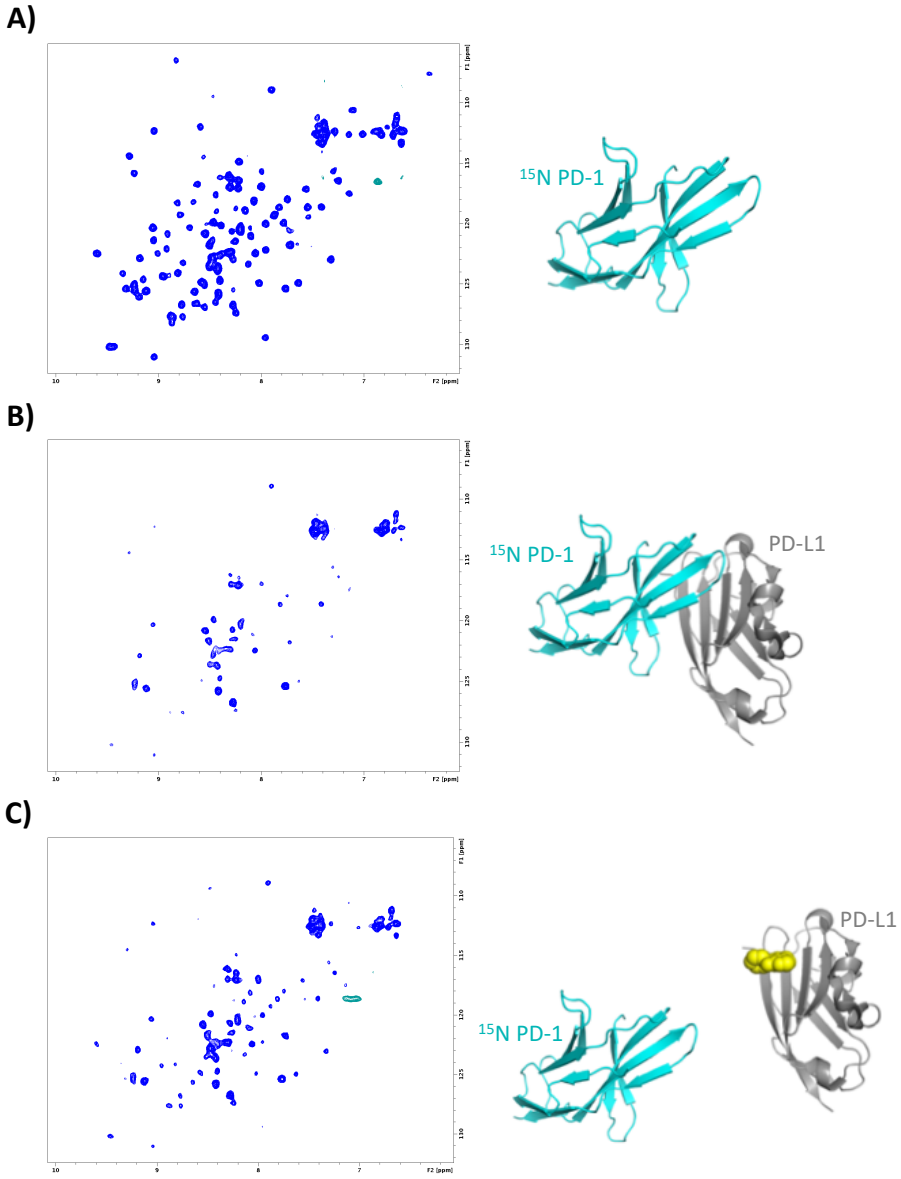

Figure 4-13: PD-1 displacement assay by NMR spectroscopy

A) HMQC of 15N PD-1. B) HMQC of 15N PD-1 and equal molar concentrations of unlabeled PD-L1 C) HMQC of 15N PD-1, unlabeled PD-L1 and 4 mM of fragment hit. Rescue in signal intensity from C) compared to B) suggests PD-1 is partially displaced by fragment binding to PD-L1.

and 5-6 and 6-6 ring systems with a 1 atom linker were also highly prevalent (cluster 5 – 6). Commonly observed modalities include thiazol rings, mono and disubstituted phenyl rings and sulfur-containing heterocycles. Each hit cluster is associated with a hit class

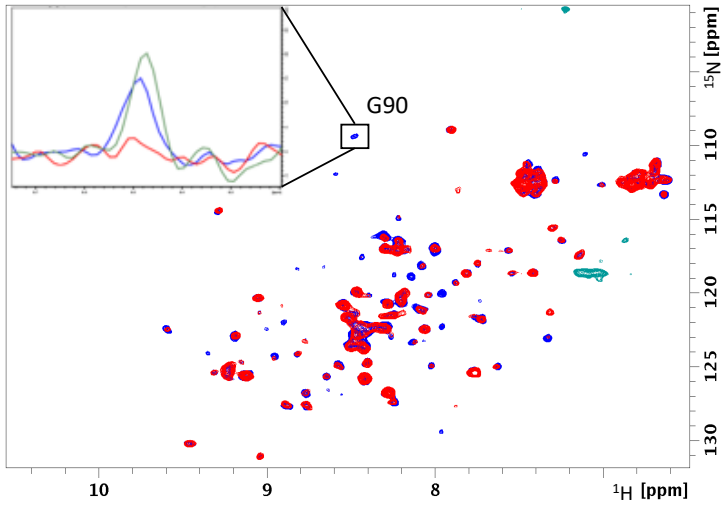

Figure 4-14: Percent rescue of PD-1 G90 with 2 mM VU0432747.

^{15}N HMQC PD-1 spectrum is broadened by the addition of unlabeled PD-L1 (red HMQC). Rescue of signal intensity by addition of 2 mM of VU0432747 (blue HMQC). Stronger signal intensity of blue peaks suggests VU0432747 displaces PD-L1 from PD-1 resulting in stronger signal intensity. Inset 1D slice of the HMQC spectra shows rescue of signal intensity from G90 of PD-1. G90 peak intensity is broadened to baseline by the addition of ^{14}N PD-L1 (red line) compared to ^{15}N PD-1 alone (green line). Addition of 2 mM of VU0432747 rescues approximately 75% of the signal intensity (blue line). Image adapted from Perry et al 2019.[172]

(class A – C) although there are exceptions in each case. For example, hit cluster 1 is primarily class A whereas hit cluster 4 is primarily class B. Certain hit clusters also tend to have higher V-scores compared to other clusters, suggesting certain hit clusters were stronger than others.

PD-1 displacement scores appear to be dispersed over most hit clusters, although there are a few hit clusters with higher prevalence (cluster 4, 7 and 11). Notably, cluster 7 is a strong hit cluster with high V-scores and PD-1 displacement scores. This cluster consists of substituted biphenyl fragments that are highly similar to BMS patented PD-L1 inhibitors (Chapter 6). To further develop SAR trends a 400-compound analog screen was designed by substructure similarity searches of each fragment chemotype in the

Vanderbilt High throughput Screening Facility. 70 class A hits were identified, 33 class B hits were identified, and 22 class C hits were identified. However, most analogs had weak V-scores (5 class A hits > 3, 13 class B hits > 3).

4.2.8 Co-crystal structures of fragments bound to PD-L1

Generating structural information of fragments bound to the protein is crucial to guide the structure-based design of more potent analogs. The most straightforward and quickest way to generate structural information is by X-ray crystallography. While apo PD-L1 crystalizes easily in many different crystallization conditions, all attempts to soak fragments into apo crystals failed. Analysis of the crystal packing reveals that the PD-1 binding site of PD-L1 is completely blocked in both the IgV and IgV-IgC constructs in multiple different space groups (Figure 4-15, teal sticks). Thus, co-crystallization methods were needed to obtain co-crystal structures of the fragments bound to PD-1 binding site. Co-crystallization protocols recommend using ligand concentrations that are up to 10 times the K_d to saturate the protein for the highest chance of getting ligand bound to the protein.[160] Because the binding affinity of the fragment hits were weak, many fragments were not expected to reach saturation levels (estimated to be > 10 mM) due to limited solubility. For this reason, an emphasis was placed on fragments with the highest solubility to increase the chances of getting a bound structure. Attempts to co-crystallize PD-L1 in the presence of fragments near their respective solubility limit using IgV-IgC, IgV-6His and IgV-6His-H140E constructs were all unsuccessful despite screening numerous protein crystallization kits containing a diverse set of conditions and different co-crystallization and seeding methods.

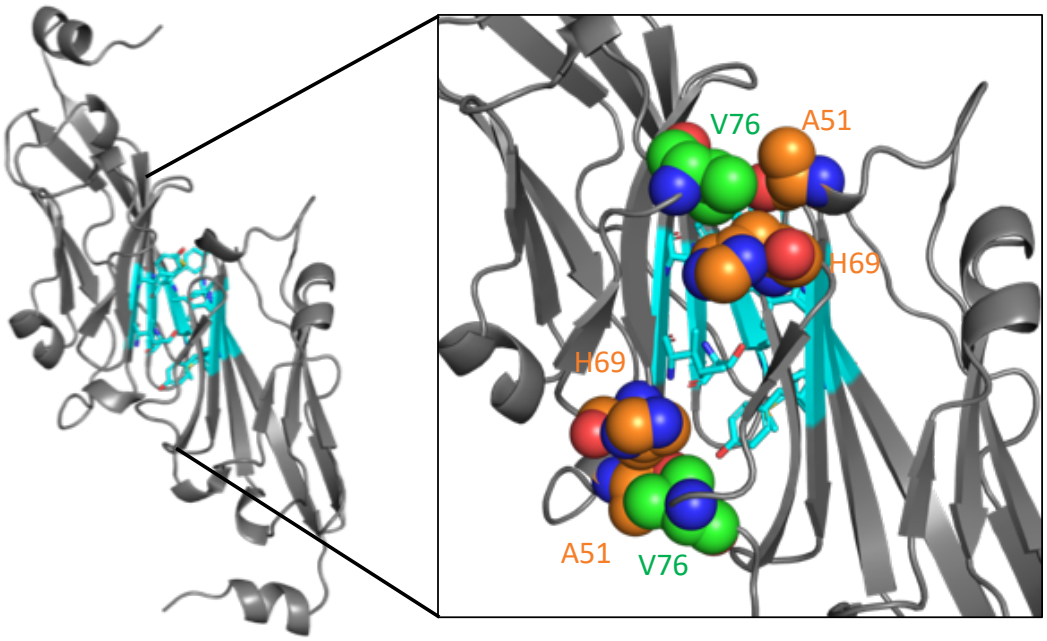

Figure 4-15: Crystal packing of unliganded PD-L1.

Crystal packing of unliganded PD-L1. PD-1 binding site (teal) comes together in a head to toe arrangement blocking the predicted fragment binding site. Blowup of the crystal packing interface suggests residues on the neighboring loop (V76, A51 and H69) could be mutated to block this crystal packing to encourage other packing that may yield an open PD-1 binding site.

It was evident that the crystal packing mechanism of PD-L1 was limiting our success in generating co-crystal structures. A series of mutants were designed were designed that would alter the crystal packing preventing PD-L1 from crystalizing with the PD-1 binding site blocked. Mutations were carefully designed to not interfere with the PD-1 binding site where our fragments were predicted to bind. Notably, V76 was found to make crystal contacts and was in a loop region next to the PD-1 site that may offer some flexibility (Figure 4-15). V76 was mutated to a threonine to slightly change the physicochemical properties of this residue that may influence crystal packing while maintaining the binding interactions with PD-1 and the fragments. Concentrating dilute

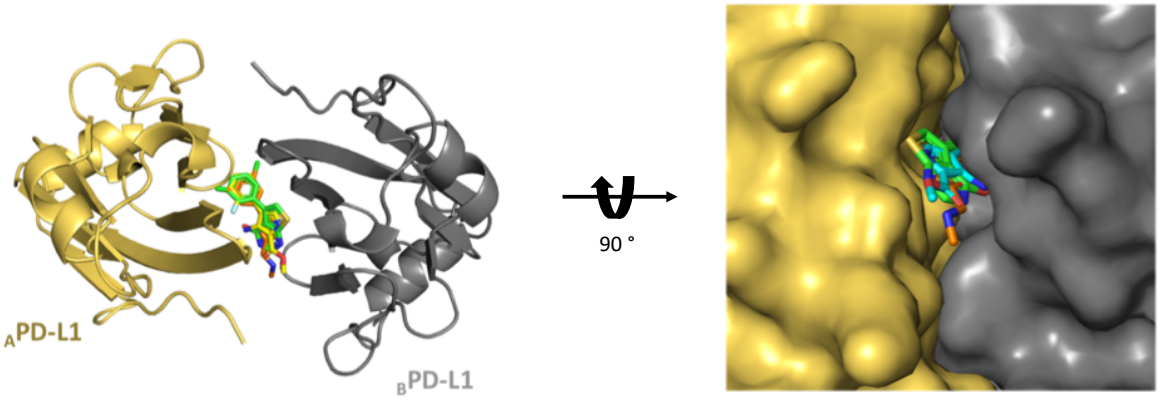

Figure 4-16: Co-crystal structures of fragments bound to PD-L1.

Fragments co-crystalize to PD-L1 by formation of a PD-L1 homodimer with a fragment inserted at the interface of the two monomers. PD-L1 monomer A is shown in yellow surface and monomer B is shown as gray surface. Fragments are shown as sticks and overlaid from multiple crystal structures to highlight the similar binding orientation of each fragment. Image adapted from Perry et al 2019.[172]

(30 µM) IgV-6His-V76T in the presence of a fragment at 2 – 4 mM concentration and screening a Hampton index HT screen resulted in crystal formation in new conditions (1.4 K_2HPO_4, 0.56 $NaAH_2PO_4$). PD-L1 in these conditions co-crystalized as a homodimer in the asymmetric unit with a fragment bound at the interface of the two monomers with a 2:1 stoichiometric ratio of PD-L1 to fragment (Figure 4-16). More than 80 of the best fragments were screened around these crystallization conditions using the V76T construct. In total 13 co-crystal structures were obtained (Table 4-2). Notably, crystal structures were obtained from mostly class B fragments with high V-scores and PD-1 displacement scores (Table 2). These results suggest the peak broadening seen in HMQC spectra may be due to transient dimer formation in solution.

All co-crystallized fragments bind to the same hydrophobic pocket on PD-L1 with similar binding poses. In the fragment co-crystal structures, M115 from both monomer A

Table 4-2: Fragments that co-crystallized with PD-L1

VU Number	Structure	PD-1 Score	Class	V-score
VU0091290		2	B	4
VU0417453		2	B	4
VU0432747		2	B	4
VU0153947		2	A	3
VU0180070		2	B	3
VU0061254		1	B	4
VU0240047		1	B	4
VU0126711		1	A	3
VU0411373		1	A	3
VU0416396		1	B	3
VU0004583		0	B	4
VU0419276		0	B	4
VU0115538		0	A	2
VU0411655		N/A	B	4

and monomer B are in a downward position compared to an upward position in the PD-1 co-crystal structure (Figure 4-17A). The positioning of M115 opens a shallow hydrophobic

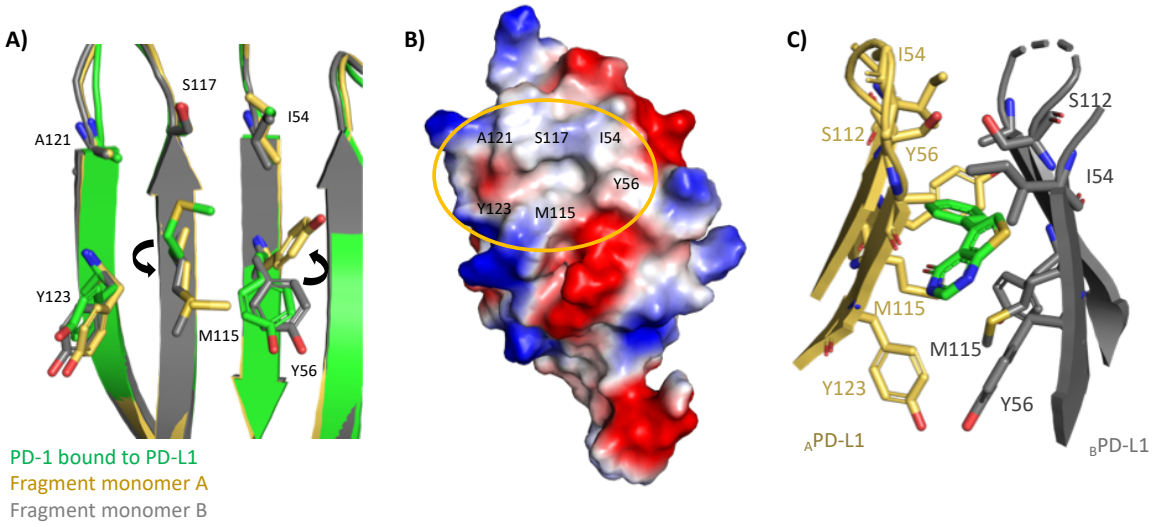

Figure 4-17: PD-L1 homodimer forms a hydrophobic pocket capable of binding small molecules.

A) M115 and Y56 residue conformational changes form a narrow binding cleft between residues on the beta sheet. M115 of PD-L1 bound to PD-1 (green sticks) is flipped up compared to down in PD-L1 fragment structures (yellow and gray sticks). Y56 of monomer B of fragment bound PD-L1 (yellow) is flipped up to form the back end of the hydrophobic pocket. B) electrostatic surface of one monomer in the PD-L1 co-crystal structure showing the hydrophobic region that comes together to form a cylinder-shaped hydrophobic pocket that binds fragments. C) Dimer interface highlighting the hydrophobic residues (sticks) that bind to fragment hits.

channel on the surface of the beta sheet lined by the residues I54, Y56, M115, Y123, and A121 of each PD-L1 monomer (Figure 4-17B). In the dimer crystal structure, these residues on each monomer come together to form a cylinder-shaped hydrophobic pocket in which the fragments occupy. One end of the hydrophobic pocket is closed off from the solvent by the upward positioning of Y56 on monomer A (Figure 4-17). Y56 on monomer B remains in the downward position allowing the other side of the pocket to be solvent exposed. Indeed, many of the fragments protrude from the pocket from this opening (Figure 4-16).

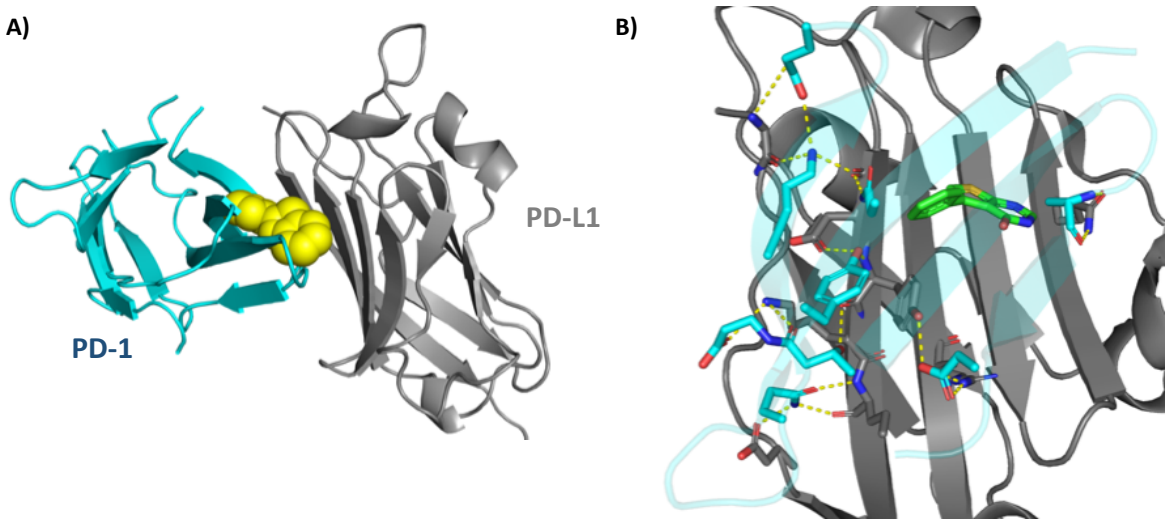

Figure 4-18: Fragments bind to PD-L1 at the PD-1 binding site.

A) Fragments (yellow spheres) bind to the PD-1 binding site and compete with PD-1 binding. B) Fragments (green sticks) bind to the hydrophobic region of PD-L1 which is the core of the PD-1 interaction to PD-L1 surrounded by electrostatic interactions (yellow dashed lines). This overlay suggests various opportunities to expand fragment hits with charged substitutions to mimic electrostatics interactions made by PD-1 to PD-L1 to increase the binding affinity.

The residues that form this pocket are also critical for the hydrophobic interactions with PD-1 and thus rationalize the results obtained in the AIDA NMR assay (Figure 4-17B, orange circle). Specific interactions of the fragment with PD-L1 are mostly hydrophobic with a few examples forming hydrogen bonds to nearby residues. Specific interactions of VU0432747 with monomer A including face-to-edge π stacking interactions with $_{A}$Y56, π-alkyl interactions with $_{A}$M115 and $_{A}$A121 and water-mediated hydrogen bonding with $_{A}$D122 and with the amide of $_{A}$Y123 (Figure 4-19). Additional interactions with monomer B include π-alkyl interactions with $_{B}$A121, $_{B}$M115 and $_{B}$Y56 and a σ-hole interaction with the amide carbonyl of $_{B}$M115. (Figure 4-19).

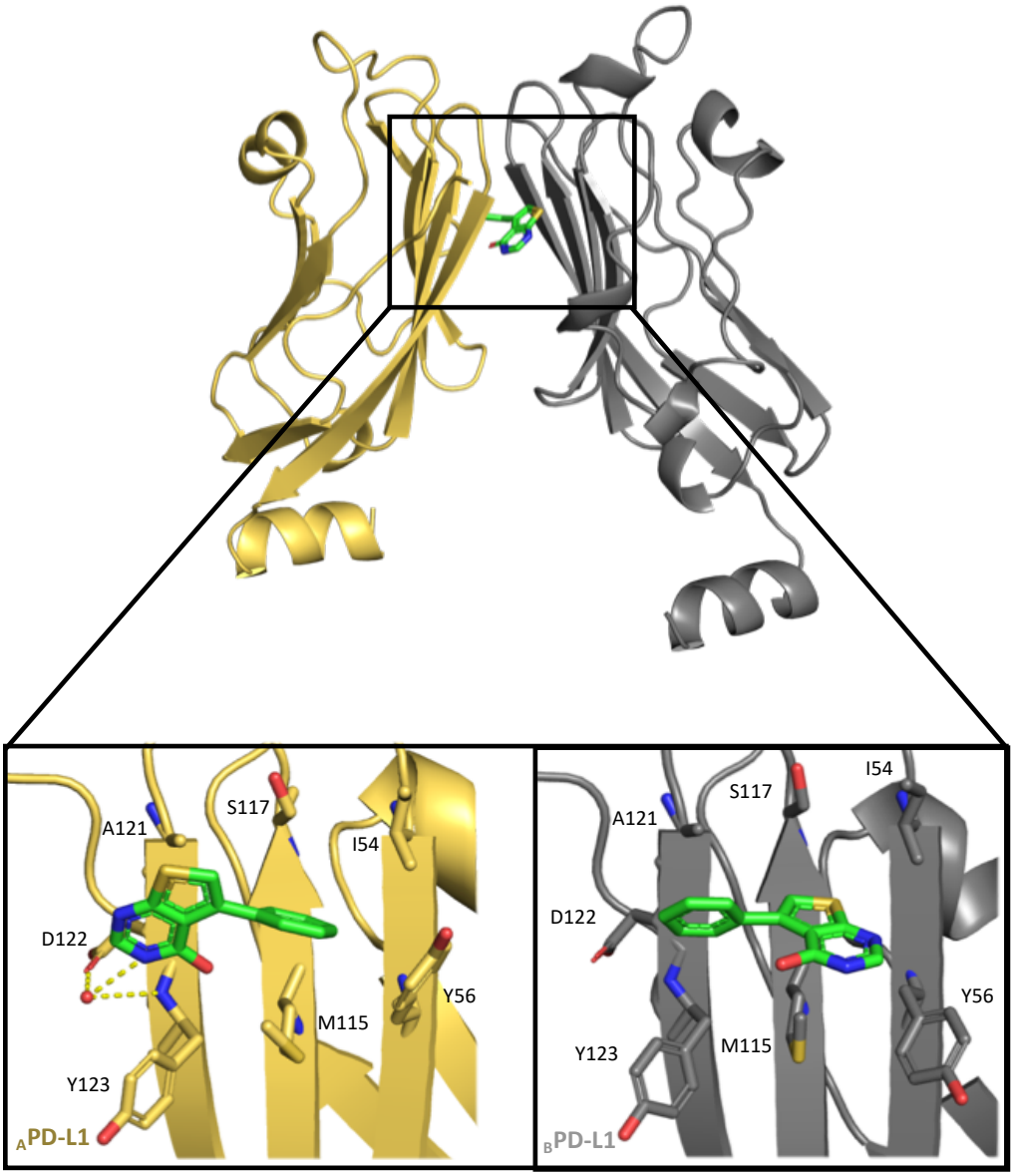

Figure 4-19: Fragment binding to a PD-L1 dimer results in two binding poses.

VU0432747 is shown bound to the PD-L1 homodimer. Specific interactions are shown for both monomer A (left, yellow cartoon and sticks) and monomer B (right, gray cartoon and sticks). Image adapted from Perry et al 2019.[172]

4.2.9 Hit to lead optimization by structure-based design

X-ray co-crystal structures of 14 fragments bound to PD-L1 allows for the rational design of analogs via structure-based design. With over 300 hits identified in the screen,

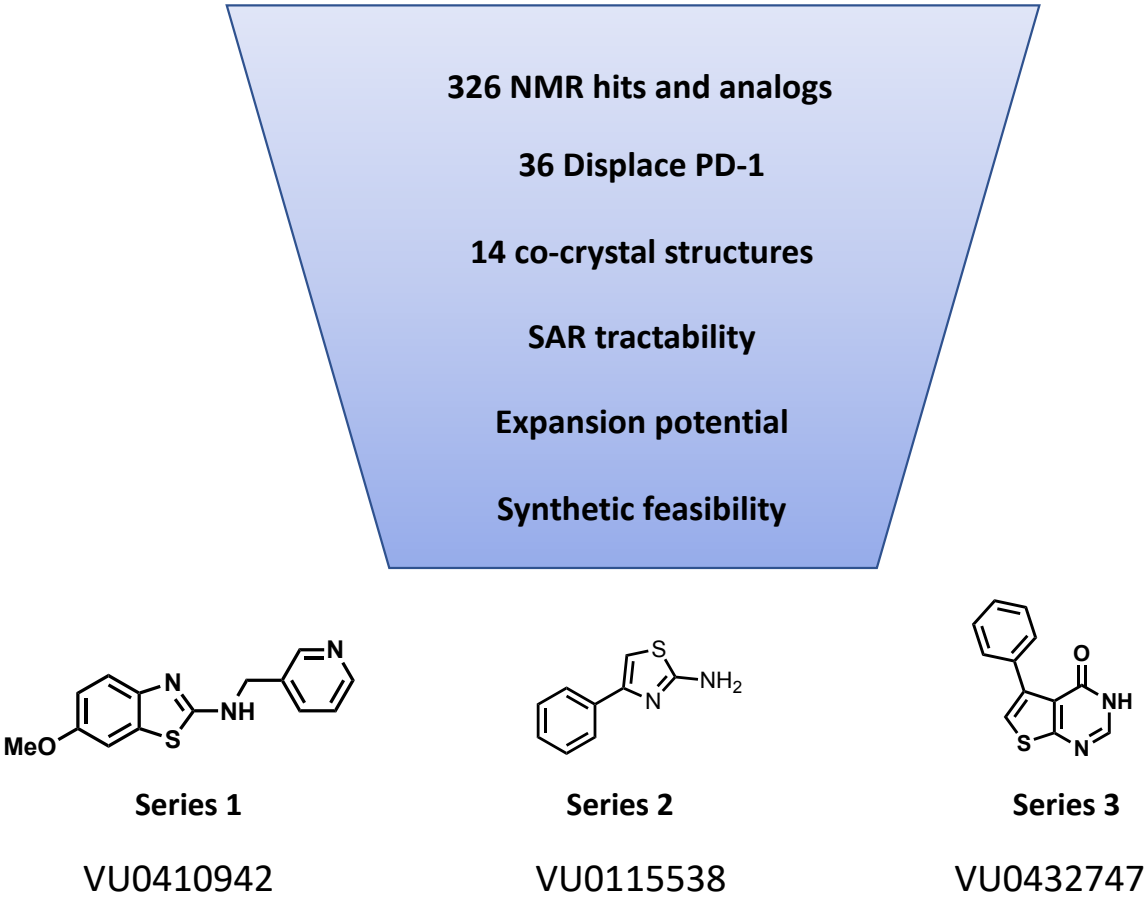

Figure 4-20: Triage of fragment hits to 3 lead series for medicinal chemistry

Fragments hits were triaged by V-scores, K_d values, PD-1 displacement assay results, co-crystal structures, SAR tractability from primary screen and analog screen, expansion potential and the synthetic feasibility of each series. Based on these filters, three series were chosen for medicinal chemistry optimization.

three lead series were selected by triaging hits by the V-scores, K_d values, PD-1 displacement scores, co-crystal structures obtained, SAR tractability from the screen, expansion potential and synthetic feasibility (Figure 4-20). Series 1 focused on a hit series identified in the screen containing a methoxy substituted benzothiazole core linked to a 3-pyridine ring (Cluster 1). Because a thiazole moiety appeared to be a prominent feature of the screen, series 2 focused on a thiazole containing 6-5 ring system (Cluster 1). Series 3 focused on phenyl substituted thieno-pyrimidinone core (Cluster 4).

Series 1 was the only series that did not have an X-ray structure prior to medicinal chemistry effort. Because this was one of the stronger series identified in the screen, it was thought that a crystal structure could be obtained of a more potent analog. Docking models of Series 1 suggested that the methoxy group was pointed towards solvent. Using this binding pose, analogs were designed to utilize this binding pose to incorporate amino acids to increase the solubility of the fragment and potential form electrostatic interactions with neighboring charged residues. Strikingly, substitution of the methoxy group to hydrogen or hydroxyl resulted in compounds that no longer bound to PD-L1. These results suggest that methoxy is forming important contacts with the protein.

While a co-crystal structure was unable to be generated for this lead series, a related fragment (VU0126711) was successfully co-crystalized shortly after chemistry support was initiated. Like previous co-crystal structures, the thiazole ring of VU0126711 forms a sigma-hole interaction with the carbonyl of $_{A}$I116. The crystal structure reveals that the 6-5 fused core backs into $_{A}$Y56 which is in contrast with the previously used docking model. Furthermore, this structure suggests that the methoxy of VU0410942 points towards $_{A}$Y56 causing a steric clash. This could explain why crystal structures were unable to be obtained with VU0410942 as no crystal structures were obtained with $_{A}$Y56 in another conformation. Using the core from VU0126711, the pyridine ring of VU0410942 is expected to point towards the S1 region of PD-L1 (Figure 4-21). Modifications and extensions from the pyridine ring were made to expand into this region to form electrostatic interactions. Removal of the nitrogen from the pyridine ring (benzyl) negated compound binding to PD-L1 and addition of other nitrogen atoms in the ring

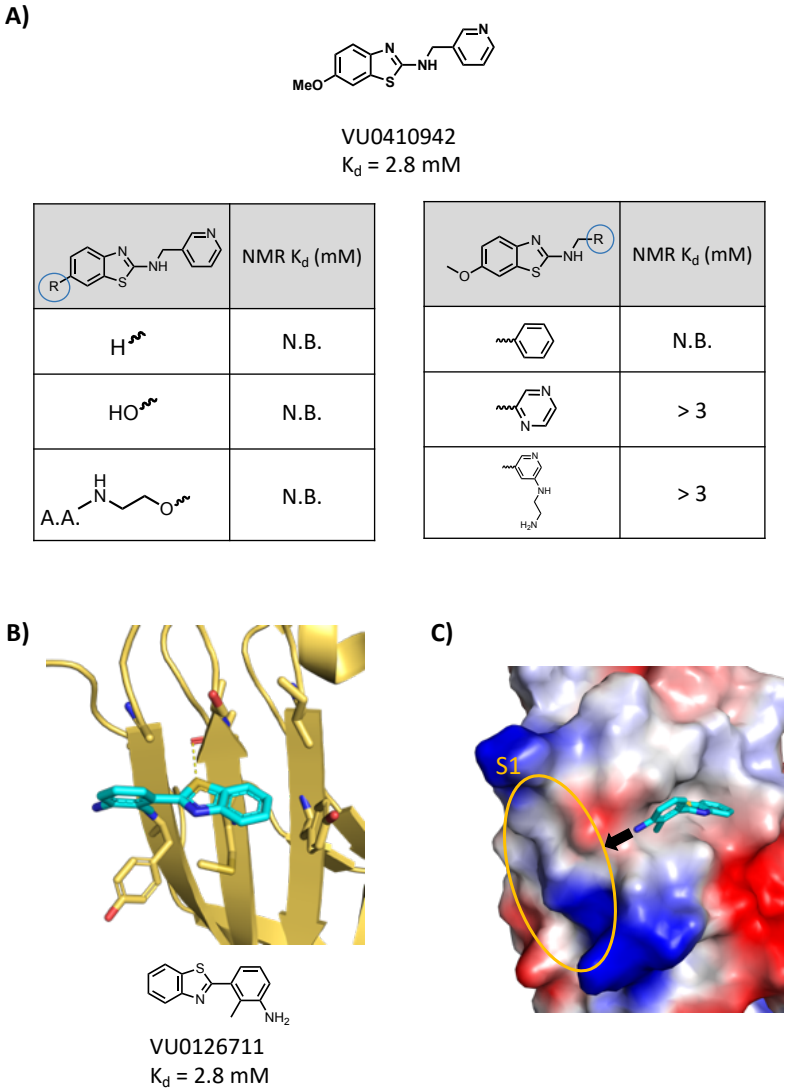

Figure 4-21: Series 1 hit to lead optimization

A) SAR table of modifications made to the methoxy and pyridine ring of VU0410942. B) Co-crystal structure of closely related analog VU0126711 rationalizes SAR observed from VU0410942. C) Co-crystal structures suggests expansion opportunities to the S1 region of PD-L1.

decreased the binding affinity. Extensions with charged substituents also resulted in weaker binding. In total, more than 80 compounds were made for this series of compounds and none were able to significantly increase the binding affinity. Given these challenges, chemistry support for series 1 was discontinued. I would like to thank Dr. Jianwen Cui for his hard work in synthesizing series 1 compounds.

Series 2 was focused on a phenyl-linked thiazole core. This series had 3 related co-crystal structures to facilitate structure-based design (Figure 4-22). Fragment merging strategies and structure-guided design of the phenyl ring substitutions were utilized to optimize binding in the hydrophobic cleft and facilitate expansion towards the S3 regions (Figure 4-22). Additionally, extensions with many different functional groups from the 2-position of the thiazole core were synthesized to expand towards the S1 region. Using molecular modeling, overlays of Series 1 and Series 2 suggested pyridine rings may be incorporated to series 1 to extend towards S1. Pyridine rings with differing linkers were synthesized but failed to show improvement in the binding affinity. In other attempts to extend to the S1 region to form hydrogen bonds with D26, 5 atom linkers were designed with charged amines. From this series, an acetamide containing analog was the best with a K_d of 2.6 mM. To further expand into S3, a handle to conjugate a series of amino acids were made off the 2 and 3 positions of the phenyl ring. However, substitutions off the phenyl ring did not bind. These results suggest that dimer formation for this series is important as these substitutions were predicted to clash with the formation of the dimer and point towards solvent. In total 120 compounds were made for this series, but the binding affinity was too weak (> 3 mM) to give reliable and tractable SAR. Due to these challenges, efforts on this series were also discontinued. I would like to thank Dr. Chris Tarr for his hard work synthesizing series 2 compounds.

Series 3 focused on a phenyl-linked thienopyrimidinone core. This series had two examples with co-crystal structures and many opportunities for expansion. The medicinal chemist on this series, Dr. Jonathan Mills, first sought to increase the solubility of this

A)

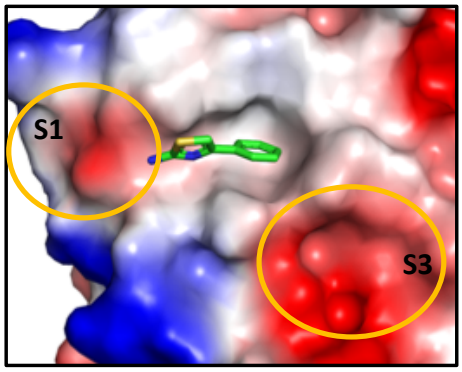

B)

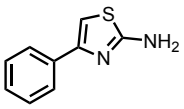

VU0115538
K_d > 3 mM

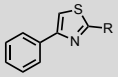	NMR K_d (mM)
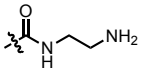	> 3
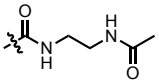	2.6
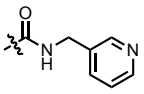	> 3
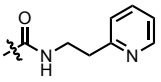	N.B.

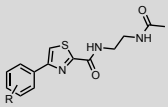	NMR K_d (mM)
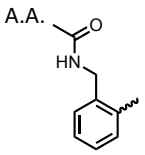	N.B.
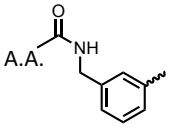	N.B.

Figure 4-22: Series 2 hit to lead optimization

A) Co-crystal structure of VU0115538 bound to PD-L1 shown on monomer A. B) SAR table of analogs synthesized to expand into the S1 and S3 regions of PD-L1 (orange circles in A). N.B. indicates no binding.

fragment and pick up nearby electrostatic interactions by adding a short linker and carboxylic acid from the carbonyl that could be functionalized to include a series of amino acids. When this analog was tested by NMR, the peaks transitioned from class B

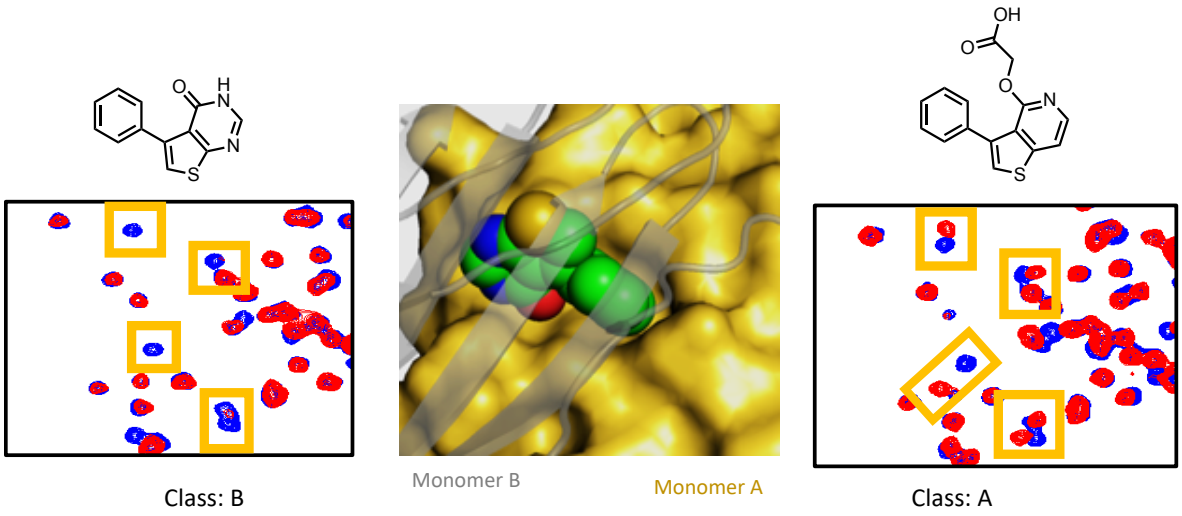

Figure 4-23: Series 3 analogs switch from peak broadening to peak shifting and prevent a protein dimer.

Fragment is expected to bind to one monomer of PD-L1 prior to the second monomer binding to form a dimer. VU0432747 HMQC (left) has broadened peaks) an analog containing a carboxylic acid off the carbonyl position retains binding to PD-L1 as indicated by peak shifts (right) suggesting VU0432747 binds to monomer B and prevents formation of a protein dimer.

(broadened) of the fragment to class A (shifted) (Figure 4-23). Based on the dimer crystal structure, the carboxylic acid is predicted to clash with monomer A (Figure 4-23). Thus, the change from peak broadening to peak shifting is likely explained by the inability to form a PD-L1 dimer with this analog. Indeed, the co-crystal structures of analogs of this fragment with substitutions that are predicted to clash with monomer A were unable to be obtained.

The solubility of this compound was greatly improved over the fragment by the addition of a carboxylic acid allowing for concentrations above 3 mM for NMR titration experiments to more accurately determine K_d values of analogs. To maintain solubility and increase the binding affinity simultaneously, molecular modeling was used to design analogs that contained a carboxylic acid group close to R113 towards the S2 region.

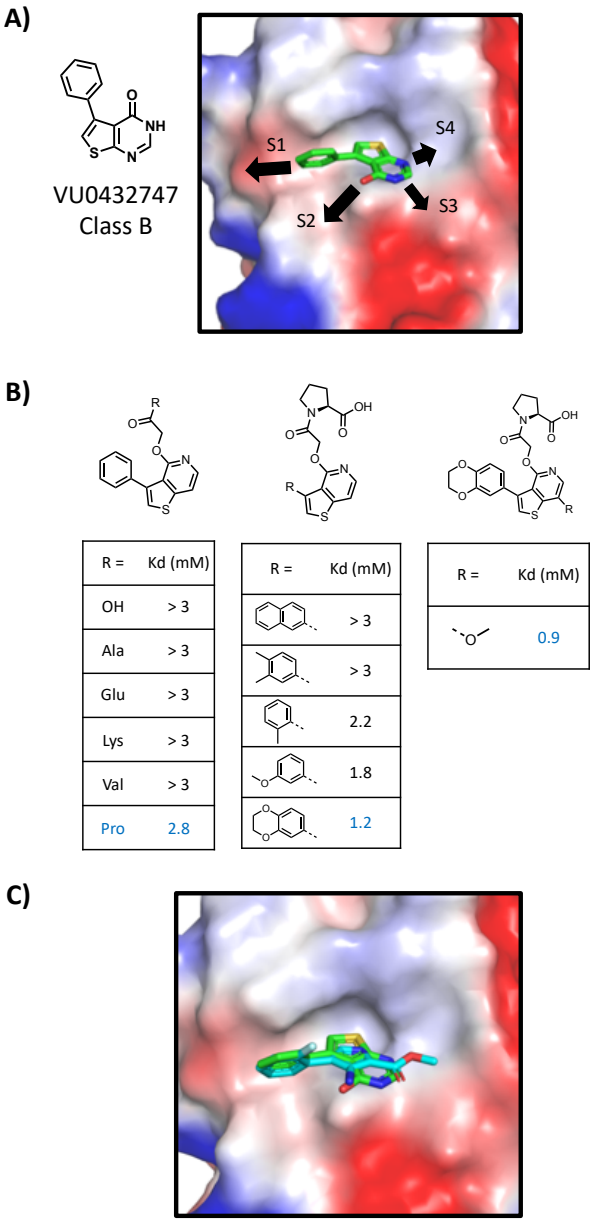

Figure 4-24: Series 3 hit to lead optimization

A) Co-crystal structure of VU0432747 bound to PD-L1 shown on monomer B. B) SAR table of analogs synthesized to expand into the S2, S1, and S4 regions of PD-L1 (black arrows in A). C) Fragment merging approach to add a methoxy to S4 pocket of PD-L1. Overlay of VU0432747 and VU0416396 suggests a methoxy substitution could be added to increase the binding affinity.

Consistent to modeling predictions, the proline-containing compound gave the best K_d

(2.8 mM) due to the more rigid placement of the carboxylic acid in proximity to R113.

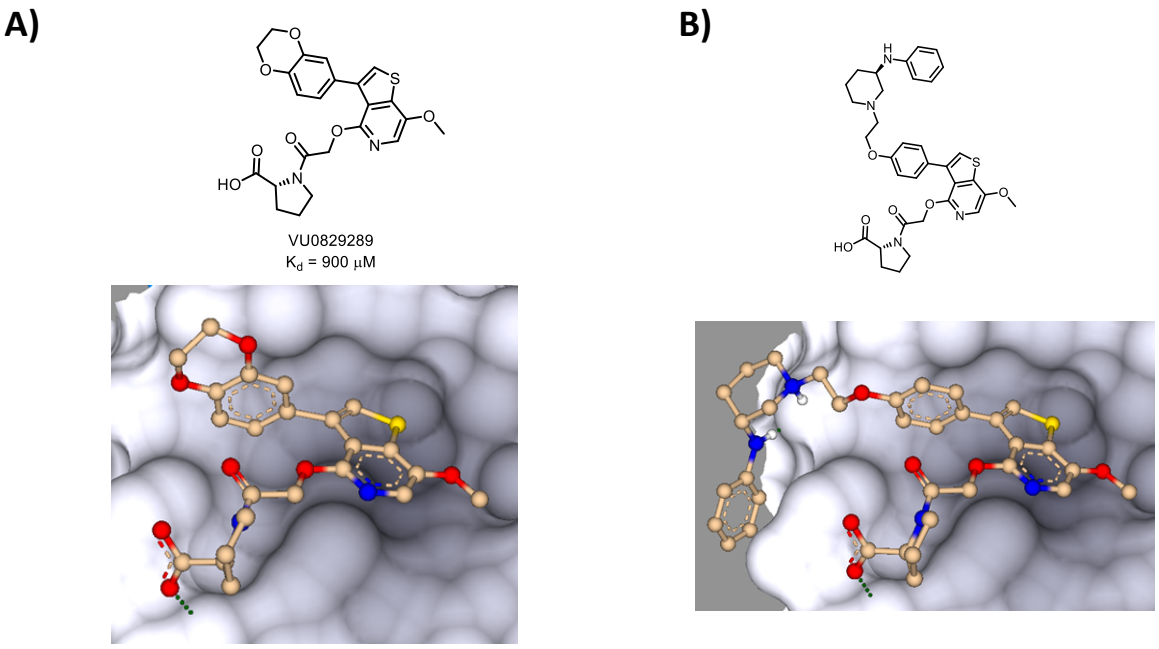

Figure 4-25: Molecular modeling of fragment analogs.

A) Modeling using SeeSAR of lead compound binding to PD-L1. B) Modeling of a suggested compound to make to further expand into the S1 region of PD-L1.

One of the most striking observations from the fragment crystal structures and related analogs was the diversity of phenyl substitutions that were tolerated in this pocket. A set of commonly observed phenyl substitutions in stronger fragments were designed to optimize the phenyl ring and provide a handle into S1. Of all substitutions tested, dioxane had the best K_d of 1.2 mM. Overlays of other crystal structures provided many opportunities for fragment merging approaches. VU0416396 overlaid with VU0432474 suggested a methoxy towards the small S4 pocket could be beneficial (Figure 4-25C). Adding a methoxy to compound increased the binding affinity to 0.9 mM. Molecular modeling of the lead compound supports the predicted binding pose based on the rational design of this compound (Figure 4-25A). Further modeling studies suggest

additional interactions could be formed by expanding more into the S1 pocket (Figure 4-25). However, no such molecules have been synthesized to date. I would like to thank Jonathan Mills for his hard work synthesizing series 3 compounds.

4.2.10 High throughput screen of PD-L1

While the optimization of fragment hits towards PD-L1 was disappointing, we were encouraged by the high hit rate suggesting that PD-L1 is druggable. With hopes of finding more elaborated molecules that may bind to PD-L1 with higher affinity than our fragments and serve as better starting points, we initiated a high throughput screen with assistance from the Vanderbilt High Throughput Screening Facility. Any HTS hit identified from the screen that bound to PD-L1 could complement the fragment hits by using linking or merging approaches to quickly gain more potent molecules. Indeed, other projects in the lab, namely WDR5, have benefited from having hits from both HTS and fragment screens.

The Vanderbilt discovery collection of 100,000 compounds was screened using an FPA assay developed in our lab (chapter 5) using previously optimized assay conditions (15 nM PD-L1, 10 nM FITC labeled MCP probe) containing10 µM of the screening compound. To minimize potential fluorescent artifacts commonly observed in FPA assays, hit criteria were set to > 15% inhibition and +/- 20% of total fluorescence measurements relative to controls. In total, 106 hits were identified that fit the screening criteria (hit rate = 0.1%). However, measurements of the total fluorescence increased considerably when progressing hits to dose-response experiments suggesting interference from the

compounds. Given that the compound concentration was 1000x over the probe concentration, we hypothesized these compounds had inherent fluorescence properties at the FITC excitation and emission wavelengths (ex: 490 nm, em: 512) causing interference with anisotropy readings. To test this hypothesis, we conjugated an AlexaFluor 594 probe (ex: 594 em: 617) to the same macrocyclic peptide and re-screened the hits found by the FITC assay. None of the 106 hits reconfirmed by the AlexaFluor assay and orthogonal validation by ^{1}H-^{15}N HMQC NMR confirmed no binding to PD-L1.

4.3 Conclusions and Discussion

While modest improvements in the binding affinities have been made for series 3, the compounds were large (> 500 Da) and bind with low ligand efficiencies. Furthermore, additional crystal structures of analogs were unable to be obtained after extensive crystallization screening and additional changes to the protein construct. These challenges are thought to be caused by modifying the analogs to prevent dimerization of PD-L1. Because the binding of these fragments are weak, they fail to reach saturation of monomeric PD-L1 (10 x K_d = 9 mM) due to limited compound solubility at concentrations above 4 mM. Structural information of analogs binding to the target is highly important to continuously guide SAR. Modifications that are designed by modeling experiments often have unexpected binding poses or novel interactions resulting from protein binding dynamics not seen in previous structures or rigid docking models. Thus, only obtaining dimer structures of the initial fragment make the structure-guided design of monomeric binding analogs highly speculative.

Ideally, fragments would have been identified that bind to a nearby site and could be linked or merged for large gains in binding affinities. However, only one shifting pattern was observed in the HMQC spectra during screening. Of the 80+ fragments screened only 13 were able to be co-crystallized and all have similar binding poses. It is possible that other fragments have different binding poses that prevented co-crystallization and thus our structures are biased towards one binding pose. Fragments that failed to co-crystallize were docked to PD-L1 using Induced Fit docking allowing for flexible side chains. However, the flat binding surface resulted in many different poses with similar binding energies and docking scores making it difficult to confidently suggest analogs to be synthesized. Given these challenges, efforts to continue optimizing the fragment hits to PD-L1 were discontinued.

Encouraged by the high hit rate from the fragment screen, we initiated an HTS to find additional starting points. However, after screening 100,000 compounds using an FPA assay, we found no hits to follow up. The data presented in this chapter suggests that generating high-affinity molecules towards PD-L1 will be technically challenging. The lack of a deep pocket at the PD-L1 hot spot is likely why small molecules have weak binding interactions with the monomeric form of the protein. Fragments that were able to be co-crystallized to PD-L1 formed PD-L1 homodimers around the fragments that create a larger hydrophobic pocket typically found in more druggable targets. However, attempts to optimize the binding to monomeric and dimeric PD-L1 resulted in only minor improvements.

4.4 Methods

Cloning and site-directed mutagenesis

PD-L1 sequences were ligated into different plasmids containing N- and C-terminal fusion partners and purification tags (pET28b, pGEX6-1, pAT108 and pBG102). Restriction sites were added if donor vectors lacked desired restriction digest sites for proper ligation into destination vectors using site-directed mutagenesis. Mutants to PD-L1 sequences were made using protocols published by QuickChange II Site-Directed Mutagenesis Kit (Agilent). Primers were designed using Primer X (www.bioinformatics.org/primerx) to adhere to recommended primer design guidelines (25 to 45 bases in length, Tm > 78 °C, and GC content > 40%). PCR reactions were set up by addition of 50 ng of template DNA (plasmid), 125 ng forward primer, 125 ng reverse primer, 25 µL of 2X Phusion High-Fidelity master mix (NEB) and water to a final volume of 50 µL. Thermocycler settings were: 98 °C initial denaturation, Step 1: 98 °C denature for 15 seconds. Step 2: 55 °C anneal for 1 minute. Step 3: Extend 72 °C for 3 minutes. Repeat steps 1 – 3 for 17 cycles. Extension at 98 °C for 6 minutes. Store at 4 °C. DPN1 (1 µL/50 µL reaction) was added to digest parent plasmid for 1 – 4 hours at room temperature. The digested PCR product was transformed to BL21 using electrocompetent DH5α *E. coli* cells (ThermoFisher). Transformed cells were plated on antibiotic plates overnight. Colonies were picked the next morning and grown in 12 mL overnight cultures. Minipreps were performed to extract plasmid DNA from each overnight culture (NEB). Extracted plasmids were sequenced (Genhunter) using a T7 promoter primer to check if the mutation was present. Successful mutagenesis clones were transformed to *E. coli* BL21 cells for expression.

Expression tests of PD-L1 constructs

Preliminary constructs of the extracellular portion of PD-L1 was cloned into the pET28b vector using *NdeI* and *XhoI* restriction sites to contain a thrombin cleavable N-terminal 6His tag and transformed into E*. coli* DH5a cells. Transformed cells were grown on kanamycin plates overnight at 37 ˚C. Overnight cultures consisting of LB with 50 ug/mL kanamycin and picking colonies on the kanamycin treated plate. Small aliquots of media (10 mL of LB + 50 ug/mL Kan) were inoculated with 100 µL of overnight culture to 10 mL cultures for expression tests (1% inoculation rate). Samples were taken before and after IPTG induced expression of PD-L1. Post IPTG samples were lysed by sonication and centrifuged to separate soluble from insoluble fractions. SDS PAGE was run on each sample to determine the percentage of PD-L1 in the insoluble fraction. Consistent with previous reports, all PD-L1 constructs were expressed near 100% as insoluble inclusion bodies regardless of variation of expression temperature or IPTG concentrations.

New England Biolabs (NEB) has engineered strains of E. coli to have reducing cytosols allowing for the potential for proteins with disulfide bonds to be correctly folded after translation and expressed as soluble proteins. PD-L1 constructs containing chaperone protein fusion partners were transformed to two strains of the Shuffle Cells (C3026 and C3029). Expression tests were performed identically to previous expression tests in E. coli BL21. SDS PAGE was used to analyze the percentage of protein in the soluble fraction.

Protein expression and purification

For each construct, 500 mL of cell culture (LB media) was inoculated with 1% overnight culture and grown at 37 °C until cells reached an OD600 of 0.8 to 1. Cell pellets were resuspended in lysis buffer (50 mM Tris-HCl pH = 8.5, 150 mM NaCl, 20 mM DTT, 2 mM EDTA and 1 mM PMSF) at 10 mL/g of cell pellet and lysed by homogenization at 4 °C (APV-2000, APV). Inclusion bodies were collected by centrifugation (10,000 x g for 20 minutes). Inclusion bodies were washed using a series of washes containing lysis buffer and 2% Triton X-100, 1% Triton X-100, 0.5% Triton X-100 and 1.5 M NaCl wash steps (5,000 x g for 10 minutes per wash). Purified inclusion bodies were solubilized at 2 mg/mL in denaturing buffer (50 mM Tris-HCl pH = 8.5, 250 mM, 6M Guanidine HCl) for 4 hours at room temperature. The solubilized inclusion bodies were filtered through a 0.45 µm filter and refolded dropwise into refolding buffer (100 mM Tris pH = 8, 1 M arginine, 2 mM EDTA, 0.25 mM oxidized glutathione and 0.25 mM glutathione) at 4 °C overnight.1 The final protein concentration in the refolding buffer was 0.1 mg/mL. Refolded PD-L1 was dialyzed 3 times over 48 hours into dialysis buffer (10 mM Tris pH = 8, 20 mM NaCl). Buffer exchanged PD-L1 was concentrated using a stirred ultrafiltration cell with a 10 MWCO filter (Amicon, Millipore). Constructs were concentrated until significant precipitation was seen (typically around 0.3 mg/mL for initial unstable constructs). Constructs with improved stability were concentrated to 0.5 - 1 mg/mL and loaded to a size exclusion column (Superdex75 26/60) pre-equilibrated with NMR buffer (50 mM Sodium Phosphate pH = 7, 25 mM NaCl) using an AKTA purifier. The elution profile from size exclusion was also used to evaluate the integrity of the construct by the elution of

monomeric protein verse soluble aggregation.

Large scale protein production

The IgV domain of human PD-L1 (residues 18 – 134) was codon optimized and cloned into the pET28b vector using *NcoI* and *NotI* restriction sites to include a C-terminal 6His tag (Genscript). The resulting vector was used to transform E. coli BL21 (DE3) GOLD cells (Strategene). Unlabeled PD-L1 for X-ray crystallography was expressed in LB media. Uniformly ^{15}N labeled PD-L1 for NMR studies was expressed in M9 media containing ^{15}N ammonium chloride (Cambridge Isotope Laboratories) as the sole nitrogen source. Inclusion body purification, refolding and further purification was the same protocol listed above.

Fragment screen and titrations by NMR spectroscopy

NMR screening was performed at 30 °C using a Bruker Avance III 600 MHz spectrometer equipped with a 5 mm single-axis z-gradient cryoprobe and Bruker SampleJet sample changer. Screening samples (500 µL) contained 35 µM (0.5 mg/mL) of 15N PD-L1 IgV-6His-H140E and fragment mixtures containing 400 µM of each fragment and 5% DMSO-d_6. $^{1}H,^{15}N$ SOFAST-HMQC spectra were obtained using 26 scans (12 minutes) and analyzed using Topspin (Bruker BioSpin). Deconvolution of hit mixtures was performed as a single fragment at 800 µM concentration. NMR titration experiments were performed by monitoring the change in ^{1}H and ^{15}N chemical shifts of 6-point 2-fold serial dilutions (3 mM, 1.5 mM, 0.75 mM, 0.375 mM, 0.188 mM, 0.093 mM). K_d measurements were calculated by fitting using an in-house script. Signal intensity of

ligand peaks in ^{1}H NMR spectra (zgesgp) of each sample prior to HMQC acquisition was used to monitor ligand solubility. Data points with poor ligand solubility were excluded from analysis.

NMR-based PD-1 displacement assay

NMR samples for the PD-1 displacement assay were made containing the same NMR buffer (50 mM NaPO4, 25 mM NaCl, 4% DMSO). PD-1 reference sample contained 20 µM ^{15}N labeled PD-1. PD-1 / PD-L1 reference sample contained 20 µM ^{15}N labeled PD-1 and 23 µM PD-L1 IgV-IgC. Test samples contained 20 µM ^{15}N labeled PD-1, 23 µM PD-L1 IgV-IgC and 2 mM fragment hits. ^{1}H,^{15}N SOFAST-HMQC spectra were obtained of all samples. Qualitative displacement scores were assigned by overlaying the HMQC spectra of test samples to the PD-1 / PD-L1 samples. Higher amounts signal intensity rescue was assigned a score of 2 while weak signal intensity was assigned a score of 1. No signal intensity was assigned a score of 0.

X-ray crystallography

Unlabeled PD-L1 IgV-6His-H140E in X-ray buffer (10 mM Tris pH 8, 20 mM NaCl) was concentrated to 3 – 5 mg/mL (200 – 345 µM) and centrifuged at 13,000 rpm for 5 minutes to remove precipitation. The Hampton Index HT screen was used to test 96 diverse conditions for crystallization. Ligand-free crystals of PD-L1 IgV-6His-H140E were obtained in conditions containing 100 mM HEPES pH 7.5 and 2M ammonium sulfate overnight at 18 °C. Fragment bound crystals were generated by incubating PD-L1 IgV-6his-V76T at 35 µM (0.5 mg/mL) with 2 – 4 mM of a fragment on ice for 3 hours in X-ray buffer.

Any precipitated fragment was removed by centrifugation (13,000 rpm for 5 minutes). The complex was concentrated to 200 µM (3 mg/mL) using 3 kDa MWCO amicon ultra-0.5 mL centrifugal filters (Millipore). Crystals of the fragment / PD-L1 complex were formed in conditions containing 0.056 M NaH2PO4, 1.344 M K_2HPO_4 within 48 hours at 18 °C. All crystals were cryoprotected in mother liquor containing 20% glycerol prior to freezing in liquid nitrogen. Data were collected on the Life Sciences Collaborative Access Team (LS-CAT) beamlines at the Advanced Photon Source (APS), Argonne National Laboratory. Indexing, integration, and scaling were performed with HKL2000. The phases were determined by molecular replacement (Phaser-MR) using the PD-L1 IgV-6His construct (PDB code 5C35). The models were refined using phenix.refine and manual fitting the model to electron density using COOT. All figures were generated using PyMOL.

Molecular modeling using SeeSAR

Co-crystal structures of fragments bound to either monomer were uploaded to SeeSAR. The binding pocket was defined to the residues surrounding the binding pocket. The compound was edited to explore binding possibilities in neighboring sub-pockets. Compounds were iteratively submitted for energy minimization and binding pose predictions. Results from SeeSAR modeling were used to design analogs of compounds and provide insight to the predicted binding pose of lead compounds.

Chapter 5

Validation of literature reported PD-L1 inhibitors

5.1 Introduction

Given the strong rationale for why small molecules would be advantageous over antibody therapies, there has been some interest in the field to develop such inhibitors.[111, 161, 162] Indeed, inhibitors of the PD-1 / PD-L1 signaling pathway have been reported including small molecules, peptidomimetics and peptides.[113, 163-165] Peptidomimetic antagonists containing a central 1,3,4-oxa or thiadiazole cores and 1,2,4-oxadiazole cores were discovered by researchers at Aurigene Ltd (Figure 5-1 A-B).[113] Examples of this series include amino acid substitutions from the 2 and 5 positions for 1,3,4 oxadiazole series and 3 and 5 positions for the 1,2,4 oxadiazole series (Figure 5-1A-B). A second peptidomimetic series containing dipeptides conjugated by a urea unit were

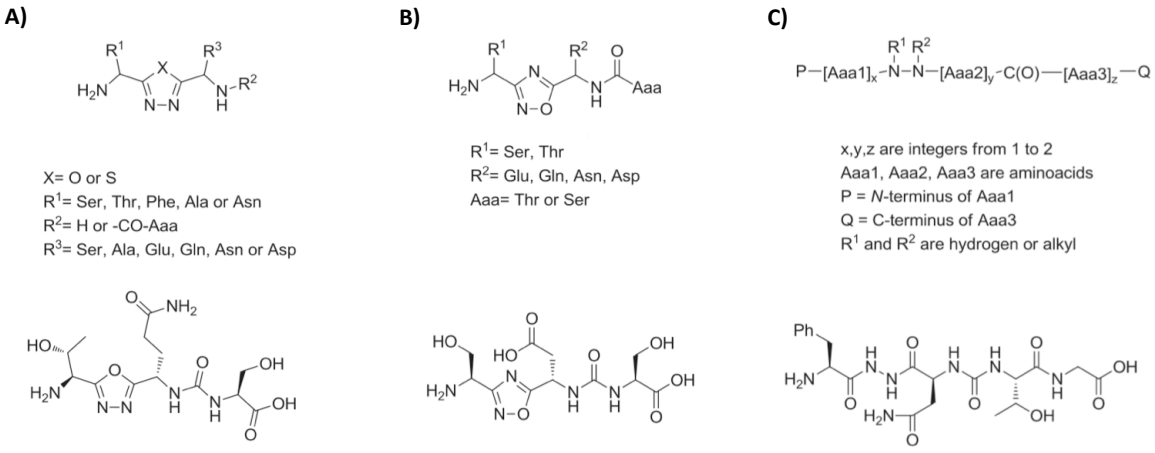

Figure 5-1: Aurigene reported peptidomimetic inhibitors of the PD-1 signaling pathway

Patented peptidomimetic inhibitors by Aurgine containing a 1,3,4-oxa or thiadiazole core (A), a 1,2,4 oxadiazole core (B) and dipeptide conjugated by a urea unit (C). Image adapted from Zarganes-Tzitzikas et al 2017. [111]

also reported (Figure 5-1C). Aurigene has also disclosed multiple different peptides that range from 7 – 30 amino acids and have homology to portions of PD-1 sequence critical for the PD-L1 interaction.[164] All Aurigene compounds are reported to have activity in a mouse splenocyte rescue assay that is dependent on the PD-1 signaling pathway. This assay monitors the inhibition T cell proliferation by addition of soluble mouse PD-L1 and CFSE dye that covalently binds to proliferating cells. Addition of compounds that inhibit the PD-1 / PD-L1 interaction results in a rescue in splenocyte proliferation. These reported compounds have reported rescue values ranging from 47 to 93% in this assay.[113]

Bristol-Myers Squibb (BMS) have also disclosed small molecule and peptide-based antagonists of the PD-1 pathway. The disclosed small molecule scaffold consists of a mono-ortho substituted biphenyl 3-phenoxymethyl core (Figure 5-2).[163] These compounds have low nanomolar IC_{50} values in a homogenous time-resolved fluorescence

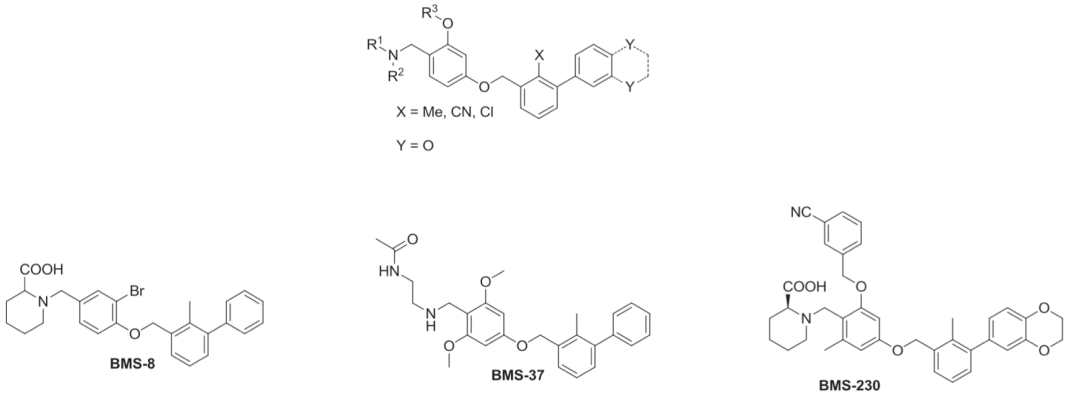

Figure 5-2: BMS reported small molecule inhibitors of PD-L1

Mono-ortho substituted biphenyl 3-phenoxymethyl core of small molecule inhibitors patented by BMS with examples given below (BMS-8, BMS-37 and BMS-230). These molecules were found to have < 100 nM IC50 values in a HTRF assay. Image adapted by Zarganes-Tzitziaks et al. 2017. [111]

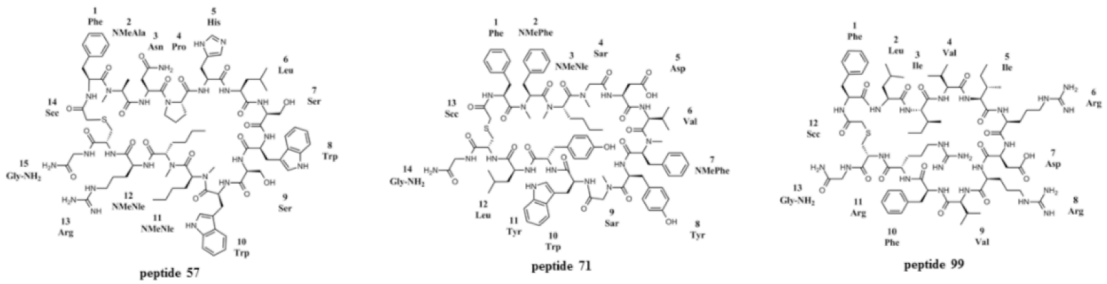

Figure 5-3: BMS reported macrocyclic peptides inhibitors of PD-L1

Three series of macrocyclic peptides patented by BMS. Series is divided by the number of amino acids in the macrocycle Peptide 57 contains 14, peptide-71 contains 13 and peptide 99 contains 12. Image adapted from Zarganes-Tzitziaks et al. 2017. [111]

assay (HTRF) binding assay using Ig-tagged PD-1 and 6-His tagged PD-L1. However, no further *in vitro* or *in vivo* assays have been disclosed to support the biological activity of these molecules. Macrocyclic peptides MCP that target the PD-1 signaling pathway have also been disclosed by BMS.[165] These peptides are divided into 3 main series containing 14, 13 or 12 residue macrocycles and have low nanomolar affinity in both HRTF assays and nanomolar EC_{50} values in a variety of different cell-based assays (Figure 5-3). In this chapter, I discuss our efforts to validate these disclosed molecules and utilize structural information of these compounds to further develop our fragment hits into novel PD-L1 inhibitors.

5.2 Results

5.2.1 Validation of Aurigene compounds

To validate these reported molecules, examples from each class were selected based on their reported activity and by the synthetic feasibility. Aurigene compounds were synthesized by Chris Tarr and Jianwen Cui. BMS small molecules were synthesized

Table 5-1: Synthesized PD-1/L1 inhibitors reported in the patent literature.

Compound	Reported activity	Binding to PD-L1	Binding to PD-1
Aurigene Peptidomimetic 1 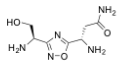	93% splenocyte rescue @ 100 nM	No	No
Aurigene Peptidomimetic 2 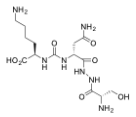	95% splenocyte rescue @ 100 nM	No	No
Aurigene Peptide 1 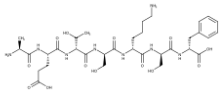	80% splenocyte rescue @ 100 nM	No	No
BMS Small Molecule 1 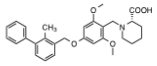	6 – 100 nM in HTRF assay	Yes	No
BMS Small Molecule 2 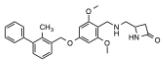	22 nM in HTRF assay	Yes	No
BMS Small Molecule 3 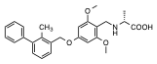	110 – 1000 nM in HTRF	Yes	No
BMS Macrocyclic Peptide 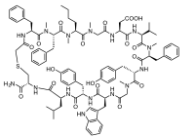	7 nM in HTRF assay	Yes	No

by Viva Biotech and the BMS macrocyclic peptide was synthesized by Plamen Christov of the Vanderbilt synthesis core. These compounds were first tested for direct binding to either PD-1 or PD-L1 by monitoring chemical shift changes in ^{1}H-^{15}N HMQC spectra.

Surprisingly, none of the peptidomimetics or peptides reported by Aurigene bound to either human PD-1 or human PD-L1 (Table 5-1). This result is consistent with

other reports that tested molecules in this series for binding to PD-1 and PD-L1[115]. One explanation to this discrepancy is that these molecules are specific for mouse PD-1 / PD-L1 interaction as the assay used to report the activity of these molecules utilizes mouse splenocytes expressing mouse PD-1 with the addition of mouse PD-L1 to dampen the proliferation. While mouse and human PD-1 / PD-L1 proteins have high homology, crystal structures have revealed distinct binding modes between species that would have implications in small molecule binding.[112] However, we have not tested this possibility by testing these compounds against mouse PD-1 or PD-L1. Notably, Aurigene recently partnered with Curis to initiate the first phase 1 clinical trial in humans with an orally available checkpoint inhibitor CA-170. CA-170 is claimed to be a dual antagonist of PD-L1 and VISTA checkpoints, however, no direct binding studies to either protein has been disclosed. Thus, the precise mechanism of action of these compounds remains unclear.

5.2.2 Validation of the BMS macrocyclic peptide

One MCP example was synthesized with the addition of an extra lysine residue as a synthetic handle to attach a fluorescent tag to facilitate biochemical assay development. The MCP causes large chemical shifts in PD-L1 HMQC spectra and has slow exchange peak broadening kinetics in NMR titrations suggesting the binding affinity of the peptide to be in the nanomolar range (Figure 5-4). X-ray structures of the MCP bound to PD-L1 were obtained to identify the binding site on PD-L1. Indeed, the MCP binds to the PD-1 binding site on PD-L1 (Figure 5-4 C) making this peptide an ideal probe molecule for assay development purposes. Conjugation of a FTIC probe at the extra lysine was used for the development of a high throughput fluorescence polarization anisotropy (FPA) assay to

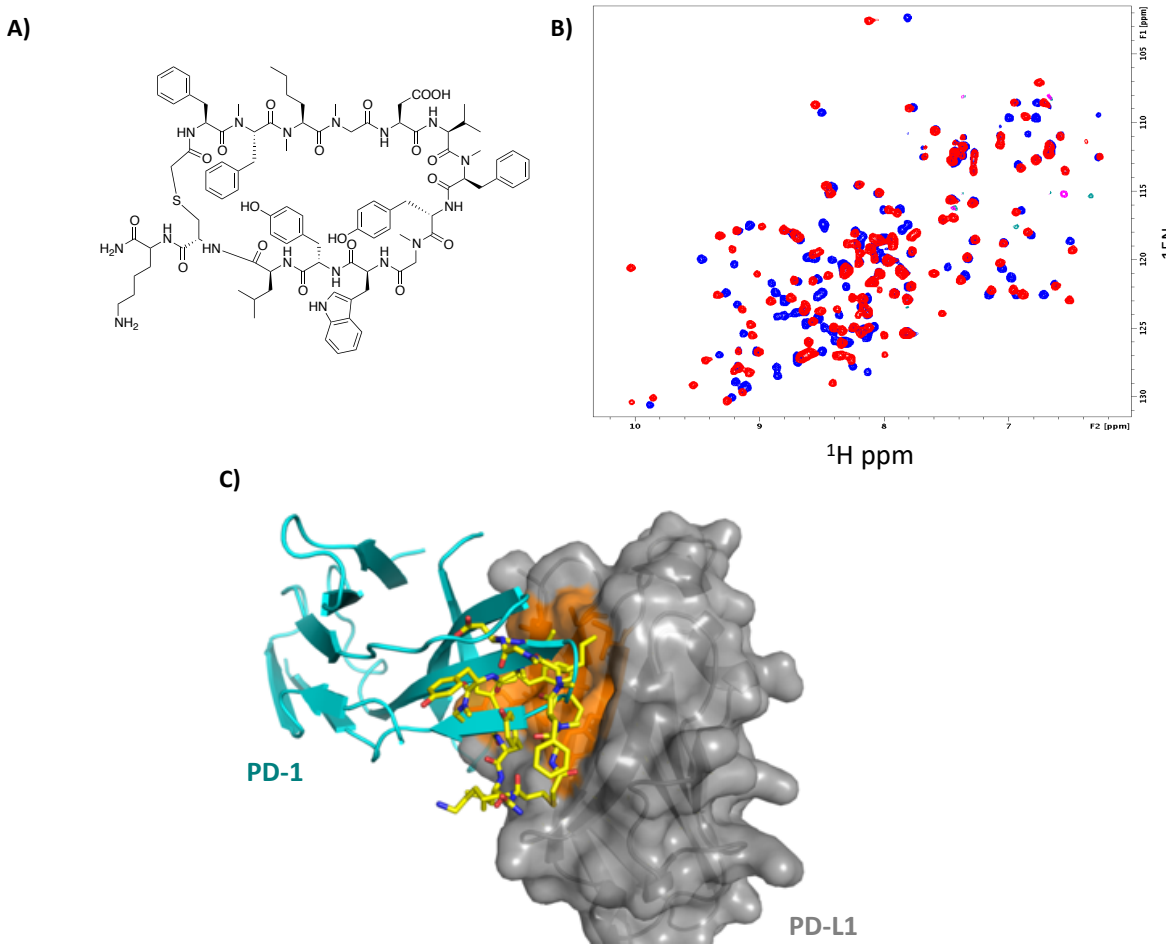

Figure 5-4: BMS macrocyclic peptide inhibitors bind to PD-L1 at the PD-1 binding site.

A) 2D structure of the BMS macrocyclic peptide synthesized with an addition lysine residue (left). B) ^{1}H-^{15}N HMQC spectra of 30 µM IgV-6His-H140E alone (blue) and 30 µM IgV-6His-H140E with 100 µM of the peptide (red). Large chemical shift changes are indicative of binding. No chemical shifts changes were observed for HMQC spectra of PD-1 with the peptide (not shown). C) X-ray structure of MCP bound to PD-L1 (gray surface). MCP (yellow sticks) binds to the PD-1 binding site (orange surface) shown by an overlay of PD-1 (teal cartoon) bound to PD-L1.

rapidly assess the binding affinity of molecules made for this project.

Using saturation binding experiments, the K_d of the FITC-labeled MCP probe to PD-L1 was determined to be 2 nM (Figure 5-5B). The PD-L1 concentration and probe concentration was varied to obtain to the largest anisotropy window for optimal assay performance for a competition-based assay (Figure 5-5 C). The optimum buffer conditions

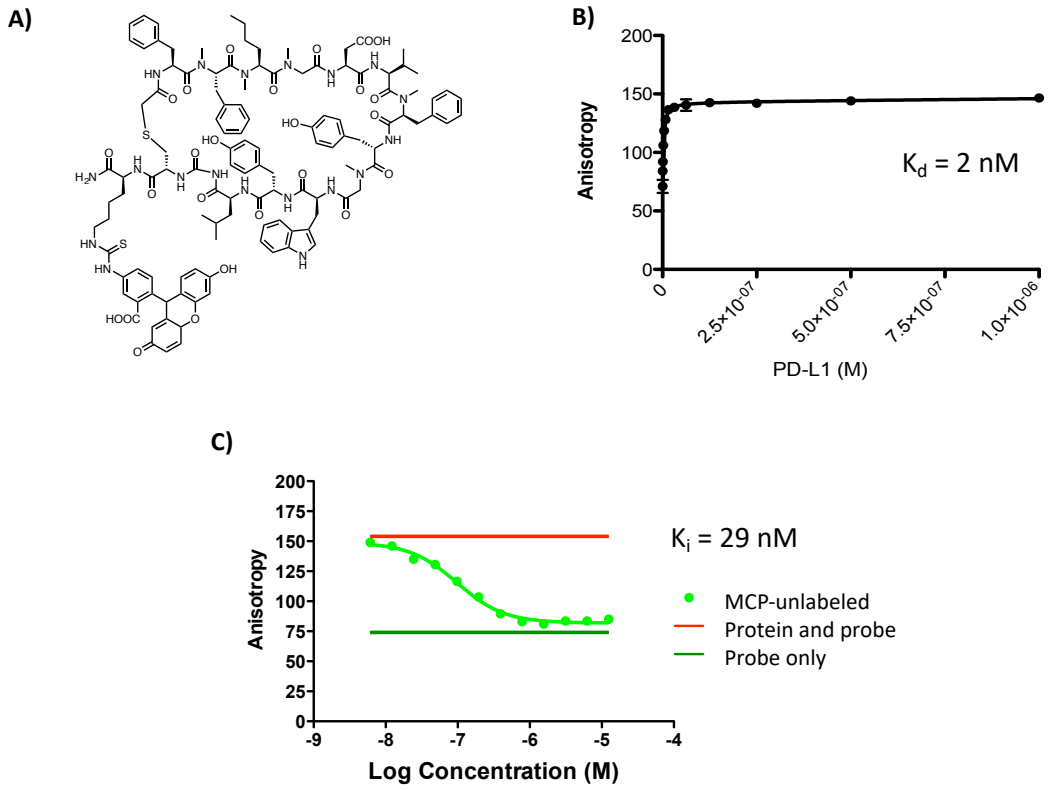

Figure 5-5: Biochemical assay development using a FITC-labeled macrocyclic peptide

A) 2D structure of the macrocyclic peptide with a FITC tag conjugated to the additional lysine residue. B) Saturation binding experiments to determine the K_d of the probe to PD-L1. PD-L1 was titrated from 1 µM to 0.5 µM in the presence of 10 nM FITC probe. The K_d of the probe was determined to be 2 nM. C) Example of the optimized FPA competition assay using increasing concentrations of the unlabeled MCP. Red and green lines are control wells setting the upper and lower limits of the assay containing only probe and protein (red line) and only protein (green line).

for this assay were found to be 1X PBS pH = 7.4, 0.05% Pluronic F-68 and 5% DMSO. The K_i of the unlabeled MCP in these conditions was found to be 29 nM. The optimized assay was found to be highly reproducible between days and multiple freeze-thaws of proteins.

Due to the high affinity of the FITC-conjugated MCP, this probe molecule was given to our collaborator Dr. Young Kim to test for *in vivo* efficacy. Dr. Kim tested this peptide in established protocols for testing anti-PD-1 antibodies in combination with anti-tumor vaccines developed in his lab.[166, 167] Dr. Kim's research focuses on the combinations

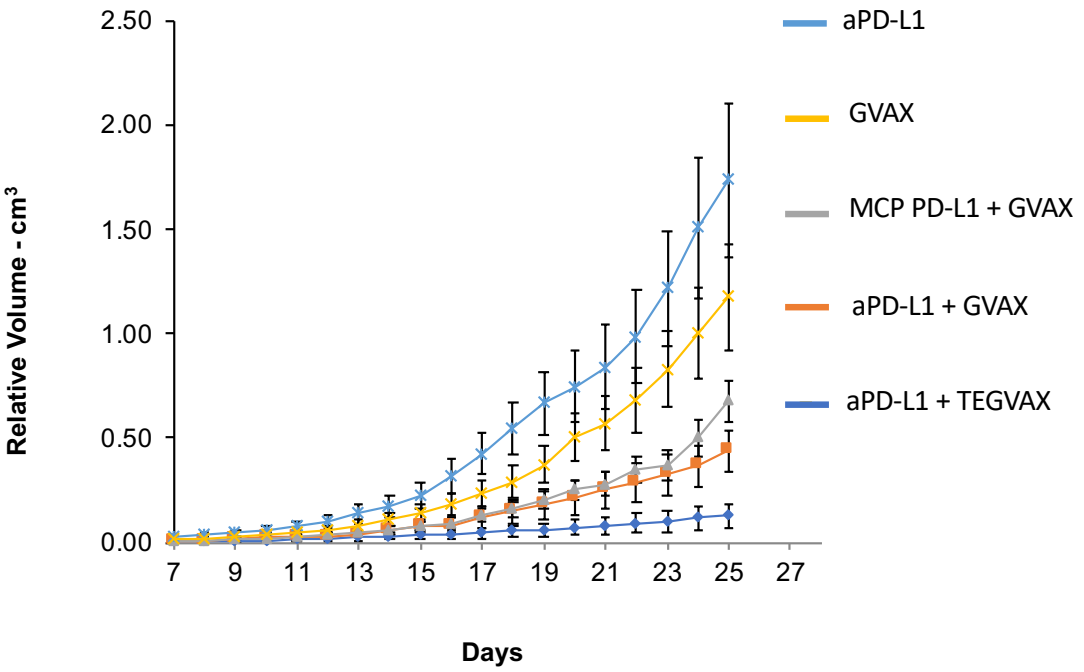

Figure 5-6: BMS macrocyclic peptide has comparable activity to anti-PD-1 in vivo

Measured tumor volume from a B16 melanoma mouse model treated with anti-PD-L1 (light blue), GVAX vaccine (yellow), combination of MCP and GVAX (gray), combination of anti-PD-L1 and GVAX (orange) and anti-PD-L1 and TEGVAX (blue). Data and figure generously provided by Dr. Young Kim.

of checkpoint inhibitors with anti-cancer vaccines, namely GVAX vaccines. GVAX vaccines are composed of irradiated tumor cells that have been genetically modified to secrete stimulatory cytokines that enhance dendritic cells activity.[168] Importantly, these vaccines have been shown to be synergistic with anti-PD-1/L1 therapy.[169] Dr. Kim's research has been focused on enhancing the activity of GVAX vaccines by the development of TEGVAX vaccines that also express multiple TLR agonists to further support activation to APCs.[166]

Dr. Kim's research lab tested the BMS MCP molecule in combination with GVAX in an *in vivo* assay using B16 melanoma mouse models. Consistent with previous reports, anti-PD-L1 and GVAX combinations were more effective than either therapy alone (Figure

5-6, light blue, yellow, and orange).[166] Strikingly, the MCP PD-L1 compound in combination with GVAX had comparable anti-tumor performance compared to the anti-PD-L1 and GVAX combination. These results are an exciting example for developing low molecular weight inhibitors with nanomolar affinity to PD-L1 that demonstrate equivalent *in vivo* efficacy to currently used therapeutic antibodies.

5.2.3 Validation of BMS small molecule inhibitors

Three examples of the BMS small molecules were also synthesized and tested for binding by NMR. Like the MCP, all three of these molecules bind to PD-L1, but not PD-1. Interestingly, BMS small molecules cause significant peak broadening and shifting in ^{1}H-^{15}N HMQC spectra suggesting that PD-L1 forms oligomers in solution resulting in signal broadening (Figure 5-7 A). Indeed, PD-L1 incubated with BMS compounds elutes as a dimer on size exclusion chromatography (Figure 5-7 B). Co-crystal structures obtained of BMS #3 reveal BMS molecules induce a PD-L1 homodimer with one copy of the molecule at the interface of the two monomers as seen in previous fragment crystal structures. Indeed, the conformation of residues at the binding site in both PD-L1 monomers are identical to those obtained of the 14 fragment co-crystal structures previously obtained (Figure 5-8). The binding poses of fragments and the BMS molecules are also highly similar (Figure 5-9). However, the more elaborated BMS small molecules extend out of the hydrophobic pocket and make additional interactions with both monomers. These interactions include pi-stacking with $_{B}$Y56 and hydrogen bonding interactions with $_{A}$D122 and with the carbonyl of $_{A}$F19 (Figure 5-8). These interactions outside the core of the pocket likely contribute to the reported high affinity of these molecules compared to the

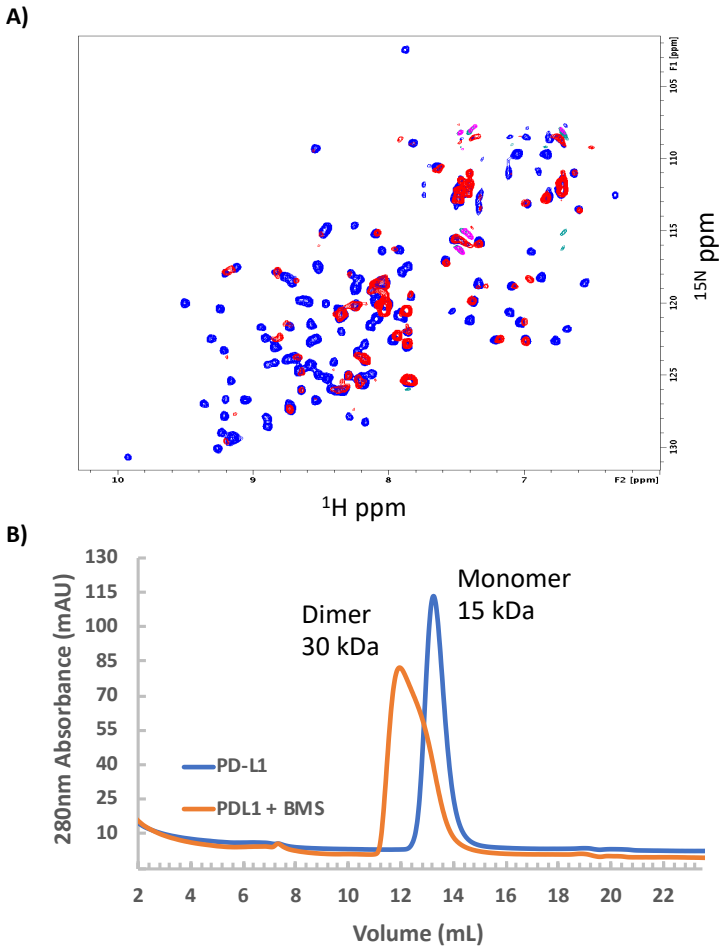

Figure 5-7: BMS small molecule inhibitors bind to PD-L1 and form PD-L1 homodimers.

A) ^{1}H-^{15}N HMQC spectra of 30 µM IgV-6His-H140E alone (blue) and 30 µM IgV-6His-H140E with 200 µM of the BMS small molecule #3 (red). Peak broadening seen in red peaks suggest oligomers of PD-L1 causing larger complexes with slow tumbling rates. B) Elution profile of NMR samples from size exclusion indicate that PD-L1 elutes as a dimer when bound to BMS small molecule #3 (orange line).

weak affinity of our fragment hits.

Because peak broadening in HMQC spectra prevented generating a K_d by NMR, these compounds were tested in the FPA assay developed using the FITC-labeled MCP probe. Surprisingly, none of these compounds were able to displace the MCP probe even

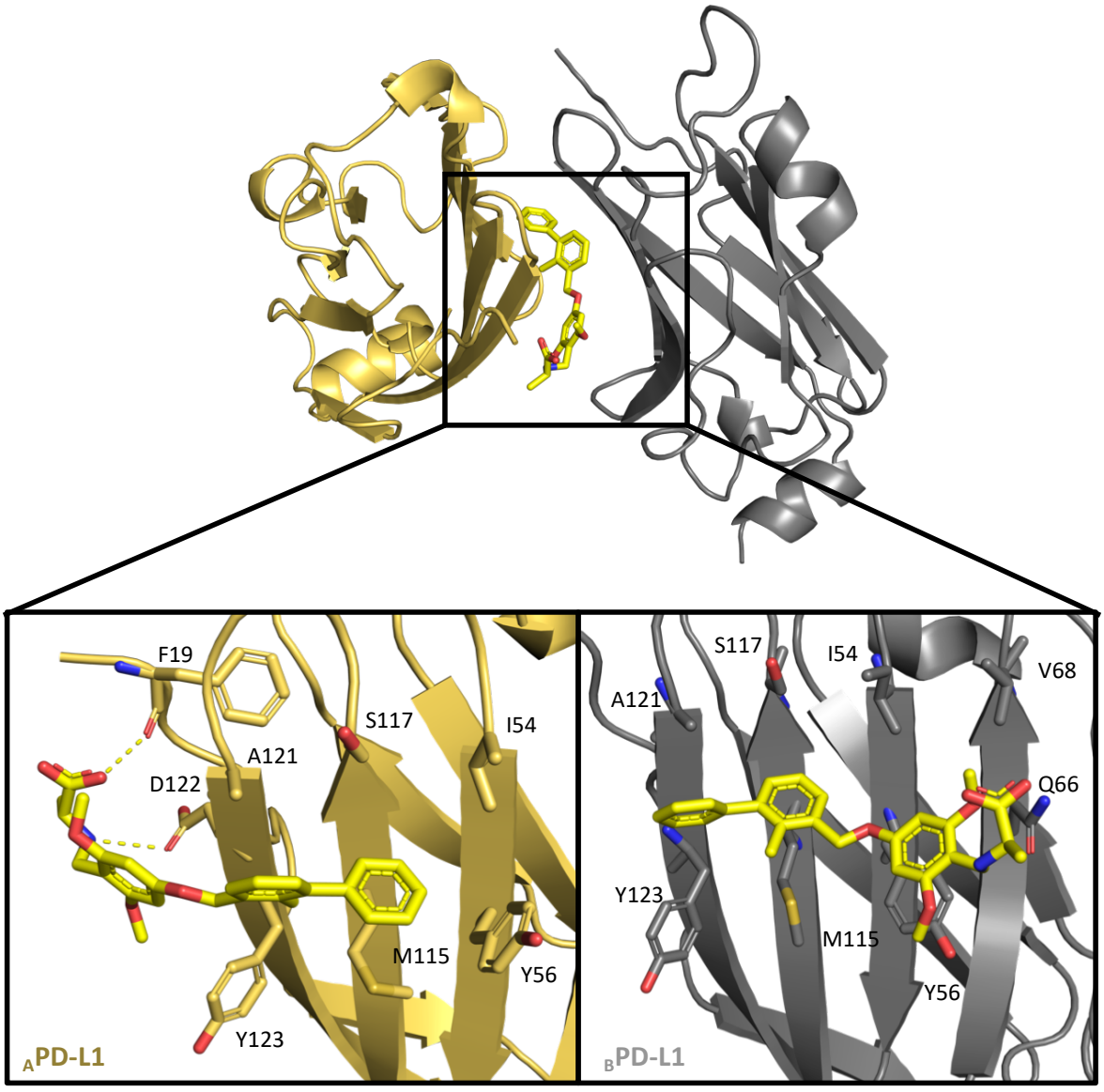

Figure 5-8: BMS compounds co-crystalize as a PD-L1 homodimer

BMS small molecule #3 co-crystalizes as a PD-L1 homodimer with a compound at the interface of the two monomers. These structures are highly similar to the fragment obtained structures in Chapter 4. Interactions of the BMS compound #3 and each PD-L1 monomer are displayed. BMS compounds extend out of the dimer interface and form hydrogen bonding interactions with F19 and D122 (yellow dotted lines).

at the top concentration of 1.5 mM (150,000 times higher than the probe and protein concentration) (Figure 5-10). Interestingly, the anisotropy was found to increase at higher BMS compound concentrations which we attributed to fluorescence artifacts of the

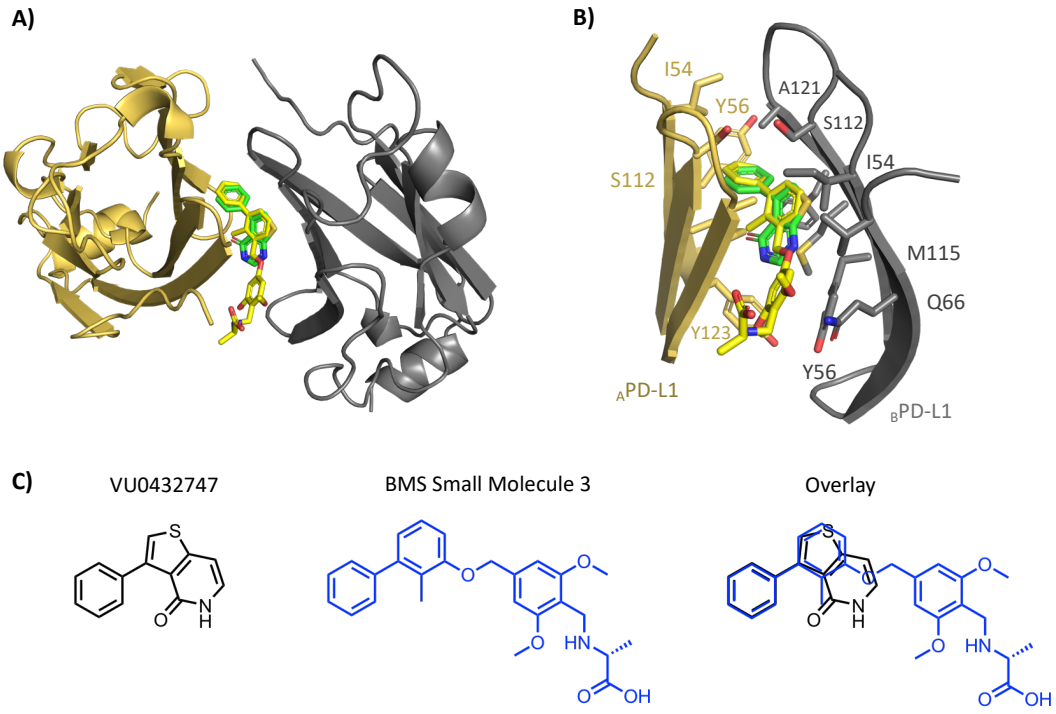

Figure 5-9: BMS small molecule and fragment structures have similar binding poses

A) Overlay of the BMS compound #3 (yellow sticks) and VU0432747 (green sticks) in the PD-L1 dimer interface. B) Highlighted residues that interact with BMS compound 3 have identical configurations in fragment bound structures. C) 2D structures of both compounds and the overlay show similarity between the core of the BMS compound and our fragment hit. These overlays suggest potential fragment analogs that may have increased binding affinity to PD-L1.

compounds being used at higher concentrations (mM).[170]

The FPA results suggest that PD-L1 dimerization may be heavily influenced by protein concentrations. PD-L1 concentrations used for *in vitro* experiments including NMR and X-ray crystallography can range from 15 µM to greater than 300 µM which may favor protein dimerization. Conversely, PD-L1 concentration in the FPA is 15 nM. Low protein concentrations would be less amenable to PD-L1 dimerization and may suggest the binding affinity to PD-L1 as a monomer is too weak to see an effect. However, BMS reports these molecules to have nanomolar IC_{50} values in a HTRF assay in which PD-L1 is

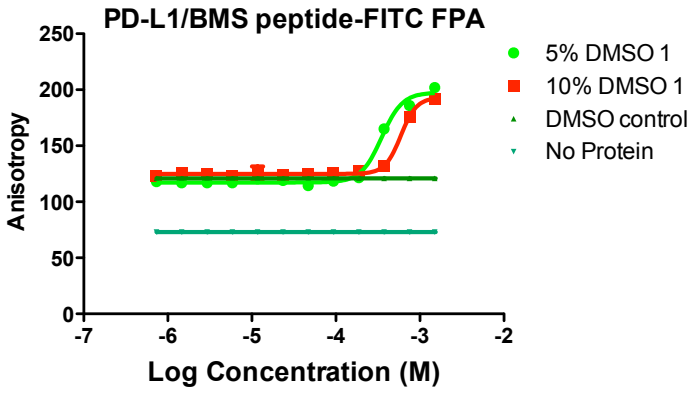

Figure 5-10: BMS compounds are not active in a PD-L1 FPA assay

FPA competition assay using FITC-labeled MCP with titrated BMS compounds starting at 1.5 mM. No decrease in anisotropy suggests these compounds fail to displace the FITC labeled MCP probe. To aid in solubility assays containing both 5% and 10% DMSO were utilized. Increases in anisotropy for the last 3 points (1.5 mM, 0.75 mM and 0.375 mM) are due to fluorescence properties of small molecules at high concentrations.

used in low nanomolar concentrations. It is not clear why there may be a discrepancy between the HTRF and FPA assay formats.

Assuming these BMS molecules had nanomolar IC_{50} values in a TR-FRET assay we hypothesized that these compounds should be active in a cellular assay. To test this possibility the BMS compounds were tested in a PD-1 / PD-L1 cell-based assay purchased from Promega (Figure 5-11 A). This assay consists of Jurkat T cells are engineered to express luciferase via TCR signaling and CHO cells engineering to express PD-L1 on the cell surface. If PD-L1 is bound to PD-1, luciferase expression is inhibited. If the PD-1 / PD-L1 interaction is inhibited, TCR signaling causes luciferase expression. Luciferase activity is then measured by measuring luminescence after the addition of luciferase substrate.

A PD-1 mAB was used as a positive control and had an EC_{50} value of 0.83 µg/mL which is close to the reported 0.72 µg/mL for this assay (Figure 5-11B). High

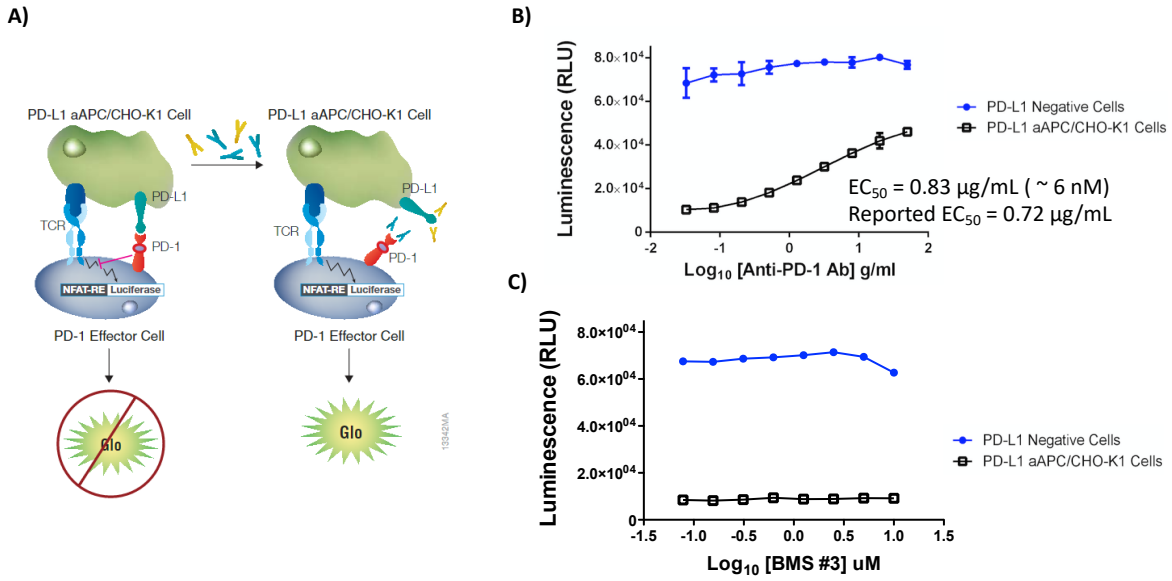

Figure 5-11: BMS small molecules are not active in PD-1 / PD-L1 cell-based assays

PD-1 / PD-L1 cell based assay purchased from Promega. A) Assay principal. aAPC/CHO-K1 cells engineered to express PD-L1 bind to T cells engineered to express luciferase by TCR signaling. PD-L1 bound to PD-1 inhibits luciferase expression and luminescence after addition of luciferase substrate. If PD-1/L1 inhibitors are present, TCR signaling induces expression of luciferase and luminescence is observed by luciferase substrates. B) Positive control assay using anti-PD-1 antibody purchased from Promega. Anti-PD-1 titration shows a dose response in luminescence suggesting the inhibitor is inhibiting PD-1 signaling. EC50 values obtained from this inhibitor is close to reported values. Blue line is of negative control cell line of aAPC/CHO-K1 cells that do not express PD-L1. C) BMS compounds fail to increase luminescence suggesting these compounds fail to inhibit the PD-1/L1 interaction. Image adapted from Promega.

concentrations of the BMS compound the µM range were used to account for any weak activity from the compound. However, the BMS compounds had no activity and were found to be toxic at concentrations above 10 µM (Figure 5-11C).

These results suggest that while these molecules may bind to soluble PD-L1 at higher protein concentrations used for structural biology type experiments (NMR and X-ray), their ability to inhibit PD-L1 at lower protein concentrations (FPA assay and on the surface of cells) may not be as effective and further optimization of these compounds

may be required. Furthermore, no evidence has been produced that a glycosylated and membrane-anchored PD-L1 can adapt the conformation of a homodimer on the surface of cells and may explain why these compounds are inactive in cellular assays. While we were initially interested in using our fragments as alternative scaffolds to the BMS molecules to incorporate the extensive SAR published in BMS patents to rapidly increase the potency of our fragments, we were not convinced that this was a viable strategy to develop an inhibitor that would be active in cellular assays and *in vivo* studies.

5.2.4 Fragment incorporation to the BMS macrocyclic peptide

The crystal structure of the MCP bound to PD-L1 was used to study the interactions that result in high affinity binding (Figure 5-12). Phe1, Phe7, and Trp10 of the BMS MCP make hydrophobic contacts with PD-L1 at the PD-1 binding site (Figure 5-12,

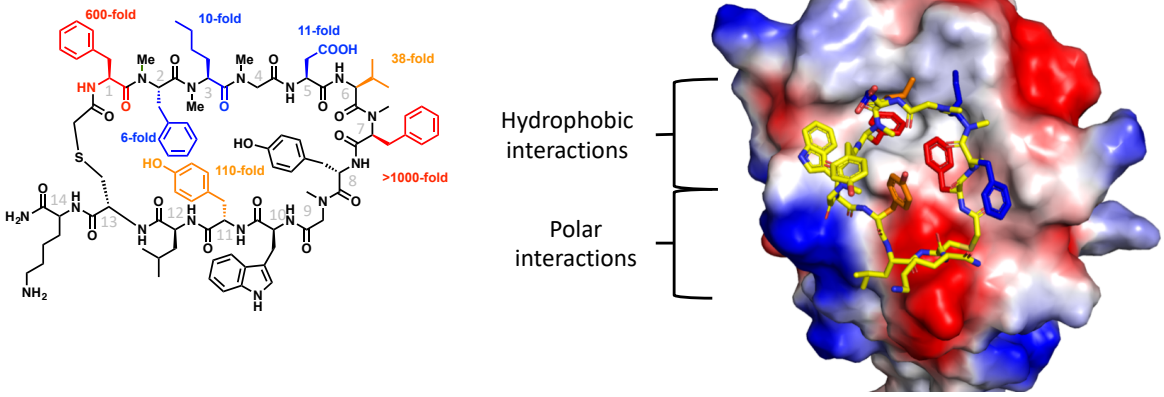

Figure 5-12: BMS MCP co-crystal structure reveals key hydrophobic and polar interactions

2D-structure of the BMS MCP peptide color coded with data from the BMS patent of affinity loss when mutated to alanine (left). Co-crystal structure shows Phe1 and Phe7 to bind at the hydrophobic pocket of PD-L1. Mutations to either of these residues result in > 600 fold loss in affinity to PD-L1. Affinity loss from 2D structure is also color coded on the MCP in the crystal structure (Red = major loss, orange = moderate loss, blue = some loss). No data was provided by uncolored residues.

right). Backbone amides of Cys11 and Lue12 and carbonyl of Trp10 make electrostatic interactions with charged residues nearby the hydrophobic pocket. BMS reported extensive SAR in their patent including alanine scanning of most of the residues.[165] Substituting Phe1 or Phe7 for alanine resulted in 600-fold and greater than a 1000-fold loss in binding affinity, respectively (Figure 5-12, left). Norleucine3 and Val6 also make hydrophobic interactions with PD-L1 and lost significant affinity when mutated to alanine. Notably, Tyr11 forms important intramolecular interactions that stabilize the conformation of the peptide loses 110-fold when mutated to alanine.

Overlay with fragment co-crystal structures reveals that fragment hits overlay with Phe7 highlighting the importance of Phe7. Strikingly, the placement of Phe7 is in the exact location and orientation of phenyl rings from BMS compounds and multiple fragments (Figure 5-13). This structural information highlights the key hydrophobic interaction is at this phenyl binding site. Given this structural similarity, fragments could be incorporated as a non-natural amino acid at Phe7 to further enhance the binding affinity and develop a novel MCP that could be outside the scope of BMS patents (Figure 5-13). Indeed, our lab has had success in merging fragment screening results into peptides to enhance the binding affinity in other projects, namely RPA.[171] Molecular modeling was used to explore the possibility of incorporating the fragment hits into the MCP structure. It was evident that the neighboring Trp10 could clash with fragments and would need to be mutated to either alanine or histidine (Figure 5-13). Modeling experiments suggest that incorporation of VU0115538 has the best potential to avoid steric clashes with Trp10 substituted residue. VU0115538 also contains a vector to further expand into the S1 region to make

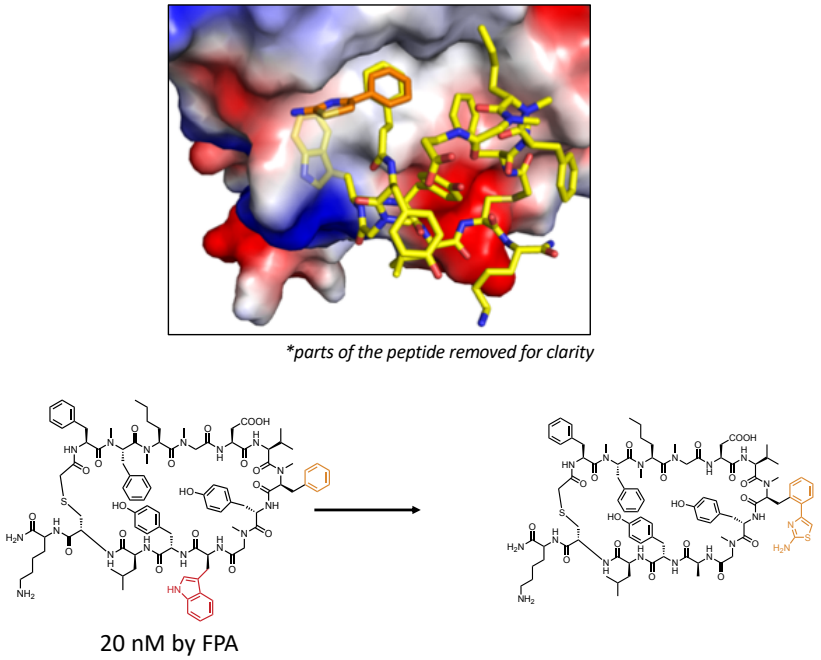

Figure 5-13: Fragment incorporation strategy to macrocyclic peptide

Overlay of VU0115538 with the BMS MCP show identical placement of Ph9 and the phenyl ring of the fragment. Trp10 (transparent) may clash with fragment incorporation. To incorporate the fragment into the peptide, Trp10 will be mutated to alanine and VU0115538 will be added to Phe7 as a non-natural amino acid.

additional electrostatic interactions made by PD-1 (Figure 5-13). While Trp10 is expected to have major contributions to the binding affinity, mutations of Trp10 to Ala were not reported in the patent. To test the importance of Trp10 to the binding affinity an MCP with Ala10 was synthesized and tested in our FPA assay. Unfortunately, Ala10 MCP was found to be completely inactive in the FPA assay and no detectable binding by NMR suggesting this residue is required for binding to PD-L1. It is unknown if a fragment incorporated into the MCP that would occupy similar space as Trp10 would retain binding affinity, as a fragment synthesized peptide was never synthesized.

5.2.5 Modification of the BMS macrocyclic peptide linker

An additional strategy to generate a novel MCP is to modify the linker portion of the peptide to be outside of the BMS patents. BMS claims S, SO, SO2, O, and CH2 linked macrocycles do not claim cyclized linkers (Figure 5-14).[165] We utilized modeling tools to design a series of different cyclized linkers at this position. To test the feasibility of this approach, a cyclohexane linked peptide was synthesized and had a K_i in the FPA assay of 7 µM, representing a 280-fold loss in affinity to PD-L1. Additional linkers that were designed and tested also resulted in significant loss in affinity. Closer analysis of the linker portion

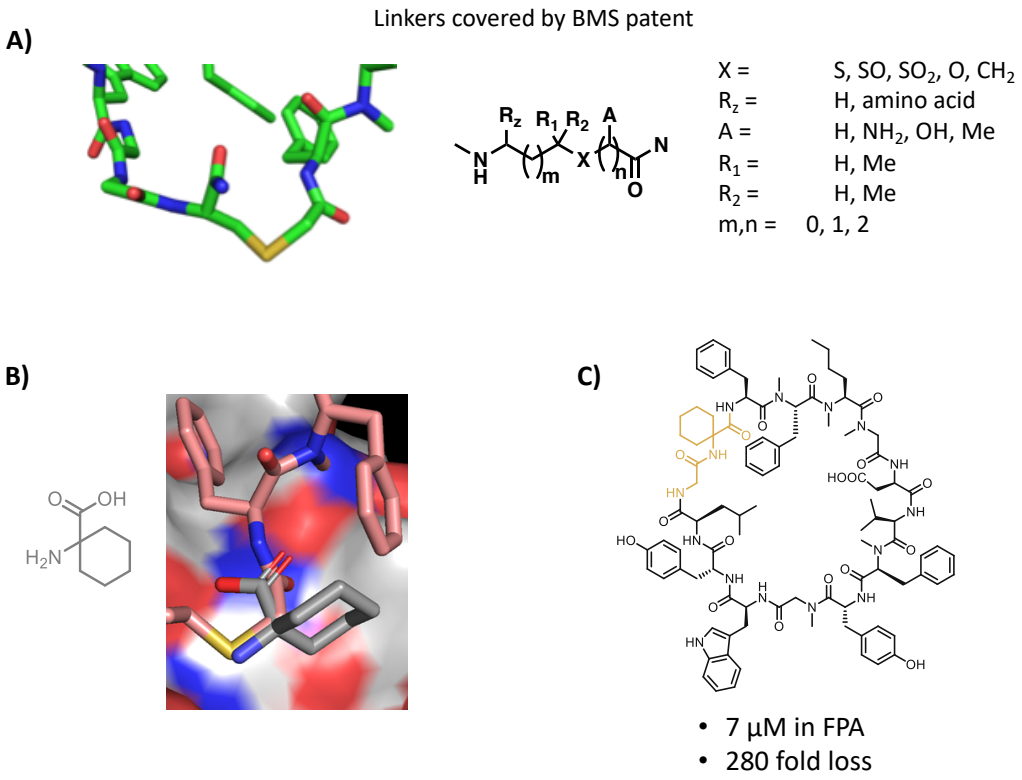

Figure 5-14: Modification of the linker portion of the macrocyclic peptide

A) Macrocyclic peptide linker portion from the X-ray co-crystal structure (green sticks) and the 2D drawing of the linker and what is claimed by BMS patents. B) Modeling of a cyclohexane linker on the X-ray structure. C) 2D structure of the synthesized macrocyclic peptide with a cyclohexane linker (orange). This peptide had a 280-fold loss in binding affinity monitored by the FPA assay.

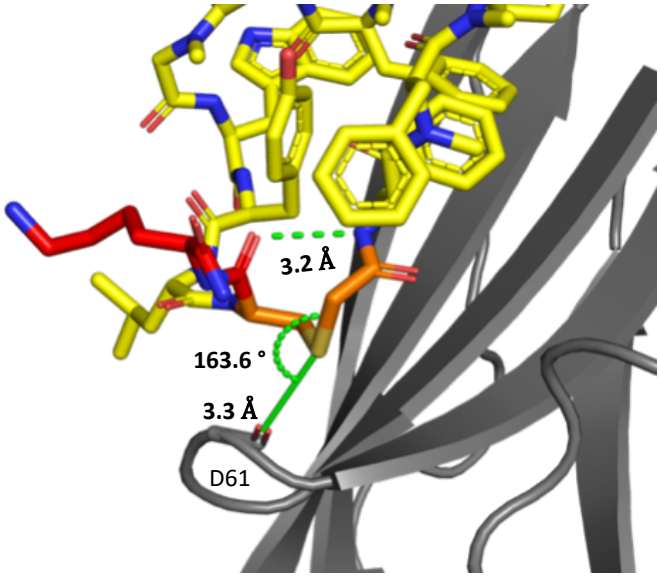

Figure 5-15: Macrocyclic peptide linker has inter and intra molecular interactions

Removal of residues on the MCP results in the loss of a sigma hole interaction with D61 (green solid line and angle) and intramolecular hydrogen bond (green dashed line). Loss of these interactions can rationalize the loss of binding affinity with novel linker pieces.

reveals a sigma hole interaction of the MCP linker sulfur atom and backbone carbonyl of D61 (Figure 5-15). Additionally, the synthetic route to make the MCP resulted in the amide of residue 13 to be removed. This amide group forms intermolecular hydrogen bonding that presumably stabilized the MCP conformation (Figure 5-15, red sticks). These results are consistent with other modifications made that may alter peptide confirmation, such as removing other N-methyl groups, that also resulted in a dramatic loss in affinity. These results suggest that the conformation of the peptide is critical for high binding affinity to PD-L1.

5.2.6 Modeling of fragment analogs to mimic BMS macrocyclic peptide interactions

We also utilized the structure of the MCP to guide the structure-based design of fragment hits. As mentioned previously, the MCP makes three key hydrophobic contacts

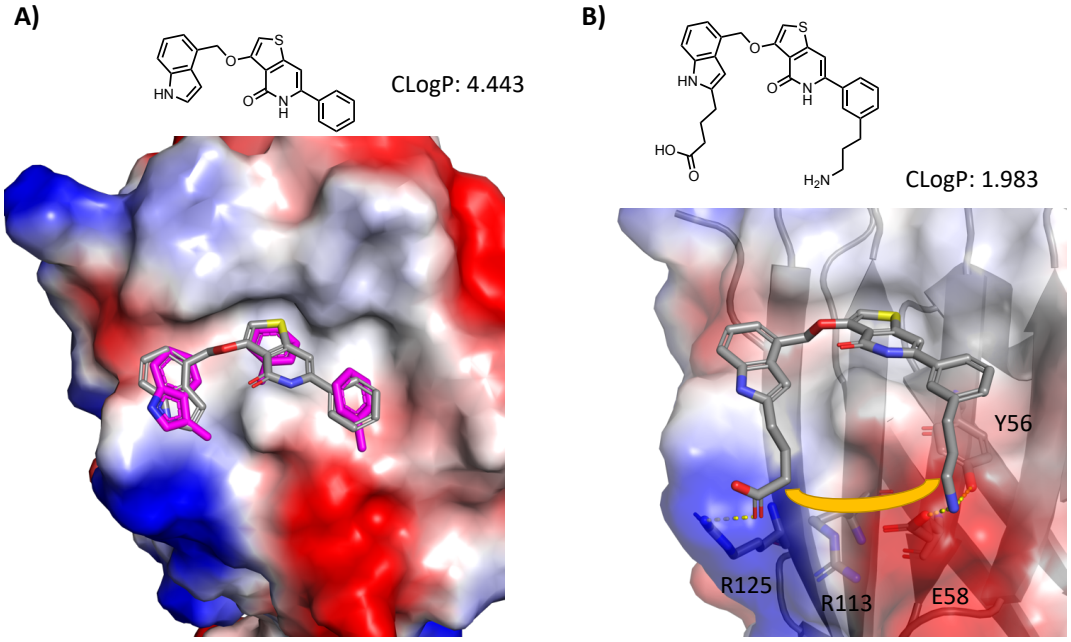

Figure 5-16: Modeling of VU0432747 analogs that mimic hydrophobic interactions from the macrocyclic peptide.

A) docking model of an indole and phenyl substituted analog of VU0432747 that mimetics hydrophobic interactions made by the macrocyclic peptide (purple sticks). B) Docking model of compound in A) but with solubilizing groups that form polar interactions with R125 and E58. Potential cyclization of this molecule to form a macrocycle is shown by orange shape.

at the hydrophobic pocket. Overlay with VU0432747 on monomer B suggests the thiophene moiety of the fragment hits overlays with the Phe7. Docking experiments VU0432747 analogs with indole substitutions to mimic Trp10 and an addition phenyl ring to mimic Phe1 suggested a small molecule containing these substitutions may be capable of mimicking the key hydrophobic contacts made by the peptide (Figure 5-16 A). However, these molecules are very hydrophobic which could result in solubility issues in our biochemical assay. Thus, further docking studies were performed to add either a carboxylic acid or primary amine moieties to form electrostatic interactions with either R125 or E58, respectively. Extensions from the indole and phenyl rings were designed to reach R125 or E58 to form hydrogen bonds to R125, E58, and Y56 (Figure 5-16 B). The

addition of 3 and 4 atom linkers induced some flexibility to the molecule which increases the entropy. To account for the increase in entropy, many different linkers were designed to generate a macrocycle (Figure B, orange shape). With enhanced occupancy of the hydrophobic pocket and additional electrostatic interactions, these molecules are predicted to bind with low micromolar affinity based on binding energies predicted from Maestro. However, these molecules would need to be synthesized and tested in the FPA to validate the docking results.

5.3 Conclusions and Discussion

Given the discouraging results obtained in optimizing fragment hits to PD-L1, we hoped to utilize structural information of other disclosed PD-L1 inhibitors to rapidly improve our lead molecules. Interestingly, the Aurgiene compounds did not bind to either PD-1 or PD-L1. BMS small molecules were found to bind to PD-L1 by inducing a PD-L1 homodimer in solution. Co-crystal structures reveal a highly similar binding pose to the fragment hits identified of our screen. Compared to our fragment hits, the BMS small molecules appear to be more optimized molecules that retain the ability to form a PD-L1 homodimer. However, we found that these molecules were inactive in our FPA assay and cellular assays suggesting that these molecules need further optimization to have cell activity and raises concern about the ability of PD-L1 to homodimerize when anchored on the surface of cells.

BMS macrocyclic peptides were found to bind to PD-L1 with high affinity. Importantly, the peptides bind to monomeric PD-L1 as evidence by both NMR and

crystallography. These molecules are active in cellular assays reported in BMS patents and active *in vivo* with results obtained from Dr. Young Kim's lab. These exciting results prompted us to utilize structural information of the macrocyclic peptide to guide the design of a novel inhibitor. We utilized various strategies to mimic the MCP including the incorporation of a fragment to the MCP structure, modifying the linker portion of the MCP, and designing fragment analogs to mimic key interactions with PD-L1. However, we found that even minor changes to the peptide resulted in dramatic losses of binding affinity. Due to this sensitivity of the MCP, we found it exceedingly difficult to design analogs that differ from patent-protected molecules and retained nanomolar binding affinity to PD-L1.

5.4 Methods

Binding of reported compounds

Binding of synthesized compounds to was tested by NMR with samples containing 30 µM 15N PD-L1 IgV-6His-H140E and 200 µM BMS compounds in NMR buffer (50 mM $NaPO_4$ pH = 7, 25 mM NaCl and 4% DMSO). Size exclusion was run using 200 µL of the NMR samples injected to a Superdex 75 10/300 GL column. The predicted molecular weight of elution peaks from size exclusion was calculated using the calibration curve reported in the user manual of the Superdex 75 column.

X-ray crystallography of BMS small molecule and MCP

BMS #3 bound crystals were generated by incubating PD-L1 IgV-6his-V76T at 35 µM (0.5 mg/mL) in X-ray buffer (10 mM Tris pH 8, 20 mM NaCl) with 1 mM of BMS #3 on

ice for 3 hours. The complex was concentrated to 200 µM (3 mg/mL) using 3 kDa MWCO amicon ultra- 0.5 mL centrifugal filters (Millipore). Crystals were obtained in conditions containing 29% PEG_{4000}, 0.28 M NaCl, 0.01 M Tris pH = 8.5 within 48 hours at 18 °C. The macrocyclic peptide was incubated with 35µM PD-L1 IgV-6his-V76T,H140E and 200 µM peptide. The complex was concentrated to 200 µM (3 mg/mL) and screened against the Hampton Index HT screen. Crystals of the PD-L1 macrocyclic peptide was obtained in 3.5 M sodium formate within 48 hours at 18 °C.

All crystals were cryoprotected in mother liquor containing 20% glycerol prior to freezing in liquid nitrogen. Data were collected on the Life Sciences Collaborative Access Team (LS-CAT) beamlines at the Advanced Photon Source (APS), Argonne National Laboratory. Indexing, integration, and scaling were performed with HKL2000. The phases were determined by molecular replacement (Phaser-MR) using the PD-L1 IgV-6His construct (PDB code 5C35). The models were refined using phenix.refine and manual fitting the model to electron density using COOT. All figures were generated using PyMOL.

Cell assay methods

The PD-1/PD-L1 blockade Bioassay kit (J1250) was ordered from Promega. In addition to the kit positive and negative controls containing anti-PD-1 mAB (Cat.# J1201) and PD-L1 negative cells (Cat.# J1191), respectively. The assay was run according to the protocol using the recommended dose response (9-point curve, top concentration = 50 µg/mL, 2.5-fold dilution) for the anti-PD-1 mAB. The BMS small molecule dose response consisted of a 9 point curve with a top concentration of 10 µM with a 2 fold dilution.

Concentrations past 10 µM of BMS #3 were toxic to the cells.

FPA assay methods

Saturation binding experiments for the BMS MCP consisted of a 12-point, 2-fold serial dilution of PD-L1 IgV-IgC-6his produced by HEK293 cells with a starting concentration of 1 µM. The assay buffer consisted of 1X PBS pH 7.4, 0.05% F-68 Pluronic and 5% DMSO. To run the assay 25 µL of assay buffer was added to a black solid polystyrene 384 well plate. Next, 12.5 µL of 4X protein in assay buffer was added followed by 12.5 µL of 4X probe in assay buffer. Plates were spun at 300 rpm for 1 minute. The plate was incubated at room temperature for 15 minutes. Anisotropy was measured using 485/20 528/20 wavelength filter. Graphs were plotted using Prism 5 Version 5.0b.

Optimized FPA competition assays using FITC-MCP were run using 15 nM PD-L1 IgV-IgC-6his produced by HEK293 cells with 10 nM FITC-MCP in assay buffer (1X PBS pH = 7.5, 0.05% F-68 Pluronic and 5% DMSO). Dose-response curves were generated using an 11-point 2-fold dilution of untagged MCP starting at 25 µM. Control wells included wells with protein but no test compound and probe only wells (no protein) that determined the upper and lower anisotropy readings, respectively. The assay was performed by addition of 25 µL of 2X unlabeled MCP (or compound) to a black solid polystyrene 384 well plate followed up 12.5 µL of 4X PD-L1. The plate was spun at 300 rpm for 1 minute and incubated at room temperature for 15 minutes. Next, 12.5 µL of 4X probe was added to each well. Plates were spun again and incubated for 15 minutes at room temperature. Anisotropy was measured on a X machine with a 485/20 528/20 wavelength filter. Graphs

were plotted using Prism 5 Version 5.0b.

Molecular modeling

Maestro (Schrodinger) was used for all molecular modeling. The PD-L1 crystal structure bound to BMS MCP was prepared for modeling by adding missing side chains/residues, charged in pH 7 buffer, and energy minimized by the Protein Prep Wizard. A docking grid was generated around amino acids that bind to the MCP. All docked compounds were either drawn into maestro using the ligand sketch window or uploaded as SDF files. All ligands were prepared for docking using Ligprep. Compounds were docked using Glide rigid protein docking with normal settings and extra precision. Docking results were exported to Pymol to generate images.

Chapter 6

General Conclusions and Future Outlook

Immunotherapy offers an exciting therapeutic strategy to harness the power of the immune system to aggressively fight cancer. The development of mABs that target immune checkpoints to stimulate T cell activity towards cancer have been successful in a variety of cancer types and have revolutionized cancer care. However, the intrinsic properties of mABs may have negative implications when targeting immune checkpoint signaling pathways. These concerns include suboptimal tumor penetration, higher cost of production, potential immunogenicity, and prevalence of immune-related adverse events. An alternative therapeutic approach is to use small molecule inhibitors of immune checkpoint proteins. Indeed, small molecules have the potential to address many of these concerns with mABs. Some advantages of small molecule inhibitors include improved tumor penetration, potential oral bioavailability, lower cost of production and a longer shelf-life. Because the pharmaceutical and pharmacokinetic profile can be easily modulated, the design of inhibitors that are rapidly cleared from the body can minimize irAEs and allow for flexible dosing regimens. Despite these potential advantages, the development of small molecules that target immune checkpoints has lagged behind the development of mAbs. Given the limited reports of small molecules targeting CTLA-4, PD-1, or PD-L1 and the potential impact small molecules could have on immunotherapy, the goal of this dissertation was to utilize fragment-based methods to assess the druggability of these targets and discover novel chemotypes that could serve as starting points for lead optimization towards potent inhibitors of these proteins.

In summary, CTLA-4 and PD-1 were separately screened against our fragment library. The CTLA-4 screen resulted in no hits. The PD-1 screen resulted in only 8 hits. The PD-1 hits have weak binding affinity and are expected to bind to the opposite side of PD-1 from the PD-L1 binding site.

Analogs were identified using substructure-similarity searches and screened against PD-1. However, none of the hits were found to have improved binding affinity to PD-1 or able to displace PD-L1.

Unlike CTLA-4 and PD-1, the fragment screen of PD-L1 resulted in a diverse set of fragment hits (1.6% hit rate) that were clustered into 18 different chemotypes. While the binding affinities of these fragments were weak, many were found to displace PD-1 in an NMR-based displacement assay. In total, 14 co-crystal structures of fragments bound to a PD-L1 homodimer were determined. Fragments occupy a cylinder-shaped hydrophobic pocket formed at the interface of two PD-L1 monomers. PD-L1 homodimer structures presented unique challenges for structure-based design as each fragment had distinct binding poses on each PD-L1 monomer making it unclear which pose should be utilized for the design of analogs. Synthesized analogs were made to probe the correct binding pose by adding functional groups that clashed with the other protein monomer. Using these structures hundreds of compounds were modeled and synthesized to increase the binding affinity of these fragment hits. However, only minor improvements were made in each series. Furthermore, analogs that prevented PD-L1 homodimers were unable to be co-crystallized. Without iterative structural information of compounds binding to PD-L1, structure-based design becomes challenging as the exact binding pose of more elaborate compounds becomes highly speculative.

During our work on this project, patents disclosing small molecules and peptides that target PD-L1 were published. One series of small molecule inhibitors of PD-L1 that have nanomolar IC_{50} values in a FRET assay was disclosed by BMS. Like the fragments, the BMS compounds also co-crystallized as a PD-L1 homodimer with the compound at the interface of the two monomers. Overlays of a BMS compound and fragments revealed that the methylated bi-phenyl cores of these molecules have highly similar binding poses to PD-L1. However, BMS

compounds extend out of the dimer-induced hydrophobic pocket and make additional interactions with PD-L1. We found that the BMS compounds formed PD-L1 homodimers in solution at protein concentrations for NMR (30 μM). However, we found that these compounds were inactive in a cellular assay where PD-L1 is anchored to the membrane. Thus, it is unlikely that small molecules that induce PD-L1 homodimers will be a viable therapeutic strategy.

Large 16 amino acid macrocyclic peptides (MCP) that bind to PD-L1 with low nanomolar affinity were also reported by BMS. We found these peptides have comparable *in vivo* efficacy to anti-PD-L1 antibodies in a mouse model for human melanoma. Inspired by this result, we shifted chemistry support from optimizing fragments to generating macrocyclic peptides that target PD-L1. To understand how the MCP binds to PD-L1 with high affinity, a co-crystal structure of the MCP bound to PD-L1 was obtained. The MCP binds to the PD-1 binding site and occupies the same hydrophobic region of PD-L1 as our fragment hits. We employed two strategies to develop our own macrocyclic peptide outside the scope of the BMS patent. The first strategy was to incorporate our fragment hits into the MCP structure using structure-based design. The second strategy was to modify the linker portion of the peptide. However, we found that any modification to the peptide resulted in a dramatic loss of peptide binding affinity that ultimately discouraged us from synthesizing additional macrocycles.

Taken together, these results highlight the challenges of targeting immune checkpoints by small molecules. PD-1 and CTLA-4 are likely undruggable. We identified many different chemotypes that bind to PD-L1, but the optimization of these fragments to bind with high affinity will be difficult. These challenges result from the relatively flat binding surfaces and lack of hydrophobic pockets that favor small molecule binding. Indeed, the only co-crystal structures obtained for fragments and BMS compounds were of a PD-L1 homodimer. We suspect that PD-L1 dimer formation was amenable due to relatively high concentrations of soluble protein used for

NMR and X-ray crystallography experiments. However, it remains to be seen if more optimized small molecules can induce PD-L1 homodimers on the surface of cells.

Small molecules that bind with high affinity to PD-L1 in a monomeric state would be preferred. However, our attempts to optimize fragment hits to bind to monomeric PD-L1 resulted in very weak binding affinities. Compared to the BMS macrocyclic peptide that binds to PD-L1 with high affinity, the fragments occupy a very small area on PD-L1. Thus, designing small molecules that would occupy more surface area while making additional hydrophobic and electrostatic interactions may be required to bind to PD-L1 with higher affinity. Thus, designing macrocycles based on these fragments could be an effective strategy moving forward. Ideally, we would have identified fragments that bind to an adjacent site on PD-L1 and could be linked to rapidly increase the affinity of our compounds. However, no such fragments were identified and the fragments that bound to the primary site were too weak to conduct a second site screen. Furthermore, we were unable to get co-crystal structures of larger analogs that might have suggested new strategies to expand our molecules.

In conclusion, these results are the first reported instances of using fragment-based methods to assess the druggablility and identify small molecule inhibitors of immune checkpoint proteins. While these proteins were predicted to be highly challenging targets for small molecules, we were able to successfully identify many fragments that bind to PD-L1 and displace PD-1. These fragments serve as an important starting point towards the design of small molecule inhibitors of PD-L1. Other drug discovery groups that are targeting PD-L1 with small molecules, peptides, or macrocycles could incorporate the fragment chemotypes identified from our screen to rapidly improve the binding or pharmaceutical properties of their lead compounds. These results also suggest fragment-based methods could be used to address the druggability of other immune checkpoint proteins. While other checkpoint proteins are also predicted to be undruggable

targets, these results suggest other checkpoint proteins could be druggable and should be validated experimentally by conducting fragment-based screens.

Appendix A. Hits from the fragment screen of PD-L1.

Structure	VU Number	Structure	VU Number	Structure	VU Number
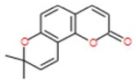	VU0417453	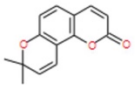	VU0417453	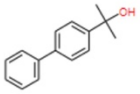	VU0412466
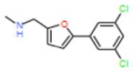	VU0153947	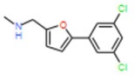	VU0153947	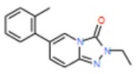	VU0419276
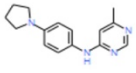	VU0411373	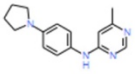	VU0411373	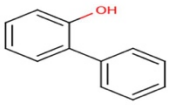	VU0413536
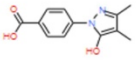	VU0411620	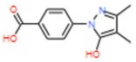	VU0411620	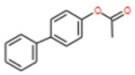	VU0004435
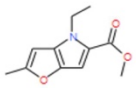	VU0416609	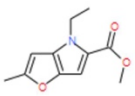	VU0416609	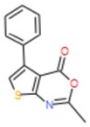	VU0006187
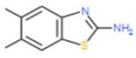	VU0166401	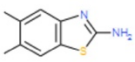	VU0166401	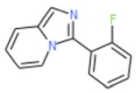	VU0061254
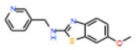	VU0410942	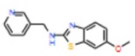	VU0410942	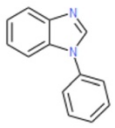	VU0330093
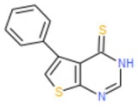	VU0091290	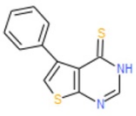	VU0091290	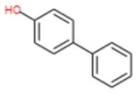	VU0413528
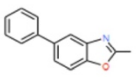	VU0240047	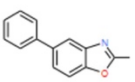	VU0240047	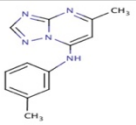	VU0415995
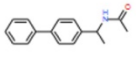	VU0411100	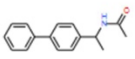	VU0411100	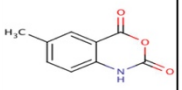	VU0421388

Structure	VU Number	Structure	VU Number	Structure	VU Number
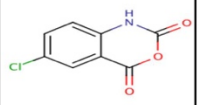	VU0421053	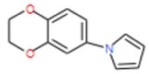	VU0431033	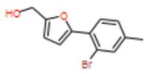	VU0045982
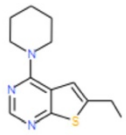	VU0238287	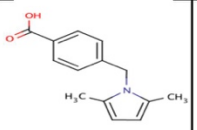	VU0178542	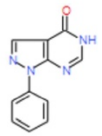	VU0062266
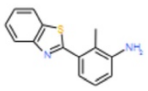	VU0126711	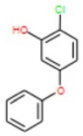	VU0012717	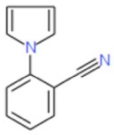	VU0138698
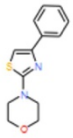	VU0163889	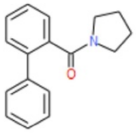	VU0172471	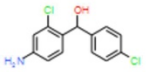	VU0412002
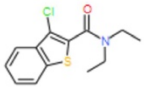	VU0410524	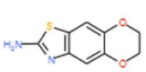	VU0008115	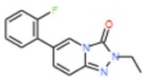	VU0419275
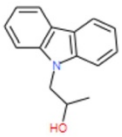	VU0410566	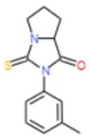	VU0148911	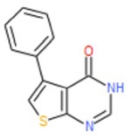	VU0432747
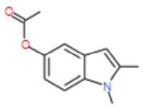	VU0180070	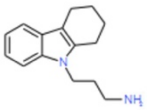	VU0412414	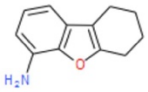	VU0432768
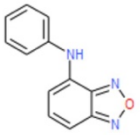	VU0410529	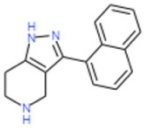	VU0432887	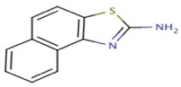	VU0085331
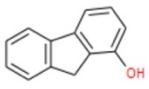	VU0412467	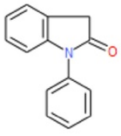	VU0004583	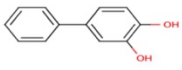	VU0406544
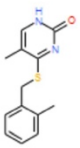	VU0421797	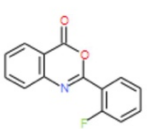	VU0034731	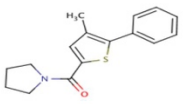	VU0411655

Structure	VU Number	Structure	VU Number	Structure	VU Number
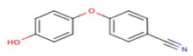	VU0410805	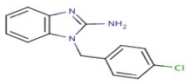	VU0026922	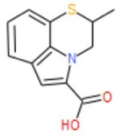	VU0416643
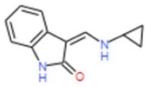	VU0027700	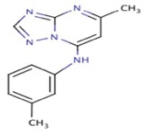	VU0415995	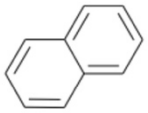	VU0421544
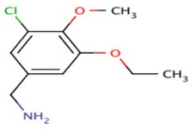	VU0410969	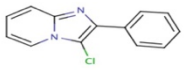	VU0412490	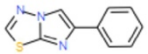	VU0431053
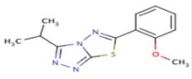	VU0410993	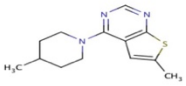	VU0117934	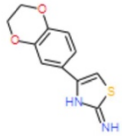	VU0433155
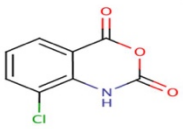	VU0421411	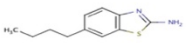	VU0044466	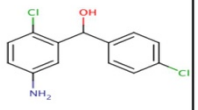	VU0412026
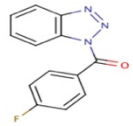	VU0412539	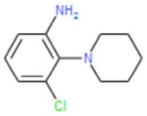	VU0412991	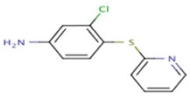	VU0417630
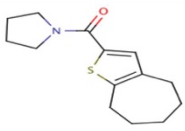	VU0411646	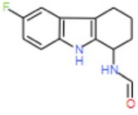	VU0407069	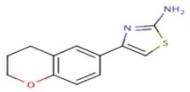	VU0432670
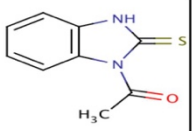	VU0013796	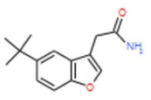	VU0408461	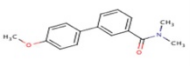	VU0410764
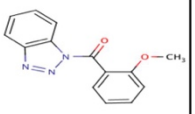	VU0412896	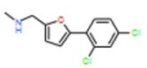	VU0411348	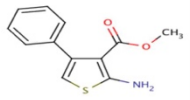	VU0026121
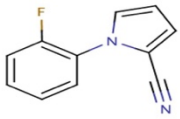	VU0417393	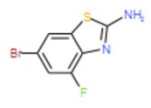	VU0412177	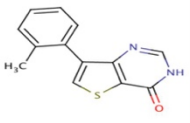	VU0416387

Structure	VU Number	Structure	VU Number	Structure	VU Number
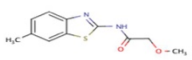	VU0180709	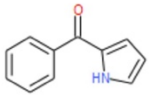	VU0417388	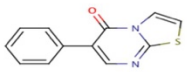	VU0407767
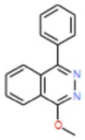	VU0009826	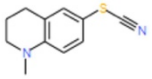	VU0417596	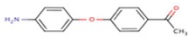	VU0008922
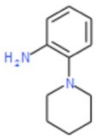	VU0067704	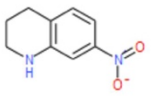	VU0421650	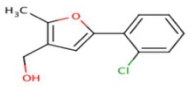	VU0412062
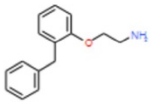	VU0164412	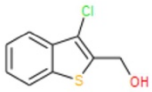	VU0421911	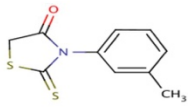	VU0012487
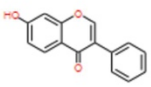	VU0254646	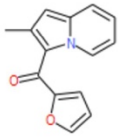	VU0430496	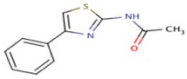	VU0415889
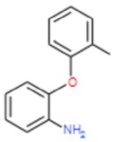	VU0327092	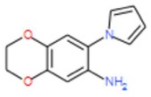	VU0433031	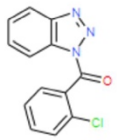	VU0012455
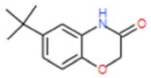	VU0407768	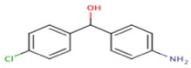	VU0408589	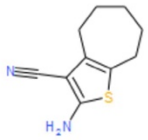	VU0118450
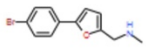	VU0411337	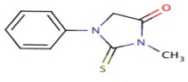	VU0407174	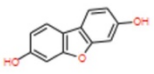	VU0130568
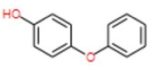	VU0413530	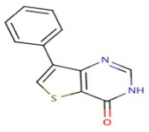	VU0416371	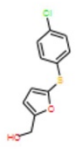	VU0410783
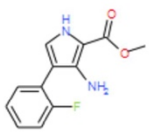	VU0416396	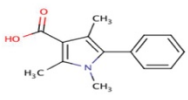	VU0411553	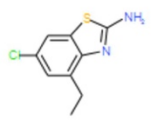	VU0412178

Structure	VU Number	Structure	VU Number	Structure	VU Number
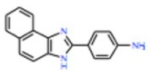	VU0415969	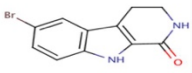	VU0415857	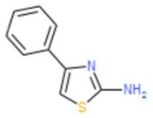	VU0115538
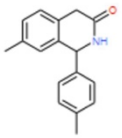	VU0419001	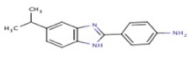	VU0085576	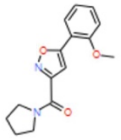	VU0142284
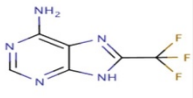	VU0421481	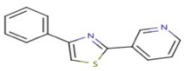	VU0296399	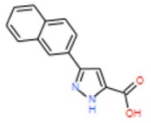	VU0151829
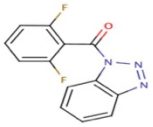	VU0410618	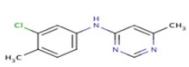	VU0411264	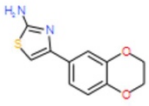	VU0242371
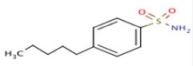	VU0406064	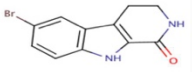	VU0415857	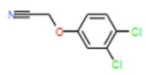	VU0407656
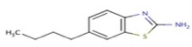	VU0044466	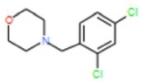	VU0018847	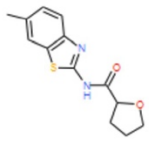	VU0410630
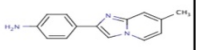	VU0430352	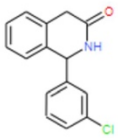	VU0031248	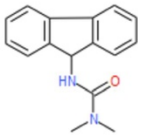	VU0410699
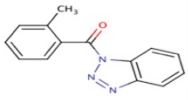	VU0433366	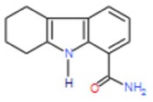	VU0032911	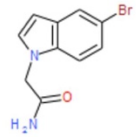	VU0410810
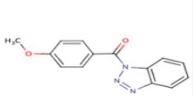	VU0054263	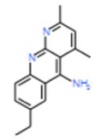	VU0050445	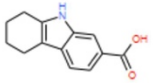	VU0411235
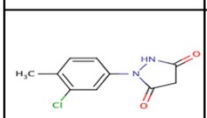	VU0415963	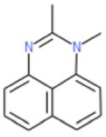	VU0099944	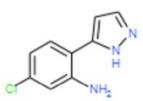	VU0412420

Structure	VU Number	Structure	VU Number	Structure	VU Number
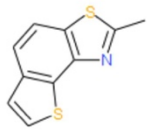	VU0416223	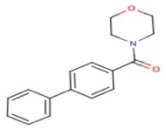	VU0052694	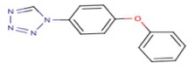	VU0017602
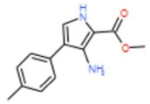	VU0416394	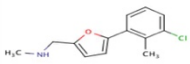	VU0411292	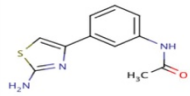	VU0330676
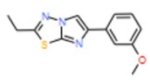	VU0416826	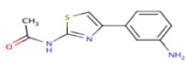	VU0408014	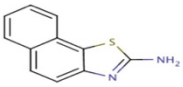	VU0416106
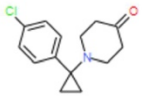	VU0432703	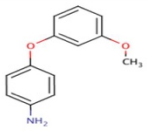	VU0184562	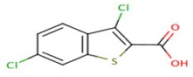	VU0022894
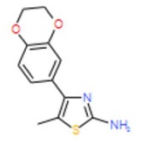	VU0433130	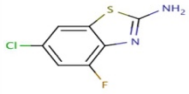	VU0408731	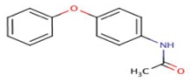	VU0344569
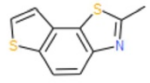	VU0433437	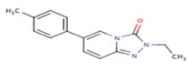	VU0419272	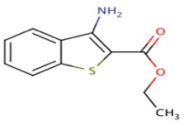	VU0421311
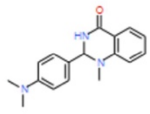	VU0446911	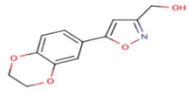	VU0421506	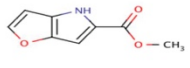	VU0433172
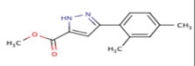	VU0411474	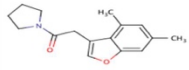	VU0410970	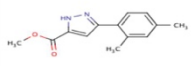	VU0411474
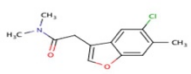	VU0411003	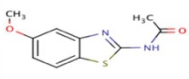	VU0225128	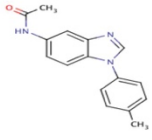	VU0301616
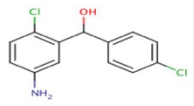	VU0412026	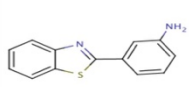	VU0169790	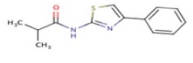	VU0410646

Structure	VU Number	Structure	VU Number	Structure	VU Number
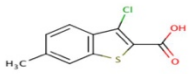	VU0432613	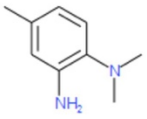	VU0408818	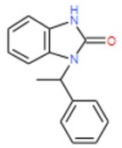	VU0421237
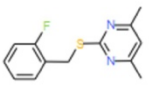	VU0021614	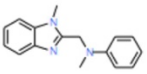	VU0411055	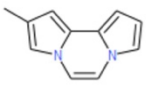	VU0430493
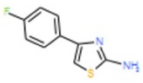	VU0031174	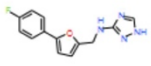	VU0411606	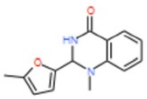	VU0430526
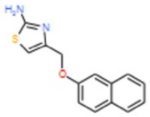	VU0175890	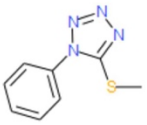	VU0412562	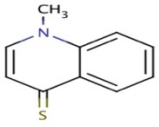	VU0289048
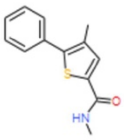	VU0179427	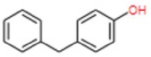	VU0413525	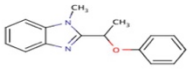	VU0413065
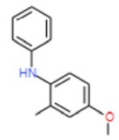	VU0186739	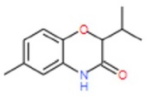	VU0416666	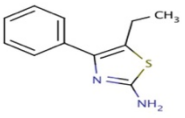	VU0258138
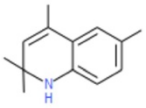	VU0222527	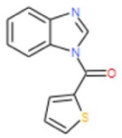	VU0416727	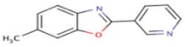	VU0086015
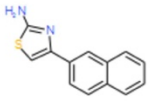	VU0291960	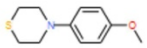	VU0417538	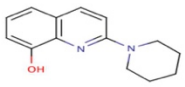	VU0006896
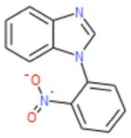	VU0310710	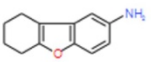	VU0417577	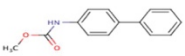	VU0410858
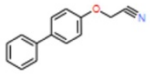	VU0406820	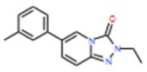	VU0419265	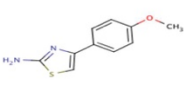	VU0102880

Structure	VU Number	Structure	VU Number	Structure	VU Number
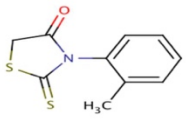	VU0406621	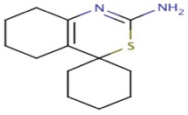	VU0034125	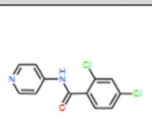	VU0000379
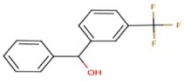	VU0412444	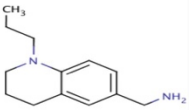	VU0213213	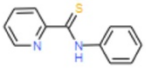	VU0005141
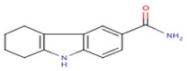	VU0032915	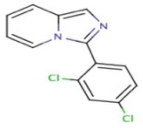	VU0310233	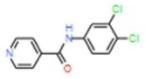	VU0010145
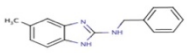	VU0232108	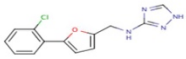	VU0411550	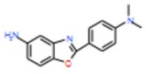	VU0017880
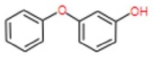	VU0052067	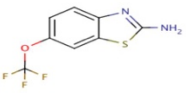	VU0239571	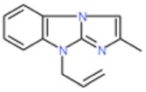	VU0024421
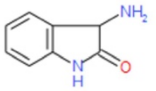	VU0071933	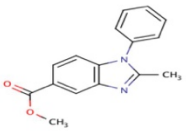	VU0412461	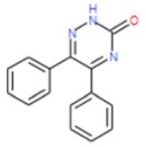	VU0037335
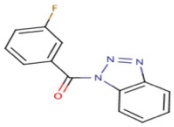	VU0040405	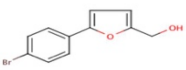	VU0034407	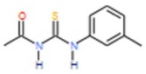	VU0037678
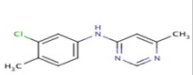	VU0411264	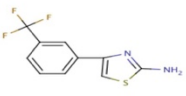	VU0071536	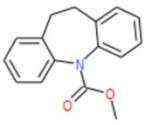	VU0042704
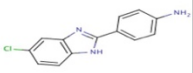	VU0433080	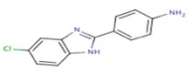	VU0433080	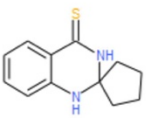	VU0071036
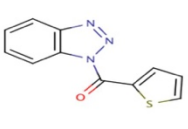	VU0129988	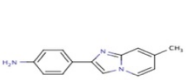	VU0430352	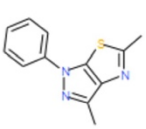	VU0086617

Structure	VU Number	Structure	VU Number	Structure	VU Number
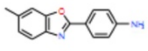	VU0089810	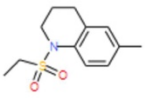	VU0407976	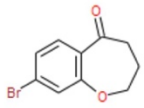	VU0430534
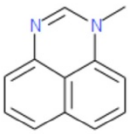	VU0128696	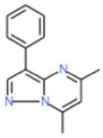	VU0410655	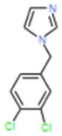	VU0432780
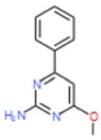	VU0155840	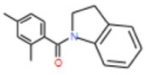	VU0410817	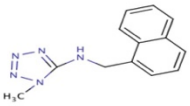	VU0432867
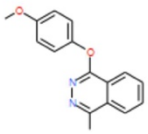	VU0160554	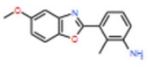	VU0411035	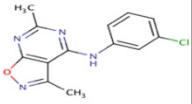	VU0417145
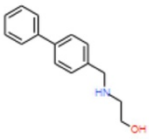	VU0255452	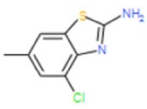	VU0412175	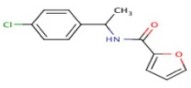	VU0040895
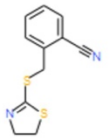	VU0296371	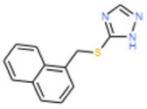	VU0412726	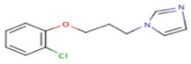	VU0410573
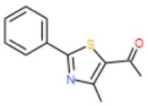	VU0326971	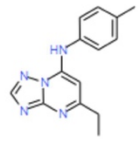	VU0416514	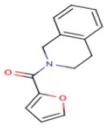	VU0406644
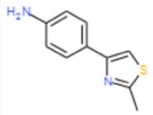	VU0406023	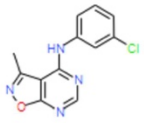	VU0417109	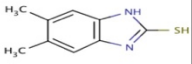	VU0088512
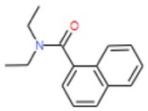	VU0407132	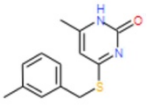	VU0421793	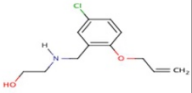	VU0412975
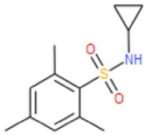	VU0407194	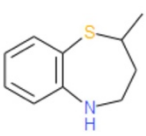	VU0430215	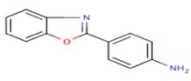	VU0009224

Structure	VU Number	Structure	VU Number	Structure	VU Number
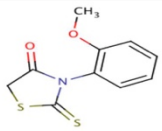	VU0406420	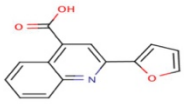	VU0024103	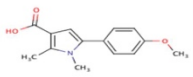	VU0411581
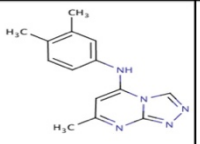	VU0416769	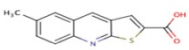	VU0003646	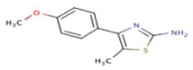	VU0015038
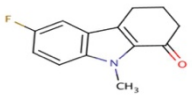	VU0059476	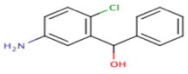	VU0408552	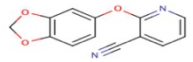	VU0411127
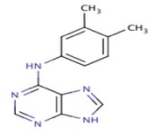	VU0421116	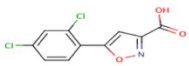	VU0412981	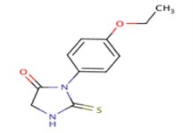	VU0065442
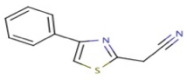	VU0406199	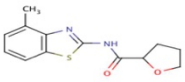	VU0410868	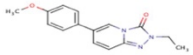	VU0419267
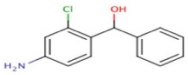	VU0408616	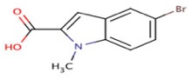	VU0411855	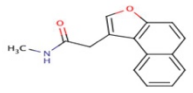	VU0407422
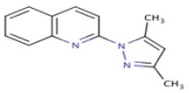	VU0006920	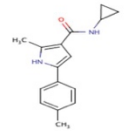	VU0417447	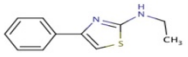	VU0416501
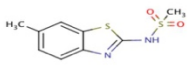	VU0304280	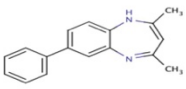	VU0424377	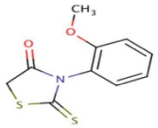	VU0406420
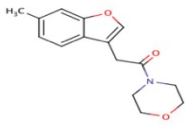	VU0325294	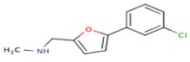	VU0411360	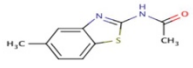	VU0408479
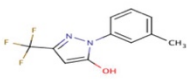	VU0411815	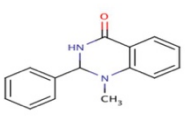	VU0430440	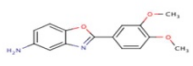	VU0091745

Structure	VU Number	Structure	VU Number	Structure	VU Number
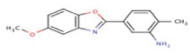	VU0153834	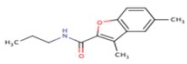	VU0411769	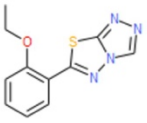	VU0411029
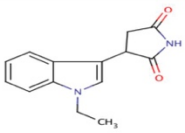	VU0416761	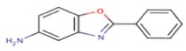	VU0406590	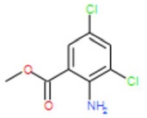	VU0411317
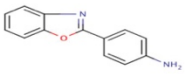	VU0009224	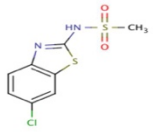	VU0412546	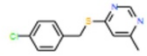	VU0411346
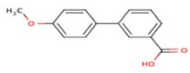	VU0043149	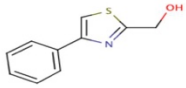	VU0006441	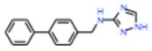	VU0411544
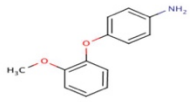	VU0406959	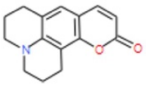	VU0026306	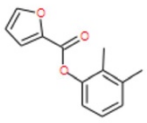	VU0412577
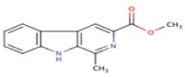	VU0104591	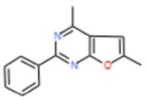	VU0029840	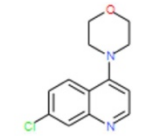	VU0412942
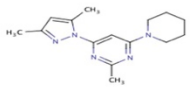	VU0014874	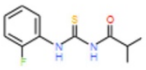	VU0198503	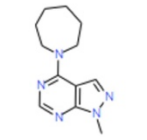	VU0417351
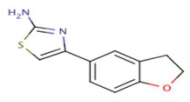	VU0298700	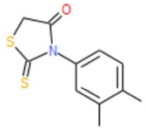	VU0303673	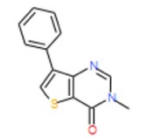	VU0417425
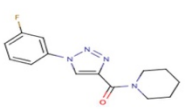	VU0417675	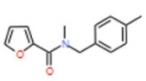	VU0408805	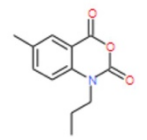	VU0421391
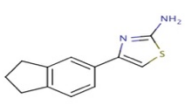	VU0432758	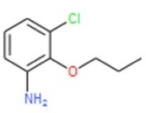	VU0408814	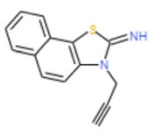	VU0421534

Structure	VU Number	Structure	VU Number	Structure	VU Number
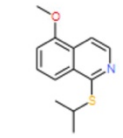	VU0422055	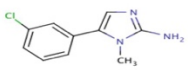	VU0432603	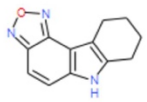	VU0035268
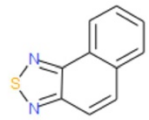	VU0433247	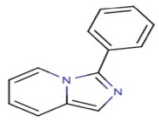	VU0344519	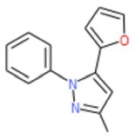	VU0240048
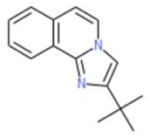	VU0433378	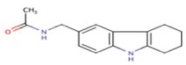	VU0407323	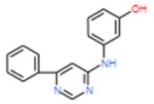	VU0416886
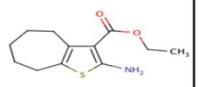	VU0421159	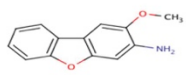	VU0415957	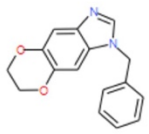	VU0417046
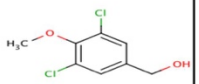	VU0045408	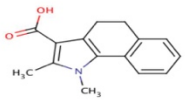	VU0411575	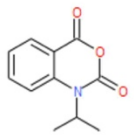	VU0421318
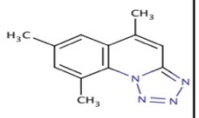	VU0060952	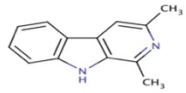	VU0029725	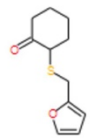	VU0430041
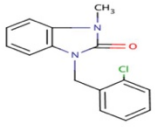	VU0057544	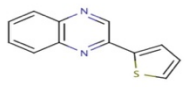	VU0000205	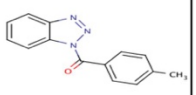	VU0179407
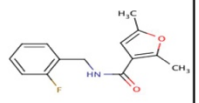	VU0408421	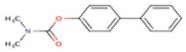	VU0411314	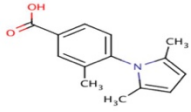	VU0182457
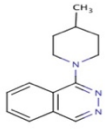	VU0098972	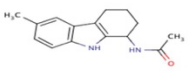	VU0406472	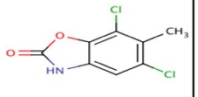	VU0412047
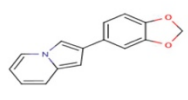	VU0322448	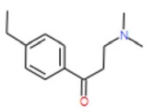	VU0014184	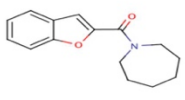	VU0179450

Structure	VU Number
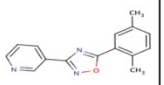	VU0410815
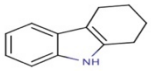	VU0122379
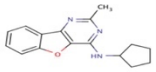	VU0411759
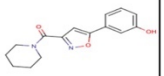	VU0246382

Appendix B: Hit clusters from PD-L1 screen with V-scores and PD-1 displacement scores:

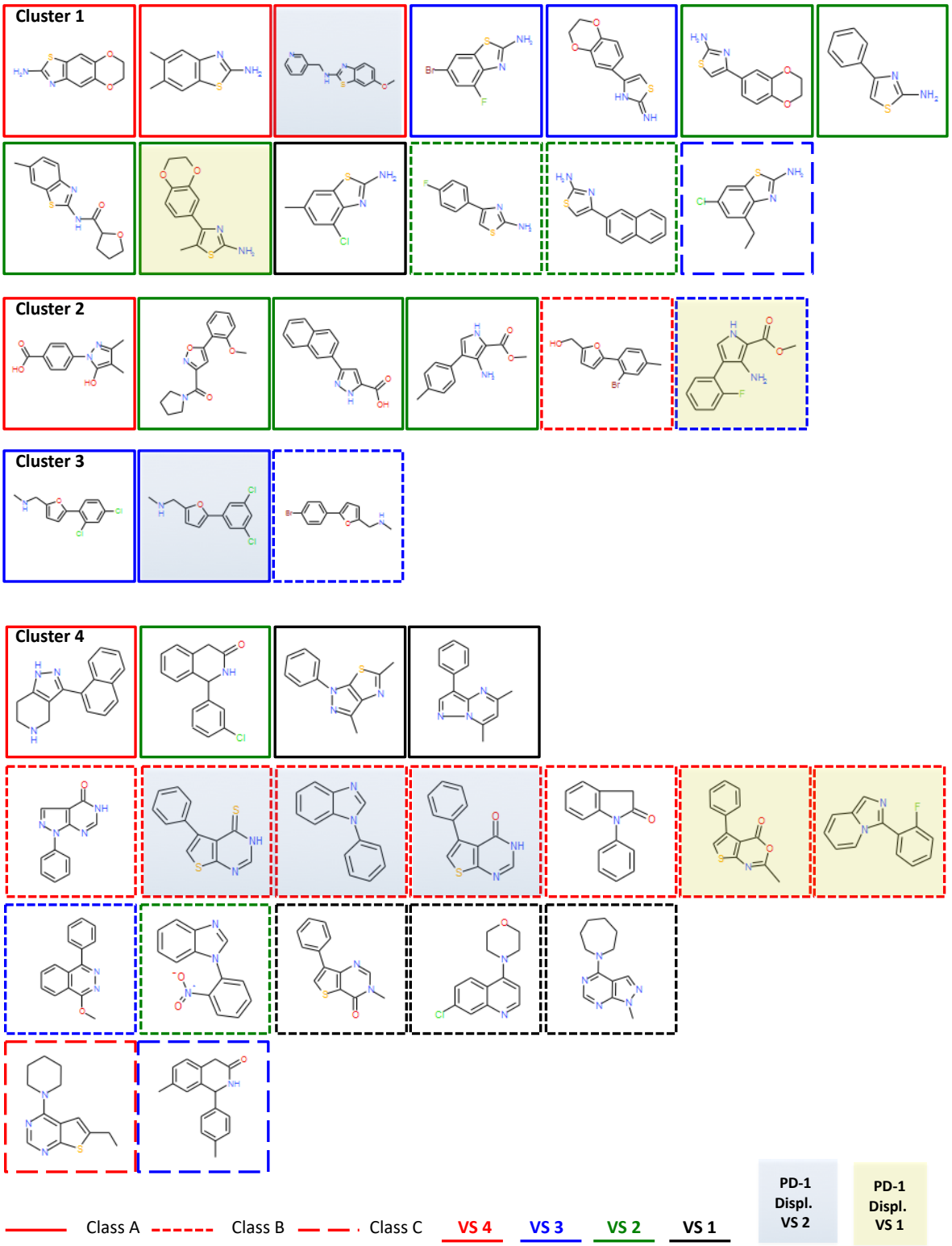

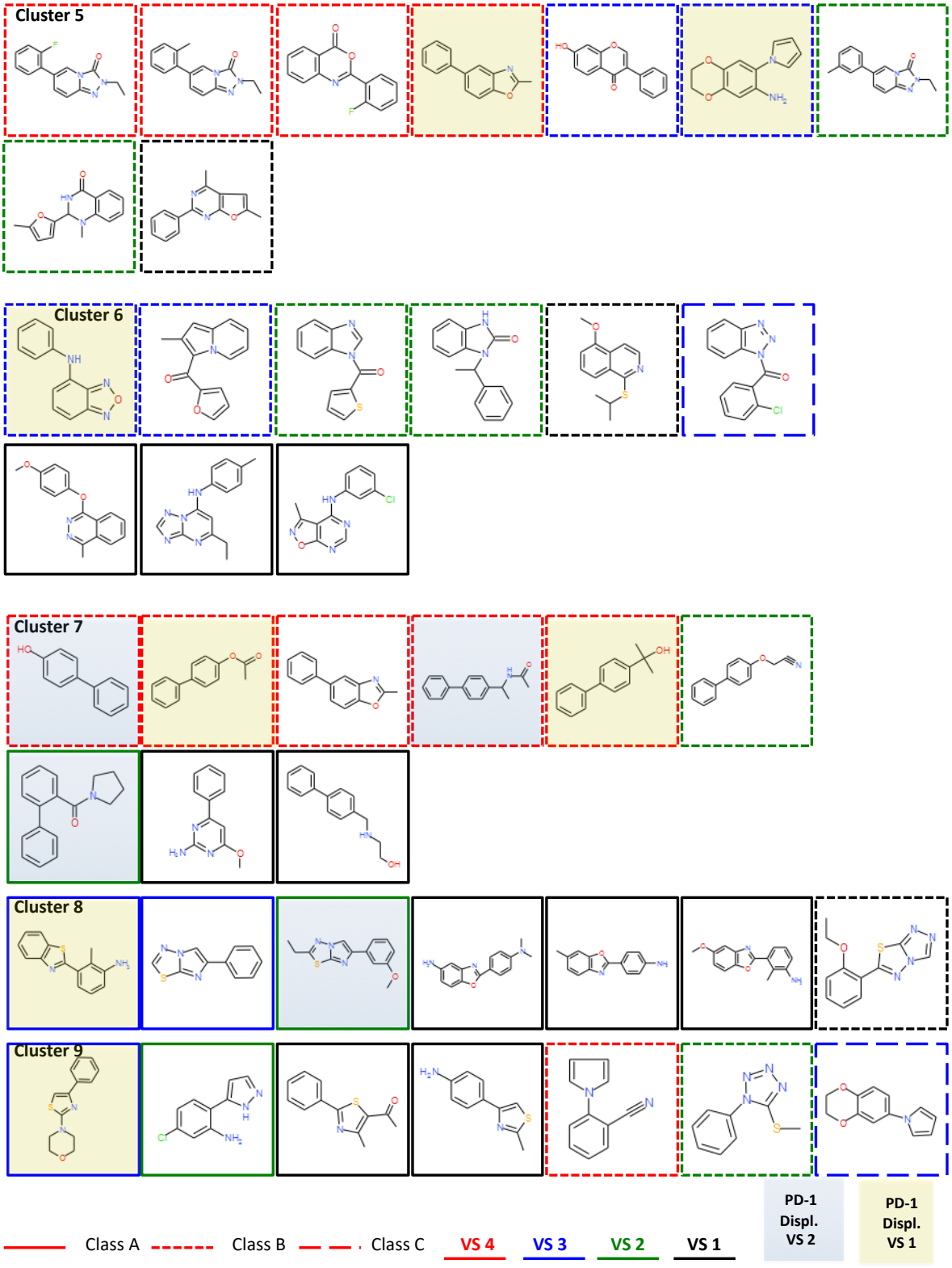
Cluster 5
Cluster 6
Cluster 7
Cluster 8
Cluster 9
Class A
Class B
Class C
VS 4
VS 3
VS 2
VS 1
PD-1 Displ. VS 2
PD-1 Displ. VS 1

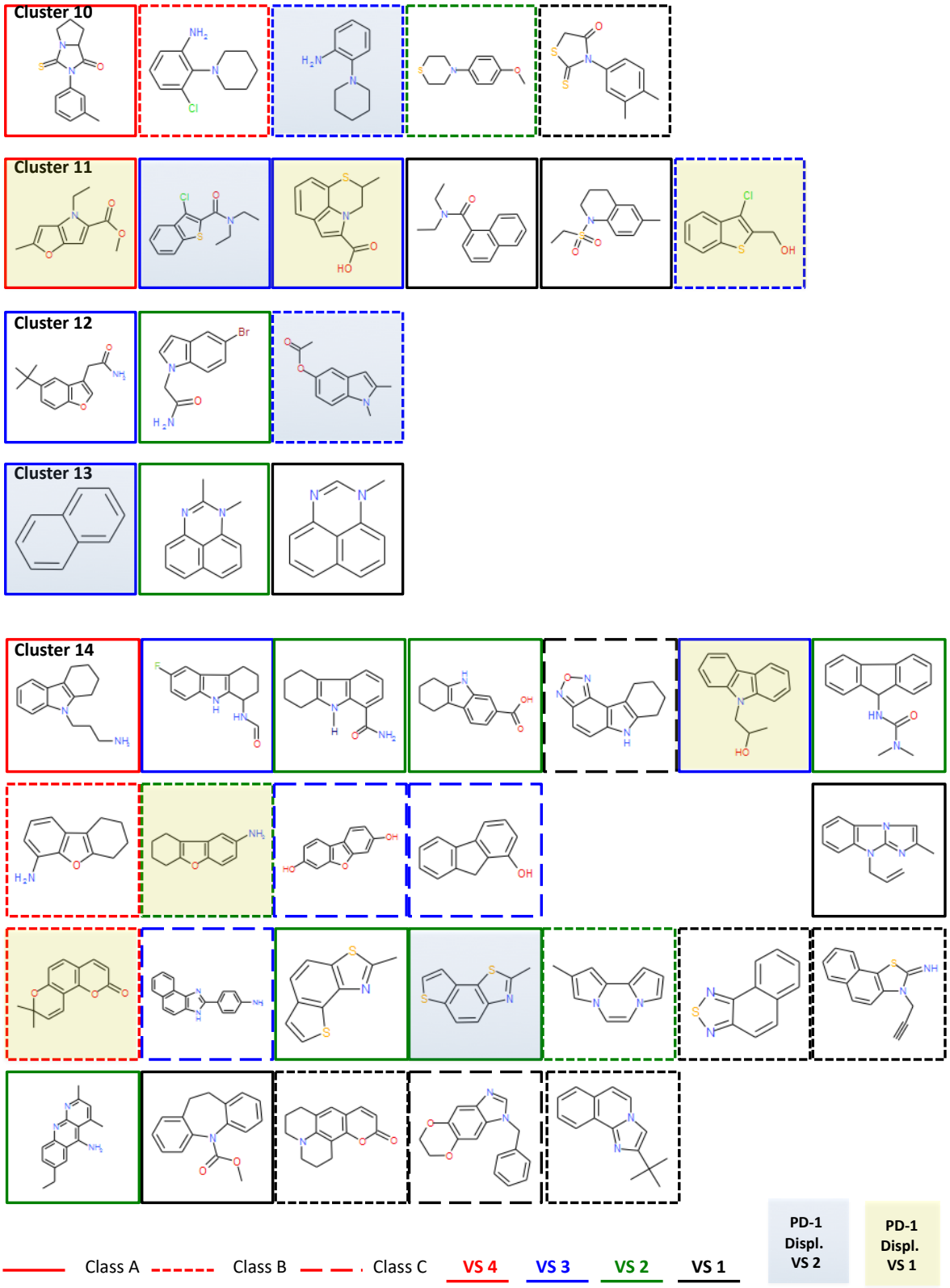
Cluster 10
Cluster 11
Cluster 12
Cluster 13
Cluster 14
Class A
Class B
Class C
VS 4
VS 3
VS 2
VS 1
PD-1 Displ. VS 2
PD-1 Displ. VS 1

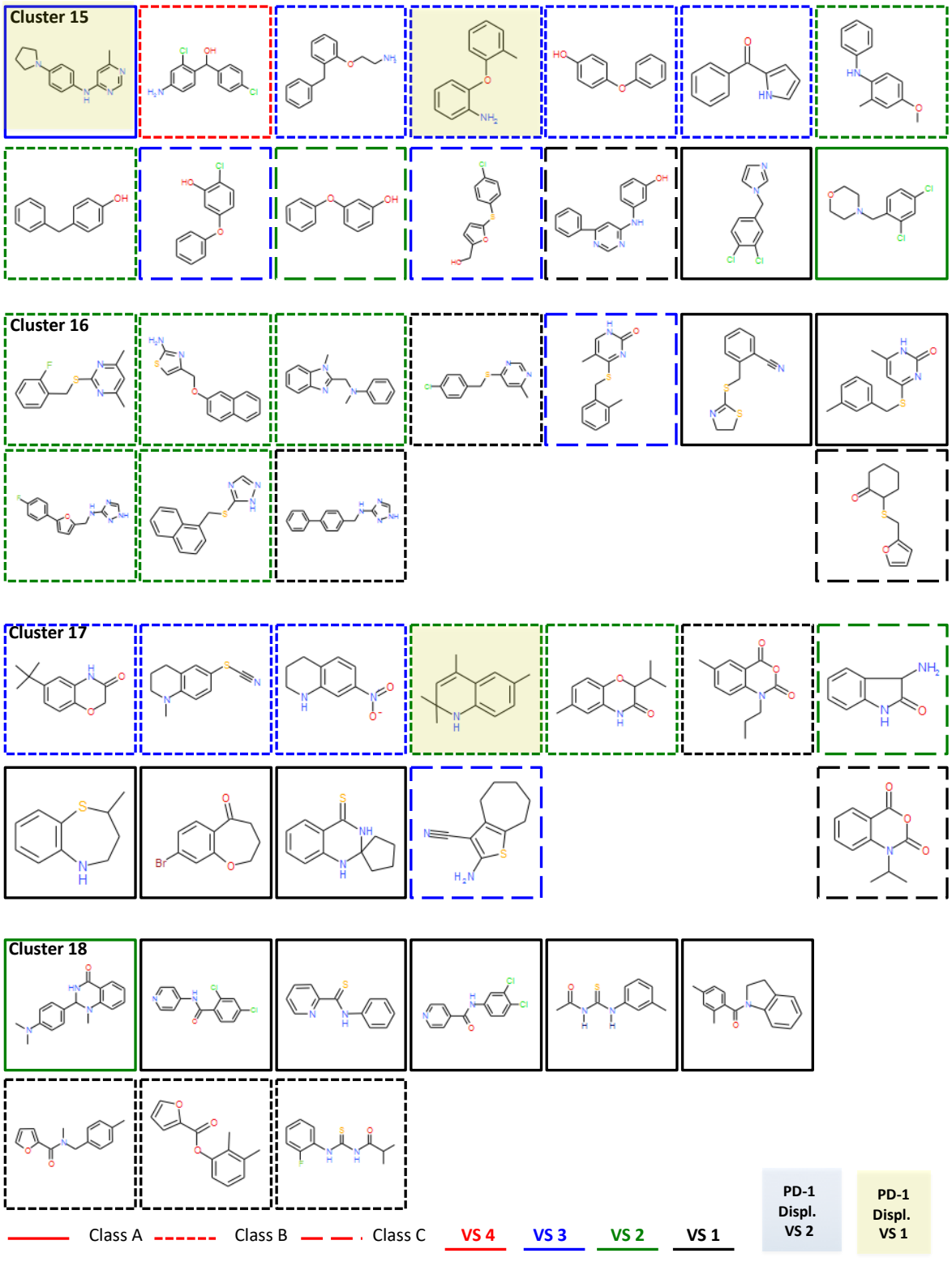
Cluster 15
Cluster 16
Cluster 17
Cluster 18
Class A
Class B
Class C
VS 4
VS 3
VS 2
VS 1
PD-1 Displ. VS 2
PD-1 Displ. VS 1

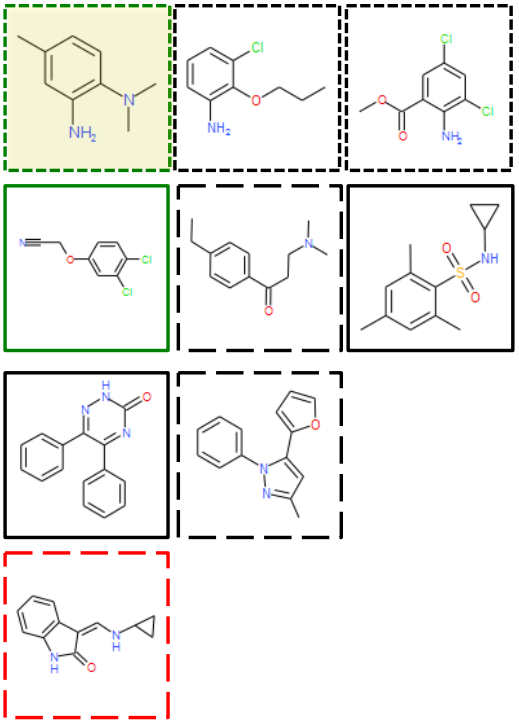

Class A Class B Class C VS 4 VS 3 VS 2 VS 1 PD-1 Displ. VS 2 PD-1 Displ. VS 1

BIBLIOGRAPHY

[1] Siegel, R. L., Miller, K. D., and Jemal, A. (2017) Cancer Statistics, 2017, *CA Cancer J Clin 67*, 7-30.

[2] AACR Cancer Progress Report 2017.

[3] Hanahan, D., and Weinberg, R. A. (2011) Hallmarks of cancer: the next generation, *Cell 144*, 646-674.

[4] Ashley, E. A. (2015) The precision medicine initiative: a new national effort, *JAMA 313*, 2119-2120.

[5] Mardis, E. R., and Wilson, R. K. (2009) Cancer genome sequencing: a review, *Hum Mol Genet 18*, R163-168.

[6] Baudino, T. A. (2015) Targeted Cancer Therapy: The Next Generation of Cancer Treatment, *Curr Drug Discov Technol 12*, 3-20.

[7] Fisher, R., Pusztai, L., and Swanton, C. (2013) Cancer heterogeneity: implications for targeted therapeutics, *Br J Cancer 108*, 479-485.

[8] Ramos, P., and Bentires-Alj, M. (2015) Mechanism-based cancer therapy: resistance to therapy, therapy for resistance, *Oncogene 34*, 3617-3626.

[9] Redmond, K. L., Papafili, A., Lawler, M., and Van Schaeybroeck, S. (2015) Overcoming Resistance to Targeted Therapies in Cancer, *Semin Oncol 42*, 896-908.

[10] Sharma, P., and Allison, J. P. (2015) Immune checkpoint targeting in cancer therapy: toward combination strategies with curative potential, *Cell 161*, 205-214.

[11] Pardoll, D. M. (2012) The blockade of immune checkpoints in cancer immunotherapy, *Nat Rev Cancer 12*, 252-264.

[12] Shankaran, V., Ikeda, H., Bruce, A. T., White, J. M., Swanson, P. E., Old, L. J., and Schreiber, R. D. (2001) IFNgamma and lymphocytes prevent primary tumour development and shape tumour immunogenicity, *Nature 410*, 1107-1111.

[13] Decker, W. K., da Silva, R. F., Sanabria, M. H., Angelo, L. S., Guimarães, F., Burt, B. M., Kheradmand, F., and Paust, S. (2017) Cancer Immunotherapy: Historical Perspective of a Clinical Revolution and Emerging Preclinical Animal Models, *Front Immunol 8*, 829.

[14] Mellman, I., Coukos, G., and Dranoff, G. (2011) Cancer immunotherapy comes of age, *Nature 480*, 480-489.

[15] Ceeraz, S., Nowak, E. C., Burns, C. M., and Noelle, R. J. (2014) Immune checkpoint receptors in regulating immune reactivity in rheumatic disease, *Arthritis Res Ther 16*, 469.

[16] Leach, D. R., Krummel, M. F., and Allison, J. P. (1996) Enhancement of antitumor immunity by CTLA-4 blockade, *Science 271*, 1734-1736.

[17] Ribas, A., and Wolchok, J. D. (2018) Cancer immunotherapy using checkpoint blockade, *Science 359*, 1350-1355.

[18] Gong, J., Chehrazi-Raffle, A., Reddi, S., and Salgia, R. (2018) Development of PD-1 and PD-L1 inhibitors as a form of cancer immunotherapy: a comprehensive review of registration trials and future considerations, *J Immunother Cancer 6*, 8.

[19] Couzin-Frankel, J. (2013) Breakthrough of the year 2013. Cancer immunotherapy, *Science 342*, 1432-1433.

[20] Lohmueller, J., and Finn, O. J. (2017) Current modalities in cancer immunotherapy: Immunomodulatory antibodies, CARs and vaccines, *Pharmacol Ther 178*, 31-47.

[21] Huehls, A. M., Coupet, T. A., and Sentman, C. L. (2015) Bispecific T-cell engagers for cancer immunotherapy, *Immunol Cell Biol 93*, 290-296.

[22] Guo, C., Manjili, M. H., Subjeck, J. R., Sarkar, D., Fisher, P. B., and Wang, X. Y. (2013) Therapeutic cancer vaccines: past, present, and future, *Adv Cancer Res 119*, 421-475.

[23] Smyth, M. J. (2017) Multiple approaches to immunotherapy - the new pillar of cancer treatment, *Immunol Cell Biol 95*, 323-324.
[24] Smith-Garvin, J. E., Koretzky, G. A., and Jordan, M. S. (2009) T cell activation, *Annu Rev Immunol 27*, 591-619.
[25] Brodsky, F. M., and Guagliardi, L. E. (1991) The cell biology of antigen processing and presentation, *Annu Rev Immunol 9*, 707-744.
[26] Bretscher, P. A. (1999) A two-step, two-signal model for the primary activation of precursor helper T cells, *Proc Natl Acad Sci U S A 96*, 185-190.
[27] Krummel, M. F., and Allison, J. P. (1995) CD28 and CTLA-4 have opposing effects on the response of T cells to stimulation, *J Exp Med 182*, 459-465.
[28] Tivol, E. A., Borriello, F., Schweitzer, A. N., Lynch, W. P., Bluestone, J. A., and Sharpe, A. H. (1995) Loss of CTLA-4 leads to massive lymphoproliferation and fatal multiorgan tissue destruction, revealing a critical negative regulatory role of CTLA-4, *Immunity 3*, 541-547.
[29] Egen, J. G., Kuhns, M. S., and Allison, J. P. (2002) CTLA-4: new insights into its biological function and use in tumor immunotherapy, *Nat Immunol 3*, 611-618.
[30] Egen, J. G., and Allison, J. P. (2002) Cytotoxic T lymphocyte antigen-4 accumulation in the immunological synapse is regulated by TCR signal strength, *Immunity 16*, 23-35.
[31] Buchbinder, E. I., and Desai, A. (2016) CTLA-4 and PD-1 Pathways: Similarities, Differences, and Implications of Their Inhibition, *Am J Clin Oncol 39*, 98-106.
[32] Collins, A. V., Brodie, D. W., Gilbert, R. J., Iaboni, A., Manso-Sancho, R., Walse, B., Stuart, D. I., van der Merwe, P. A., and Davis, S. J. (2002) The interaction properties of costimulatory molecules revisited, *Immunity 17*, 201-210.
[33] Thompson, C. B., and Allison, J. P. (1997) The emerging role of CTLA-4 as an immune attenuator, *Immunity 7*, 445-450.
[34] Walker, L. S., and Sansom, D. M. (2011) The emerging role of CTLA4 as a cell-extrinsic regulator of T cell responses, *Nat Rev Immunol 11*, 852-863.
[35] Takahashi, T., Tagami, T., Yamazaki, S., Uede, T., Shimizu, J., Sakaguchi, N., Mak, T. W., and Sakaguchi, S. (2000) Immunologic self-tolerance maintained by CD25(+)CD4(+) regulatory T cells constitutively expressing cytotoxic T lymphocyte-associated antigen 4, *J Exp Med 192*, 303-310.
[36] Qureshi, O. S., Zheng, Y., Nakamura, K., Attridge, K., Manzotti, C., Schmidt, E. M., Baker, J., Jeffery, L. E., Kaur, S., Briggs, Z., Hou, T. Z., Futter, C. E., Anderson, G., Walker, L. S., and Sansom, D. M. (2011) Trans-endocytosis of CD80 and CD86: a molecular basis for the cell-extrinsic function of CTLA-4, *Science 332*, 600-603.
[37] Hodi, F. S., O'Day, S. J., McDermott, D. F., Weber, R. W., Sosman, J. A., Haanen, J. B., Gonzalez, R., Robert, C., Schadendorf, D., Hassel, J. C., Akerley, W., van den Eertwegh, A. J., Lutzky, J., Lorigan, P., Vaubel, J. M., Linette, G. P., Hogg, D., Ottensmeier, C. H., Lebbé, C., Peschel, C., Quirt, I., Clark, J. I., Wolchok, J. D., Weber, J. S., Tian, J., Yellin, M. J., Nichol, G. M., Hoos, A., and Urba, W. J. (2010) Improved survival with ipilimumab in patients with metastatic melanoma, *N Engl J Med 363*, 711-723.
[38] Robert, C., and Mateus, C. (2011) [Anti-CTLA-4 monoclonal antibody: a major step in the treatment of metastatic melanoma], *Med Sci (Paris) 27*, 850-858.
[39] Maio, M., Di Giacomo, A. M., Robert, C., and Eggermont, A. M. (2013) Update on the role of ipilimumab in melanoma and first data on new combination therapies, *Curr Opin Oncol 25*, 166-172.

[40] Schadendorf, D., Hodi, F. S., Robert, C., Weber, J. S., Margolin, K., Hamid, O., Patt, D., Chen, T. T., Berman, D. M., and Wolchok, J. D. (2015) Pooled Analysis of Long-Term Survival Data From Phase II and Phase III Trials of Ipilimumab in Unresectable or Metastatic Melanoma, *J Clin Oncol 33*, 1889-1894.

[41] Mansh, M. (2011) Ipilimumab and cancer immunotherapy: a new hope for advanced stage melanoma, *Yale J Biol Med 84*, 381-389.

[42] Yang, J. C., Hughes, M., Kammula, U., Royal, R., Sherry, R. M., Topalian, S. L., Suri, K. B., Levy, C., Allen, T., Mavroukakis, S., Lowy, I., White, D. E., and Rosenberg, S. A. (2007) Ipilimumab (anti-CTLA4 antibody) causes regression of metastatic renal cell cancer associated with enteritis and hypophysitis, *J Immunother 30*, 825-830.

[43] Carthon, B. C., Wolchok, J. D., Yuan, J., Kamat, A., Ng Tang, D. S., Sun, J., Ku, G., Troncoso, P., Logothetis, C. J., Allison, J. P., and Sharma, P. (2010) Preoperative CTLA-4 blockade: tolerability and immune monitoring in the setting of a presurgical clinical trial, *Clin Cancer Res 16*, 2861-2871.

[44] van den Eertwegh, A. J., Versluis, J., van den Berg, H. P., Santegoets, S. J., van Moorselaar, R. J., van der Sluis, T. M., Gall, H. E., Harding, T. C., Jooss, K., Lowy, I., Pinedo, H. M., Scheper, R. J., Stam, A. G., von Blomberg, B. M., de Gruijl, T. D., Hege, K., Sacks, N., and Gerritsen, W. R. (2012) Combined immunotherapy with granulocyte-macrophage colony-stimulating factor-transduced allogeneic prostate cancer cells and ipilimumab in patients with metastatic castration-resistant prostate cancer: a phase 1 dose-escalation trial, *Lancet Oncol 13*, 509-517.

[45] Dong, H., Zhu, G., Tamada, K., and Chen, L. (1999) B7-H1, a third member of the B7 family, co-stimulates T-cell proliferation and interleukin-10 secretion, *Nat Med 5*, 1365-1369.

[46] Freeman, G. J., Long, A. J., Iwai, Y., Bourque, K., Chernova, T., Nishimura, H., Fitz, L. J., Malenkovich, N., Okazaki, T., Byrne, M. C., Horton, H. F., Fouser, L., Carter, L., Ling, V., Bowman, M. R., Carreno, B. M., Collins, M., Wood, C. R., and Honjo, T. (2000) Engagement of the PD-1 immunoinhibitory receptor by a novel B7 family member leads to negative regulation of lymphocyte activation, *J Exp Med 192*, 1027-1034.

[47] Latchman, Y., Wood, C. R., Chernova, T., Chaudhary, D., Borde, M., Chernova, I., Iwai, Y., Long, A. J., Brown, J. A., Nunes, R., Greenfield, E. A., Bourque, K., Boussiotis, V. A., Carter, L. L., Carreno, B. M., Malenkovich, N., Nishimura, H., Okazaki, T., Honjo, T., Sharpe, A. H., and Freeman, G. J. (2001) PD-L2 is a second ligand for PD-1 and inhibits T cell activation, *Nat Immunol 2*, 261-268.

[48] Keir, M. E., Butte, M. J., Freeman, G. J., and Sharpe, A. H. (2008) PD-1 and its ligands in tolerance and immunity, *Annu Rev Immunol 26*, 677-704.

[49] Tarrio, M. L., Grabie, N., Bu, D. X., Sharpe, A. H., and Lichtman, A. H. (2012) PD-1 protects against inflammation and myocyte damage in T cell-mediated myocarditis, *J Immunol 188*, 4876-4884.

[50] Mandai, M., Hamanishi, J., Abiko, K., Matsumura, N., Baba, T., and Konishi, I. (2016) Dual Faces of IFNγ in Cancer Progression: A Role of PD-L1 Induction in the Determination of Pro- and Antitumor Immunity, *Clin Cancer Res 22*, 2329-2334.

[51] Arasanz, H., Gato-Canas, M., Zuazo, M., Ibanez-Vea, M., Breckpot, K., Kochan, G., and Escors, D. (2017) PD1 signal transduction pathways in T cells, *Oncotarget*.

[52] Mahoney, K. M., Rennert, P. D., and Freeman, G. J. (2015) Combination cancer immunotherapy and new immunomodulatory targets, *Nat Rev Drug Discov 14*,

561-584.
[53] Sharpe, A. H., and Pauken, K. E. (2018) The diverse functions of the PD1 inhibitory pathway, *Nat Rev Immunol 18*, 153-167.
[54] Frebel, H., Nindl, V., Schuepbach, R. A., Braunschweiler, T., Richter, K., Vogel, J., Wagner, C. A., Loffing-Cueni, D., Kurrer, M., Ludewig, B., and Oxenius, A. (2012) Programmed death 1 protects from fatal circulatory failure during systemic virus infection of mice, *J Exp Med 209*, 2485-2499.
[55] Francisco, L. M., Sage, P. T., and Sharpe, A. H. (2010) The PD-1 pathway in tolerance and autoimmunity, *Immunol Rev 236*, 219-242.
[56] Topalian, S. L., Drake, C. G., and Pardoll, D. M. (2015) Immune checkpoint blockade: a common denominator approach to cancer therapy, *Cancer Cell 27*, 450-461.
[57] Casey, S. C., Tong, L., Li, Y., Do, R., Walz, S., Fitzgerald, K. N., Gouw, A. M., Baylot, V., Gütgemann, I., Eilers, M., and Felsher, D. W. (2016) MYC regulates the antitumor immune response through CD47 and PD-L1, *Science 352*, 227-231.
[58] Azuma, K., Ota, K., Kawahara, A., Hattori, S., Iwama, E., Harada, T., Matsumoto, K., Takayama, K., Takamori, S., Kage, M., Hoshino, T., Nakanishi, Y., and Okamoto, I. (2014) Association of PD-L1 overexpression with activating EGFR mutations in surgically resected nonsmall-cell lung cancer, *Ann Oncol 25*, 1935-1940.
[59] Wang, Q., Liu, F., and Liu, L. (2017) Prognostic significance of PD-L1 in solid tumor: An updated meta-analysis, *Medicine (Baltimore) 96*, e6369.
[60] Zhang, M., Li, G., Wang, Y., Zhao, S., Haihong, P., and Zhao, H. (2017) PD-L1 expression in lung cancer and its correlation with driver mutations: a meta-analysis, *Sci Rep 7*, 10255.
[61] Sabatier, R., Finetti, P., Mamessier, E., Adelaide, J., Chaffanet, M., Ali, H. R., Viens, P., Caldas, C., Birnbaum, D., and Bertucci, F. (2015) Prognostic and predictive value of PDL1 expression in breast cancer, *Oncotarget 6*, 5449-5464.
[62] Emens, L. A., Ascierto, P. A., Darcy, P. K., Demaria, S., Eggermont, A. M. M., Redmond, W. L., Seliger, B., and Marincola, F. M. (2017) Cancer immunotherapy: Opportunities and challenges in the rapidly evolving clinical landscape, *Eur J Cancer 81*, 116-129.
[63] Maleki Vareki, S., Garrigós, C., and Duran, I. (2017) Biomarkers of response to PD-1/PD-L1 inhibition, *Crit Rev Oncol Hematol 116*, 116-124.
[64] Lim, S. H., Sun, J. M., Lee, S. H., Ahn, J. S., Park, K., and Ahn, M. J. (2016) Pembrolizumab for the treatment of non-small cell lung cancer, *Expert Opin Biol Ther 16*, 397-406.
[65] Rizvi, N. A., Hellmann, M. D., Snyder, A., Kvistborg, P., Makarov, V., Havel, J. J., Lee, W., Yuan, J., Wong, P., Ho, T. S., Miller, M. L., Rekhtman, N., Moreira, A. L., Ibrahim, F., Bruggeman, C., Gasmi, B., Zappasodi, R., Maeda, Y., Sander, C., Garon, E. B., Merghoub, T., Wolchok, J. D., Schumacher, T. N., and Chan, T. A. (2015) Cancer immunology. Mutational landscape determines sensitivity to PD-1 blockade in non-small cell lung cancer, *Science 348*, 124-128.
[66] Van Allen, E. M., Miao, D., Schilling, B., Shukla, S. A., Blank, C., Zimmer, L., Sucker, A., Hillen, U., Foppen, M. H. G., Goldinger, S. M., Utikal, J., Hassel, J. C., Weide, B., Kaehler, K. C., Loquai, C., Mohr, P., Gutzmer, R., Dummer, R., Gabriel, S., Wu, C. J., Schadendorf, D., and Garraway, L. A. (2015) Genomic correlates of response to CTLA-4 blockade in metastatic melanoma, *Science 350*, 207-211.
[67] Chen, P. L., Roh, W., Reuben, A., Cooper, Z. A., Spencer, C. N., Prieto, P. A., Miller,

J. P., Bassett, R. L., Gopalakrishnan, V., Wani, K., De Macedo, M. P., Austin-Breneman, J. L., Jiang, H., Chang, Q., Reddy, S. M., Chen, W. S., Tetzlaff, M. T., Broaddus, R. J., Davies, M. A., Gershenwald, J. E., Haydu, L., Lazar, A. J., Patel, S. P., Hwu, P., Hwu, W. J., Diab, A., Glitza, I. C., Woodman, S. E., Vence, L. M., Wistuba, I. I., Amaria, R. N., Kwong, L. N., Prieto, V., Davis, R. E., Ma, W., Overwijk, W. W., Sharpe, A. H., Hu, J., Futreal, P. A., Blando, J., Sharma, P., Allison, J. P., Chin, L., and Wargo, J. A. (2016) Analysis of Immune Signatures in Longitudinal Tumor Samples Yields Insight into Biomarkers of Response and Mechanisms of Resistance to Immune Checkpoint Blockade, *Cancer Discov 6*, 827-837.

[68] Ott, P. A., Hodi, F. S., Kaufman, H. L., Wigginton, J. M., and Wolchok, J. D. (2017) Combination immunotherapy: a road map, *J Immunother Cancer 5*, 16.

[69] Topalian, S. L., Taube, J. M., Anders, R. A., and Pardoll, D. M. (2016) Mechanism-driven biomarkers to guide immune checkpoint blockade in cancer therapy, *Nat Rev Cancer 16*, 275-287.

[70] Larkin, J., Chiarion-Sileni, V., Gonzalez, R., Grob, J. J., Cowey, C. L., Lao, C. D., Schadendorf, D., Dummer, R., Smylie, M., Rutkowski, P., Ferrucci, P. F., Hill, A., Wagstaff, J., Carlino, M. S., Haanen, J. B., Maio, M., Marquez-Rodas, I., McArthur, G. A., Ascierto, P. A., Long, G. V., Callahan, M. K., Postow, M. A., Grossmann, K., Sznol, M., Dreno, B., Bastholt, L., Yang, A., Rollin, L. M., Horak, C., Hodi, F. S., and Wolchok, J. D. (2015) Combined Nivolumab and Ipilimumab or Monotherapy in Untreated Melanoma, http://dx.doi.org/10.1056/NEJMoa1504030.

[71] Melero, I., Berman, D. M., Aznar, M. A., Korman, A. J., Pérez Gracia, J. L., and Haanen, J. (2015) Evolving synergistic combinations of targeted immunotherapies to combat cancer, *Nat Rev Cancer 15*, 457-472.

[72] Tang, J., Shalabi, A., and Hubbard-Lucey, V. M. (2018) Comprehensive analysis of the clinical immuno-oncology landscape, *Ann Oncol 29*, 84-91.

[73] Popovic, A., Jaffee, E. M., and Zaidi, N. (2018) Emerging strategies for combination checkpoint modulators in cancer immunotherapy, *J Clin Invest 128*, 3209-3218.

[74] Fukushima, S. (2016) A review of adverse events caused by immune checkpoint inhibitors, In *Nihon Rinsho Meneki Gakkai Kaishi* 2016/05/18 ed., pp 30-36.

[75] Alatrash, G., Jakher, H., Stafford, P. D., and Mittendorf, E. A. (2013) Cancer immunotherapies, their safety and toxicity, In *Expert Opin Drug Saf* 2013/05/15 ed., pp 631-645.

[76] Kumar, V., Chaudhary, N., Garg, M., Floudas, C. S., Soni, P., and Chandra, A. B. (2017) Current Diagnosis and Management of Immune Related Adverse Events (irAEs) Induced by Immune Checkpoint Inhibitor Therapy, In *Front Pharmacol* 2017/02/24 ed., p 49.

[77] Day, D., and Hansen, A. R. (2016) Immune-Related Adverse Events Associated with Immune Checkpoint Inhibitors, In *BioDrugs* 2016/11/17 ed., pp 571-584.

[78] Michot, J. M., Bigenwald, C., Champiat, S., Collins, M., Carbonnel, F., Postel-Vinay, S., Berdelou, A., Varga, A., Bahleda, R., Hollebecque, A., Massard, C., Fuerea, A., Ribrag, V., Gazzah, A., Armand, J. P., Amellal, N., Angevin, E., Noel, N., Boutros, C., Mateus, C., Robert, C., Soria, J. C., Marabelle, A., and Lambotte, O. (2016) Immune-related adverse events with immune checkpoint blockade: a comprehensive review, In *Eur J Cancer* 2016/01/15 ed., pp 139-148.

[79] Kroschinsky, F., Stolzel, F., von Bonin, S., Beutel, G., Kochanek, M., Kiehl, M., and Schellongowski, P. (2017) New drugs, new toxicities: severe side effects of modern

targeted and immunotherapy of cancer and their management, In *Crit Care* 2017/04/15 ed., p 89.

[80] Kong, Y. C., and Flynn, J. C. (2014) Opportunistic Autoimmune Disorders Potentiated by Immune-Checkpoint Inhibitors Anti-CTLA-4 and Anti-PD-1, In *Front Immunol* 2014/06/07 ed., p 206.

[81] Naidoo, J., Page, D. B., Li, B. T., Connell, L. C., Schindler, K., Lacouture, M. E., Postow, M. A., and Wolchok, J. D. (2015) Toxicities of the anti-PD-1 and anti-PD-L1 immune checkpoint antibodies, In *Ann Oncol* 2015/09/16 ed., pp 2375-2391.

[82] Haanen, J. B., Thienen, H., and Blank, C. U. (2015) Toxicity patterns with immunomodulating antibodies and their combinations, In *Semin Oncol* 2015/05/13 ed., pp 423-428.

[83] Wolchok, J. D., Kluger, H., Callahan, M. K., Postow, M. A., Rizvi, N. A., Lesokhin, A. M., Segal, N. H., Ariyan, C. E., Gordon, R. A., Reed, K., Burke, M. M., Caldwell, A., Kronenberg, S. A., Agunwamba, B. U., Zhang, X., Lowy, I., Inzunza, H. D., Feely, W., Horak, C. E., Hong, Q., Korman, A. J., Wigginton, J. M., Gupta, A., and Sznol, M. (2013) Nivolumab plus ipilimumab in advanced melanoma, *N Engl J Med 369*, 122-133.

[84] Postow, M. A. (2015) Managing immune checkpoint-blocking antibody side effects, In *Am Soc Clin Oncol Educ Book* 2015/05/21 ed., pp 76-83.

[85] Joseph, R. W., Cappel, M., Goedjen, B., Gordon, M., Kirsch, B., Gilstrap, C., Bagaria, S., and Jambusaria-Pahlajani, A. (2015) Lichenoid Dermatitis in Three Patients with Metastatic Melanoma Treated with Anti–PD-1 Therapy.

[86] El-Khoueiry, A. B., Melero, I., Crocenzi, T. S., Welling, T. H., Yau, T. C., Yeo, W., Chopra, A., Grosso, J., Lang, L., Anderson, J., Cruz, C. M. D., and Sangro, B. (2017) Phase I/II safety and antitumor activity of nivolumab in patients with advanced hepatocellular carcinoma (HCC): CA209-040., *http://dx.doi.org/10.1200/jco.2015.33.18_suppl.lba101*.

[87] Patnaik, A., Kang, S. P., Rasco, D., Papadopoulos, K. P., Elassaiss-Schaap, J., Beeram, M., Drengler, R., Chen, C., Smith, L., Espino, G., Gergich, K., Delgado, L., Daud, A., Lindia, J. A., Li, X. N., Pierce, R. H., Yearley, J. H., Wu, D., Laterza, O., Lehnert, M., Iannone, R., and Tolcher, A. W. (2015) Phase I Study of Pembrolizumab (MK-3475; Anti-PD-1 Monoclonal Antibody) in Patients with Advanced Solid Tumors, *Clin Cancer Res 21*, 4286-4293.

[88] Corsello, S. M., Barnabei, A., Marchetti, P., De Vecchis, L., Salvatori, R., and Torino, F. (2013) Endocrine side effects induced by immune checkpoint inhibitors, *J Clin Endocrinol Metab 98*, 1361-1375.

[89] Nishino, M., Sholl, L. M., Hodi, F. S., Hatabu, H., and Ramaiya, N. H. (2015) Anti-PD-1-Related Pneumonitis during Cancer Immunotherapy, *N Engl J Med 373*, 288-290.

[90] Somasundaram, A., and Burns, T. F. (2017) Pembrolizumab in the treatment of metastatic non-small-cell lung cancer: patient selection and perspectives, In *Lung Cancer (Auckl)*, pp 1-11.

[91] Orlov, S., Salari, F., Kashat, L., and Walfish, P. G. (2015) Induction of painless thyroiditis in patients receiving programmed death 1 receptor immunotherapy for metastatic malignancies, *J Clin Endocrinol Metab 100*, 1738-1741.

[92] Loochtan, A. I., USA, D. U. M. C. D. o. N. D. N. C., Nickolich, M. S., USA, D. U. M. C. D. o. M. D. N. C., Hobson-Webb, L. D., and USA, D. U. M. C. D. o. N. D. N. C. (2017) Myasthenia gravis associated with ipilimumab and nivolumab in the treatment of small cell lung cancer, *Muscle & Nerve 52*, 307-308.

[93] Robert, C., Schachter, J., Long, G. V., Arance, A., Grob, J. J., Mortier, L., Daud, A., Carlino, M. S., McNeil, C., Lotem, M., Larkin, J., Lorigan, P., Neyns, B., Blank, C. U., Hamid, O., Mateus, C., Shapira-Frommer, R., Kosh, M., Zhou, H., Ibrahim, N., Ebbinghaus, S., and Ribas, A. (2015) Pembrolizumab versus Ipilimumab in Advanced Melanoma, In *N Engl J Med* 2015/04/22 ed., pp 2521-2532.

[94] Hamid, O., Robert, C., Daud, A., Hodi, F. S., Hwu, W. J., Kefford, R., Wolchok, J. D., Hersey, P., Joseph, R. W., Weber, J. S., Dronca, R., Gangadhar, T. C., Patnaik, A., Zarour, H., Joshua, A. M., Gergich, K., Elassaiss-Schaap, J., Algazi, A., Mateus, C., Boasberg, P., Tumeh, P. C., Chmielowski, B., Ebbinghaus, S. W., Li, X. N., Kang, S. P., and Ribas, A. (2013) Safety and tumor responses with lambrolizumab (anti-PD-1) in melanoma, *N Engl J Med 369*, 134-144.

[95] Jain, V., Bahia, J., Mohebtash, M., and Barac, A. (2017) Cardiovascular Complications Associated With Novel Cancer Immunotherapies, In *Curr Treat Options Cardiovasc Med* 2017/04/13 ed., p 36.

[96] Wang, D. Y., Okoye, G. D., Neilan, T. G., Johnson, D. B., and Moslehi, J. J. (2017) Cardiovascular Toxicities Associated with Cancer Immunotherapies, *Curr Cardiol Rep 19*, 21.

[97] Ansell, S. M., Lesokhin, A. M., Borrello, I., Halwani, A., Scott, E. C., Gutierrez, M., Schuster, S. J., Millenson, M. M., Cattry, D., Freeman, G. J., Rodig, S. J., Chapuy, B., Ligon, A. H., Zhu, L., Grosso, J. F., Kim, S. Y., Timmerman, J. M., Shipp, M. A., and Armand, P. (2015) PD-1 blockade with nivolumab in relapsed or refractory Hodgkin's lymphoma, *N Engl J Med 372*, 311-319.

[98] Le, D. T., Uram, J. N., Wang, H., Bartlett, B. R., Kemberling, H., Eyring, A. D., Skora, A. D., Luber, B. S., Azad, N. S., Laheru, D., Biedrzycki, B., Donehower, R. C., Zaheer, A., Fisher, G. A., Crocenzi, T. S., Lee, J. J., Duffy, S. M., Goldberg, R. M., de la Chapelle, A., Koshiji, M., Bhaijee, F., Huebner, T., Hruban, R. H., Wood, L. D., Cuka, N., Pardoll, D. M., Papadopoulos, N., Kinzler, K. W., Zhou, S., Cornish, T. C., Taube, J. M., Anders, R. A., Eshleman, J. R., Vogelstein, B., and Diaz, L. A., Jr. (2015) PD-1 Blockade in Tumors with Mismatch-Repair Deficiency, *N Engl J Med 372*, 2509-2520.

[99] Robert, C., Ribas, A., Wolchok, J. D., Hodi, F. S., Hamid, O., Kefford, R., Weber, J. S., Joshua, A. M., Hwu, W. J., Gangadhar, T. C., Patnaik, A., Dronca, R., Zarour, H., Joseph, R. W., Boasberg, P., Chmielowski, B., Mateus, C., Postow, M. A., Gergich, K., Elassaiss-Schaap, J., Li, X. N., Iannone, R., Ebbinghaus, S. W., Kang, S. P., and Daud, A. (2014) Anti-programmed-death-receptor-1 treatment with pembrolizumab in ipilimumab-refractory advanced melanoma: a randomised dose-comparison cohort of a phase 1 trial, *Lancet 384*, 1109-1117.

[100] Topalian, S. L., Hodi, F. S., Brahmer, J. R., Gettinger, S. N., Smith, D. C., McDermott, D. F., Powderly, J. D., Carvajal, R. D., Sosman, J. A., Atkins, M. B., Leming, P. D., Spigel, D. R., Antonia, S. J., Horn, L., Drake, C. G., Pardoll, D. M., Chen, L., Sharfman, W. H., Anders, R. A., Taube, J. M., McMiller, T. L., Xu, H., Korman, A. J., Jure-Kunkel, M., Agrawal, S., McDonald, D., Kollia, G. D., Gupta, A., Wigginton, J. M., and Sznol, M. (2012) Safety, activity, and immune correlates of anti-PD-1 antibody in cancer, *N Engl J Med 366*, 2443-2454.

[101] Heinzerling, L., Ott, P. A., Hodi, F. S., Husain, A. N., Tajmir-Riahi, A., Tawbi, H., Pauschinger, M., Gajewski, T. F., Lipson, E. J., and Luke, J. J. (2016) Cardiotoxicity associated with CTLA4 and PD1 blocking immunotherapy, *J Immunother Cancer 4*.

[102] Gaudy, C., Clévy, C., Monestier, S., Dubois, N., Préau, Y., Mallet, S., Richard, M.-

A., Grob, J.-J., Valéro, R., and Béliard, S. (2015) Anti-PD1 Pembrolizumab Can Induce Exceptional Fulminant Type 1 Diabetes.

[103] Imai, K., and Takaoka, A. (2006) Comparing antibody and small-molecule therapies for cancer, *Nat Rev Cancer 6*, 714-727.

[104] Maute, R. L., Gordon, S. R., Mayer, A. T., McCracken, M. N., Natarajan, A., Ring, N. G., Kimura, R., Tsai, J. M., Manglik, A., Kruse, A. C., Gambhir, S. S., Weissman, I. L., and Ring, A. M. (2015) Engineering high-affinity PD-1 variants for optimized immunotherapy and immuno-PET imaging, *Proc Natl Acad Sci U S A 112*, E6506-6514.

[105] Lee, C. M., and Tannock, I. F. (2010) The distribution of the therapeutic monoclonal antibodies cetuximab and trastuzumab within solid tumors, *BMC Cancer 10*, 255.

[106] Scott, A. M., Wolchok, J. D., and Old, L. J. (2012) Antibody therapy of cancer, *Nat Rev Cancer 12*, 278-287.

[107] Brahmer, J. R., Drake, C. G., Wollner, I., Powderly, J. D., Picus, J., Sharfman, W. H., Stankevich, E., Pons, A., Salay, T. M., McMiller, T. L., Gilson, M. M., Wang, C., Selby, M., Taube, J. M., Anders, R., Chen, L., Korman, A. J., Pardoll, D. M., Lowy, I., and Topalian, S. L. (2010) Phase I study of single-agent anti-programmed death-1 (MDX-1106) in refractory solid tumors: safety, clinical activity, pharmacodynamics, and immunologic correlates, *J Clin Oncol 28*, 3167-3175.

[108] Beasley, D. (2017) The cost of cancer: new drugs show success at a steep price, Reuters.com.

[109] Elvidge, S. (2017) NICE opts not to recommend Opdivo for head and neck cancer, biopharmadive.

[110] Dong, H., Strome, S. E., Salomao, D. R., Tamura, H., Hirano, F., Flies, D. B., Roche, P. C., Lu, J., Zhu, G., Tamada, K., Lennon, V. A., Celis, E., and Chen, L. (2002) Tumor-associated B7-H1 promotes T-cell apoptosis: a potential mechanism of immune evasion, *Nat Med 8*, 793-800.

[111] Zarganes-Tzitzikas, T., Konstantinidou, M., Gao, Y., Krzemien, D., Zak, K., Dubin, G., Holak, T. A., and Domling, A. (2016) Inhibitors of programmed cell death 1 (PD-1): a patent review (2010-2015), *Expert Opin Ther Pat 26*, 973-977.

[112] Zak, K. M., Kitel, R., Przetocka, S., Golik, P., Guzik, K., Musielak, B., Dömling, A., Dubin, G., and Holak, T. A. (2015) Structure of the Complex of Human Programmed Death 1, PD-1, and Its Ligand PD-L1, *Structure 23*, 2341-2348.

[113] Sasikumar, P., Ramachandra, M., and Naremaddepalli, S. (2015) 1,2,4-oxadiazole and 1,3,4-thiadiazole derivatives as immunomodulators.

[114] Sasikumar, P., Ramachandra, M., and SSS, N. (2015) 1,2,4-Oxadiazole Derivatives as Immunomodulators.

Aurigene Discovery Technologies Limited (Limited, A. D. T., Ed.).

[115] Zak, K. M., Grudnik, P., Guzik, K., Zieba, B. J., Musielak, B., Dömling, A., Dubin, G., and Holak, T. A. (2016) Structural basis for small molecule targeting of the programmed death ligand 1 (PD-L1), *Oncotarget 7*, 30323-30335.

[116] Shuker, S. B., Hajduk, P. J., Meadows, R. P., and Fesik, S. W. (1996) Discovering high-affinity ligands for proteins: SAR by NMR, *Science 274*, 1531-1534.

[117] Roberts, A. W., Davids, M. S., Pagel, J. M., Kahl, B. S., Puvvada, S. D., Gerecitano, J. F., Kipps, T. J., Anderson, M. A., Brown, J. R., Gressick, L., Wong, S., Dunbar, M., Zhu, M., Desai, M. B., Cerri, E., Heitner Enschede, S., Humerickhouse, R. A., Wierda, W. G., and Seymour, J. F. (2016) Targeting BCL2 with Venetoclax in Relapsed Chronic Lymphocytic Leukemia, *N Engl J Med 374*, 311-322.

[118] Chapman, P. B., Hauschild, A., Robert, C., Haanen, J. B., Ascierto, P., Larkin, J., Dummer, R., Garbe, C., Testori, A., Maio, M., Hogg, D., Lorigan, P., Lebbe, C., Jouary, T., Schadendorf, D., Ribas, A., O'Day, S. J., Sosman, J. A., Kirkwood, J. M., Eggermont, A. M., Dreno, B., Nolop, K., Li, J., Nelson, B., Hou, J., Lee, R. J., Flaherty, K. T., McArthur, G. A., and Group, B.-S. (2011) Improved survival with vemurafenib in melanoma with BRAF V600E mutation, *N Engl J Med 364*, 2507-2516.

[119] Erlanson, D. A., Fesik, S. W., Hubbard, R. E., Jahnke, W., and Jhoti, H. (2016) Twenty years on: the impact of fragments on drug discovery, *Nat Rev Drug Discov 15*, 605-619.

[120] Murray, C. W., and Rees, D. C. (2009) The rise of fragment-based drug discovery, *Nat Chem 1*, 187-192.

[121] Erlanson, D. A., McDowell, R. S., and O'Brien, T. (2004) Fragment-based drug discovery, *J Med Chem 47*, 3463-3482.

[122] Scott, D. E., Coyne, A. G., Hudson, S. A., and Abell, C. (2012) Fragment-based approaches in drug discovery and chemical biology, *Biochemistry 51*, 4990-5003.

[123] Harner, M. J., Frank, A. O., and Fesik, S. W. (2013) Fragment-based drug discovery using NMR spectroscopy, *J Biomol NMR 56*, 65-75.

[124] Harner, M. J., Mueller, L., Robbins, K. J., and Reily, M. D. (2017) NMR in drug design, *Arch Biochem Biophys 628*, 132-147.

[125] Schanda, P., Kupce, E., and Brutscher, B. (2005) SOFAST-HMQC experiments for recording two-dimensional heteronuclear correlation spectra of proteins within a few seconds, *J Biomol NMR 33*, 199-211.

[126] Patschull, A. O., Gooptu, B., Ashford, P., Daviter, T., and Nobeli, I. (2012) In silico assessment of potential druggable pockets on the surface of α1-antitrypsin conformers, *PLoS One 7*, e36612.

[127] Schmidtke, P., and Barril, X. (2010) Understanding and predicting druggability. A high-throughput method for detection of drug binding sites, *J Med Chem 53*, 5858-5867.

[128] Hajduk, P. J., Huth, J. R., and Fesik, S. W. (2005) Druggability indices for protein targets derived from NMR-based screening data, *J Med Chem 48*, 2518-2525.

[129] Vasaturo, A., Di Blasio, S., Peeters, D. G., de Koning, C. C., de Vries, J. M., Figdor, C. G., and Hato, S. V. (2013) Clinical Implications of Co-Inhibitory Molecule Expression in the Tumor Microenvironment for DC Vaccination: A Game of Stop and Go, *Front Immunol 4*, 417.

[130] Fong, L., and Small, E. J. (2008) Anti-cytotoxic T-lymphocyte antigen-4 antibody: the first in an emerging class of immunomodulatory antibodies for cancer treatment, *J Clin Oncol 26*, 5275-5283.

[131] Oosterwegel, M. A., Greenwald, R. J., Mandelbrot, D. A., Lorsbach, R. B., and Sharpe, A. H. (1999) CTLA-4 and T cell activation, *Curr Opin Immunol 11*, 294-300.

[132] Metzler, W. J., Bajorath, J., Fenderson, W., Shaw, S. Y., Constantine, K. L., Naemura, J., Leytze, G., Peach, R. J., Lavoie, T. B., Mueller, L., and Linsley, P. S. (1997) Solution structure of human CTLA-4 and delineation of a CD80/CD86 binding site conserved in CD28, *Nat Struct Biol 4*, 527-531.

[133] Schwartz, J. C., Zhang, X., Fedorov, A. A., Nathenson, S. G., and Almo, S. C. (2001) Structural basis for co-stimulation by the human CTLA-4/B7-2 complex, *Nature 410*, 604-608.

[134] Stamper, C. C., Zhang, Y., Tobin, J. F., Erbe, D. V., Ikemizu, S., Davis, S. J., Stahl,

M. L., Seehra, J., Somers, W. S., and Mosyak, L. (2001) Crystal structure of the B7-1/CTLA-4 complex that inhibits human immune responses, *Nature 410*, 608-611.

[135] Darlington, P. J., Kirchhof, M. G., Criado, G., Sondhi, J., and Madrenas, J. (2005) Hierarchical regulation of CTLA-4 dimer-based lattice formation and its biological relevance for T cell inactivation, *J Immunol 175*, 996-1004.

[136] Yu, C., Sonnen, A. F., George, R., Dessailly, B. H., Stagg, L. J., Evans, E. J., Orengo, C. A., Stuart, D. I., Ladbury, J. E., Ikemizu, S., Gilbert, R. J., and Davis, S. J. (2011) Rigid-body ligand recognition drives cytotoxic T-lymphocyte antigen 4 (CTLA-4) receptor triggering, *J Biol Chem 286*, 6685-6696.

[137] He, M., Chai, Y., Qi, J., Zhang, C. W. H., Tong, Z., Shi, Y., Yan, J., Tan, S., and Gao, G. F. (2017) Remarkably similar CTLA-4 binding properties of therapeutic ipilimumab and tremelimumab antibodies, *Oncotarget 8*, 67129-67139.

[138] Iwai, Y., Ishida, M., Tanaka, Y., Okazaki, T., Honjo, T., and Minato, N. (2002) Involvement of PD-L1 on tumor cells in the escape from host immune system and tumor immunotherapy by PD-L1 blockade, *Proc Natl Acad Sci U S A 99*, 12293-12297.

[139] Zarganes-Tzitzikas, T., Konstantinidou, M., Gao, Y., Krzemien, D., Zak, K., Dubin, G., Holak, T. A., and Dömling, A. (2016) Inhibitors of programmed cell death 1 (PD-1): a patent review (2010-2015), *Expert Opin Ther Pat 26*, 973-977.

[140] College, P. a. F. o. H. (2011) Modulators of immunoinhibitory receptor PD-1, and methods of use thereof.

[141] Liu, A., Dong, L., Wei, X. L., Yang, X. H., Xiao, J. H., and Liu, Z. Q. (2016) Development of amino- and dimethylcarbamate-substituted resorcinol as programmed cell death-1 (PD-1) inhibitor, *Eur J Pharm Sci 88*, 50-58.

[142] Riley, J. L. (2009) PD-1 signaling in primary T cells, *Immunol Rev 229*, 114-125.

[143] Cheng, X., Veverka, V., Radhakrishnan, A., Waters, L. C., Muskett, F. W., Morgan, S. H., Huo, J., Yu, C., Evans, E. J., Leslie, A. J., Griffiths, M., Stubberfield, C., Griffin, R., Henry, A. J., Jansson, A., Ladbury, J. E., Ikemizu, S., Carr, M. D., and Davis, S. J. (2013) Structure and interactions of the human programmed cell death 1 receptor, *J Biol Chem 288*, 11771-11785.

[144] Tan, S., Zhang, H., Chai, Y., Song, H., Tong, Z., Wang, Q., Qi, J., Wong, G., Zhu, X., Liu, W. J., Gao, S., Wang, Z., Shi, Y., Yang, F., Gao, G. F., and Yan, J. (2017) An unexpected N-terminal loop in PD-1 dominates binding by nivolumab, *Nat Commun 8*, 14369.

[145] Lee, J. Y., Lee, H. T., Shin, W., Chae, J., Choi, J., Kim, S. H., Lim, H., Won Heo, T., Park, K. Y., Lee, Y. J., Ryu, S. E., Son, J. Y., Lee, J. U., and Heo, Y. S. (2016) Structural basis of checkpoint blockade by monoclonal antibodies in cancer immunotherapy, *Nat Commun 7*, 13354.

[146] Balar, A. V., and Weber, J. S. (2017) PD-1 and PD-L1 antibodies in cancer: current status and future directions, *Cancer Immunol Immunother 66*, 551-564.

[147] Vanella, V., Festino, L., Strudel, M., Simeone, E., Grimaldi, A. M., and Ascierto, P. A. (2017) PD-L1 inhibitors in the pipeline: Promise and progress, *Oncoimmunology 7*, e1365209.

[148] Akbari, O., Stock, P., Singh, A. K., Lombardi, V., Lee, W. L., Freeman, G. J., Sharpe, A. H., Umetsu, D. T., and Dekruyff, R. H. (2010) PD-L1 and PD-L2 modulate airway inflammation and iNKT-cell-dependent airway hyperreactivity in opposing directions, *Mucosal Immunol 3*, 81-91.

[149] Chen, D. S., Irving, B. A., and Hodi, F. S. (2012) Molecular pathways: next-

generation immunotherapy--inhibiting programmed death-ligand 1 and programmed death-1, *Clin Cancer Res 18*, 6580-6587.

[150] Pillai, R. N., Behera, M., Owonikoko, T. K., Kamphorst, A. O., Pakkala, S., Belani, C. P., Khuri, F. R., Ahmed, R., and Ramalingam, S. S. (2018) Comparison of the toxicity profile of PD-1 versus PD-L1 inhibitors in non-small cell lung cancer: A systematic analysis of the literature, *Cancer 124*, 271-277.

[151] Khunger, M., Rakshit, S., Pasupuleti, V., Hernandez, A. V., Mazzone, P., Stevenson, J., Pennell, N. A., and Velcheti, V. (2017) Incidence of pneumonitis with use of PD-1 and PD-L1 inhibitors in non-small cell lung cancer: A Systematic Review and Meta-analysis of trials, *Chest*.

[152] Li, C. W., Lim, S. O., Xia, W., Lee, H. H., Chan, L. C., Kuo, C. W., Khoo, K. H., Chang, S. S., Cha, J. H., Kim, T., Hsu, J. L., Wu, Y., Hsu, J. M., Yamaguchi, H., Ding, Q., Wang, Y., Yao, J., Lee, C. C., Wu, H. J., Sahin, A. A., Allison, J. P., Yu, D., Hortobagyi, G. N., and Hung, M. C. (2016) Glycosylation and stabilization of programmed death ligand-1 suppresses T-cell activity, *Nat Commun 7*, 12632.

[153] Gato-Cañas, M., Zuazo, M., Arasanz, H., Ibañez-Vea, M., Lorenzo, L., Fernandez-Hinojal, G., Vera, R., Smerdou, C., Martisova, E., Arozarena, I., Wellbrock, C., Llopiz, D., Ruiz, M., Sarobe, P., Breckpot, K., Kochan, G., and Escors, D. (2017) PDL1 Signals through Conserved Sequence Motifs to Overcome Interferon-Mediated Cytotoxicity, *Cell Rep 20*, 1818-1829.

[154] Zak, K. M., Grudnik, P., Magiera, K., Dömling, A., Dubin, G., and Holak, T. A. (2017) Structural Biology of the Immune Checkpoint Receptor PD-1 and Its Ligands PD-L1/PD-L2, *Structure 25*, 1163-1174.

[155] Lin, D. Y., Tanaka, Y., Iwasaki, M., Gittis, A. G., Su, H. P., Mikami, B., Okazaki, T., Honjo, T., Minato, N., and Garboczi, D. N. (2008) The PD-1/PD-L1 complex resembles the antigen-binding Fv domains of antibodies and T cell receptors, *Proc Natl Acad Sci U S A 105*, 3011-3016.

[156] LaVallie, E. R., DiBlasio, E. A., Kovacic, S., Grant, K. L., Schendel, P. F., and McCoy, J. M. (1993) A thioredoxin gene fusion expression system that circumvents inclusion body formation in the E. coli cytoplasm, *Biotechnology (N Y) 11*, 187-193.

[157] Chang, H. N., Liu, B. Y., Qi, Y. K., Zhou, Y., Chen, Y. P., Pan, K. M., Li, W. W., Zhou, X. M., Ma, W. W., Fu, C. Y., Qi, Y. M., Liu, L., and Gao, Y. F. (2015) Blocking of the PD-1/PD-L1 Interaction by a D-Peptide Antagonist for Cancer Immunotherapy, *Angew Chem Int Ed Engl 54*, 11760-11764.

[158] Williamson, M. P. (2013) Using chemical shift perturbation to characterise ligand binding, *Prog Nucl Magn Reson Spectrosc 73*, 1-16.

[159] Krajewski, M., Rothweiler, U., D'Silva, L., Majumdar, S., Klein, C., and Holak, T. A. (2007) An NMR-based antagonist induced dissociation assay for targeting the ligand-protein and protein-protein interactions in competition binding experiments, *J Med Chem 50*, 4382-4387.

[160] Müller, I. (2017) Guidelines for the successful generation of protein-ligand complex crystals, *Acta Crystallogr D Struct Biol 73*, 79-92.

[161] Li, K., and Tian, H. (2018) Development of small-molecule immune checkpoint inhibitors of PD-1/PD-L1 as a new therapeutic strategy for tumour immunotherapy, *J Drug Target*, 1-13.

[162] Dhanak, D., Edwards, J. P., Nguyen, A., and Tummino, P. J. (2017) Small-Molecule Targets in Immuno-Oncology, *Cell Chem Biol 24*, 1148-1160.

[163] Chupak, L., and Zheng, X. (2015) Compounds useful as immunomodulators.

BIBLIOGRAPHY

[164] Sasikumar, P., and Ramachandra, M. (2013) Immunomodulating cyclic compounds from the bc loop of human pd1.

[165] Miller, M. M. P., NJ, US), Mapelli, Claudio (Langhorne, PA, US), Allen, Martin Patrick (Flemington, NJ, US), Bowsher, Michael S. (Prospect, CT, US), Boy, Kenneth M. (Durham, CT, US), Gillis, Eric P. (Cheshire, CT, US), Langley, David R. (Meriden, CT, US), Mull, Eric (Guilford, CT, US), Poirier, Maude A. (Pennington, NJ, US), Sanghvi, Nishith (Franklin Park, NJ, US), Sun, Li-qiang (Glastonbury, CT, US), Tenney, Daniel J. (Madison, CT, US), Yeung, Kap-sun (Madison, CT, US), Zhu, Juliang (North Haven, CT, US), Reid, Patrick C. (Tokyo, JP), Scola, Paul Michael (Glastonbury, CT, US). (2014) MACROCYCLIC INHIBITORS OF THE PD-1/PD-L1 AND CD80(B7-1)/PD-L1 PROTEIN/PROTEIN INTERACTIONS, BRISTOL-MYERS SQUIBB COMPANY, United States.

[166] Fu, J., Malm, I. J., Kadayakkara, D. K., Levitsky, H., Pardoll, D., and Kim, Y. J. (2014) Preclinical evidence that PD1 blockade cooperates with cancer vaccine TEGVAX to elicit regression of established tumors, *Cancer Res 74*, 4042-4052.

[167] Jackson, C. M., Kochel, C. M., Nirschl, C. J., Durham, N. M., Ruzevick, J., Alme, A., Francica, B. J., Elias, J., Daniels, A., Dubensky, T. W., Lauer, P., Brockstedt, D., Baxi, E. G., Calabresi, P. A., Taube, J. M., Pardo, C. A., Brem, H., Pardoll, D. M., Lim, M., and Drake, C. G. (2015) Systemic Tolerance Mediated by Melanoma Brain Tumors is Reversible by Radiotherapy and Vaccination.

[168] Nemunaitis, J. (2005) Vaccines in cancer: GVAX, a GM-CSF gene vaccine, *Expert Rev Vaccines 4*, 259-274.

[169] Duraiswamy, J., Freeman, G. J., and Coukos, G. (2013) Therapeutic PD-1 pathway blockade augments with other modalities of immunotherapy T-cell function to prevent immune decline in ovarian cancer, *Cancer Res 73*, 6900-6912.

[170] Thorne, N., Auld, D. S., and Inglese, J. (2010) Apparent activity in high-throughput screening: origins of compound-dependent assay interference, *Curr Opin Chem Biol 14*, 315-324.

[171] Frank, A. O., Vangamudi, B., Feldkamp, M. D., Souza-Fagundes, E. M., Luzwick, J. W., Cortez, D., Olejniczak, E. T., Waterson, A. G., Rossanese, O. W., Chazin, W. J., and Fesik, S. W. (2014) Discovery of a potent stapled helix peptide that binds to the 70N domain of replication protein A, *J Med Chem 57*, 2455-2461.

[172] Perry, E., Mills, J., Zhao, B., Wang, F., Sun, Q., Christov, P., Tarr, J., Rietz, T., Olejniczak, E., Lee, T., and Fesik, S. (2019) Fragment-based screening of programmed death ligand 1 (PD-L1), Bioorganic and Medicinal Chemistry Letters